

Synthesis of Manganese-Based Electrode Materials Prepared by a Novel Dynamic
Floating Electrodeposition (DFE) Method for Energy Storage Devices

by

Mingwen Gao

A thesis submitted in partial fulfillment of the requirements for the degree of

Doctor of Philosophy

in

Materials Engineering

Department of Chemical and Materials Engineering

University of Alberta

Abstract

Electrochemical energy storage and conversion devices such as batteries and supercapacitors have been widely applied in many different fields. Electrode materials play a key role in improving the electrochemical performance of energy storage devices. Among various electrode materials, Mn-based electrode materials have attracted considerable interests, however the complicated methods for synthesizing nano-sized manganese-based materials hinder their commercialization. The aim of this thesis is to cultivate an efficient method, Dynamic Floating Electrodeposition (DFE), to synthesize high performance – manganese based electrode materials. The method can be widely used to fabricate MnO_x , MnCO_3 , Cobalt-doped MnCO_3 and LiMn_2O_4 crystals.

In this research, carbon nanotubes (CNTs) were added into fabrication systems to improve the electrochemical performance of the final products. CNTs were processed in an acidic solution to obtain functionalized CNTs. Nano-crystal active materials can only be electrodeposited on the walls of functionalized CNTs. MnO_2 -CNT composites can deliver a superior electrochemical performance when used as an anode of Lithium Ion Batteries (LIBs). The capacity of MnO_2 -CNT can achieve to 1003 mAh/g, which is close to the theoretical capacity of MnO_2 , 1230 mAh/g. The mechanism of the charging-discharging process is also discussed to gain a better understanding of the

MnO₂-CNTs composites' electrochemical behavior.

A one-step process, Dynamic Floating Electrodeposition (DFE), was developed to synthesize graphene-wrapped MnCO₃ mesoporous single crystals (MSCs). In this method, graphene oxide sheets (GOs) were added into electrolytes. The electrodeposition was made through a special setup that can simultaneously achieve the following three goals: the reduction of GOs to reduced graphene oxides (RGOs), the deposition of MnCO₃ on RGOs and the wrapping of MnCO₃ by RGOs. The as-deposited MnCO₃ was characterized to be submicron single crystals and highly porous. Graphene-wrapped MnCO₃ MSCs delivered more than 1,000 mAh/g after 130 cycles, demonstrating their significant potential to be used as anodes in LIBs. It is the first time that such a high performance has been achieved on MnCO₃ for lithium-ion storage.

The graphene-wrapped MnCO₃ MSCs synthesized through DFE were electrochemically converted to graphene-wrapped amorphous (GWA) MnO_x. The latter was investigated as electrodes for a pseudocapacitor. Such GWA manganese oxide composites showed distinct microstructural features between 0.7 – 2.8 V. The highest capacitance was measured to be 430 F/g at a sweeping rate of 0.2 mV/s. A capacitance of 200 F/g was also obtained under a high sweeping rate of 10 mV/s. The capacitance of GWA manganese oxide composites can maintain 86% even after 2,000 cycles. It was found, for the first time, that GWA manganese oxide composites

showed high pseudo-capacitive performance in the potential range of 0.7 – 2.8 V.

In order to further explore the potential of the DFE method in fabricating electrode materials, cobalt-containing compounds were introduced into an electrodeposition solution to fabricate Co-doped MnCO_3 . Different cobalt-doped Co- MnCO_3 crystals were successfully fabricated, and the morphology of the Co- MnCO_3 crystals could also be altered by adjusting the conditions of electro-deposition. The dumbbell-shaped Co- MnCO_3 structure exhibited outstanding electrochemical performance as an anode for LIBs. The specific capacities can reach to 1000 mAh/g at 100 mA/g current density, and 400mAh/g at 1000mA/g current density. These doped manganese-carbonate crystals provide a new strategy and possibility for synthesizing advanced electrode materials for LIBs.

Finally, and surprisingly, cathode material LiMn_2O_4 crystals were able to be synthesized using DFE. This is also the first time that spinel LiMn_2O_4 crystals have been synthesized at 210°C under atmospheric pressure in a relatively short processing time (five hours). The eutectic molten salts method was utilized to provide a liquid environment for DFE. By performing electrochemical synthesis using DFE in molten salts, porous spinel LiMn_2O_4 crystals were fabricated and characterized. The synthesized final products exhibited good rate capability. The specific discharge capacity reached 117, 63 and 45 mAh/g at 1, 2 and 4C, respectively. The good rate performance and good cyclability are believed to be rooted to the graphene-wrapped

porous structure, which is the one of the prominent features of DFE.

This thesis cultivated the method for synthesizing nanostructured Mn-based materials. All of the materials displayed superior electrochemical performances because of their unique structure and morphology. It is believed that this research will further the development of advanced nanostructured Mn-based electrode materials, improving the performance of batteries and pseudocapacitors.

Preface

This thesis is an original work by Mingwen Gao. Chapter 3 of this thesis has been published as X. Cui, R. Wang, T.Wang, and Professor W. Chen, “Graphene-Wrapped Mesoporous MnCO_3 Single Crystals Synthesized from Dynamic Floating Electrodeposition Method for High Performance Lithium-ion Storage” Journal of Materials Chemistry A - Royal Society of Chemistry, Volume 3, 21 July 2015, Pages 14126-14133. I was responsible for the data collection and analysis as well as the manuscript composition. R. Wang, and T.Wang assisted with the electrodes preparation. X. Cui contributed to manuscript edits. Professor W. Chen was the supervisory author and was involved with concept formation and manuscript composition. Chapter 4 of this thesis was submitted to Journal of Electrochemical Society. I was responsible for the data collection and analysis as well as the manuscript composition. Professor W. Chen was the supervisory author and was involved with concept formation and manuscript composition.

The data analysis and manuscript composition work in chapter 2, Chapter 5 and chapter 6 are my original work as well as the literature review in chapter 1.

Acknowledgements

Foremost, I would like to acknowledge my supervisor, Prof. Weixing Chen, for his superior supervision and mentoring during my PhD research program. I was fortunate to have a wonderful and supportive advisor who introduced me to the field of materials science and electrochemistry and provided hands-on instruction on materials characterization techniques. His support, encouragement and patience were very important in helping me to complete this thesis.

I am grateful to Dr. Xinwei Cui, Dr. Tianfei Wang, Dr. Xiaojing Liu, Dr. Xiaotian Zhang and Master Renfei Wang for their many contributions, constructive discussions and suggestions on lithium ion batteries and supercapacitor fields.

I would like to acknowledge research funding from the Natural Sciences and Engineering Research Council of Canada (NSERC).

I would like to acknowledge Dr. Jian Chen and Greg Popowich for their generous help and discussions on transmission electron microscopy (TEM). I would also like to thank the many technical contributions of Dr. Shihong in scanning electron microscopy (SEM), Dr. Changan He, and Dr. Dimitre Karpuzov in X-ray photoelectron spectroscopy (XPS).

I am very grateful to my wife, Yaying Shen. This thesis work would not have been finished without her love, support and encouragement.

Table of Contents

Introduction.....	1
1 Chapter 1 Literature review	4
1.1 Energy Crisis and Electrochemical Storage Systems	4
1.2 Manganese Oxides.....	6
1.2.1 Manganese oxides as an electrode material for primary batteries	6
1.2.2 Mn-based oxides as electrode materials for rechargeable Li-ion batteries.....	11
1.2.3 Mn-based oxides as electrode materials for pseudocapacitors.....	20
1.3 MnCO ₃	25
1.4 Carbon Materials.....	28
1.4.1 Carbon nanotube for LIBs and ECs	30
1.4.2 Graphene for LIBs and ECs.....	35
1.5 Synthesis Method.....	39
1.6 Motivation.....	44
1.7 References.....	46
2 Chapter 2 Electrochemical deposition of MnO₂ on CNT.....	51
2.1 Introduction.....	51
2.2 Experimental methods	53
2.3 Results and Discussion	57
2.3.1 The type and morphologies of manganese oxide being plated.....	57
2.3.2 Effect of electrodeposition conditions on the deposition of manganese oxide.....	61
2.3.3 Charging and discharging performance of MnO ₂ - CNTs composite electrodes for lithium ion battery.....	66
2.4 Conclusion	71
2.5 References.....	72
3 Chapter 3 Electrochemical deposition MnCO₃ on Reduced Graphene Oxides for LIBs.....	73
3.1 Introduction.....	73
3.2 Experimental Procedure.....	75
3.2.1 Material synthesis.....	75
3.2.2 Characterization.....	77
3.2.3 Electrochemical measurement	78
3.3 Results and discussion	79
3.3.1 Dynamic flowing electrodeposition	79
3.3.2 Superior electrochemical performance of graphene-wrapped MnCO ₃ MSCs	89

3.3.3 Structural advantages from graphene-wrapped MnCO ₃ MSCs	93
3.4 Conclusions.....	102
3.5 References.....	104
4 Chapter 4 Electrochemical deposition of MnO_x on Reduced Graphene Oxides for Pseudo-capacitive Lithium-ion Storage.....	106
4.1 Introduction.....	106
4.2 Experimental Method	108
4.2.1 Material synthesis.....	108
4.2.2 Characterization.....	110
4.2.3 Electrochemical measurement	110
4.3 Results and Discussion	111
4.3.1 Morphology and structure	111
4.3.2 Electrochemical performance.....	117
4.3.3 Pseudo-capacitive lithium-ion storage.....	120
4.3.4 Lithium-ion pseudo-capacitors (LIPC)	125
4.4 Conclusion	128
4.5 References.....	129
5 Chapter 5 Electrochemical Deposition of Co-MnCO₃ on Reduced Graphene Oxides for LIBs	131
5.1 Introduction.....	131
5.2 Experimental Procedure.....	133
5.2.1 Material synthesis.....	133
5.2.2 Characterization.....	134
5.2.3 Electrochemical measurement	135
5.3 Results.....	136
5.3.1 Synthesis and Morphology Analysis.....	136
5.3.2 Structural analysis	143
5.3.3 Electrochemical performance of Co-MnCO ₃ as a cathode in LIBs.....	148
5.4 Discussion: Crystal Transformation Mechanism.....	151
5.5 Conclusions.....	155
5.6 References.....	156
6 Chapter 6 Electrochemical deposition of LiMn₂O₄ on Reduced Graphene Oxides for LIBs	158
6.1 Introduction.....	158
6.2 Experimental.....	161
6.2.1 Material synthesis.....	161
6.2.2 Characterization.....	162
6.2.3 Electrochemical measurement	163
6.3 Results and Discussion	163

6.3.1 Synthesis and structural analysis.....	163
6.3.2 Morphology.....	166
6.3.3 Electrochemical performance of LiMn ₂ O ₄ Crystals	171
6.3.3 Discussion of Morphology Mechanism.....	174
6.4 Conclusions.....	177
6.5 References.....	178
7 Chapter 7 General conclusions and recommendations.....	180
7.1 Dynamic Floating Electrodeposition (DFE) for the synthesis of manganese-based electrode materials	180
7.2 Electrochemical evaluations of electrode materials synthesized by Dynamic Floating Electrodeposition.	182
7.3 Recommendations.....	184

List of Tables

Table 1-1. Electrochemical reactions, potential, and discharge capacity of selected primary batteries.	10
Table 1-2. Electrochemical reactions, potential, and discharge capacity of Mn-base oxides as electrode materials of LIBs.	14
Table 2-1. d-spacing and Miller indices of these rings.	61
Table 5-1. Mn:Co atom ratio of Co-doped MnCO ₃ obtained at different electrodeposition conditions as determined by EDX.....	137

List of Figures

Figure 1-1. (a) Estimated renewable energy share of global electricity production. (b) World net electricity generation from renewable power by fuel, 2012-40.	5
Figure 1-2. (a) Schematic presentation of the solid phase during the discharge of MnO_2 , (b) polyhedron crystal structure of $\alpha\text{-MnO}_2$, (c) polyhedron crystal structure of $\beta\text{-MnO}_2$, (d) polyhedron crystal structure of $\gamma\text{-MnO}_2$	8
Figure 1-3. The discharging curves of $\alpha\text{-MnO}_2$, $\beta\text{-MnO}_2$ and $\gamma\text{-MnO}_2$ crystals when they are used as the cathode of lithium ion batteries (LIBs).....	9
Figure 1-4. Schematic illustration of the reaction in an LIB.....	12
Figure 1-5. (a) Spinel crystal structure of LiMn_2O_4 . (b) Polyhedral lattice structure of LiMn_2O_4 where Li ions exist at 8a tetrahedral sites. (c) Polyhedral lattice structure of LiMn_2O_4 where Li ions exist at 16c octahedral sites.	18
Figure 1-6. Schematic illustration of the reaction in a supercapacitor.	22
Figure 1-7. Synthesis of Li-Mn-O mesocrystals with controlled crystal phases through topotactic transformation of MnCO_3	26
Figure 1-8. Schematic of lithium intercalation in graphite. (a) Lithium is inserted in every second carbon hexagon and (b) between the graphite layers.	30
Figure 1-9. Atomic structure of carbon nanotubes, (a) schematic diagram showing how a graphene sheet is “rolled” according to a pair of chiral vectors, (b) zig-zag (n,0) (c) chiral (n,m) and (d) armchair (n,n).....	31
Figure 1-10. Volume change effects associated with the charge and discharge process of metal alloy electrodes in lithium cells. (a) Scheme of Li ion insertion and related volume change during discharge. (b) SEM image of Li-Si before and after cycling (right). (c) Comparison of volume changes of difference materials.	33
Figure 1-11. Schematic of structural models of graphene/metal oxide composites: (a) Anchored model. (b) Wrapped model. (c) Encapsulated model. (d) Sandwich-like model. (e) Layered model. (f) Mixed model. Red: metal oxide particles; Blue: graphene sheets.....	38
Figure 2-1. Tree-electrodes cell configuration for electrodeposition.	54
Figure 2-2. The morphology of the CNT before and after coating with manganese oxides from TEM bright field results. (a) Morphology of CNT without coating. (b) Morphology of CNT after coating with manganese oxide. (c) Morphology of manganese oxide deposited on stainless steel without CNTs.	58
Figure 2-3. EDS spectrum of the CNT after electrodeposition.	60
Figure 3-1. (a) A schematic illustration of the dynamic floating electrodeposition method. SEM images of (b) the novel composite, (c) the graphene wrapping structure, and (d) the mesoporous structure.	79
Figure 3-2. (a) The setup of the comparative experiment, in which the electrolyte was separated by a membrane at the center. Parameters were controlled as same as DFE method in Figure 3-1(a). (b) XPS and (c) TEM analyses of the products collected from electrodes. .	82
Figure 3-3. TEM and EDX analyses of the products collected from the plating solution of 0.3 M MnSO_4 and 0.3 M sodium EDTA. All other parameters were controlled exactly the same	

as those in DFE method in Figure 3-1(a).	83
Figure 3-13. (a) TEM and (b) selected-area diffraction of graphene-wrapped MnCO ₃ MSCs after 10 cycles. (c) TEM and (d) selected-area diffraction of nc-MnCO ₃ -RGO after 10 cycles.	99
Figure 4-1. TEM morphology of precursor MnCO ₃ MSCs. (a) TEM morphology of MnCO ₃ MSCs and its electron diffraction pattern. (b) HTEM morphology of MnCO ₃ MSCs from JEOL JEM-2100 with LaB6 cathode	112
Figure 4-2. (a) Mn 3s high-resolution spectrum of GWA MnO _x composites at 2.8 V vs Li/Li+. (b) Mn 3s high-resolution spectrum of GWA MnO _x composites at 0.7 V vs Li/Li+. (c) Secondary SEM image of GWA MnO _x composites. (d) Backscattered SEM image of GWA MnO _x composites. (e, f) TEM images of GWA MnO _x composites and the electron diffraction pattern of GWA MnO _x composites is shown in (e).	113
Figure 4-3. XPS results for the precursor of MnCO ₃ MSCs (a), Mn 3s high-resolution spectrum of MnCO ₃ MSCs composites. (b), Comparison of C1s high-resolution spectrum for GMA MnO _x and MnCO ₃ MSCs indicating disappearance of carbonated group (-CO ₃).	115
Figure 4-4. (a) Cyclic voltammetric curves at different sweeping rates from 0.2 mV/s – 1.0mV/s. (b) Cyclic voltammetric curves at different sweeping rates from 5mV/s – 20mV/s. (c) Capacitance of GMA MnO _x and nano-crystalline MnO ₂ -RGO at different sweeping rates . (d) CV curves of GMA MnO _x and nano-crystalline MnO ₂ -RGO at 0.2 mV/s sweeping rate and same voltage window.	118
Figure 4-5. (a) b-value determination of the peak anodic and cathodic currents on different log(sweep rates). (b) Capacitance versus $v^{-1/2}$ for the separation of diffusion-controlled capacitance and capacitive-controlled capacitance. (c) Cycle performance and coulombic efficiency of GWA MnO _x composites for 2000 cycle under 1.0 mV/s sweeping rate.	123
Figure 4-6. (a) Galvanostatic cycling of GWA MnO _x composite electrodes. (b) Comparison of the rate capability of GWA MnO _x composites with Li ₄ T ₅ O ₁₂ and Nb ₂ O ₅ at different C-rates.	126
Figure 4-7. Galvanostatic cycling of MnCO ₃ MSCs from 0.01V-3.0V demonstrating high potential hysteresis.	127
Figure 5-1. Effect of Co:Mn ratio in the electrodeposition electrolyte and electrodeposition current density on the Co content being incorporated into MnCO ₃ .	137
Figure 5-2. (a) SEM result of Co-MnCO ₃ plated under -50mA/cm ² electrodeposition current density with a 4:1 atom ratio of Mn:Co in the electrodeposition solution. (b) High magnification of Co-MnCO ₃ plated under -50mA/cm ² electrodeposition current density with a 4:1 atom ratio of Mn:Co in the electrodeposition solution. (c) TEM result of Co-MnCO ₃ plated under -50mA/cm ² electrodeposition current density with a 4:1 atom ratio of Mn :Co in the electrodeposition solution. (d) Details of the nano crystal tube of Co-MnCO ₃ plated under -50mA/cm ² electrodeposition current density with a 4:1 atom ratio of Mn :Co in the electrodeposition solution. (e) SEM morphology of the MnCO ₃ single crystal synthesized by DFE under -50mA/cm ² . (f) TEM morphology of the MnCO ₃ single crystal synthesized by DFE under -50mA/cm ² .	139
Figure 5-3. (a) TEM bright field result of Co-MnCO ₃ plated with a 1:1 atom ratio of Mn:Co in an electrodeposition solution under -10mA/cm ² electrodeposition current density. (b) TEM bright field result of Co-MnCO ₃ plated with a 4:1 atom ratio of Mn:Co in an	

electrodeposition solution under $-10\text{mA}/\text{cm}^2$ electrodeposition current density. (c) TEM bright field result of Co-MnCO ₃ plated with an 8:1 atom ratio of Mn:Co in an electrodeposition solution under $-10\text{mA}/\text{cm}^2$ electrodeposition current density.	140
Figure 5-4. (a) TEM bright field result of Co-MnCO ₃ plated with a 1:1 atom ratio of Mn:Co in an electrodeposition solution under $-50\text{mA}/\text{cm}^2$ electrodeposition current density. (b) TEM bright field result of Co-MnCO ₃ plated with a 4:1 atom ratio of Mn:Co in an electrodeposition solution under $-50\text{mA}/\text{cm}^2$ electrodeposition current density. (c) TEM bright field result of Co-MnCO ₃ plated with an 8:1 atom ratio of Mn:Co in an electrodeposition solution under $-50\text{mA}/\text{cm}^2$ electrodeposition current density.	142
Figure 5-5. (a) The XRD results of Co-MnCO ₃ crystals with different cobalt content whose Mn:Co atom ratios are 44:1 and 12:1. (b) The polyhedral crystal structure of MnCO ₃ and CoCO ₃	144
Figure 5-6. (a) TEM result of Co-MnCO ₃ plated with a 1:1 atom ratio of Mn:Co in an electrodeposition solution under $-10\text{mA}/\text{cm}^2$ electrodeposition current density. (b) Selected area electron diffraction pattern of sample displayed in (a). (c) TEM result of Co-MnCO ₃ plated with a 4:1 atom ratio of Mn:Co in an electrodeposition solution under $-10\text{mA}/\text{cm}^2$ electrodeposition current density. (d) Selected area electron diffraction pattern of sample displayed in (c). (e) TEM result of Co-MnCO ₃ plated with a 1:1 atom ratio of Mn:Co in an electrodeposition solution under $-50\text{mA}/\text{cm}^2$ electrodeposition current density. (f) Selected area electron diffraction pattern of sample displayed in (e).	148
Figure 5-7. (a) Charging-discharging curves and (b) cyclability data of graphene-wrapped Co-MnCO ₃ crystals within 0.01~3.0 V at 100mA/g. These crystals are plated in under $10\text{mA}/\text{cm}^2$ electrodeposition current density. The Mn:Co ratio in these crystals is 40:1 (c) Charging-discharging curves and (d) cyclability data of graphene-wrapped Co- MnCO ₃ at different current densities, ranging from 100 mA/g to 5,000 mA/g. These crystals are plated under $50\text{mA}/\text{cm}^2$ electrodeposition current density. The Mn:Co ratio in these crystals is 10:1.	149
Figure 5-8. Calculated Pourbaix diagrams for 0.3M sodium citrate solutions with 0.3M CoSO ₄ •7H ₂ O + MnSO ₄ •7H ₂ O at 70°C.	152
Figure 6-1. The schematic diagram of DFE in a eutectic molten salt solution.	164
Figure 6-2. XRD results of final products of eutectic electrodeposition under 50, 70 and $100\text{mA}/\text{cm}^2$ electrodeposition current densities. The precursor MnCO ₃ MSCs are shown in blue. XRD patterns of products from 50 and 70 mA/cm^2 electrodeposition current densities are the same, they are Mn ₂ O ₃ crystals. The XRD peaks of the product from $100\text{mA}/\text{cm}^2$ are shown in red denoted peaks.	166
Figure 6-3. SEM image of as-synthesized graphene-wrapped LiMn ₂ O ₄ crystals by different magnifications. These products are fabricated under $100\text{mA}/\text{cm}^2$ electrodeposition current density at 210°C.	169
Figure 6-4. TEM images of LiMn ₂ O ₄ polycrystalline and LiMn ₂ O ₄ polycrystalline selected area electron diffraction patterns. (a), (c), and (e) are morphology images of products from $100\text{mA}/\text{cm}^2$ electrodeposition current density at 210°C. (b), (d), and (f) are SAED results of samples in the (a), (c), and (e) areas respectively.	171
Figure 6-5. (a) CV results of a porous spinel LiMn ₂ O ₄ electrode at a scan rate of 0.50 mV/s. (b) Galvanostatic charge/discharge curves of the porous spinel LiMn ₂ O ₄ crystals from the	

first to 10 th cycles. (c) Galvanostatic discharge curves of the porous spinel LiMn ₂ O ₄ crystals at different discharging rates. (d) Cycle performance of porous spinel LiMn ₂ O ₄ crystals under 1C rate.	173
Figure 6-6. (a) TEM image of samples from the eutectic molten salt electrodeposition process after an hour reaction under 100mA/cm ² electrodeposition current density at 210°C. (b) SAED result of samples from the area as shown in (a). (c) TEM image of samples from eutectic molten salt electrodeposition process after a two-hour reaction under 100mA/cm ² electrodeposition current density at 210°C. (d) SAED result of samples from the area as shown in (c).....	175
Figure 6-7. The schematic diagram of the porous LiMn ₂ O ₄ polycrystalline formation process.	177

Introduction

The present energy economy is mainly based on fossil fuels which have caused a lot of issues such as the emission of CO₂, global warming and air pollution. It is critically necessary to develop a new sustainable energy supply to replace traditional fossil fuels. Electrochemical energy storage devices such as lithium ion batteries (LIBs) and electrochemical supercapacitors (ESs) are the most popular devices to store renewable energy and transform it to electricity.

Of a wide variety of rechargeable batteries, LIBs take up the greatest share of the rechargeable battery market because of their high energy density, stable working voltage and long cycle life without memory effect. Memory effect is the phenomena by which batteries lose their maximum energy capacity if they are repeatedly recharged after being only partially discharged. However, it is becoming increasingly difficult for current commercial LIBs, which are based on the LiCoO₂ cathode and graphite anode, to meet the demand of the rapid pace at which new electronic devices are being developed. Many Mn-based oxides, including manganese oxides anode and layered lithium manganese oxides cathode, have been studied as possible replacements for current LIB electrodes. These manganese-based electrode materials attracted a lot of interest because of their excellent electrochemical performance and natural abundance.

In recent years, ESs have attracted significant attention, mainly due to their high power density, long lifecycle, and bridging function for the power/energy gap of LIBs. which are limited by their slow release of energy within a relatively short time. For the operation of some heavy duty machinery, ESs are essential for providing sufficient power density. There are two kinds of ESs, often categorized as electrical double-layer supercapacitors (EDLCs) and faradaic supercapacitors (FSs) or pseudocapacitors. EDLCs have limited specific capacitance which is closely related to the surface area of electrode materials and is difficult to improve upon. However, FSs can yield much higher specific capacitance than EDLCs because fast redox reactions happen on the surface of electrode materials and make additional contributions to capacitance. Mn-based oxide materials exhibit advantages over graphite or polymers due to their high specific capacitance, convenient synthesis procedures and long cycle life. The morphology, structure and crystallinity of Mn-based materials are also very important for the performance of pseudocapacitors. Consequently, many efforts have been made to synthesize Mn-based crystals with desirable morphologies that could yield better excellent electrochemical performances.

Electrodeposition is an efficient and cost-effective technique to synthesize the metal oxide electrode materials of energy storage devices. The morphology, composition and crystal structure of electrodeposition products can be carefully controlled by adjusting parameters such as temperature, pH value, current density and composition of the electrolyte solution. It is not easy to achieve these features of oxide electrode

using conventional chemical synthesis. A novel electrodeposition method, dynamic floating electrodeposition (DFE), has been developed in this thesis. It has shown great flexibility in modifying the morphology, chemistry and crystal structure of oxide electrode materials. This method combined the advantages of electrodeposition with the features of barrel plating in which materials to be synthesized are floated between the cathode and anode, enabling both oxidation and reduction reactions to occur repeatedly. It is believed that the DFE method may lead to new directions in developing advanced, better-performing electrode materials.

Chapter 1 Literature review

1.1 Energy Crisis and Electrochemical Storage Systems

The daily life of modern society is greatly dependent on fossil fuel-based energy which has caused many problems such as global warming and environmental pollution.¹ Consequently, the average annual temperature of the planet is increasing dramatically, leading to climate changes. CO₂ emissions and acid gases are leading to acid rain and smog, which are damaging our environment and health.

Finding proper renewable power resources has become a popular topic and an urgent task to solve problems caused by the consumption of fossil fuel. Capital for and research into the exploitation of renewable energy resources have increased extensively. Of the main forms of clean electricity generation, the renewable energy technologies of harvesting wind and solar energy are the most mature and widely used. As shown in Figure 1-1 (a)², the share of these renewable energy sources has taken up 22.8% of electricity production all over the world. Solar and wind energy power occupy 4% of the market which has doubled in only four years.^{3,4} Most importantly, there is no sign that indicates the trend of renewable energy sources is stopping or even slowing down; renewable energy is anticipated to increase to 32% of the energy market by 2040 according to the data in Figure 1-1 (b). Therefore, how to efficiently store and transfer energy from renewable sources is more important than ever because most of these resources are unstable, intermittent and highly reliant on weather.

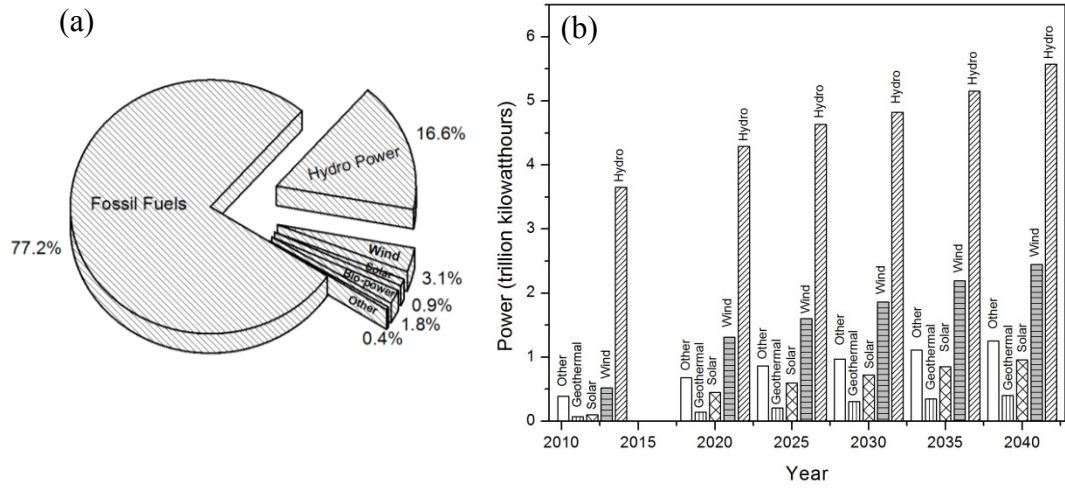


Figure 1-1. (a) Estimated renewable energy share of global electricity production. (b) World net electricity generation from renewable power by fuel, 2012-40.

To improve the storage efficiency and delivering capability of renewable energy, especially from wind and solar power energy, proper energy storage system must be provided. Electrochemical systems such as batteries and electrochemical capacitors are the most commonly used devices to transfer renewable energy to electricity. Batteries and supercapacitors can be also used in vehicles either to work together with a traditional internal combustion engine, which has been a design concept of major automotive manufacturers including Toyota, Ford, Nissan and BMW, or to replace the internal combustion engine, which is what electrical vehicle pioneer Tesla recently did in its newly released Model S electrical SUV. The above design concepts require batteries and supercapacitors that can perform comparably to or better than those in traditional cars. To meet these demands, extensive efforts have been made in

constructing appropriate electrochemical systems for storing and delivering energy and power under different situations. In this thesis, several major electrochemical systems —among them primary batteries, secondary batteries and super capacitors — are introduced and discussed to illustrate the challenges of using electrochemical systems for renewable energy storage and electrical vehicles, and also to address new opportunities to further improve existing electrochemical systems.

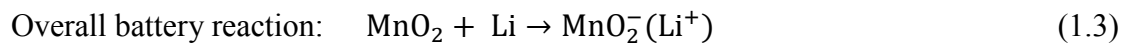
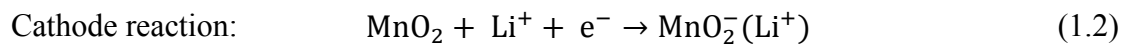
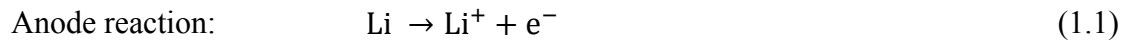
1.2 Manganese Oxides

1.2.1 Manganese oxides as an electrode material for primary batteries

Primary batteries as convenient electrochemical energy storage devices have been widely used in daily life for decades. Products relying on batteries include portable lights, electronic devices and vehicles. Primary batteries are fabricated to be fully charged but cannot be used again after they have been discharged. The types of primary batteries mainly include Mg–MnO₂, Zn–MnO₂, and Li–MnO₂. A lithium electrode has a low weight, low potential (-3.01V) and provides stable performance in a wide range of temperatures compared to a normal hydrogen electrode (NHE). As a result, lithium primary batteries, especially Li-MnO₂ batteries, can offer high voltage, high energy density, a short responding time, long storage time and economical production cost. Thus, these batteries occupy a large share of the primary battery market. In 1975, the Sanyo Electric Company investigated the reaction between lithium and MnO₂ and assembled the first Li-MnO₂ battery. Sanyo licensed the

technology of Li-MnO₂ batteries to other manufacturers all over the world.

The following equations present the discharging reactions of the Li-MnO₂ primary battery.



Here, MnO₂⁻(Li⁺) represents the structure of MnO₂ crystal after a lithium ion is inserted into the crystal lattice. Figure 1-2 (a) is a schematic diagram which shows the solid phase of the cathode material, MnO₂, during the discharging progress. Lithium ions diffuse into the lattice of the MnO₂ crystal from the electrolyte, and form a chemical bond with O²⁻. When the lithium ion combines with oxygen, Mn⁴⁺ is reduced to Mn³⁺. Then, to complete the transport process, the Li⁺ migrates from one tunnel of MnO₂ to another formed by a chain and edge-sharing MnO₆ octahedral as shown in Figures 1- 2 (b), (c), and (d). Accordingly, the diameter of the tunnel affects the diffusion rate of Li⁺ and therefore the performance of the battery.

There are various forms of MnO₂ crystals, which include α-MnO₂^{5,6}, β-MnO₂^{7,8,9} and γ-MnO₂^{10,11,12}, as shown in Figures 1-2 (b), (c) and (d), respectively. The [MnO₆] octahedral is the basic structural unit to build up the crystal. Different crystal

structures of MnO_2 exhibit different performances when they are used as cathodes of a lithium primary battery.

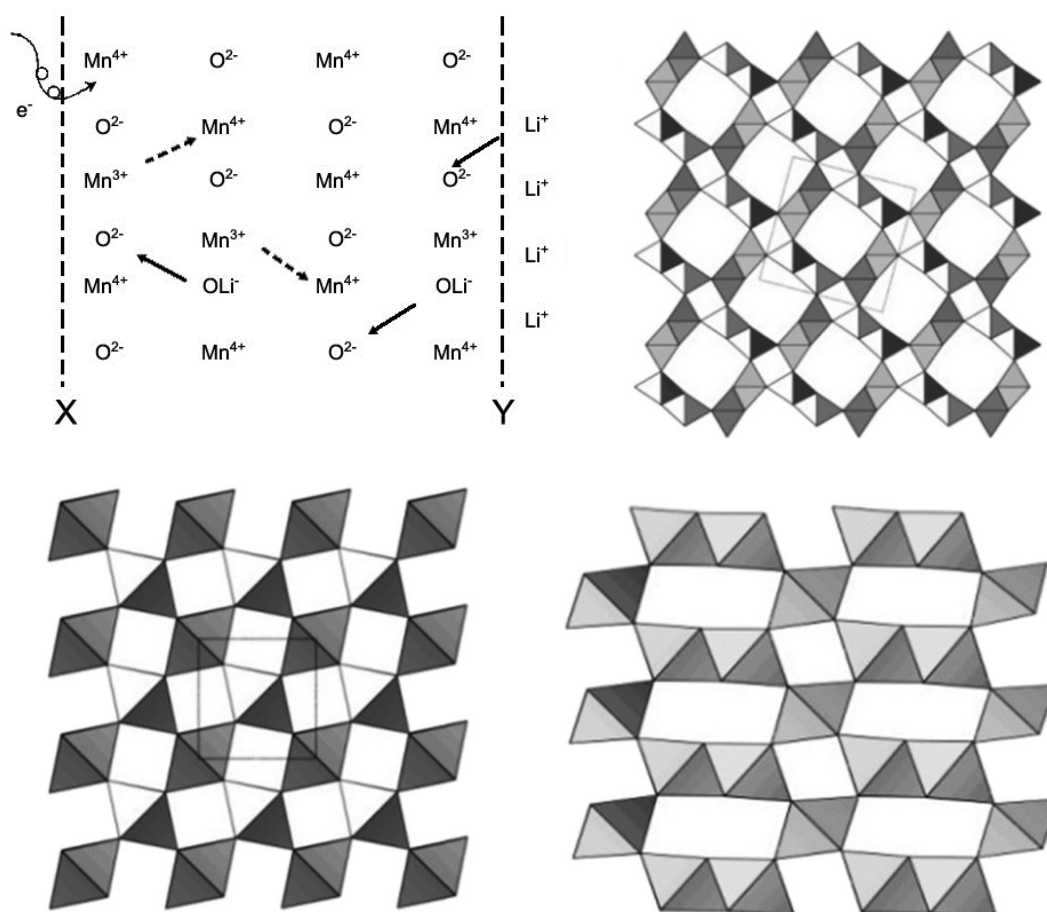


Figure 1-2. (a) Schematic presentation of the solid phase during the discharge of MnO_2 , (b) polyhedron crystal structure of $\alpha\text{-MnO}_2$, (c) polyhedron crystal structure of $\beta\text{-MnO}_2$, (d) polyhedron crystal structure of $\gamma\text{-MnO}_2$.

The discharge curves of different MnO_2 crystals are given in Figure 1-3. The $\beta\text{-MnO}_2$ crystal with the smallest tunnel diameter (1×1) exhibits the lowest capacity among all MnO_2 crystals.¹³ A large tunnel is favorable for ionic diffusion, so nanostructured $\gamma\text{-MnO}_2$ and $\alpha\text{-MnO}_2$ exhibit a higher capacity than that of nanostructured $\beta\text{-MnO}_2$.

However, the tunnels of α -MnO₂ usually contain some other cations and small molecules rather than lithium ions such as NH⁴⁺, K⁺, or H₂O, which are usually from the raw materials in the sol-gel process.¹⁰ These cation and small molecule impurities can make α -MnO₂ stable but also hinder the diffusion and intercalation of lithium ions, leading to poorer performance than that of nanostructured γ -MnO₂. It is generally believed that the oxide crystals affect the performance of primary batteries depending on their crystal structure, crystalline size, and morphology. By adjusting the synthetic methods, the particle size and morphology of the MnO₂ cathode can be controlled. The cost and ease of synthesizing appropriate MnO₂ will directly affect the future of the battery industry.

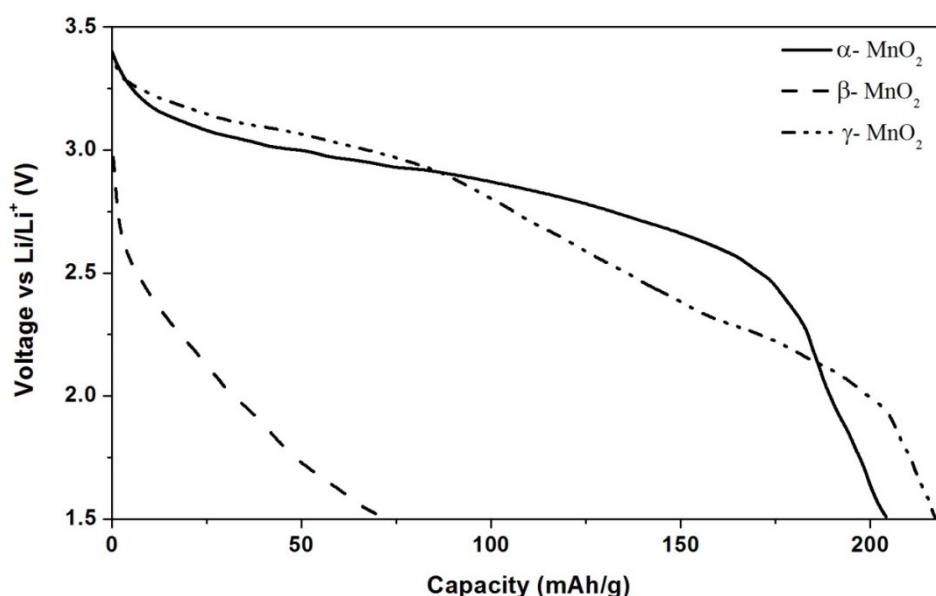


Figure 1-3. The discharging curves of α -MnO₂, β -MnO₂ and γ -MnO₂ crystals when they are used as the cathode of lithium ion batteries (LIBs).

Table 1-1 lists the main properties of MnO₂ when it is used for cathode materials in primary batteries.^{10, 14} The shortcomings of primary batteries are obvious: low

efficiency of active materials, low operating voltage, low capacity and lack of cyclability. Further, the development of nanotechnology led to the fabrication of all kinds of nano-sized MnO_x crystals, such as nano-tube,¹⁵ nano-flake,¹⁶ and nano-cube¹⁷ crystals. All of these materials can improve the capacity and elevate the operating voltage of LIBs, and thus accelerate the development of secondary lithium ion batteries. This is leading to the demise of the primary battery, with its environmental disadvantages (it has to be disposed of after one use and its disposal leads to water and soil pollution).

Table 1-1. Electrochemical reactions, potential, and discharge capacity of selected primary batteries.

Primary batteries	Reactions	Potential (V)	Capacity (mA h/g)
Alkaline Zn– MnO_2 batteries	(+) $\text{MnO}_2 + \text{H}_2\text{O} + \text{e}^- \rightarrow \text{MnOOH} + \text{OH}^-$ (-) $\text{Zn} \rightarrow \text{Zn}^{2+} + 2\text{e}^-$ Overall: $\text{Zn} + 2\text{MnO}_2 + 2\text{H}_2\text{O} \rightarrow 2\text{MnOOH} + \text{Zn}^{2+} + 2\text{OH}^-$	1.20	267
Mg– MnO_2 batteries	(+) $\text{MnO}_2 + \text{H}_2\text{O} + \text{e}^- \rightarrow \text{MnOOH} + \text{OH}^-$ (-) $\text{Mg} \rightarrow \text{Mg}^{2+} + 2\text{e}^-$ Overall: $\text{Mg} + 2\text{MnO}_2 + 2\text{H}_2\text{O} \rightarrow 2\text{MnOOH} + \text{Mg}^{2+} + 2\text{OH}^-$	1.44	768
Li– MnO_2 batteries	(+) $\text{MnO}_2 + x\text{Li}^+ + \text{xe}^- \rightarrow \text{Li}_x\text{MnO}_2$ (-) $\text{Li} \rightarrow \text{Li}^+ + \text{e}^-$ Overall: $x\text{Li} + \text{MnO}_2 \rightarrow \text{Li}_x\text{MnO}_2$	2.65	>210

1.2.2 Mn-based oxides as electrode materials for rechargeable Li-ion batteries

Compared to primary batteries, rechargeable batteries have distinct advantages because of their repeated transfer between electrical and chemical energy. This feature enables renewable energy resources to be stored and transferred without additional environment damage.¹⁸ It also makes it possible to repeatedly charge electrical vehicles using a simple operation. Of the many kinds of rechargeable batteries, rechargeable LIBs are the prevalent form of secondary batteries and take up most of the market share because of their excellent electrochemical performance.^{19,20,21,22} LIBs represent the future of secondary batteries and are further introduced below.

LIBs are light in weight and highly compact. They can work with a voltage of the order of 4V with a specific energy ranging from 100Wh/kg to 265Wh/kg. In their most conventional structure, LIBs are made of a graphite anode and a LiCoO_2 (layered lithium cobalt oxide) cathode, as shown schematically in Figure 1-4. This prototype was developed, mass-produced, and commercialized by Sony Inc. This battery is capable of good performance as well as a high voltage of 4.0V. It can be charged and discharged through the transportation of Li ions between the anode and cathode, with the electron exchange resulting from the insertion and extraction of Li^+ . This battery is also named as rocking chair or swing battery due to charge carriers shuttling back and forth between two intercalating electrodes during the charging and discharging processes..^{23,24}

The following reactions are suggested to occur in the charging process of conventional LIBs composed of a LiCoO₂ cathode and a graphite anode:

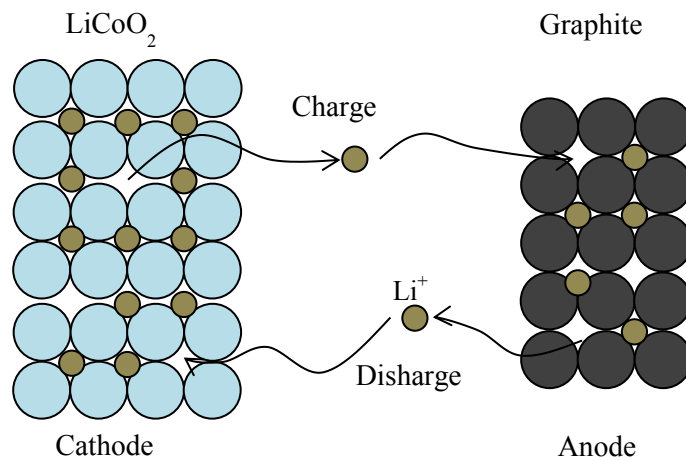
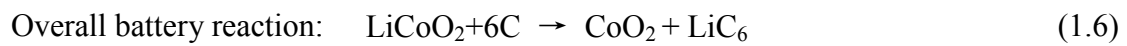
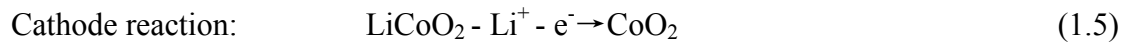


Figure 1-4. Schematic illustration of the reaction in an LIB.

The maximum electric energy that at standard condition can be extracted from any electrochemical cell depends on the change in Gibbs energy of the overall reaction in the cell, ΔG^0

$$\Delta G^0 = -nFE^0 \quad (1.7)$$

Here, F is the Faraday constant, E^0 is the electromotive force, and n is the number of electrons that pass through the circuit. However, the theoretical energy cannot be achieved by a practical battery because of the losses that occur in the cell. These

losses can be classified mainly into losses caused by activation polarization, concentration polarization, and ohmic polarization.

Activation polarization comes from the electrochemical reaction which results in a solid-electrolyte interphase (SEI) film at the surfaces of both electrodes.^{25,26} This SEI film is a protecting layer which is created by electrolyte decomposition and happens mainly during the first few cycles. Concentration gradients are formed at the interface between the electrolyte and the electrode materials due to the natural resistance to mass transport in the cell. Ohmic polarization, commonly referred to as IR drop in potential, is due to the current passing through the internal resistance of the battery. These polarization losses will be more serious with the increasing cycle numbers and can cause the entire battery to fail. Due to these shortcomings, LIBs made of a LiCoO_2 cathode and a graphite anode can hardly satisfy ever-increasing energy demands. Although LIBs have been widely used in cellular phones, laptop computers and hybrid vehicles, these applications and new demands for energy storage due to environment pollution require LIBs to possess better electrochemical properties such as higher energy and power density, better durability, and a longer cycle life. As a result, materials with better conductivity, a wider range of operational temperatures, and a durable crystal structure are highly desirable for the next generation of LIBs. There is an increasing urgency to develop batteries with these properties. Thanks to nano-technology it is possible to improve specific capacity and power density, and to buffer the large volume changes during discharging/charging, thus ensuring a longer cycle life by tailoring electrode materials with a desired morphology and structure.

Mn-based materials are most attractive for rechargeable LIBs not only because of their high theoretical capacity but also because they have varied valence states, a controlled crystal structure and a stable discharging voltage plateau. They can be used as anodes due to the reversible conversion reactions between manganese oxides and Mn metal but also as cathodes in LIBs due to their special layer structure, leading to excellent cyclability.^{27,28,29,30} Table 1-2 lists the electrochemical reactions, plateau potential, and theoretical capacity of Mn-based oxides as electrode materials of LIBs.

Table 1-2. Electrochemical reactions, potential, and discharge capacity of Mn-based oxides as electrode materials of LIBs.

Electrode materials	Reactions	Plateau potential (V)	Theoretical capacity (mA h g ⁻¹)
MnO ₂	$\text{MnO}_2 + 0.92\text{Li}^+ + 0.92\text{e}^- \leftrightarrow \text{Li}_{0.92}\text{MnO}_2$ (2.0–4.5 V)	2.8	284 ³¹
	$\text{MnO}_2 + 4\text{Li}^+ + 4\text{e}^- \leftrightarrow \text{Mn} + 2\text{Li}_2\text{O}$ (0.02–3.3 V)	0.4	1233 ³²
Mn ₃ O ₄	$\text{Mn}_3\text{O}_4 + 8\text{Li}^+ + 8\text{e}^- \leftrightarrow 3\text{Mn} + 4\text{Li}_2\text{O}$	~0.4	936 ³³
MnO	$\text{MnO} + 2\text{Li}^+ + 2\text{e}^- \leftrightarrow \text{Mn} + \text{Li}_2\text{O}$	<0.8	756 ³⁴
o-LiMnO ₂	$\text{LiMnO}_2 \leftrightarrow \text{MnO}_2 + \text{Li}^+ + \text{e}^-$	~4.0	285 ³⁵
		~3.0	
LiNi _{0.5} Mn _{0.5} O ₂	$\text{LiNi}_{0.5}\text{Mn}_{0.5}\text{O}_2 \leftrightarrow \text{Ni}_{0.5}\text{Mn}_{0.5}\text{O}_2 + \text{Li}^+ + \text{e}^-$	3.8	280 ³⁶
O ₂			
LiMn ₂ O ₄	$\text{LiMn}_2\text{O}_4 \leftrightarrow \lambda\text{-MnO}_2 + \text{Li}^+ + \text{e}^-$	~4.0	148 ³⁷
LiMnPO ₄	$\text{LiMnPO}_4 \leftrightarrow \text{MnPO}_4 + \text{Li}^+ + \text{e}^-$	4.1	171 ³⁸

Binary manganese oxides

Research on new anode materials has focused on titanium oxides, manganese oxides, and many kinds of carbon materials like carbon nanotubes, graphene, or amorphous carbon. In this range of materials, binary manganese oxides MnO_x nano crystals are the most attractive negative electrode materials for advanced LIBs because of their lower potential and high cost effectiveness. The lithium insertion potential of Manganese oxides are between 0.4V and 0.7V vs Li/Li^+ , i.e., within the stability window of common organic electrolytes. MnO_x can offer some important advantages in terms of capacity, durability and safety. Its maximum theoretical capacity can be above the 1700 mAh/g associated with a complete $\text{Mn}^{x+} \rightarrow \text{Mn}^0$ reduction. However, the electrochemical performance of MnO_x is also strongly dependent on the structure of crystals and morphology of particles.

MnO_2 as a typical binary manganese oxide was not always used in Li- MnO_2 primary batteries but attempts were made to apply it in Li- MnO_2 secondary batteries because of its layered structure. However, the use of MnO_2 was limited by its poor reversible conversion reaction, which leads to an unsatisfactory cyclability performance. Lithium ions can be easily inserted into MnO_2 to form LiMn_2O_4 , but they are difficult to be extracted out of MnO_2 matrix as discussed in Section 1.1.1. In short, a lithium ion's capacity dramatically decreases after only several cycles. Since Poizot et al. demonstrated that the nanostructure of transition metal oxides can be used in secondary LIBs with decent cycle numbers,³⁹ many efforts have been made to

synthesize different kinds of nano-sized binary manganese oxides for LIBs, from a 1D manganese oxide nanotube,¹⁵ to a 2D manganese oxide nano flake¹⁶ to 3D mesoporous manganese oxide nano spheres.³² All of these attempts have successfully shortened the lithium ion diffusion path, and can better accommodate the volume change, resulting in an improved cycle life.

Nanoporous γ -MnO₂, hollow nanocubes and microspheres synthesized by hydrothermal route combined with thermal treatment can achieve a capacity of 1289 mAh/g.¹⁷ After 20 cycles, the discharge capacities of γ -MnO₂ hollow nanocubes decayed to 656.5 mAh/g. MnO is another anode material widely used in LIBs but has lower valence deliveries and lower capacity compared to other binary manganese oxides. The nano film MnO synthesized by Yu et al. can reach a capacity up to 472 mAh/g.⁴⁰ The porous MnO microspheres achieved a higher capacity at 800 mAh/g and a cycle number greater than 50.⁴¹ The porous MnO nano-flakes exhibited better cyclability, which is more than 100 cycles, but with a 569 mAh/g capacity after cycling.⁴² Mn₃O₄ is also a potential anode material for LIBs, but its low electric conductivity ($\sim 10^{-7}$ – 10^{-8} S cm⁻¹) and significant volume change during cycling limit its capacity. Loading Mn₃O₄ nanoparticles on reduced graphene oxide (rGO) sheets is an effective approach to improve the charge/discharge capacity, rate capability, and cycling stability. The Mn₃O₄-rGO composites showed 780 mAh/g discharge capacities under 400 mA/g current density.³³ The high performance was attributed to the high conductive rGOs which not only enhance the electronic conductivity but also

restrict the growth and aggregation of Mn_3O_4 nanoparticles during cycling. These researches proved that binary manganese oxides are good anode materials for LIBs. Moreover, the size and morphology of crystals can greatly affect their electrochemical performance. Consequently, research on this material focuses on the fabrication processes and synthesis methods suitable to produce manganese oxides with nano-sizes. Attempts are being made to develop crystal structures and grain morphologies combining effective electronic conductive networks with the goal of increasing industrial production and efficiency.

Spinel-type LiMn_2O_4

Another Mn-based layer structure, LiMn_2O_4 crystal, has been extensively investigated and commonly recognized as a promising candidate for cathode material of LIBS from among a variety of lithium manganese oxides, because it is more structurally durable and economically comparable to Co- and Ni-based material. Spinel-structured LiMn_2O_4 can deliver high-power density and more cycle numbers due to its stable host structure, which was found in the 1980s as shown in Figure 1-6 (a).^{43,44} In a spinel structure, $\text{Mn}^{3+/4+}$ and Li^+ occupy the 16d octahedral and the 8a tetrahedral sites, respectively, of the cubic close-packed oxygen array. The stable 3d $[\text{Mn}_2]\text{O}_4$ spinel structure allows lithium ions insert into and extract from the tetrahedral sites repeatedly, because the two $[\text{Mn}_2]\text{O}_4$ groups share one edge and are strongly bonded together. Furthermore, the spinel structural can provide good conductivity because these interstitial sites are interconnected. Lithium ions move between interstitial sites

by an adjacent 16c site as shown in Figures 1-5 (b) and (c).

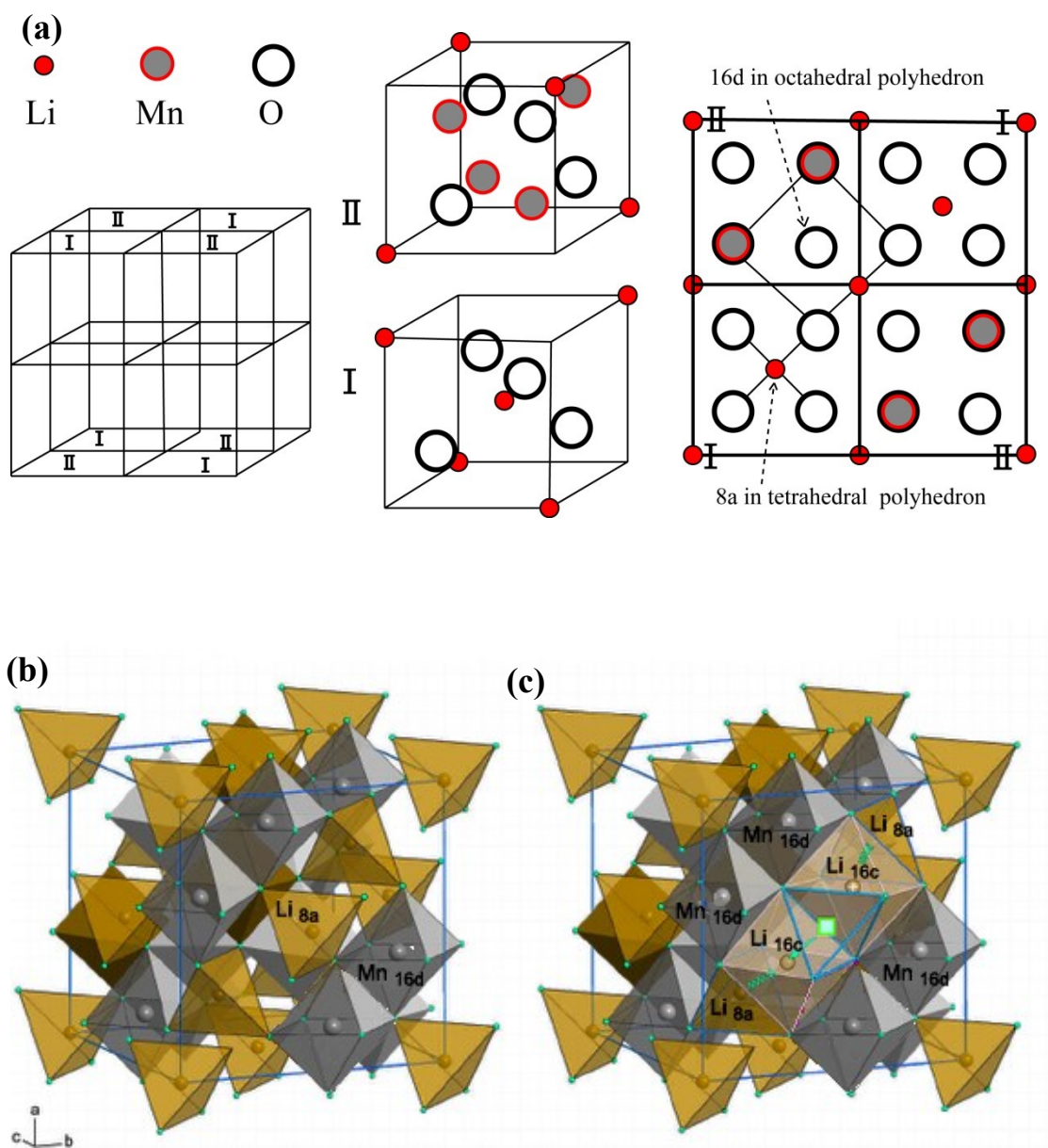


Figure 1-5. (a) Spinel crystal structure of LiMn_2O_4 . (b) Polyhedral lattice structure of LiMn_2O_4 where Li ions exist at 8a tetrahedral sites. (c) Polyhedral lattice structure of LiMn_2O_4 where Li ions exist at 16c octahedral sites.

Spinel LiMn_2O_4 was successfully utilized as a cathode in LIBs vs graphite anode

around 1990s where it was preferable to a graphite anode because of its superior electrochemical performance including a high operating voltage plateau (4.1 V vs Li/Li⁺), high power density, and a long lifecycle.^{45, 46} Recently, in order to further improve their cyclability and rate capability, different morphologies of spinel LiMn₂O₄ were synthesized. The Bruce group synthesized porous nano-LiMn₂O₄ spinel using a one-pot resorcinol-formaldehyde route.⁴⁷ The initial capacity reached 131 mA h/g and remained at 118 mAh/g after 200 cycles at 0.5 C. Porous LiMn₂O₄ nano particles can provide better reversible electrochemical reactions because they can cushion the stress during lithiation/delithiation as mentioned in Chapter 1.2.1. The porous structure also allows electrolyte diffusing inside of the particles. Cui's group prepared LiMn₂O₄ nanorods using a solid-state reaction with β-MnO₂ nanorods as a precursor.⁴⁸ These nanorods delivered a capacity of 100 mAh/g at 1 C with a capacity retention of 85% after 100 cycles. Here, the 1D nanostructure is an advantage because it can provide a 1D electron transport path to elevate the electrical conductivity of the whole electrode material and increase the surface area to create more active sites for the electrolytes to make contact. Bak et al. fabricated LiMn₂O₄-rGO nanocomposites with a microwave-assisted hydrothermal method. The composites exhibited high specific capacities of 137 mAh/g at 1 C, 117 mAh/g at 50C, and 101 mAh/g at 100C⁴⁹. Bak's is a typical method used to improve the performance of a cathode by combining spinel LiMn₂O₄ crystal with other carbon allotropes. However, it is still difficult to achieve the goal of one-step synthesis at low cost. Obtaining an appropriate structure involves multiple steps

including heating to temperatures as high as 700 °C. The complexity and high energy cost of the synthesis method makes spinel LiMn_2O_4 commercialized as a cathode of LIBs. It is necessary to develop more efficient ways to fabricate desired spinel LiMn_2O_4 crystals, especially at lower temperatures.

1.2.3 Mn-based oxides as electrode materials for pseudocapacitors

Primary batteries and secondary LIBs can provide high energy for a variety of applications such as watches (0.1–0.5 Wh), mobile phones (2–4 Wh), and laptop computers (30–100Wh). However, the intrinsic limitation of LIB is their low power density, which hinders their utilization in some industrial applications such as electric cars (5–10 kW h), buses (a few 100 kW h) and even electric grids.^{50,51} In contrast, another category of energy storage devices - ESs - has been attracting much attention lately, although the first patent for ES was filed in 1957.⁵² Electrochemical supercapacitors can provide higher power density and longer cycle life to boost the application of batteries in electric vehicles by providing the necessary power for acceleration and storing additional brake energy. Further developments have led to the conclusion that ES can play an important role in complementing batteries in renewable energy storage functions by transferring intermittent natural power to stable electrical power for batteries. ES can protect batteries from over charging or discharging and ensure that the operation voltage of batteries is in a safe range, and still satisfy the demand of industrial applications when incorporated with batteries. It

is expected that ES will bridge the energy gap between traditional capacitors and batteries.

In terms of design and manufacturing, the ES structure is similar to that of batteries. As shown in Figure 1-6, an ES consists of two electrodes, an electrolyte, and a separator which isolates the two electrodes. Materials in both electrodes are the most important parts of an ES. In general, materials for ES electrodes need to have a high surface area and high porosity to store a large amount of charge. As shown in Figure 1-5, charges are stored on the surface of both electrodes and separated at the interface between the solid carbon and liquid electrolyte. This interface can be seen as an electrical double-layer capacitor, which can be expressed by the equation below:

$$C = \frac{A\varepsilon}{4\pi d} \quad (1.8)$$

where A is the area of the electrode surface; ε is the medium (electrolyte) dielectric constant, which will be equal to 1 for a vacuum and larger than 1 for all other materials, including gases; and d is the effective thickness of the electrical double layer.

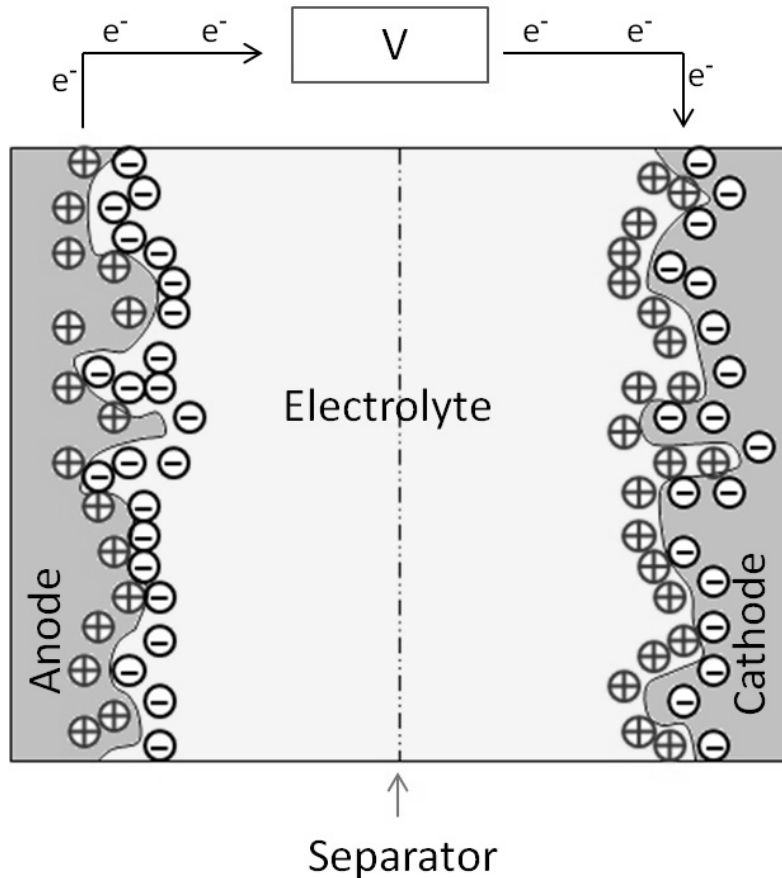


Figure 1-6. Schematic illustration of the reaction in a supercapacitor.

As discussed above, this type of ES is called an electric double-layer capacitor (EDLC), in which the electrode materials, such as porous carbon, are not electrochemically active. This means that there are no redox reactions on the surface of electrode material during charging and discharging but only physical adsorption of ions on a solid/liquid interface. However, these physical charging discharging progresses are not happen in all ESs. Compared to EDLCs there is another type of electrochemical supercapacitor called faradaic supercapacitor (FS) or pseudocapacitor, in which the electrode is made of active materials rather than porous carbon. FSs are electrochemically active and can directly store charges inside of these materials due to

chemical reactions during the charging and discharging processes. The electrode materials of FSs are similar to the electrode materials of batteries but with faster reaction rates and higher rate capability.

Electrode materials for FS can be categorized as porous metals, conducting polymers, and some transition metal oxides, including RuO₂, MnO₂, and Co₃O₄.^{53,54,55,56} Three types of faradaic processes occur at FS electrodes: reversible adsorption (for example, adsorption of hydrogen on the surface of platinum or gold), reversible electrochemical doping–de-doping in conductive polymer-based electrodes, and redox reactions of transition metal oxides (MnO₂, Co₃O₄ and RuO₂).⁵⁷ Validated tests have shown that active materials in FS can efficiently improve the specific capacitance of supercapacitors due to faradaic electrochemical reactions. FS exhibits good capacitance which can be 100 times larger than the capacitance of EDLCs.^{58,59,60} As a consequence, extensive studies have been conducted to develop FS, leading to a new type of asymmetrical electrode configuration FS, which is made of porous carbon and faradaic capacitance materials. In this asymmetrical configuration, FS electrical double-layer capacitance and faradaic capacitance mechanisms are utilized at the same time to improve the overall cell voltage, capacitance, energy, and power density.^{61,62,63}

Transition metal oxides and polymer materials, not graphite, are usually chosen as the candidate materials to make a pseudocapacitors electrode, as graphite has lower

energy density and power density. With their high specific capacitance, convenient synthesis procedure, and long cycle life, Mn-based oxide materials are more useful and practical than graphite and polymers. The working mechanism of Mn-based oxides for pseudocapacitors was first noted in the 1990s and has been continuously improved since then. The faradaic reaction is proposed to occur according to the equation below:⁶⁴



Here X^+ represents alkali metal cations such as Li^+ , Na^+ , and K^+ .

As was discussed in the section on Mn-based materials for LIBs, the morphology, structure, and crystallinity of Mn-based materials are also very important for the performance of pseudocapacitors. The electrode materials with different crystal structures can exhibit different electrochemical performance. The nano-structured α - MnO_2 showed a 165 F/g capacitance⁶⁵, while the amorphous α - MnO_2 was able to deliver about 320 F/g capacitance.⁶⁶ γ - MnO_2 nano-flake films can exhibit 240 F/g⁶⁷, but the δ - MnO_2 synthesized by hydrothermal method showed 150 F/g capacitance.⁶⁸ A specific surface area is critical for the overall performance and always plays an important role in ECs. High specific surface area creates more active sites for electrolytes and improves the overall capacitance. Usually nano-sized particles have a higher specific surface area. 1D MnO_2 nanotube arrays showed good specific

capacitances even under a high charging/discharging rate, which was measured at 245 F/g under 10A/g current density.⁶⁹ A 3D α -MnO₂ nano-flower material delivered a low specific capacitance, which was 90 F/g at 2 mV/s because its specific surface area was only 206 m²/g.⁷⁰ This suggests that the synthesis method and process are crucial to the performance of pseudocapacitors.

1.3 MnCO₃

Despite extensive efforts made in developing manganese oxides materials, researchers are still exploring other types of Mn-based electrode materials that can deliver an appreciable and balanced electrochemical performance. Among Mn-based anode materials, manganese carbonate (MnCO₃) has been investigated in the field of batteries for several decades because it is widely used as a precursor for synthesizing manganese oxides and lithium manganese oxides. In particular, MnCO₃ is used as a template to synthesize metal oxides by thermal conversion with targeted morphologies.^{71,72,73,74} In general, its shape-guiding mechanism makes MnCO₃ a leading and unavoidable material in the LIB research.

Different type of lithium manganese oxides crystals including LiMn₂O₄, Li₂MnO₃, and LiMnO₂-Li₂MnO₃ were fabricated by using MnCO₃ as a precursor because the structure of the final product is greatly dependent on the structure of the precursor.^{75,76,77} MnCO₃ was calcined at above 500°C for six hours to make Mn₅O₈ and was then introduced to a hydrothermal system to react with LiOH. Three kinds of

Li–Mn–O compounds were synthesized by using the Mn_5O_8 intermediate in this hydrothermal process.⁷⁸ Their structures were mainly inherited from Mn_5O_8 but their phases were controlled by the molar ratio of Mn_5O_8 and LiOH in the hydrothermal process as shown in Figure 1-7.⁷⁹ When the LiOH concentration is lower than 80 mol/m^3 , the final product is LiMn_2O_4 . Li_2MnO_3 will be the only phase when the LiOH concentration is higher than 250 mol/m^3 . However, Li_2MnO_3 and LiMnO_2 will be obtained if the concentration of LiOH is 2000 mol/m^3 .

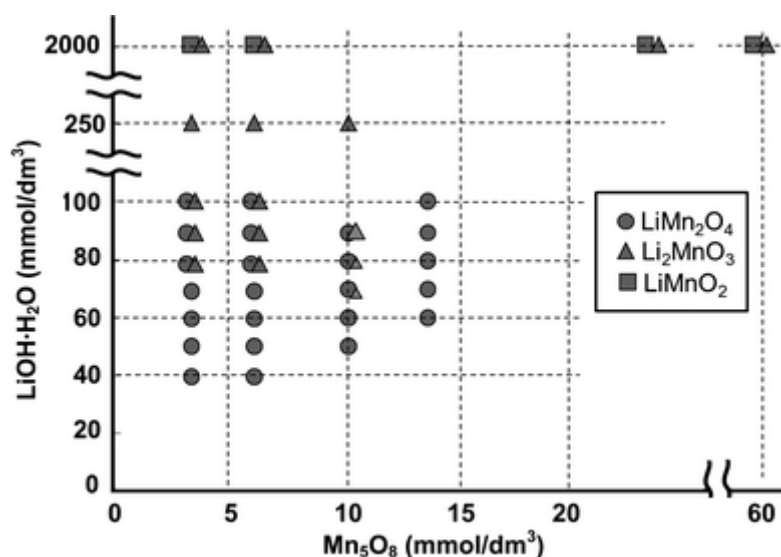


Figure 1-7. Synthesis of Li–Mn–O mesocrystals with controlled crystal phases through topotactic transformation of MnCO_3 .

Co-doped LiMn_2O_4 can also be obtained from Co-doped MnCO_3 according to recent research.^{80,81} The specifically controlled precursor phase, $\text{Mn}_x\text{Co}_{1-x}\text{CO}_3$, can lead to the specific final product of $\text{LiMn}_y\text{Co}_{2-y}\text{O}_4$ with inherited structures. By carefully designing the process of fabrication, Co-doped LiMn_2O_4 can exhibit a stable cycle

performance with less discharge capacity than pure LiMn_2O_4 crystals.

In addition to its precursor role, manganese carbonate is also considered as potential anode material for LIBs. Since Aragón et al. reported their pioneering work on the use of a submicron MnCO_3 compound as an anode material for LIBs⁸² in 2007, considerable efforts have been devoted to improving the electrochemical performance of MnCO_3 by designing MnCO_3 with different shapes, such as nanocubes,⁸³ nanospheres,⁸⁴ and hollow spheres.⁸⁵ However, the rate capability and cycle life of the MnCO_3 material are limited by its poor electrical conductivity and large volume expansion during cycling. Various types of MnCO_3 nano-sized crystals were synthesized to solve this problem. Porous sphere MnCO_3 has been successfully fabricated to deliver 1049 mAh/g capacity under 1A/g current density.⁸⁶ The electrochemical performance of MnCO_3 was improved due to the special porous structure that can buffer volume change and mitigate structure damage because of better strain accommodation.

MnCO_3 can also be used as an electrode material for supercapacitors. Devaraj et al. investigated the performance of MnCO_3 in different water-based electrolytes.⁸⁷ In 0.1M $\text{Mg}(\text{ClO}_4)_2$ EC system 216 F/g capacitance was obtained with a high level of active materials loading. Different capacitance 3 F/g and 159 F/g were obtained when tested in 0.1 M Na_2SO_4 and 6 M KOH systems, respectively. MnCO_3 -based supercapacitors can also provide good reversible and high coulombic efficiency; they

can be charged and discharged over 500 cycles in an aqueous system. MnCO_3 -based supercapacitors has the potential to compete with metal oxides because it is cost-effective, easy to synthesize and has favorable capacitive characteristics.

However, the problem of poor conductivity for MnCO_3 crystals and other manganese-based oxides cannot be solved simply. Although crystals with a porous structure can mitigate the problem of poor conductivity to some extent because of their better electrolyte-particle surface exposure, the intrinsic poor conductivity of MnCO_3 cannot be eradicated. A better approach to improve the conductivity of MnCO_3 might be to add materials with good conductivity, such as conductive polymers or carbon materials including carbon nanotubes (CNTs)^{88,89} and graphene nano sheets (GNS),^{90,91} into MnCO_3 -based electrodes. There are several methods to synthesize MnOx/polymers , MnOx/graphene , $\text{MnCO}_3/\text{graphene}$ and so on. Most of these methods involve directly mixing metal oxides or carbonates with conductive materials. However, these mechanical mixing methods can hardly exhibit advantages of crystals and conductive materials at same time. How to combine their features and reinforce their synergistic effect is still being investigated.

1.4 Carbon Materials

Carbon materials are considered prospective electrode materials for batteries and supercapacitors. Generally, it is believed that carbon materials are abundant and non-toxic, have a low cost, a high specific surface area, good electronic conductivity

and high chemical stability, and can be readily processed. However, the physical and chemical properties of different kinds of carbon allotropes can vary significantly. The specific surface area of graphite powders is around 20 m²/g but the specific surface area of single-wall CNTs (SWNTs) is 1315 m²/g, and the theoretical surface area of graphene is 2630m²/g. The price of these carbon allotropes is also different, depending on their properties and method of fabrication. Among these carbon materials, graphite has the lowest price and has been widely used in batteries for several decades.

Graphite powder is commonly used as an anode material for commercial LIBs because of its low volume expansion and contraction during lithium insertion and extraction (<5%). However, a graphite anode is limited by its relatively low capacity (372 mAh/g) due to its structure. Graphite is composed of different hexagonally bonded sheets of carbon held together by van der Waals forces. The bonding of carbon atoms on same layer (sp² hybridized bonds) is much stronger than the bonding between any two adjacent sheets. Therefore lithium ions have opportunities to insert into the sheets of graphite. This process is named as insertion or intercalation and enable graphite to be used as anodes of LIBs. However, when lithium ions insert into graphite layers, they occupy interstitial sites between two layers of graphite. Once inserted, the lithium ions prevent other lithium ions from occupying adjacent interstitial sites. As consequences, lithium ions cannot occupy every hexagon of graphite layer, it limits the lithium storage ability of graphite as anode of LIBs,^{92, 93}

as the batteries' storage density can only reach 372 mAh/g maximum. Figure 1-8 illustrates the intercalation of lithium ions into graphite.

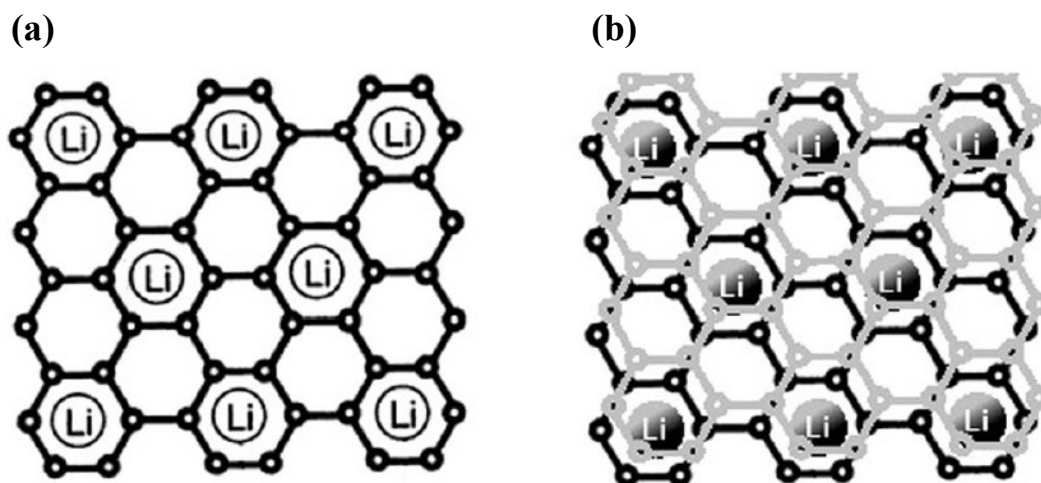


Figure 1-8. Schematic of lithium intercalation in graphite. (a) Lithium is inserted in every second carbon hexagon and (b) between the graphite layers.

1.4.1 Carbon nanotube for LIBs and ECs

As an allotrope of graphite, carbon nanotubes have been proven to be a good anode material for LIBs and ESs due to their unique structure (a one-dimensional cylindrical tubule of graphite sheet), high conductivity when it is zigzag or armchair structure as shown in Figure 1-9, low density, high rigidity (Young's modulus on the order of 1 TPa), and high tensile strength (up to 60 GPa).^{94,95} The discovery of CNTs greatly impacts the science and engineering of carbon materials. Figure 1-9 shows the atomic structures of different types of carbon nanotubes.⁹⁶

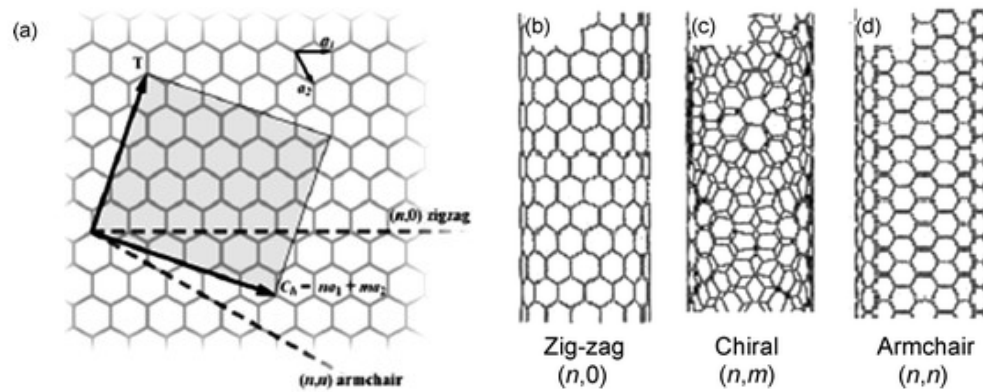


Figure 1-9. Atomic structure of carbon nanotubes, (a) schematic diagram showing how a graphene sheet is “rolled” according to a pair of chiral vectors, (b) zig-zag (n,0) (c) chiral (n,m) and (d) armchair (n,n).

CNT for LIBs

As a prospective anode electrode material for LIBs, the CNT has been extensively investigated. CNTs can have reversible capacities from 300 to 1200 mAh/g,^{97,98,99} significantly higher than those of graphite. One limitation of CNTs as anode of LIBs is their irreversible lithium ion capacity. When CNTs are charged, more lithium ions are inserted into the CNTs than are released upon discharging: that is, a fraction of the lithium ions are consumed instead of being stored. However, chemical treatment can be used to solve this problem and increase the reversible capacities of SWCNTs up to 1000 mAh/g.¹⁰⁰

Another problem when using CNTs as anode of LIBs is the lack of a voltage plateau during discharging. Unlike graphite anodes, CNT anodes typically exhibit broad

changes in voltage as the cell discharges. This can make it difficult for CNT anodes to be used in most electronics, as most electronics require a stable voltage source. It also means that the increased specific capacity (mAh/g) does not necessarily imply increased specific energy (J/g).

These problems, such as high irreversible capacity and lack of a stable voltage of CNTs, can be solved by combining CNTs with high capacity materials. As discussed at the end of Section 1.3, manganese-based electrode materials have relatively lower thermodynamic equilibrium voltage than Li/Li^+ . They also have high capacity and are naturally abundant. However, their applicability is limited by their low electrical conductivity. The best strategy for boosting the performance of manganese-based electrode materials is to introduce conductive materials. On one hand, transition metal oxides nanoparticles decorated on the wall of CNTs can produce a much flatter discharge curve than the anodes made of CNTs only.¹⁰¹ On the other hand, CNTs can be also beneficial, for example, by buffering the volume change of these particles as shown in Figure 1-10 and improving the conductivity of transition metal oxide electrodes. Moreover, CNTs can maintain their nano-structural integrity and prevent nano-sized particles from coarsening. This can also facilitate the migration of both Li^+ and e^- because of the porous structure of CNTs. In addition, CNTs can act as a flexible wire mesh, allowing these particles to remain attached to the anode's current collector. Combining the high capacity of nano materials with CNTs could provide a flatter voltage plateau and improve the lifespan of LIBs.

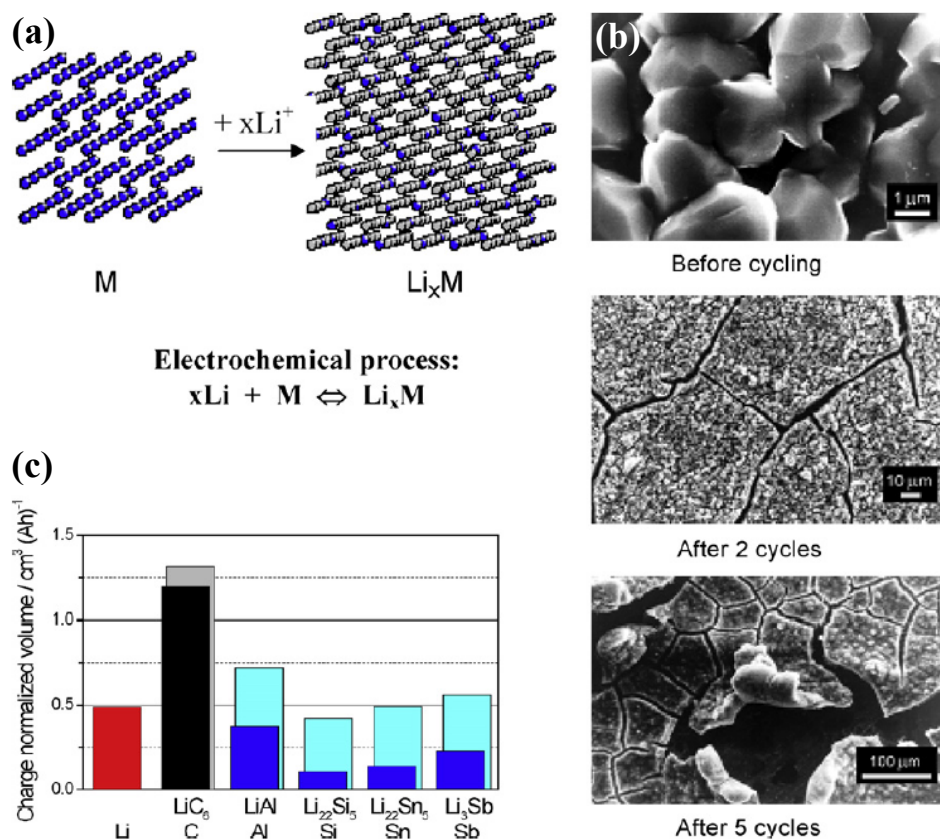


Figure 1-10. Volume change effects associated with the charge and discharge process of metal alloy electrodes in lithium cells. (a) Scheme of Li ion insertion and related volume change during discharge. (b) SEM image of Li-Si before and after cycling (right). (c) Comparison of volume changes of different materials.

Adding CNTs into cathode materials of LIBs has been studied. It was reported that the initial discharge capacities of an $LiMn_2O_4/CNT$ cathode can reach around 120 mAh/g at a rate of 0.1C.¹⁰² Xin et al. used a self-assembly method to fabricate an $LiMn_2O_4/acid$ -functionalized MWCNTs electrode, which achieved a capacity — over 150 mAh/g¹⁰³ — which was much higher than that of conventional pure $LiMn_2O_4$ (≈ 100 mAh/g).¹⁰⁴ It was concluded that the 3D networks formed by functionalized MWCNTs increased the contact area of active materials, and

effectively reduced the charge resistance. In fact, another compound LiMnO_2 has higher theoretical discharge capacity (285mAhg^{-1}) but combining LiMnO_2 with CNTs has not yet been carried out.

CNT for supercapacitors With their unique structure including porous, good conductivity, and excellent thermal stability, CNTs have also attracted extensive attention for use as supercapacitor electrodes.⁹⁶ CNTs are usually considered a high-power electrode material because of their good electrical conductivity and readily accessible surface area. Furthermore, their excellent mechanical properties can make them a good supporting material. However, the potential electrochemical performance of CNTs is still difficult to be improved because of their low specific surface area ($< 500\text{ m}^2/\text{g}$) as compared with activated carbons. The highest specific capacitance of an MWCNTs-based supercapacitor is 102 F/g in an acidic electrolyte, here the specific surface of MWCNTS is $430\text{ m}^2/\text{g}$.¹⁰⁵

It is believed that the electrochemical performance of entangled CNTs is worse than that of CNT arrays because the CNT's irregular pore structure hinders the rate of ionic transportation. The highest energy density of the electrode made from the CNT array was 300 Wh/kg at room temperature in an organic electrolyte, and the rate capability was also better than that of ACs.¹⁰⁶ These results showed the importance of the aligned tubular structures in enhancing the electrochemical performance of supercapacitor electrode materials.

Many recent studies have focused on improving the specific surface area of CNT through KOH chemical activation to increase the energy density of CNTs.¹⁰⁷ However, high surface area may sacrifice the excellent conductivity of CNT and impair the rate performance as well. A balance between the surface area and the electrical conductivity must be determined. Another way to increase the specific capacitance of CNTs is to decorate CNTs with other capacitive materials, such as transition metal oxides.

Despite many property advantages, the low porosity of CNTs still limits their utilization as electrode material of EDLCs. Most of the fabricated CNTs are multi-wall CNTs and are hardly able to reach the theoretical specific surface area of single wall CNTs (1315 m²/g). Further, the methods of CNT synthesis is still complex and need strict conditions and enhance the cost of commercialized CNT.

1.4.2 Graphene for LIBs and ECs

Graphene is another allotrope of carbon in the form of a two-dimensional, atomic-scale, honey-comb lattice in which one atom forms each vertex. It is the basic structural element of other allotropes, including graphite and carbon nanotubes. Graphene has many extraordinary properties such as a large surface area; good flexibility; good chemical and thermal stability; wide potential windows; rich surface

chemistry; and extraordinary electrical, thermal and mechanical properties, all of which are advantageous for energy storage and conversion systems.^{108, 109, 110}

Therefore, graphene has been explored as an electrode material in electrical energy storage devices such as LIBs and ECs.

Graphene for LIBs

Extensive efforts have been made to develop graphene to obtain better performance. Compared with graphite or CNTs, graphene can provide many advantages in energy storage applications. For example, the theoretical specific surface area of graphene is 2630 m²/g, much higher than CNTs (500 m²/g) and graphite (20 m²/g). The large surface areas are the key factor for energy storage because more active sites for electrochemical reactions can be provided. Graphene provides fast ion transportation to improve the rate capability, which is often a bottleneck for the traditional bulk electrode material of LIBs. In addition, compared to graphite or CNTs, the surface of graphene can be easily functionalized with desired chemical groups and can be utilized in various energy storage applications. Finally, there is no serious metallic pollution during graphene fabrication, which is important for the energy industry.¹¹¹

The specific capacity of graphene nano-sheets (GNS) was first reported in 2008 and reached 540 mAh/g as an anode of LIBs. The space between graphene layers was found to significantly influence the capacity of LIBs. CNTs were or fullerene was embedded into graphene nano-sheets to increase the space between layers and the

capacity was increased to above 730 mAh/g.¹¹² Later it was found that the lithium ions can be stored not only between graphene layers but also on the edges and covalent sites; moreover, the GNS defects benefitted to ion storage.^{113,114} However, graphene's electrochemical performance can be limited by another issue, the restacking of graphene sheets, which commonly appears between graphene nano-sheets without any chemical groups decoration.

Graphene for Supercapacitors

Recently, graphene has also been considered a promising candidate as a supercapacitor electrode material. At an early stage, the capacitance of a graphene-based supercapacitor can only achieve 75 F/g in an aqueous electrolyte and 99 F/g in an organic electrolyte.¹¹⁵ By modifying the synthesis method, the phenomenon of graphene aggregation was alleviated considerably and the maximum specific capacitance can reach to 205 F/g.¹¹⁶ However, it is still difficult to completely prevent GNSs from restacking, which means that it is not possibly to fully show all of the advantages of GNS.

As described above, one of the major issues for the use of graphene in LIBs and ECs is the restacking phenomenon due to the van der Waals between graphene sheets, consequently weakening the electrochemical performance of GNSs in LIBs and ECs. To fully use all the electrochemical advantages of graphene in energy storage and avoid GNS restacking to a great extent, a practical method was proposed. It is to fabricate graphene/metal oxide composites. This method combines the advantages of both the materials and solves the problems of these materials when they are used as

individual electrodes of LIBs. In the composite, graphene can provide additional electro-conductivity for metal oxides and support of metal oxides, and prevent aggregation during charging/discharging. The metal oxides provide a high charging/discharging plateau and high capacity for the whole composites, suppress the restacking of GNSs and increase the specific surface area of GNSs. The final metal oxide-anchored graphene forms an ideal integrated structure with an electron conductive network and short ion transport paths. Significant synergistic effects can be well-utilized in graphene/metal oxide composites.¹¹⁷ The synthesized composite is not merely the sum of these two individual materials but a new material with ideal electrochemical properties.

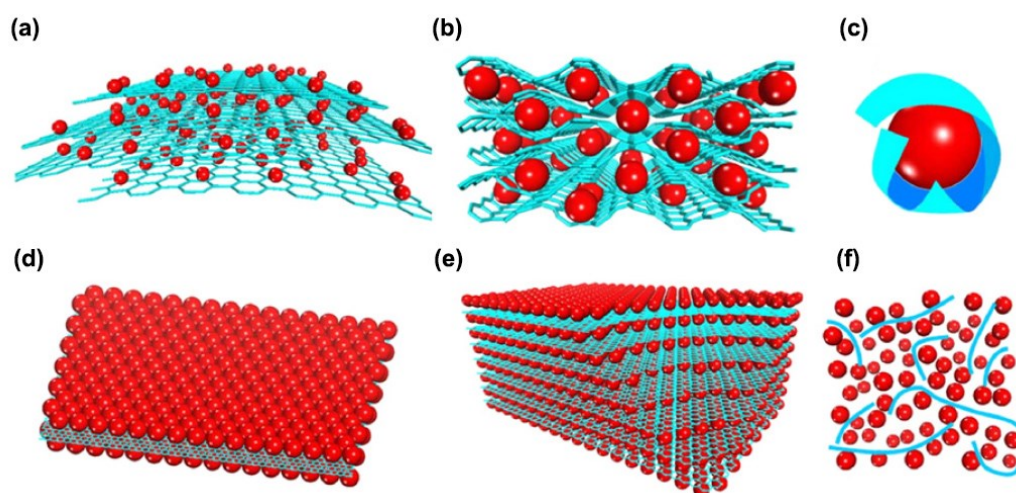


Figure 1-11. Schematic of structural models of graphene/metal oxide composites: (a) Anchored model. (b) Wrapped model. (c) Encapsulated model. (d) Sandwich-like model. (e) Layered model. (f) Mixed model. Red: metal oxide particles; Blue: graphene sheets.

Several structural models of graphene/metal oxide composites have already been

proposed as shown in Figure 1-1: (a) nano-sized oxides anchoring on graphene for LIBs; (b) graphene-wrapped metal oxide particles; (c) graphene-encapsulated metal oxides for LIBs; (d) a 2D sandwich-like model: graphene as a template for the creation of a metal oxide/GNS sandwich-like structure; (e) graphene/metal oxide-layered composites composed of aligned layers of metal oxide-anchored graphene; (f) 3D graphene (normally $\leq 10\text{wt}\%$ in composite)-conductive networks among metal oxides.¹¹⁷

1.5 Synthesis Method

As discussed above, the morphology and structure of electrode materials for energy storage devices play a crucial role in the electrochemical performance of different devices. It is a challenge and a required task to prepare electrode materials with a desirable morphology and structure and an affordable price. Furthermore, developing an effective way to integrate metal oxides and conductive materials into composites is important for the future of the energy industry. Although it is difficult to achieve these two goals with one method, some research has been carried out and cultivated to fulfill these expectations in labs and on an industrial scale.

Currently, the established techniques of fabricating electrode materials include such main routes as hydrothermal synthesis,¹¹⁸ thermally decomposing,¹¹⁹ electrodeposition,¹²⁰ and sputtering.¹²¹ Sputtering is a traditional method to synthesize

thin film on a substrate. This technique is expensive because of its low rate of deposition and the requirement of extreme conditions (high vacuum, high tension, etc.). New deposition methods, particularly the wet chemistry methods like sol/gel or hydrothermal synthesis, are free of the above drawbacks, but have limited applications because they require post annealing treatments at relatively high temperatures (≈ 600 °C). Fan et al. deposited manganese oxide on a CNT matrix by thermally decomposing manganese nitrates, and the specific capacitance of the manganese oxide/CNT composites was found to be rather high. However, the above methods to deposit metal oxides on CNTs or graphene oxides usually involve complex processing controls, multi-step activation procedures, and harsh conditions.

Electrochemical synthesis such as electrodeposition is achieved by delivering an electric current between two electrodes (working and counter electrodes) separated by a conductive electrolyte. Electrochemical synthesis takes place at the electrode-electrolyte interface. Advantages of electrochemical synthesis are listed as follows:^{122,123}

- (1) Electrochemical synthesis is a low-temperature process limited by the boiling point of the electrolyte, which may minimize inter-diffusion.
- (2) The morphology, composition, and crystal structure can be controlled through the applied potential. This is not easy to achieve by conventional chemical synthesis.
- (3) The experimental setup is not expensive and the experiments are easy to perform.

The best-known application of this technique is the synthesis of Ni(OH)_2 by the electro-reduction of aqueous nickel nitrate solutions.^{124, 125} This reaction is widely used to fabricate nickel hydroxide-based cathodes for other batteries such as Ni-Cd, Ni-Fe, and Ni-Zn batteries. Similarly, plenty of other metal oxides have also been synthesized by this method. These oxides include ZrO_2 , TiO_2 , MnO_2 , and SnO_2 . These syntheses have been successfully applied by the galvanostatic reduction of the respective mixed-metal nitrate/sulfate solutions in the presence of hydrogen peroxide at various current densities ranging from 10 to 100 mA/cm^2 . In all these syntheses, the oxides can be obtained as adherent coatings with controlled thickness, by adjusting electrolyte concentration, current density, deposition time, electrolyte pH, and temperature.

In order to achieve the goal discussed in Section 1.4.2, that is, to combine manganese-based materials with conductive materials such as CNT and graphene, the electrodeposition method was used recently to obtain MnO_x/CNT and $\text{MnO}_x/\text{graphene}$ composites by synthesizing manganese oxides on CNT or graphene substrates. Synthesizing CNT- MnO_x and graphene- MnO_x composites by electro-deposition generally involves two steps: the fabrication of substrate film by CNT and graphene, and deposition of manganese oxide on the substrate film. The first step can be hard to perform because the CNT and graphene film substrate could dissolve into the solution during the deposition. In addition, manganese oxide is often found to be coated only

on the outside of the substrate, instead of uniformly coated on the surface of the CNT throughout the thickness of the film.

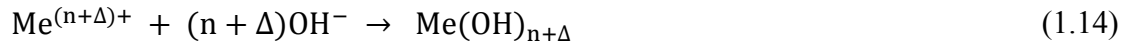
It is also a challenge to synthesize lithium manganese oxide via electrodeposition. Although all kinds of lithium manganese oxide crystals have been synthesized successfully in sealed vessels at high temperatures (above the boiling point of water) and high pressures, to date lithium manganese oxides have never been deposited on any substrate under ambient pressure and at low temperatures.

Among the many methods for synthesizing LiMnO_2 , the hydrothermal method is easy and economical. LiMnO_2 nanoparticles can be synthesized with hydrothermal method through multi-step reactions using MnSO_4 , LiOH , and H_2O_2 . The reactions are believed to take place in three steps. First, MnSO_4 reacts with LiOH to form Mn(OH)_2 in solution, which is followed by a quick oxidization of Mn(OH)_2 into Mn(OH)_3 by H_2O_2 and air. Mn(OH)_3 is then transformed into LiMnO_2 upon heating in an LiOH solution. The reactions involved are given below:



The reaction temperature in Reaction (12) is 200 °C.

It is suggested that the oxidation in Reaction (11) can be achieved by anodic oxidation through the following reactions:^{126,127}



Anodic oxidation could possibly be used to replace the second step of the hydrothermal method for synthesizing LiMnO_2 . In fact, H_2O_2 used in $\text{Mn}(\text{OH})_2 + \text{H}_2\text{O}_2 \rightarrow \text{Mn}(\text{OH})_3$ is rather active and unstable in terms of rate control during the reaction. In contrast, the rate of reaction during anodic oxidation can be controlled by adjusting current density which is easier and more accurate to operate.

The high temperature required in the third step of the hydrothermal method is rather difficult to avoid. However, it has been demonstrated that the reaction temperature can be reduced to some extent, around 200°C . At that temperature, electrodeposition of molten salts can be carried out under atmospheric pressure. With this method, a low-melting temperature salt with flux, containing the transition metal-based salts, is melted and electrolyzed at elevated temperatures using an inert Pt electrode or a reactive metal electrode, such as Fe, or C, depending on the desired products. Cathodic reduction or anodic oxidation leads to crystals of the product on electrodes, but both electrodes can be recovered by washing away the electrolyte. Some crystals of FeV_2O_4 , WS_2 , Fe_2P and TiS_2 have been prepared by this technique.¹²⁸ However, the working mechanism is not clearly understood and the synthetic conditions are mostly dependent on empirical evidence.

In this research, Innovations on electrodeposition will be made to achieve these goals

proposed at the beginning of Chapter 1.5. Further, a new method to fabricate lithium manganese oxide crystals will be developed using electrodeposition in molten salts rather than in an aqueous electrolyte. The work has not been reported so far to the best of our knowledge.

1.6 Motivation

To replace the anode and cathode materials of current LIBs and supercapacitors, different type of manganese-based materials have been fabricated and reported in the past few years. Although most of them exhibit a good electrochemical performance which can meet the increasing demand of the battery industry, there is no single step and effective method to synthesize these high performance electrode materials. This means that different types of materials such as MnO_x , CoO_x , MnCO_3 , and LiMn_2O_4 need to be synthesized by different methods; even the same crystal with a different morphology may need a new synthesis route. Enormous energy and time will be invested into the synthesis routes and thus enhance the cost of the final product and hinder the progress of commercialization. These issues were considered when developing this research, therefore the motivations of this research are listed:

1. MnO_2/CNTs composites will be fabricated and tested as anodes of LIBs because MnO_2 crystals have a high theoretical capacity, varied valence states, and a high discharging voltage plateau. Most CNTs have good electric conductivity which can compensate for the disadvantages of MnO_2 crystals.

2. To synthesize MnCO_3 / graphene composites as anode of LIBs. MnCO_3 has a high theoretical capacity and its practical capacity often exceeds its theoretical value according to published reports. In addition, MnCO_3 crystals can be synthesized to achieve different shapes/morphologies, which are critical to the electrochemical performances when they are used as anodes of LIBs or electrodes of supercapacitors. Special shapes/morphologies of MnCO_3 crystals with improved electrochemical performances will be explored.
3. Doping cobalt into MnCO_3 because the electrochemical performances of doped MnCO_3 can be improved according to published reports. In this investigation, doping of cobalt into MnCO_3 will be explored and the materials after doping will be evaluated in terms of their performances as anodes of LIBs.
4. To synthesize spinel LiMn_2O_4 crystals as cathode of LIBs because spinel LiMn_2O_4 has an intrinsic high theoretical capacity, high voltage vs. Li/Li^+ , good cyclability, and abundant availability.
5. Electrodeposition is an effective way to synthesize metal oxide because it is easy to set up experimentally and has the potential to be scaled up. An innovative method will be developed in this research. Conductive materials such as CNTs and graphene nano-sheets will be introduced into the electrodeposition system and be plated by metal oxides or metal carbonates.

1.7 References

- 1 International Energy Agency, Coal statistics, <http://www.iea.org/statistics/topics/coal/>.
- 2 Enerdata, Global Energy Statistical Yearbook 2016, <https://yearbook.enerdata.net/>
- 3 EIA report, Analysis of the Impacts of the Clean Power Plan, <http://www.eia.gov/analysis/requests/powerplants/cleanplan/>.
- 4 International Energy Agency, Energy Balances of OECD Countries (2013) and Energy Balances of Non-OECD Countries (2013), <http://www.iea.org/statistics/online-dataservice>.
- 5 M. Sugantha, P. A. Ramakrishnan, A. M. Hermann, C. P. Warmsingh and D. S. Ginley, *Int. J. Hydrogen Energy*, 2003, 28, 597–600.
- 6 N. Kijima, Y. Takahashi, J. Akimoto and J. Awaka, *J. Solid State Chem.*, 2005, 178, 2741–2750.
- 7 F. Jiao and P. G. Bruce, *Adv. Mater.*, 2007, 19, 657–660.
- 8 Q. Liu, S. Wang and H. Cheng, *Int. J. Electrochem. Sci.*, 2013, 8, 10540–10548.
- 9 S. Wang, Q. Liu, J. Yu and J. Zeng, *Int. J. Electrochem. Sci.*, 2012, 7, 1242–1250.
- 10 F. Cheng, J. Zhao, W. Song, C. Li, H. Ma, J. Chen and P. Shen, *Inorg. Chem.*, 2006, 45, 2038–2044
- 11 S. Jouanneau, S. Sarciaux, A. Le Gal La Salle and D. Guyomard, *Solid State Ionics*, 2001, 140, 223–232.
- 12 W. M. Dose and S. W. Donne, *J. Power Sources*, 2014, 247, 852–857.
- 13 J. Chen and F. Cheng, *Acc. Chem. Res.*, 2009, 42, 713–723.
- 14 C. Li, F. Cheng, W. Ji, Z. Tao and J. Chen, *Nano Res.*, 2009, 2, 713 – 721.
- 15 F. Cheng, J. Chen, X. Gou and P. Shen, *Adv. Mater.*, 2005, 17, 2753–2756.
- 16 S. Chou, F. Cheng and J. Chen, *J. Power Sources*, 2006, 162, 727–734.
- 17 Z. Yang, J. Liang, F. Cheng, Z. Tao and J. Chen, *Microporous Mesoporous Mater.*, 2012, 161, 40–47.
- 18 M. R. Palacin, *Chem. Soc. Rev.*, 2009, 38, 2565–2575.
- 19 J. Maier, *Nat. Mater.*, 2005, 4, 805–815.
- 20 J. Liu, F. Liu, K. Gao, J. S. Wu and D. F. Xue, *J. Mater. Chem.*, 2009, 19, 6073–6084.
- 21 F. Chen, Z. Tao, J. Liang and J. Chen, *Chem. Mater.*, 2008, 20, 667–681.
- 22 Y. Wang and J. Y. Lee, *Angew. Chem., Int. Ed.*, 2006, 45, 7039–7042.
- 23 W. van Schalkwijk, and B. Scrosati (Eds.), *Advances in Lithium-ion Batteries*, Kluwer Academic/Plenum, Boston, 2004.
- 24 M. Yoshio, R. J. Brodd, and A. Kozawa, *Lithium batteries, science and technologies*. Springer, New York, 2009.
- 25 U. Sacken, E. Nodwell, A. Sundher, J.R. Dahn, *Power Sources*, 1995, 54, 240–245.
- 26 H. Ota, Y. Sakata, X. Wang, J. Sasahara, and Eiki Yasukawa, *J. Electrochem. Soc.* 2004, 151, 437–446.
- 27 Y. Sun, X. Hu, W. Luo, F. Xia and Y. Huang, *Adv. Funct. Mater.*, 2013, 23, 2436–

-
- 2444.
- 28 X. Zhang, F. Cheng, J. Yang and J. Chen, *Nano Lett.*, 2013, 13, 2822–2825.
- 29 N. Yabuuchi, K. Yoshii, S. T. Myung, I. Nakai and S. Komaba, *J. Am. Chem. Soc.*, 2011, 133, 4404–4419.
- 30 D. Zeng, J. Cabana, W. S. Yoon and C. P. Grey, *Chem. Mater.*, 2010, 22, 1209–1219.
- 31 F. Jiao and P. G. Bruce, *Adv. Mater.*, 2007, 19, 657–660.
- 32 J. Zhao, Z. Tao, J. Liang and J. Chen, *Cryst. Growth Des.*, 2008, 8, 2799–2805.
- 33 H. Wang, L. Cui, Y. Yang, H. Sanchez Casalongue, J. T. Robinson, Y. Liang, Y. Cui and H. Dai, *J. Am. Chem. Soc.*, 2010, 132, 13978–13980.
- 34 H. Jiang, Y. Hu, S. Guo, C. Yan, P. S. Lee and C. Li, *ACS Nano*, 2014, 8, 6038–6046.
- 35 T. J. Kim, D. Son, J. Cho and B. Park, *J. Power Sources*, 2006, 154, 268–272.
- 36 S. B. Schougaard, J. Bre'ger, M. Jiang, C. P. Grey and J. B. Goodenough, *Adv. Mater.*, 2006, 18, 905–909.
- 37 F. Cheng, H. Wang, Z. Zhu, Y. Wang, T. Zhang, Z. Tao and J. Chen, *Energy Environ. Sci.*, 2011, 4, 3668–3675.
- 38 D. Choi, D. Wang, I. T. Bae, J. Xiao, Z. Nie, W. Wang, V. V. Viswanathan, Y. J. Lee, J. G. Zhang, G. L. Graff, Z. Yang and J. Liu, *Nano Lett.*, 2010, 10, 2799–2805.
- 39 P. Poizot, S. Laruelle, S. Grugeon, L. Dupont, and J. M. Tarascon, *Nature.*, 2000, 407, 496–499.
- 40 X. Yu, Y. He, J. Sun, K. Tang, H. Li, L. Chen and X. Huang, *Electrochem. Commun.*, 2009, 11, 791–794.
- 41 K. Zhong, B. Zhang, S. Luo, W. Wen, H. Li, X. Huang and L. Chen, *J. Power Sources*, 2011, 196, 6802–6808.
- 42 X. Li, D. Li, L. Qiao, X. Wang, X. Sun, P. Wang and D. He, *J. Mater. Chem.*, 2012, 22, 9189–9194.
- 43 M. M. Thackeray, W. I. F. David, P. G. Bruce and J. B. Goodenough, *Mater. Res. Bull.*, 1983, 18, 461–472.
- 44 M. M. Thackeray, P. J. Johnson, L. A. de Picciotto, P. G. Bruce and J. B. Goodenough, *Mater. Res. Bull.*, 1984, 19, 179–187.
- 45 J. M. Tarascon and D. Guyomard, *J. Electrochem. Soc.*, 1991, 138, 2864–2868.
- 46 J. M. Tarascon, E. Wang, F. K. Shokoohi, W. R. McKinnon and S. Colson, *J. Electrochem. Soc.*, 1991, 138, 2859–2864.
- 47 F. Jiao, J. Bao, A. H. Hill and P. G. Bruce, *Angew. Chem., Int. Ed.*, 2008, 47, 9711–9716.
- 48 D. K. Kim, P. Muralidharan, H.-W. Lee, R. Ruffo, Y. Yang, C. K. Chan, H. Peng, R. A. Huggins and Y. Cui, *Nano Lett.*, 2008, 8, 3948–3952.
- 49 S. M. Bak, K. W. Nam, C. W. Lee, K. H. Kim, H. C. Jung, X. Q. Yang and K. B. Kim, *J. Mater. Chem.*, 2011, 21, 17309–17315.
- 50 D. Linden and T. B. Reddy, *Handbook of Batteries*, McGraw-Hill, New York, 2002.
- 51 R. M. Dell and D. A. J. Rand, *Understanding Batteries*, Royal Society of

Chemistry, Cambridge, 2001.

52 R. Kotz, S. Muller, M. Bartschi, B. Schnyder, P. Dietrich, F. N. Buchi, A. Tsukada, G. G. Scherer, P. Rodatz, O. Garcia, P. Barrade, V. Hermann and R. Gallyay, *Electrochemical Society Proceedings*, 2001, 21, 564-575.

53 X. Dong, W. Shen, J. Gu, L. Xiong, Y. Zhu, H. Li and J. Shi, *J. Phys. Chem. B*, 2006, 110, 6015-6019.

54 W. Sugimoto, H. Iwata, Y. Murakami and Y. Takasu, *J. Electrochem. Soc.*, 2004, 151, 1181-1187.

55 M. S. Wu and P. C. Chiang, *Electrochem. Solid-State Lett.*, 2004, 7, 123-126.

56 B. E. Conway, *Electrochemical Supercapacitors*, Kluwer Academic/Plenum Press, New York, 1999

57 G. Wang, L. Zhang and J. Zhang, *Chem. Soc. Rev.*, 2012, 41, 797-828

58 Y. Zhang, H. Feng, X. Wu, L. Wang, A. Zhang, T. Xia, H. Dong, X. Li and L. Zhang, *Int. J. Hydrogen Energy*, 2009, 34, 4889-4899.

59 B. E. Conway, V. Birss and J. Wojtowicz, *J. Power Sources*, 1997, 66, 1-14

60 C. Ming Chuang, C. W. Huang, H. Teng and J. M. Ting, *Energy Fuels*, 2010, 24, 6476-6482.

61 A. Burke, *J. Power Sources*, 2000, 91, 37-50.

62 M. Kisacikoglu, M. Uzunoglu and M. Alam, *Int. J. Hydrogen Energy*, 2009, 34, 1497-1507.

63 S. Ma, K. Nam, W. Yoon, X. Yang, K. Ahn, K. Oh and K. Kim, *Electrochem. Commun.*, 2007, 9, 2807-2811.

64 G. Wang, L. Zhang and J. Zhang, *Chem. Soc. Rev.*, 2012, 41, 797-828.

65 V. Subramanian, H. Zhu and B. Wei, *J. Power Sources*, 2006, 159, 361-364.

66 C. C. Hu and T. W. Tsou, *Electrochem. Commun.*, 2002, 4, 105-109.

67 E. Macheaux, T. Brousse, D. Be' langer and D. Guyomard, *J. Power Sources*, 2007, 165, 651-655.

68 S. W. Donne, A. F. Hollenkamp and B. C. Jones, *J. Power Sources*, 2010, 195, 367-373.

69 H. Xia, J. Feng, H. Wang, M. O. Lai and L. Lu, *J. Power Sources*, 2010, 195, 4410-4413.

70 E. Beaudrouet, A. Le Gal La Salle and D. Guyomard, *Electrochim. Acta*, 2009, 54, 1240-1248.

71 H. K. Lee, D. Sakemi, R. Selyanchyn, C. G. Lee and S. W. Lee, *ACS Appl. Mater. Interfaces*, 2014, 6, 57-64.

72 S. Devaraj, H. Y. Liu and P. Balaya, *J. Mater. Chem. A*, 2014, 2, 4276-4281.

73 Q. Li, L. W. Yin, Z. Q. Li, X. K. Wang, Y. X. Qi and J. Y. Ma, *ACS Appl. Mater. Interfaces*, 2013, 5, 10975-10984.

74 G. N. Zhang, L. Zheng, M. Zhang, S. H. Guo, Z. H. Liu, Z. P. Yang and Z. L. Wang, *Energy Fuels*, 2012, 26, 618-623.

75 T. Kokubu, Y. Oaki, H. Uchiyama, E. Hosono, H. Zhou and H. Imai, *Chem.-Asian J.*, 2010, 5, 792-798.

76 M. M. Thackeray, H. K. Sun, S. J. Christopher, J. T. Vaughey, R. Benedek and S.

-
- A. Hackney, *J. Mater. Chem.*, 2007, 17, 3112-3125.
- 77 M. M. Thackeray, W. I. F. David, P. G. Bruce and J. B. Goodenough, *Mater. Res. Bull.*, 1983, 18, 461-472.
- 78 H. Uchiyama, E. Hosono, H. Zhou and H. Imai, *J. Mater. Chem.*, 2009, 19, 4012-4016.
- 79 F. Dang, T. Hoshino, Y. Oaki, E. Hosono, H. Zhou and H. Imai, *Nanoscale*, 2013, 5, 2352-2357.
- 80 X. Niu, H. Wei, W. Liu, S. Wang, J. Zhang and Y. Yang, *RSC Adv.*, 2015, 5, 33615-33622.
- 81 L. Yu, L. Zhang, H. Wu, G. Zhang and X. Lou, *Energy Environ. Sci.*, 2013, 6, 2664-2671.
- 82 M. J. Aragón, B. León, C. Pérez Vicente and J. L. Tirado, *J. Power Sources*, 2011, 196, 2863-2866.
- 83 S. Lei, Z. Liang, L. Zhou and K. Tang, *Materials Chemistry and Physics* 2009, 113, 445-450.
- 84 H. Li, X. Zhang, R. Ding, L. Qi and H. Wang, *Electrochim. Acta*, 2013, 108, 497-505.
- 85 X. F. Chen, L. Qie, L. L. Zhang, W. X. Zhang and Y. H. Huang, *J. Alloys Compd.*, 2013, 559, 5-10
- 86 W. Kang, D. Y. W. Yu, W. Li, Z. Zhang, X. Yang, T. Ng, R. Zou, Y. Tang, W. Zhang and C. Lee, *Nanoscale*, 2015, 7, 10146
- 87 S. Devaraj, H. Y. Liuc and P. Balaya, *J. Mater. Chem. A*, 2014, 2, 4276-4281
- 88 A. L. M. Reddy, M. M. Shaijumon, S. R. Gowda and P. M. Ajayan, *Nano Lett.*, 2009, 9, 1002-1006.
- 89 H. Xia, M. Lai and L. Lu, *J. Mater. Chem.*, 2010, 20, 6896-6902.
- 90 H. Wang, L. Cui, Y. Yang, H. S. Casalongue, J. T. Robinson, Y. Liang, Y. Cui, and H. Dai, *J. Am. Chem. Soc.* 2010, 132, 13978-13980
- 91 A. Yu, H. W. Park, A. Davies, D. C. Higgins, Z. Chen, and X. Xiao, *J. Phys. Chem. Lett.* 2011, 2, 1855-1860.
- 92 C.S. Wang, G.T. Wu, W.Z. Li, *Journal of Power Sources*, 1998, 76, 1-10.
- 93 C. Casas, W. Li, *Journal of Power Sources*, 2012, 208, 74 - 85.
- 94 B. Peng, M. Locascio, P. Zapol, S. Li, S. L. Mielke, G. C. Schatz, H. D. Espinosa, *Nature Nanotechnology*, 2008, 3, 626-631.
- 95 S. Bellucci, *Physica Status Solidi C*, 2005, 2, 34-37.
- 96 L. Zhang and X. S. Zhao, *Chem. Soc. Rev.*, 2009, 38, 2520-2531.
- 97 S. Yang, J. Huo, H. Song, X. Chen, *Electrochimica Acta*, 2008, 53, 2238-2244.
- 98 K. Nishidate, M. Hasegawa, *Physical Review B*, 2005, 71, 1-6.
- 99 C. H. Mi, G. S. Cao, X. B. Zhao. *Journal of Electroanalytical Chemistry*. 2004, 562, 217-221.
- 100 H. Shimoda, B. Gao, X. P. Tang, A. Kleinhammes, L. Fleming, Y. Wu, O. Zhou, *Physical Review Letters*, 2002, 88, 015502, 1-4.
- 101 L. Cui, Y. Yang, C. Hsu, Y. Cui, *Nano Letters*. 2009, 9, 3370-3374.
- 102 S. Liu, J. Zhang, K. Huang, J. Yu. *Journal of the Brazilian Chemical Society*.

-
- 2008, 19, 1078-1083.
- 103 X. Zhao, C. M. Hayner, H. H. Kung. *Journal of Materials Chemistry*. 2011, 21, 17297-17303.
- 104 W. Tang, X.J. Wang, Y.Y. Hou, L.L. Li, H. Sun, Y.S. Zhu, Y. Bai, Y.P. Wu, K. Zhu, T. van Ree, *Journal of Power Sources*. 2012, 198, 308-311.
- 105 C. Niu, E. K. Sichel, R. Hoch, D. Moy and H. Tennent, *Appl. Phys. Lett.*, 1997, 70, 1480-1482.
- 106 X. Cui, J. Chen, T. Wang and W. Chen, *Scientific Reports*, 2014, 4, 5310.
- 107 A. G. Pandolfo and A. F. Hollenkamp, *J. Power Sources*, 2006, 157, 11-27.
- 108 Y. B. Zhang, Y. W. Tan, H. L. Stormer, P. Kim, *Nature*, 2005, 438, 201-204.
- 109 V. I. Fal'ko, A. K. Geim, *The European Physical Journal—Special Topics*, 2007, 148, 1-3.
- 110 Y. Kopelevich, P. Esquinazi, *Advanced Materials*, 2007, 19, 4559-4563.
- 111 M. Pumera, *The Chemical Record*, 2009, 9, 211-223.
- 112 E. Yoo, J. Kim, E. Hosono, H. Zhou, T. Kudo, I. Honma, *Nano Letters*, 2008, 2277-2282.
- 113 P. Guo, H. H. Song, X. H. Chen, *Electrochemistry Communications*, 2009, 11, 1320-1324.
- 114 G. X. Wang, X. P. Shen, J. Yao, J. Park, *Carbon*, 2009, 47, 2049-2053.
- 115 S. R. C. Vivekchand, C. S. Rout, K. S. Subrahmanyam, A. Govindaraj, and C. N. R. Rao, *Journal of Chemical Sciences*, 2008, 120, 9-13.
- 116 Y. Wang, Z. Q. Shi, Y. Huang, Y. F. Ma, C. Y. Wang, M. M. Chen, and Y. S. Chen, *The Journal of Physical Chemistry C*, 2009, 113, 13103-13107.
- 117 Z. Wua, G. Zhou, L. Yin, W. Ren, F. Li, and H. Cheng, *Nano Energy*, 2012, 1, 107-131.
- 118 Z. Guo, K. Konstantinov, G. Wang, H. Liu, and S. Dou. *Journal of Power Sources*, 2003, 119, 221-225
- 119 Z. Fan, J. Chen, M. Wang, K. Cui, H. Zhou, and W. Kuang. *Diamond and Related Materials*, 2006, 9, 1478-1483.
- 120 W. Wei, W. Chen, and D. G. Ivey, *Journal of Power Sources*, 2009, 186, 428 - 434.
- 121 A. Anders, *Journal of Physics D-Applied Physics*, 2007,40.
- 122 G. Hodes, *Electrochemistry of Nanomaterials*; Wiley-VCH: Weinheim, Germany, 2001.
- 123 G. H. A. Therese, and P. V. Kamath, *Chem. Mater.* 2000, 12, 1195-1204.
- 124 M. Dixit, P. V. Kamath, V. G. Kumar, N. Munichandraiah, and A. K. J. Shukla, *Power Sources* 1996, 63, 167-171.
- 125 R. S. Jayashree, and P. V. J. Kamath, *Appl. Electrochem.* 1999, 29, 449-454.
- 126 K. R. J. Bullock, *Electroanal. Chem.* 1987, 222, 347-366.
- 127 E. J. Preisler, *Appl. Electrochem.* 1989, 19, 559-565.
- 128 A. Wold, and D. Bellavance, In *Preparative Methods in Solid State Chemistry*; Hagenmuller, P., Ed.; Academic Press: New York, 1972.

Chapter 2 Electrochemical deposition of MnO₂ on CNT

2.1 Introduction

The advent of lithium ion batteries (LIBs) for consumer products such as cameras, laptop computers and cellular phones began with the development of primary 3.0 V lithium/MnO₂ cells and rechargeable 3.5V lithium-ion cells with lithiated carbon negative electrodes and LiCoO₂ positive electrodes.^{1,2,3} Despite rapid advances over the past 10 years, LIB technology has not been optimized in terms of battery performance, safety, and cost. Extensive worldwide research and development efforts are ongoing to seek superior materials to improve the performance of LIBs.⁴ One of the approaches has been to replace current electrodes with alternative materials that possess higher capacity but can be fabricated at a lower cost. Manganese oxides are one of the promising alternatives for an LIB anode. Developing methods of synthesizing manganese oxides effectively and economically will be the main objective of this proposal.

As an allotrope of graphite, CNTs have been approved to be a good anode material for lithium batteries^{5,6,7} due to their unique structure (one-dimensional cylindrical tubule of graphite sheet), high conductivity, low density, high rigidity (Young's modulus in the order of 1 TPa), and high tensile strength (up to 60 GPa). Single wall carbon nanotubes (SWCNTs) can have reversible capacities anywhere from 300 to 600

mAh/g,^{8,9,10,11,12} significantly higher than those of graphite (320 mAh/g). Mechanical and chemical treatment can further increase the reversible capacities of SWCNTs up to 1000 mAh/g.^{13,14,15,16}

The problems of CNTs as anode of LIBs such as high irreversible capacity and the lack of stable voltage can be solved by combining with high capacity materials. In particular, CNTs decorated with metal/metal oxide nanoparticles can produce a much flatter discharge curve than the anodes made of CNTs only.¹⁷ On the other hand, CNTs can also provide benefits for these particles and can buffer the volume change of these particles. Such a large change in volume during charging and discharging is called pulverization, which is an important issue of a metal/metal oxide material electrode and can lead to poor cycling stability. In addition, CNTs can improve the electronic conductivity of the whole electrode.

In this chapter, CNTs coated with MnO₂ will be used as anodes in an effort to improve the capacity of LIBs. It is anticipated that large improvements in capacity and power density can be achieved because of the embedded CNTs possessing a large surface area and good electric conductivity. This research will use cyclic voltammetry and galvanostatic cycling at different rates. The electrodeposition process will be optimized to maximize the performance of the LIB being investigated.

2.2 Experimental methods

The plating solution consisted of 0.3M sodium acetate and 0.3M $\text{MnSO}_4 \cdot 7\text{H}_2\text{O}$. Sodium acetate was added to stabilize the deposition solutions. CNTs were obtained by water-assisted chemical vapor deposition (WACVD method¹⁸). The CNTs were functionalized by acidification. The concentration of acidified CNTs is 2 mg/L. CNTs can be well dispersed into the solution only after acidification. The acidification process was as follows: 20 mg of CNTs were introduced into 40 ml H_2SO_4 and HNO_3 solution with a 3:1 ratio. The solution was preheated to 70°C and CNTs were immersed in the acidic solution for two hours before filtration.

The three-electrode cell configuration was used for electrodeposition as shown in Figure 2-1. It consists of a platinum counter electrode placed vertically 20 mm above a horizontal 430SS working electrode which is a stainless steel substrate with a dimension of 20 mm×10 mm×1 mm. A saturated calomel electrode (SCE) was used as the reference electrode.

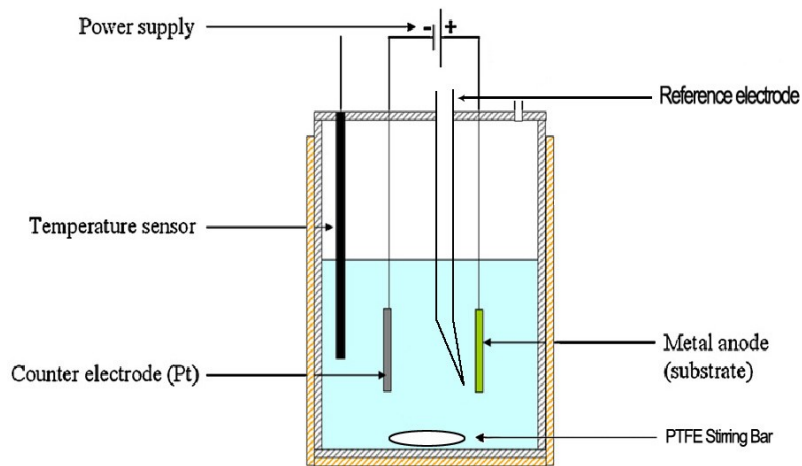


Figure 2-1. Three-electrodes cell configuration for electrodeposition.

Before anodic deposition, the 430SS substrates were polished with 600-grit SiC grinding paper, degreased in an alkaline solution at 70°C, and ultrasonically cleaned in deionized water. Agitation was introduced during electrodeposition with a magnetically driven Teflon coated stirring bar at a speed of 300 rpm.

The electrodeposition was carried out by Gamry PC4/750 potentiostat/galvanostat in a three-electrode cell configuration under galvanostatic control of the current density at 30 mA/cm², 50 mA/cm², 70 mA/cm², and 90 mA/cm², where a saturated calomel electrode (SCE) was used as the reference electrode. The positive electrode was stainless steel substrates with dimensions of 20 mm × 10 mm × 1 mm, and the negative electrode was a 52 mesh woven platinum sheet with dimensions of 20 mm × 10 mm. The cathodic and anodic electrodes were set in vertical position opposite to each other with a distance of 20 cm. The plating solution used was 0.3 M sodium acetate and 0.3 M MnSO₄ with the pH value adjusted to be 6.7~7.0. 20 mL CNT (2.0 mg/mL) solution was then dispersed into 500 mL plating solution and agitated with

Teflon-coated stirring bar at a speed of 700 rpm. During the electrodeposition, the temperature of the plating solution was controlled to be at 70°C. After electrodeposition for 4 hours, products were filtered from the plating solution, and rinsed with deionized water.

Such a setup is easy to prepare and the plating conditions can be readily adjusted. Traditionally, for electrodeposition, the working electrode where MnO₂ is deposited must be prepared first. CNT film used as a working electrode was fabricated using the filtration method.^{19, 20, 21} However, there are some drawbacks when a CNT film-working electrode is used for MnO₂ deposition. First, the CNT working electrode must be prepared through filtration, which can be costly and time consuming. Second, MnO₂ cannot be deposited uniformly throughout the thickness of a CNT substrate formed by filtration, and MnO₂ is commonly coated only on the surface of CNT film. Third, the bonding between CNTs in CNT film formed by filtration is not very strong, and CNTs on the surface of the working electrode can be washed away by a plating solution if stirring is applied during plating. To avoid the above shortcomings, we used stainless steel as the working electrode and the individual CNTs in the plating solution can serve as mobile working electrodes when they come into contact with the surface of stainless steel under stirring conditions. Thus, individual CNTs can be deposited with MnO₂ on the wall.

The weight of MnO₂ in the composites was calculated by acid dissolve method. The

final products of electrodeposition were dried in 120°C oven for 24 hours. After drying, the weight of product and a filter membrane were weighted. The dried products were added into 250ml 0.3M H₂SO₄ solution. After 2 hours stirring by Teflon coated stirrer solution was filtered. 1.0L D.I. water was used to wash away residue H₂SO₄. The filtered products and filter membrane was placed in to 120°C oven for 24 hours. Then the filter membrane and filtered product were weight together. The difference of weight before and after acid dissolving was the weight of MnO₂ in the whole composites.

The morphology and structure of products were analyzed by transmission electron microscopy in bright field mode (TEM, JEOL JEM-2100 with LaB6 cathode, 200 kV and JEOL 2010 attached with 4pi EDXS system). X-ray photoelectron spectroscopy (XPS) was carried out using a Kratos AXIS Ultra-x-ray photoelectron spectrometer. X-ray photoelectron spectroscopy (XPS) was carried out using a Kratos AXIS Ultra-x-ray photoelectron spectrometer. The standard X-ray source is supplied with aluminium and magnesium anodes. The XPS results were analyzed by CasaXPS software. The electrochemical experiments were performance using 2032-type coin cells. To prepare working electrodes, active material (MnO₂/CNTs), Super-C65 carbon black, and polyvinylidene fluoride with mass ratio 90:6:4 were mixed homogeneously in N-methyl pyrrolidone (NMP). The obtained slurry was pasted onto Cu foils, vacuum dried at 120°C overnight, and pressed. The total loading mass of the material on Cu foil was then determined to be ~2 mg/cm² for all three composite

materials. After cutting into a round disk with a diameter of 1.5 cm, the electrodes were assembled in an Argon-filled glove box, using the electrolyte of 1M LiPF₆ in ethylene carbonate/diethyl carbonate/dimethyl carbonate (EC/DEC/DMC, vol 1:1:1) (MTI Corporation), 2 pieces of separator (Celgard 2500), and a pure lithium metal foil (MTI Corporation) as a counter electrode. The cycle performance tests were carried out at 22 ± 1°C using a 1470E multi potentiostat/celltest system (Solartron).

2.3 Results and Discussion

2.3.1 The type and morphologies of manganese oxide being plated

The structure and morphology of CNT-MnO_x were investigated after electrodeposition. Figure 2-2 shows the morphology of CNTs before and after electrodeposition. Compared with the original acidified CNTs shown in Figure 2-2 (a), the carbon nanotubes after electrodeposition were decorated with many nano size particles as shown in Figure 2-2 (b). Such nano particles seem to be uniformly distributed on the surface of CNTs. Unlike the MnO_x electrodeposition without CNTs shown in Figure 2-2 (c), agglomeration of nano particles in the presence of CNTs was not observed.

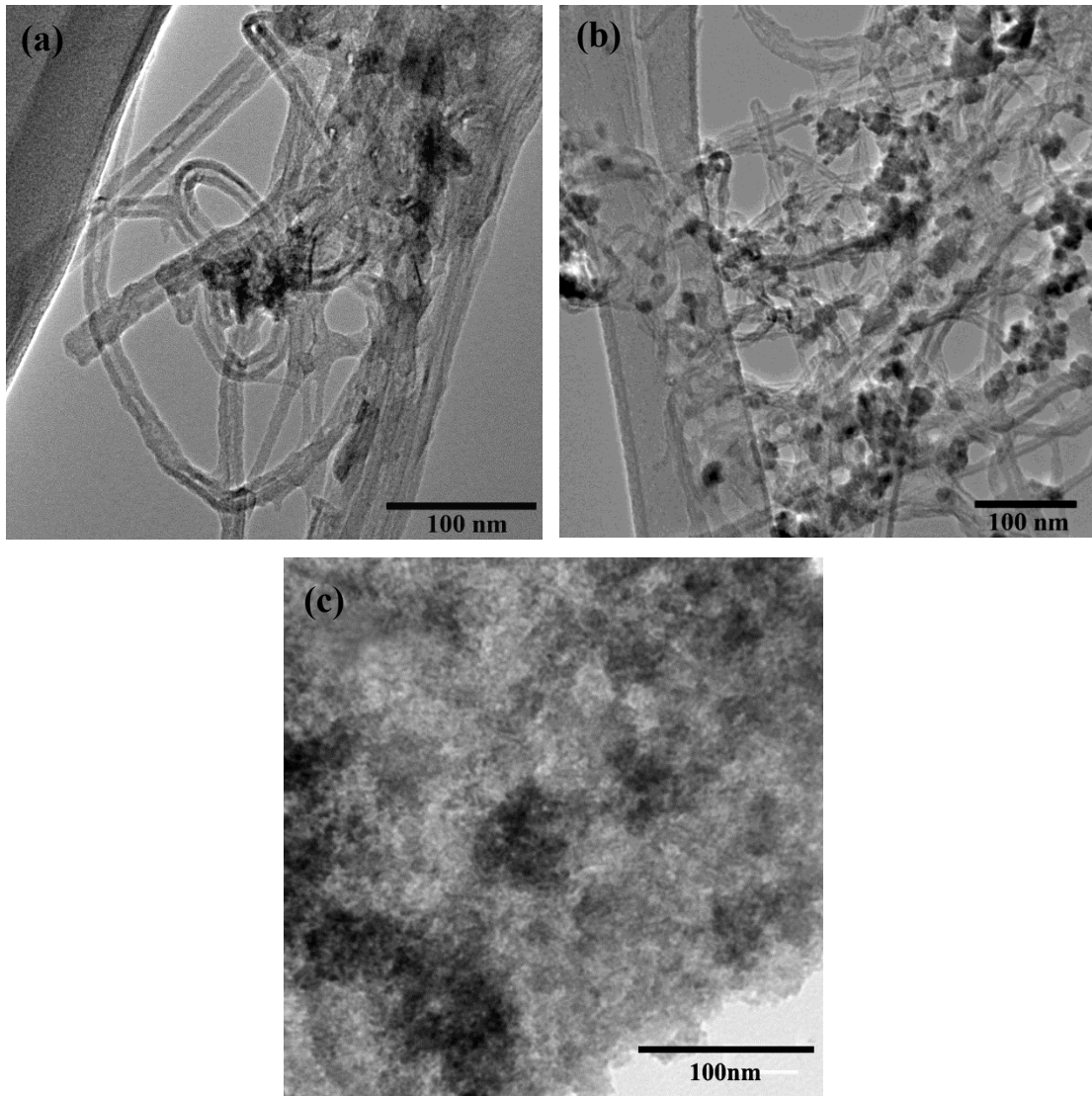


Figure 2-2. The morphology of the CNT before and after coating with manganese oxides from TEM bright field results. (a) Morphology of CNT without coating. (b) Morphology of CNT after coating with manganese oxide. (c) Morphology of manganese oxide deposited on stainless steel without CNTs.

The Energy Dispersive Spectroscopy (EDS) of the CNTs after electrodeposition is shown in Figure 2-3. Manganese and oxygen peaks are all prominent and there are no peaks of other elements detected except for Carbon (C) from CNTs and Copper (Cu) from the sample grid. Obviously, these particles must be manganese oxide. The deposited MnO_x particles are all nano sizes.

To determine the valence and structure of products being deposited, XPS and TEM)diffraction characterization was performed. EDX results of CNT after electrodeposition shows that there are only carbon, oxygen and manganese elements in the whole composites. XPS result shows the Mn 3s peaks of the plated products. The valence of manganese is +4 which is calculated by the width of binding energy of 3s peaks. An examination of the diffraction pattern in Figure 2-5 reveals several characteristic diffraction rings. Table 2-1 shows the experimental inter-planar distances determined from these rings. The d-spacing and Miller indices of these rings were compared with PDF cards #731539. The MnO_2 structure was confirmed which is γ - MnO_2 .

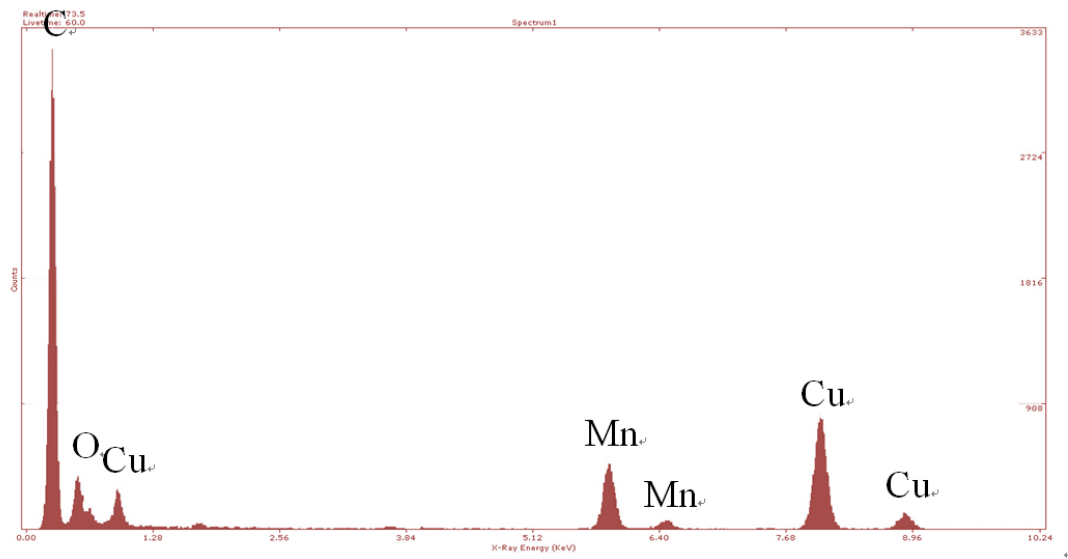


Figure 2-3. EDS spectrum of the CNT after electrodeposition.

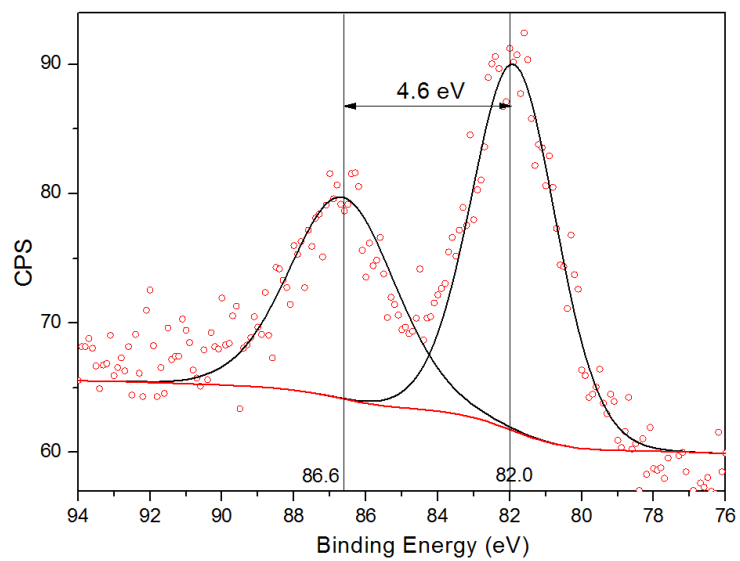
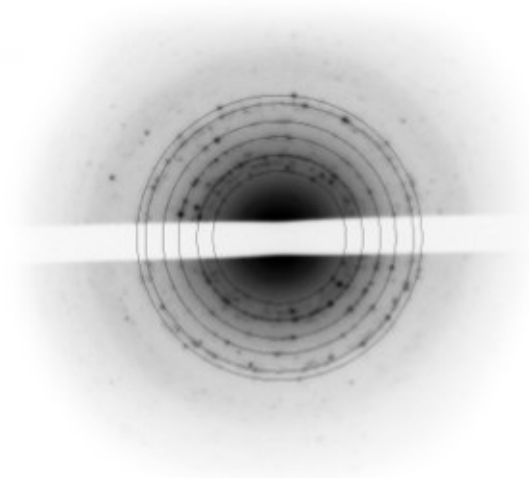


Figure 2-4. XPS spectrum of the CNT after electrodeposition.



d- Spacing (nm)	hkl
0.26	130
0.24	021
0.21	210
0.17	150
0.15	310

Figure 2-5. The diffraction pattern image of manganese dioxides.

Table 2-1. d-spacing and Miller indices of these rings.

2.3.2 Effect of electrodeposition conditions on the deposition of manganese oxide

The effect of electrodeposition parameters on the weight of deposited MnO_2 is shown in Figure 2-6. The weight of manganese dioxide being deposited increased steadily with the plating time and plating current density.

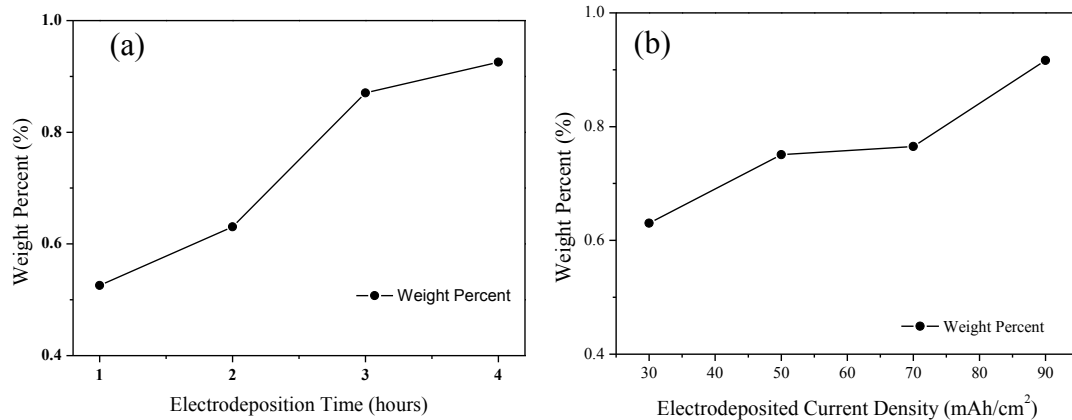


Figure 2-6. Change of weight of manganese oxide on one milligram of the CNT under various plating conditions: (a) MnO₂ weight percent changes as a function of electrodeposited time. Plating current density is 30mA/cm². (b) MnO₂ weight percent changes as a function of current density. Plating time is two hours for experiments in (b).

The plating time and the weight percent of MnO₂ in the MnO₂-CNTs composite exhibit a nearly linear relationship. This can be easily understood from the mechanism of electrodeposition. It is believed that MnO₂ is deposited on the surface of CNTs when CNTs are in contact with the stainless steel electrode. Increasing plating time means that the probability of contacting with the working electrode will be increased; therefore the amount of Mn²⁺ to be oxidized will be increased. When the plating solution is stirred with a steady stir speed, a constant rate of contacts between the ferrite stainless steel substrate and the CNT fibres can be kept. This may explain a nearly linear relation between the amount of Mn²⁺ to be oxidized and the plating time.

Figure 2-6(b) shows the relationship between the current density and the weight percent of MnO₂ coated on CNTs. Electrodeposition time for these experiments was two hours. The larger the current density was, the greater the amount of MnO₂ that

was deposited. However, a deflecting point was observed in the curve in Figure 2-6(b). The weight of MnO_2 at 90 mA/cm^2 increased dramatically. Although the CNTs and ferrite stainless steel are both conductive, MnO_2 , the electrodeposited product on the stainless steel electrode, is not a good conducting material and will reduce the electrical conductivity between the substrate and the electrolyte. Manganese dioxide can form a film covering the stainless steel surface. The film has also been found to be less porous with increasing current density because of a quick deposition at a high current density as shown in Figure 2-6(e). Although the probability of Mn^{2+} contacting with the surface of the working electrode can be constant, the probability of further oxidizing Mn^{2+} ions at each contact may decrease as the electrodeposition time increases.

It was found that the MnO_2 film that formed on the stainless steel surface is more susceptible to cracking at a higher current density. Once this non-conductive film is broken and exfoliated from the substrate, Mn^{2+} can be effectively and continuously oxidized. This explains the accelerated weight increase of MnO_2 on CNTs at the current density above the deflecting point shown in Figure 2-6 (b).

SEM and TEM characterization were performed to further confirm the impact of plating time and electrodeposition current density on the deposition of MnO_2 on CNTs shown in Figure 2-7. Figure 2-7 shows the morphology of CNTs coated with manganese dioxide at different plating times. As shown in Figure 2-7, manganese dioxide particles become denser with increasing plating time, which is consistent with the results shown in Figure 2-6(a)

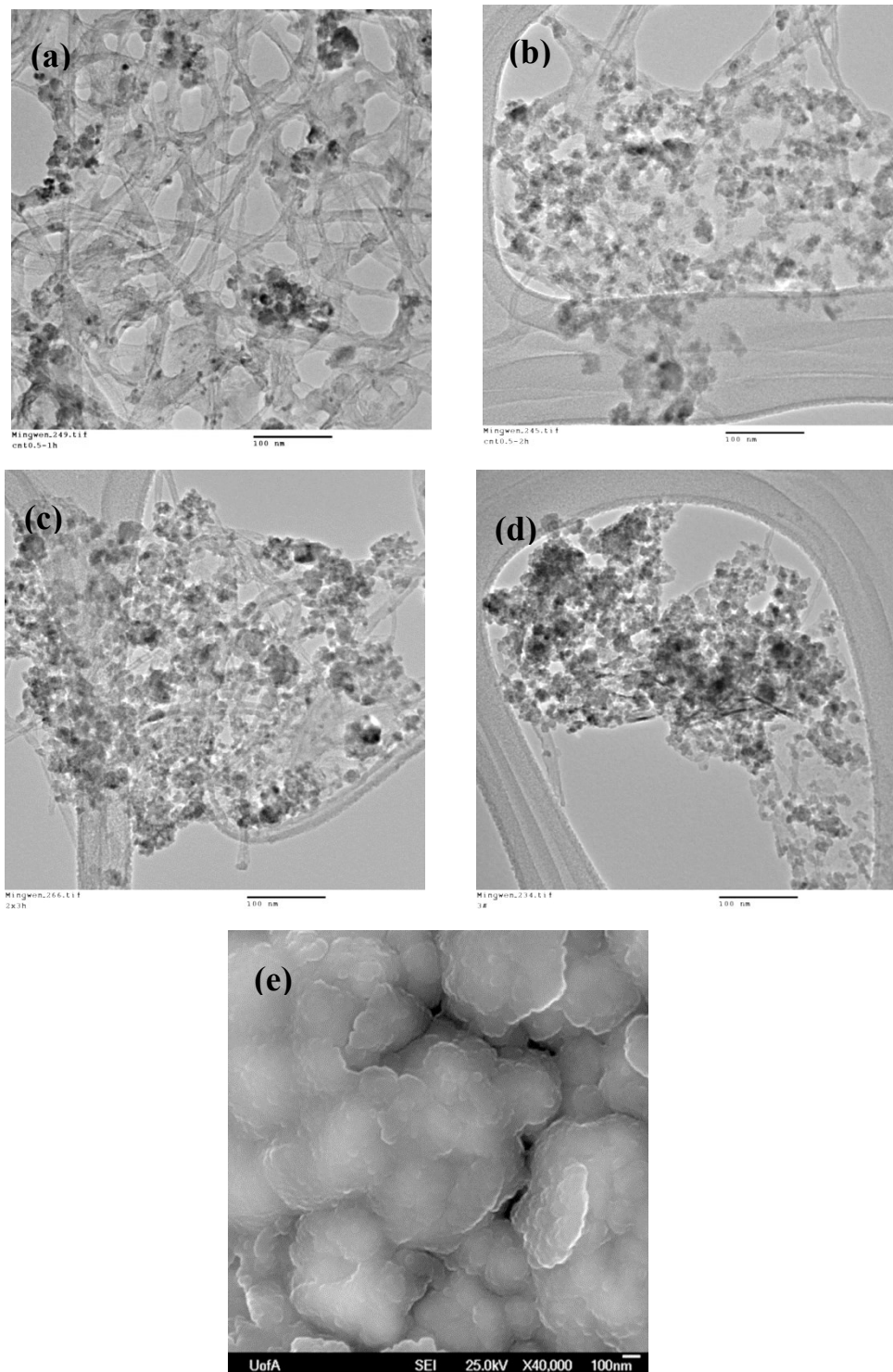


Figure 2-7. The morphology of CNT with manganese oxide from TEM bright field mode results under the same plating current density, 30mA/cm², but in different plating times: (a) one hour, (b) two hours, (c) three hours, (d) four hours, (e) SEM morphology of MnO₂ on stainless steel under 30mA/cm² 4 hours without CNTs.

The weight percent of MnO_2 in MnO_2 -CNTs is proportional to the electrodeposition time. The MnO_2 particles tend to aggregate together when the plating time is extended. The morphological features shown in Figure 2-8 are also consistent with the results displayed in Figure 2-6(b). The percentage of manganese oxide in MnO_2 -CNTs composites which are coated at $90\text{mA}/\text{cm}^2$ for two hours is 91%, which is much higher than the amount plated at other current densities, as shown in Figure 2-8(d).

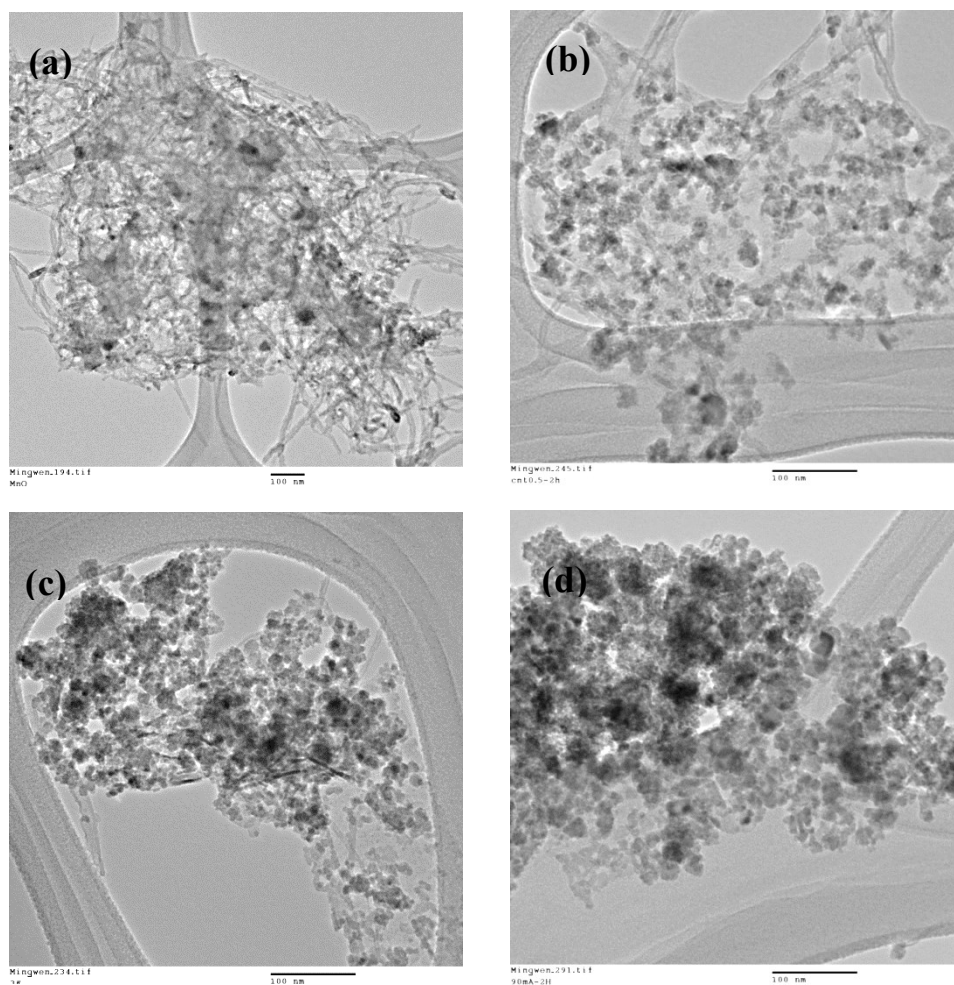


Figure 2-8. TEM Morphology of CNT with MnO_2 under different current densities: (a) $30\text{mA}/\text{cm}^2$, two hours (b) $50\text{mA}/\text{cm}^2$, two hours (c) $70\text{mA}/\text{cm}^2$, two hours (d) $90\text{mA}/\text{cm}^2$, two hours

2.3.3 Charging and discharging performance of MnO₂- CNTs composite electrodes for lithium ion battery

The electrochemical properties of MnO₂-CNTs composites were determined by a galvanostatic method. These batteries were made of a MnO₂-CNTs anode and a lithium metal cathode. The underlying mechanisms of the charging and discharging of the MnO₂-CNTs composite electrode were proposed based on the obtained galvanostatic behavior.

Figure 2-9(a) shows the voltage-capacity curves of the MnO₂-CNTs electrodes deposited under different current densities. The capacity was measured between 0.01 and 3.0 V vs Li/ Li⁺. The capacities of all electrodes in the first discharge cycle were determined and are shown in Figure 2-9(b). Obviously, the electrode made from the MnO₂-CNTs composite deposited under the 30 mA/cm² current density has the largest capacity. However, the discharge curve of such composite material manifests that this electrode is not good enough to be an ideal material for rechargeable LIB because there is no stable discharge plateau. At 30 mA/cm² electrodeposition current density, the weight percentage of MnO₂ in the MnO₂-CNTs composite is 63%, which is lower than at other conditions (70 mA/cm²: 77%; 90 mA/cm²: 91%). As seen in the discharging curve, the potential dropped quickly to around 0.2V, then decreased continuously to 0.01V. The latter reflects the discharging behavior of CNT.

As for the discharging curve for the MnO₂-CNTs composite prepared by electrodeposition at 70 mA/cm², a discharging voltage plateau around 0.4V, which coincided with the discharging voltage plateau of MnO₂, was identified. In addition,

the capacity of MnO_2 achieved as high as 1003 mAh/g, which is close to the theoretical capacity of MnO_2 , 1230 mAh/g. The weight ratio of MnO_2 in the whole electrode material coated under 70 mA/cm^2 is rather high, but is still much less than that of the electrode plated at 90 mA/cm^2 . The latter exhibited the poorest discharging performance among the four materials studied. This might have been caused by the severe aggregation of MnO_2 in the composite electrode.

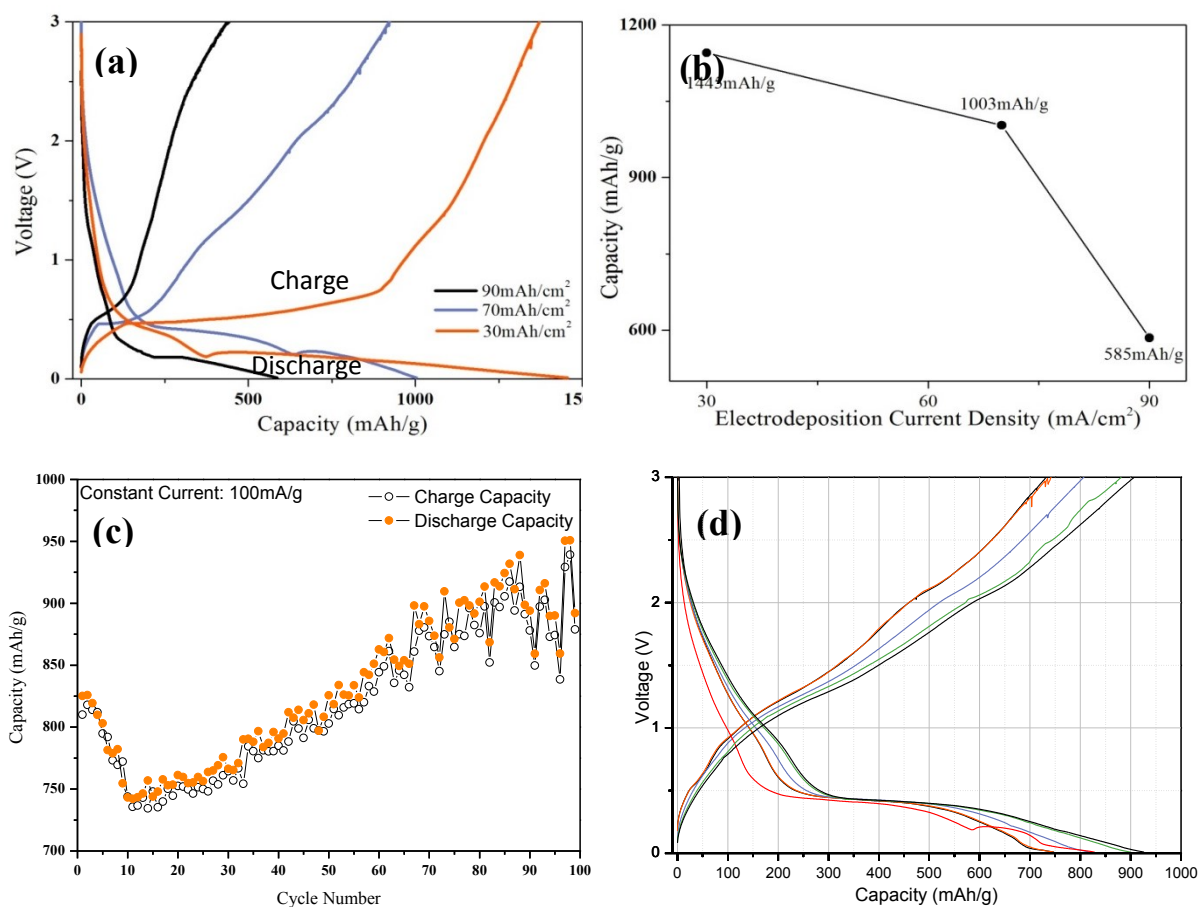


Figure 2-9. Electrochemical performance of MnO_2 -CNTs composited electrode. (a) Charging and discharging curves at different electrodeposition current density. (b) Capacity at different electrodeposition current density. (c) Cycle ability of MnO_2 -CNTs composite material at 70 mA/cm^2 current density. (d) Charging and discharging curves during different cycle numbers under 70 mA/cm^2 current density.

Although the MnO₂-CNTs composite can achieve high capacity, the cyclability of the electrode, which is another important parameter of a LIB, must be investigated. As shown in Figure 2-8 (c), the capacity of the electrode material decreased as the cycle number increased in the initial stage of charging and discharging. This is a common phenomenon in LIBs because of the formation of solid electrolyte interphase (SEI), which consumes lithium ions and prevents electrons from diffusing into MnO₂ nano particles. SEI film will result in a low columbic efficiency, which means that the energy charged into the battery is greater than the energy removed from a battery during discharge. As a result, the capacity of the battery will drop as it cycles.

The capacity of the MnO₂-CNTs composite was found to increase with the cycle number after about 15 cycles. This is an interesting trend for LIB electrodes. In order to understand this trend and the charging-discharging mechanism of MnO₂-CNTs composite electrode, several charging and discharging curves at different cycle numbers were analyzed, as shown in Figure 2-9 (d).

From the discharge curves in Figure 2-9 (d), it is clear that MnO₂ played a dominant role during all of the electrochemical reactions as the MnO₂ discharge voltage plateau remained clear and strong for all the cycles. However, some differences in these curves were observed at two voltage regions, 0.8V~0.5V and below 0.4V. The discharging time between 0.8V and 0.5V increased with the cycle number. The reaction in the potential range between 0.8V and 0.5V usually comes from the formation of SEI. In most cases SEI is formed only in the first few discharging cycles.

A TEM examination was performed to reveal the underlying mechanism in the 0.8V~0.5V voltage region. Figure 2-10 (a), (b) and (c) display the morphology and diffraction pattern of MnO₂-CNTs before discharging . Figure 2-10 (d), (e) and (f) show the morphology and the diffraction pattern of this composite material after 100 charging-discharging cycles. The Mn-O particles after the charging-discharging cycles didn't possess well-defined crystal structure from the diffraction pattern as that of the original crystalline MnO₂ nano-particles on the surface of CNTs, as shown in Figure 2-10 (c). Also, the gel-like matrix around MnO₂ should be arisen from the formation of solid electrolyte interface (SEI).

Based on the above observations, the mechanism of charging-discharging the MnO₂-CNTs composite material can be hypothesized. During repeated charging-discharging, crystalline MnO₂ nano particles continuously decomposed. In addition, SEI was repeatedly formed on the surface of freshly decomposed MnO₂ within the potential range between 0.8V and 0.5V and during the extended discharging period as the number of cycles increased because the reaction in the potential range between 0.8V and 0.5V usually comes from the formation of SEI. The voltage window between 0.4V-0.01V belongs to the extra interfacial lithium storage stage. At this stage excess lithium can be accommodated at interfacial areas between manganese and Li₂O until the lithium potential approaches the value of pure lithium. As the particle size was reduced continuously, the surface area of MnO₂ was increased, allowing the extra-lithium-storage stage to last longer.

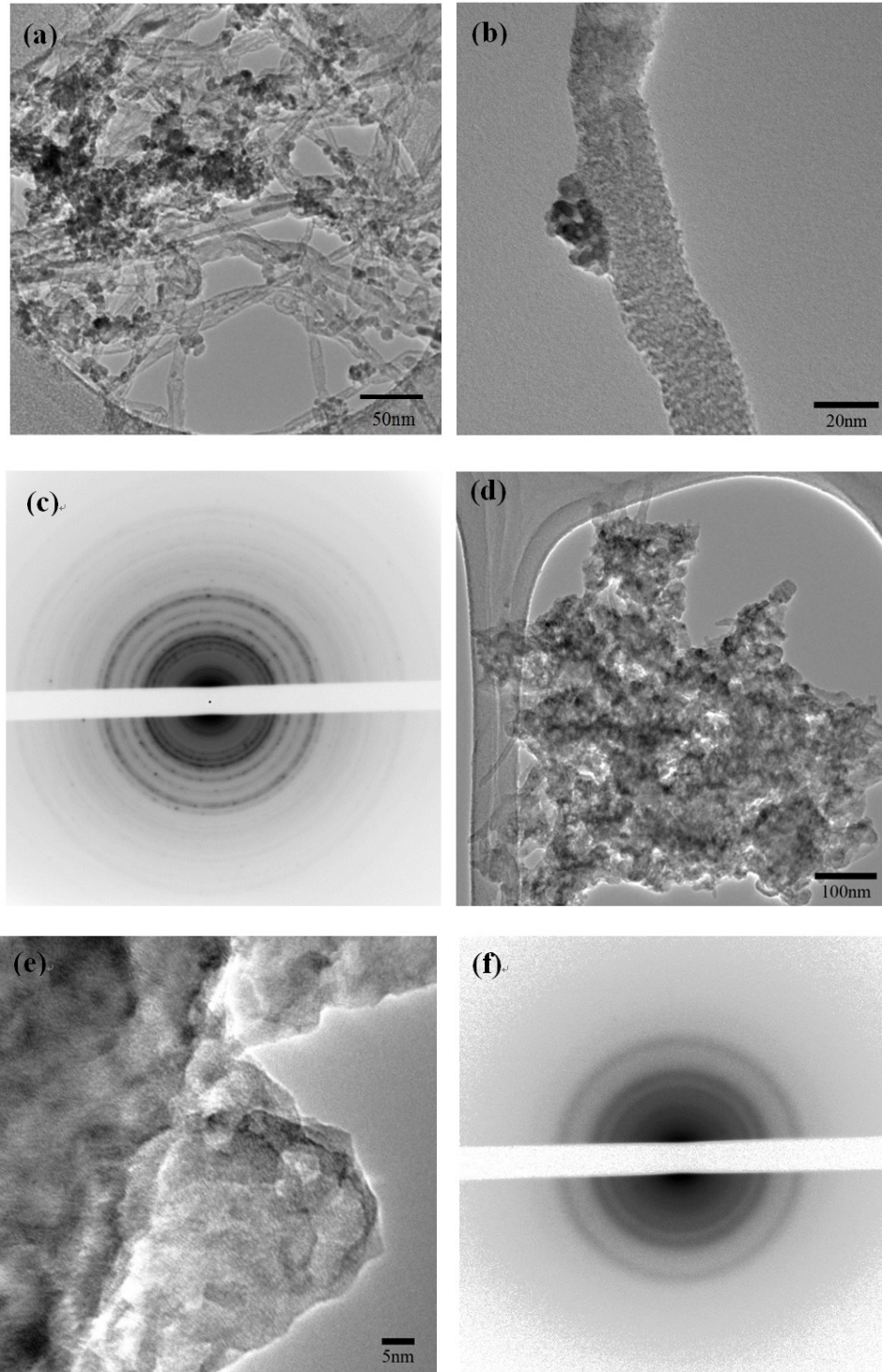


Figure 2-10. (a) morphology of MnO₂-CNTs before discharging, (b) large magnification morphology of MnO₂-CNTs before discharging, (c) diffraction pattern of MnO₂-CNTs before discharging. (d) morphology of MnO₂-CNTs after 150 recharge cycles, (e) large magnification morphology of MnO₂-CNTs after 150 recharge cycles. (f) Diffraction pattern of MnO₂-CNTs after 150 recharge cycles.

2.4 Conclusion

Compared with other electrode materials, MnO can be a promising anode candidate for LIBs because of its low cost, high capacity and environmental friendly. For LIBs, electrodes made of MnO₂-CNTs composites can tolerate larger volume expansion - contraction during the charging and discharging process and exhibit better electric conductivity. Electrodeposition is an effective way to synthesize MnO₂-CNT composites under ambient pressure and at low temperatures, which can reduce the fabrication cost of electrode materials and at the same time improve the performance of LIBs. A preliminary investigation has demonstrated the feasibility of plating MnO₂ on CNTs. The weight of MnO₂ on one milligram CNTs can be controlled by plating time and current density. TEM analysis revealed that the MnO₂ deposited on the CNT wall is MnO₂. The MnO₂-CNT composite electrode fabricated under 70 mA/cm² current density has the best charging-discharging performance. The mechanism of the charging-discharging process was also proposed.

2.5 References

- 1 J. Tellefson, *Nature*, 2008, 456, 436-440.
- 2 W. Schalkwijk, B. Scrosati, *Advances in Lithium-ion Batteries*, Kluwer Academic/Plenum, Boston, 2004.
- 3 B. Scrosati, J. Garche, *Journal of Power Sources*, 2010, 195, 2419–2430.
- 4 G. Pistoia, *Lithium batteries : new materials, developments and perspectives*. Amsterdam ; London: Elsevier; 1994.
- 5 B. Gao, A. Kleinhammes, X. Tang, C. Bower, L. Fleming, Y. Wu, O. Zhou, *Chemical Physics Letters*, 1999, 307, 153-157.
- 6 F. Leroux, K. Metenier, S. Gautier, E. Frackowiak, S. Bonnamy, F. Beguin , *Journal of Power Sources*. 1999, 81, 317-322.
- 7 A. Claye, J. Fischer, C. Huffman, A. Rinzler, R. Smalley, *Journal of the Electrochemical Society*. 2000, 147, 2845-2852.
- 8 S. Yang, J. Huo, H. Song, X. Chen. *Electrochimica Acta*. 2008, 53, 2238-2244.
- 9 C. Mi, G. Cao, X. Zhao. *Journal of Electroanalytical Chemistry*. 2004, 562, 217-221.
- 10 K. Nishidate, M. Hasegawa, *Physical Review B*. 2005, 71, 245418.
- 11 V. Meunier, J. Kephart, C. Roland, J. Bernholc. *Physical Review Letters*, 2002, 88, 075506.
- 12 T. Kumar, R. Ramesh, Y. Lin, G. Fey. *Electrochemistry Communications*, 2004, 6, 520-525.
- 13 B. Gao, C. Bower, J. D. Lorentzen, L. Fleming, A. Kleinhammes, X. P. Tang, L. E. MnNeil, Y. Wu, O. Zhou, *Chemical Physics Letters*. 2000, 327, 69-75.
- 14 H. Shimoda, B. Gao, X. P. Tang, A. Kleinhammes, L. Fleming, Y. Wu, O. Zhou, *Physical Review Letters*, 2002, 88, 015502.
- 15 Z. Yang, H. Wu, *Materials Letters*, 2001, 50, 108-114.
- 16 G. Maurin, Ch. Bousquet, F. Henn , P. Bernier, R. Almairac, B. Simon, *Solid State Ionics*, 2000, 136, 1295-1299.
- 17 L. Cui, Y. Yang, C. Hsu, Y. Cui, *Nano Letters*, 2009, 9, 3370-3374.
- 18 X. Cui, W. Wei, W. Chen, *MRS Online Proceeding Library*, 2011, 1204.
- 19 J. H. Kim, K. H. Lee, L. J. Overzet, G. S. Lee. *Nano Letters*, 2011, 11, 2611-2617.
- 20 A. L. M. Reddy, M. M. Shaijumon, S. R. Gowda, P. M. Ajayan. *Nano Letters*, 2009, 9, 1002-1006.
- 21 H. Zhang, G. Cao, Z. Wang, Y. Yang, Z. Shi, Z. Gu. *Nano Letters*, 2008, 8, 2664-2668.

Chapter 3 Electrochemical deposition MnCO₃ on Reduced Graphene Oxides for LIBs

3.1 Introduction

Electrochemically active transition metal oxides (MO_x), such as FeO_x^{1,2}, CoO_x^{3,4}, SnO₂^{5,6,7}, and MnO_x^{8,9,10,11,12}, have been widely used as promising candidates for anode materials in lithium-ion batteries (LIBs). Besides these metal oxides, MnCO₃ is naturally abundant, environmentally friendly, and often used as a precursor for MnO₂ synthesis;^{13,14,15} and hence, its cost is even lower than MnO₂ and most of the transition-metal oxides. However, very few researches were reported to use MnCO₃ directly as electrochemically active materials. Yan et al. has reported a reversible capacity of 750 mAh/g for MnCO₃ when used as anodes in LIBs, which is comparable to that reported for MnO₂ (495 mAh/g ~900 mAh/g).^{8-10,15} However, its capacity quickly drops down to 200 mAh/g after 100 cycles, which is due to the intrinsic low electrical conductivity and the compact morphology of hydrothermal MnCO₃ micro-particles.^{15, 16} Poizot et al. also found that the electrochemical performance of metal-oxide particles was affected by their morphology, e.g., the particle size and crystal structure of metal oxides¹⁷. Therefore, the electrical conductivity and the morphology of MnCO₃ need to be optimized for lithium-ion storage.

Mesoporous single crystals (MSCs) promise excellent features for energy storage, such as high-rate lithiation/delithiation capability, long-range electronic connectivity, and high structural integrity^{18,19,20,21}. However, the application of MSCs was limited by their complex and high temperature (>500°C) synthesizing processes, involving template planting and removing.^{18,22,23,24} In addition, graphene wrapped structure offers a highly conductive shell and provides additional protection to the wrapped particles during cycling.^{10,25} To the best of our knowledge, their combination, the graphene-wrapped MSC structure, although highly demanded for energy storage, hasn't been reported so far.

Here, we designed a unique morphology of graphene-wrapped MSC for MnCO₃ and directly used it as anode materials in LIBs. In a departure from previous high-temperature synthesis approaches, we developed a simple, low-temperature (70°C) and template-free method, referred to as dynamic floating electrodeposition (DFE) (Figure 3-1 (a)), to fabricate graphene-wrapped MnCO₃ MSCs. Instead of only reducing GOs to RGOs in the electrochemical cell that has been reported by previous researchers,^{26,27,28} we, for the first time, achieved the reduction of GOs to RGOs, the deposition of MnCO₃ MSCs on graphene, and graphene-wrapped morphology, all three goals in one electrochemical process. The resulting submicron, graphene-wrapped MnCO₃ MSCs reached a high reversible capacity of 900 mAh/g after the initial cycle and delivered over 1,000 mA/g after 130 cycles. Furthermore, the reversible capacity kept at this high level for more than 400

cycles and maintained 422 mAh/g at a high rate of 5,000 mA/g, demonstrating their great potential to be used as anodes in LIBs. It is also the first time that this high performance has been achieved on MnCO_3 for lithium-ion storage. The structural design of the active materials, the DFE synthesis method, and the high performance for lithium-ion storage provided in this work may point out new directions in developing high performance energy storage systems.

3.2 Experimental Procedure

3.2.1 Material synthesis

GO preparation: The graphene oxide was synthesized from natural graphite powders (MTI Corporation) based on a modified Hummers method^{29,30}. The exfoliation of graphite oxide to GO was achieved by sonication for 2 hours (Branson 2510, 1000 W, 20% amplitude), and then, GOs were filtered and rinsed with deionized water. Finally, a homogeneous GO in deionized water solution (2.0 mg/mL) was obtained and used for electrodeposition.

Synthesis of graphene-wrapped MnCO_3 MSCs by DFE method: The dynamic floating electrodeposition was carried out by Gamry PC4/750 potentiostat/galvanostat in a three-electrode cell configuration under galvanostatic control of the current density at 30 mA/cm², where Ag/AgCl was used as the reference electrode. The cathodic electrode was ferritic stainless steel substrates with dimensions of 20

mm× 10 mm × 1 mm, and the anodic electrode was a 52 mesh woven platinum sheet with dimensions of 20 mm× 10 mm. The cathodic and anodic electrodes were set in vertical position opposite to each other with a distance of 10 cm. The plating solution used was 0.3 M sodium citrate and 0.3 M MnSO₄ with the pH value adjusted to be 6.7~7.0. 20 mL GO (2.0 mg/mL) solution was then dispersed into 500 mL plating solution and agitated with Teflon-coated stirring bar at a speed of 700 rpm. During the electrodeposition, the temperature of the plating solution was controlled to be at 70°C. After electrodeposition for 4 hours, graphene-wrapped MnCO₃ MSCs were filtered from the plating solution, and rinsed with deionized water before freeze-dried (Savant supermodulyo freeze dryer, Thermo Electron Corporation) for over 10 hours.

Synthesis of nanocrystalline MnCO₃-RGO (nc-MnCO₃-RGO): Nanocrystalline MnCO₃ was synthesized by a hydrothermal method¹⁵. 0.474g KMnO₄, 0.595g glucose and 0.15g potassium sodium tartrate were dissolved in 50 mL of deionized water, which was then mixed to form a homogeneous solution by constant magnetic stirring. The resulting mixture was sealed into Teflon-lined autoclaves (60 mL) and heated at 160°C for 6 h. The final products of nanocrystalline MnCO₃ were then collected and washed with deionized water and absolute alcohol several times before vacuum dried. RGOs were reduced from GOs by refluxing with 0.8 g of glucose and 0.76 mL of ammonia solution (25 wt%) at 95°C for 1h. Nanocrystalline MnCO₃ particles were then homogeneously mixed with RGOs in deionized water with the weight ratio of 9:1 to form nc-MnCO₃-RGO, followed by freeze drying.

Synthesis of MnO₂ nanoflakes-RGO (nano-MnO₂-RGO): nano-MnO₂-RGO was prepared according to a two-step chemical method reported previously. In brief, 0.23g of KMnO₄ was slowly added to 10 mL of the homogeneous GO/MnSO₄ solution, and the mixture was refluxed at 80°C for 2 hours for the fabrication of GO/MnO₂ composites. In the second step, the resulting GO/MnO₂ composites were refluxed with 0.8 g of glucose and 0.76 mL of ammonia solution (25 wt%) at 95°C for 1 h for the reduction of GO. The resulting stable black dispersion was centrifuged and washed with deionized water, which was followed by freeze drying to obtain nano-MnO₂- RGO.

3.2.2 Characterization

The morphology and structure of graphene-wrapped MnCO₃ MSCs, nc-MnCO₃-RGO and nano-MnO₂-RGO were analyzed by scanning electron microscopy (SEM, Hitachi S-5500, Hitachi S- 4800, and Zeiss EVO SEM equipped with a Bruker Silicon Drift Detector for Energy Dispersive X-Ray analysis) and transmission electron microscopy (TEM, JEOL JEM-2100 with LaB₆ cathode, 200 kV and JEOL 2010 attached with 4pi EDXS system). X-ray photoelectron spectroscopy (XPS) was carried out using a Kratos AXIS Ultra-x-ray photoelectron spectrometer. The standard X-ray source is supplied with aluminium and magnesium anodes. The XPS results were analyzed by CasaXPS software. X-ray Diffraction (XRD) analyses were conducted on a Siemens D5000 X-ray diffractometer with Cu K α as the radiation

source ($\lambda = 1.5418 \text{ \AA}$). Thermogravimetric analysis (TGA) was carried out (TA instruments, Q500) with a heating rate of $10^\circ\text{C min}^{-1}$.

3.2.3 Electrochemical measurement

The electrochemical experiments were performed using 2032-type coin cells. To prepare working electrodes, graphene-wrapped MnCO_3 MSCs, Super-C65 carbon black, and polyvinylidene fluoride with mass ratio 90:6:4 were mixed homogeneously in N-methyl pyrrolidone (NMP). The same ratio was used for making nc- MnCO_3 -RGO and nano- MnO_2 -RGO electrodes. The obtained slurry was pasted onto Cu foils, vacuum dried at 120°C overnight, and pressed. The total loading mass of the material on Cu foil was then determined to be $\sim 2 \text{ mg/cm}^2$ for all three composite materials. After cutting into a round disk with a diameter of 1.5 cm, the electrodes were assembled in an Argon-filled glove box, using the electrolyte of 1M LiPF_6 in ethylene carbonate/diethyl carbonate/dimethyl carbonate (EC/DEC/DMC, vol 1:1:1) (MTI Corporation), 2 pieces of separator (Celgard 2500), and a pure lithium metal foil (MTI Corporation) as a counter electrode. The galvanostatic charge/discharge tests, cyclic voltammetry (CV) tests and cycle performance tests were carried out at $22 \pm 1^\circ\text{C}$ using a 1470E multi potentiostat/celltest system (Solartron).

3.3 Results and discussion

3.3.1 Dynamic flowing electrodeposition

The detailed DFE process to fabricate graphene-wrapped MnCO_3 MSCs is schematically shown in Figure 3-1(a). GOs were first prepared from expandable graphite by modified Hummers method^{29,30} and well dispersed in the aqueous electroplating bath of 0.3M Na_3Cit and 0.3M MnSO_4 at pH ~ 7.0 by magnetic stirring. The well dispersed GO suspension was formed due to a large amount of oxygenated groups bonded on the surface of GOs.²⁸ The anode was Pt mesh, the cathode used was stainless steel plate and the bath temperature was set to 70°C.

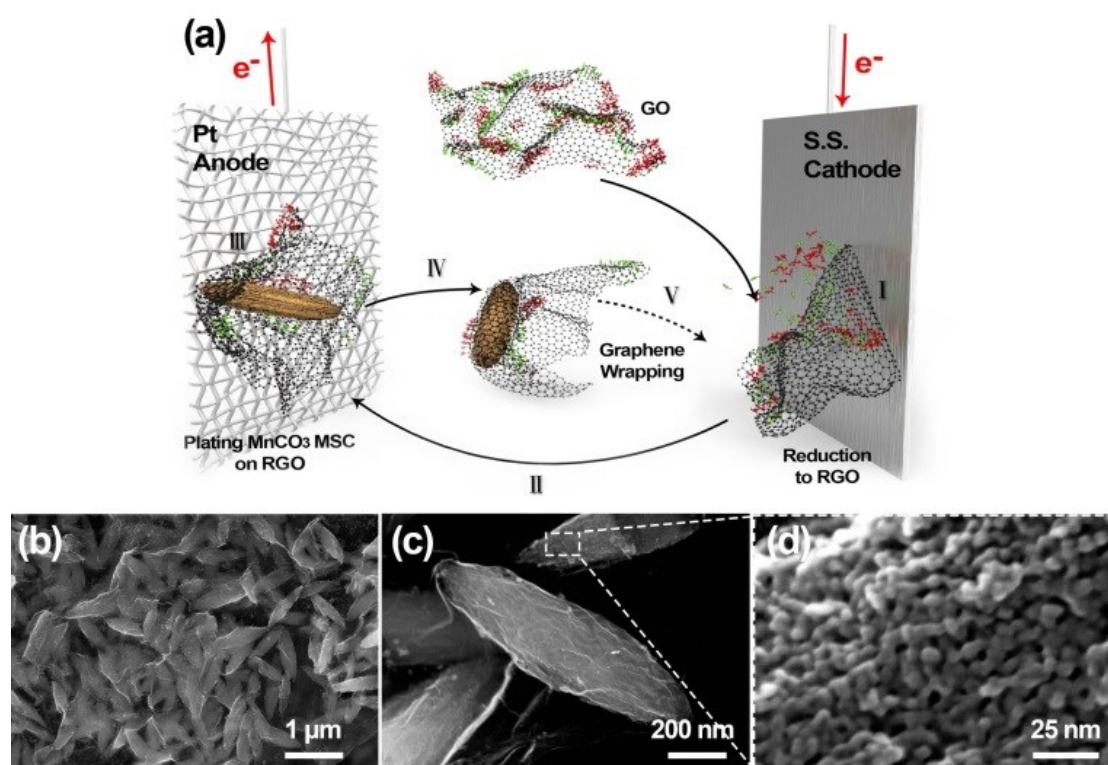


Figure 3-1. (a) A schematic illustration of the dynamic floating electrodeposition method. SEM images of (b) the novel composite, (c) the graphene wrapping structure, and (d) the mesoporous structure.

During the electrodeposition, the floating GOs were the true electrodes and the whole process was dynamic. (I) When floating to the cathode, GOs were reduced to RGOs by removing the bonded oxygen groups on GOs, which is consistent with the results reported by Guo et al²⁸. This step improves the conductivity of the floating electrodes for the subsequent electrodeposition. (II) RGOs were detached from cathode and transported to the anode by magnetic stirring. (III) At anode and at the current density of 30 mA/cm², the citrate anions were oxidized to carbonate anions (CO₃⁻²), which were bonded with Mn²⁺ to form MnCO₃ deposits. Surprisingly, these MnCO₃ deposits are mesoporous single crystals. It is believed that the electrodeposition on the floating electrodes is a process of pulse plating that facilitates the formation MSC structure. (IV) In the subsequent floating, RGOs acted as a flexible cloth that wrapped up the deposited MnCO₃ MSCs, forming graphene-wrapped MnCO₃ MSCs. (V) The whole process continued until the composite material was too heavy to be carried to the Pt and stainless steel electrodes. This DFE method is facile, cost effective and scalable because this method is originated from industrial electrodeposition method — barrel plating. DFE is believed to establish a new platform to synthesize various graphene-wrapped composite materials for many applications. It is also noticed that the inclusion of MnCO₃ MSCs prevents the restacking of RGOs during GO reduction¹⁰.

In order to confirm the reactions occurring on Pt and stainless steel electrodes, the same setup was used in a control experiment (Figure 3-2), except that the bath was

divided into two compartments separated by a filter paper. GOs were added into both parts and stirred by magnetic bars. After electrodeposition at the current densities of 30~70 mA/cm², GOs were kept intact at the anode, while RGOs were found at the cathode, as characterized by X-ray photoelectron spectroscopy (XPS) in Figure 3-2. These peaks of functional groups are also reported by others. Here we use Casa XPS software to analysis and confirm these functional peaks.^{31,32} Most importantly, the formation of MnCO₃ or MnO_x particles was not observed in either compartment, implying that MnCO₃ in Figure 3-1(a) was deposited on RGOs transported from the cathode (Figure 3-1(a)). In addition, another control experiment (Figure 3-2) was conducted in an aqueous electroplating bath of 0.3M Sodium EDTA and 0.3 M MnSO₄. No observation of MnCO₃ confirms that it is the citrate anions that were oxidized to carbonate anions (CO₃⁻²) and bonded with Mn²⁺ to form MnCO₃ deposits, only a weak sodium peak around 1k was found which the residue of plating solution. The oxidation of citrate anions at anodes have also been reported previously by other researchers³³.

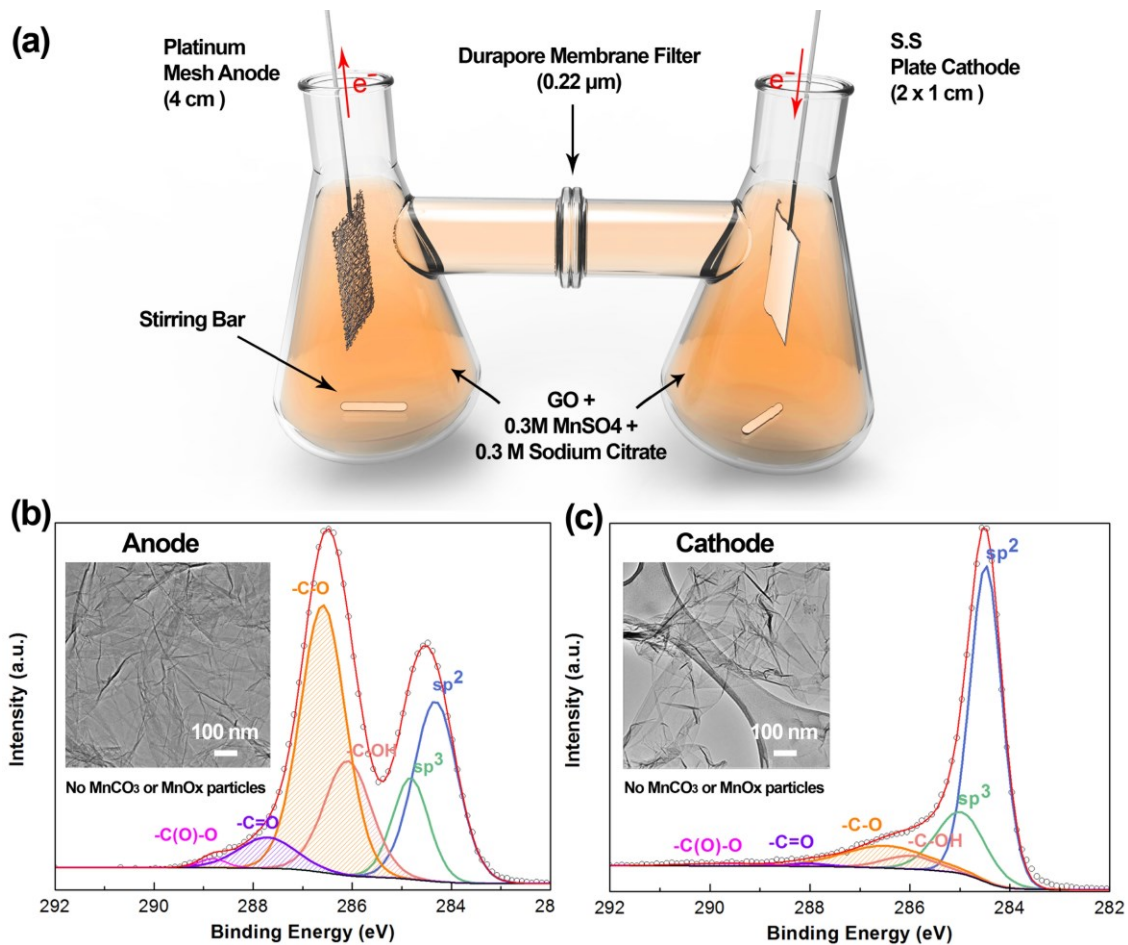


Figure 3-2. (a) The setup of the comparative experiment, in which the electrolyte was separated by a membrane at the center. Parameters were controlled as same as DFE method in Figure 3-1(a). (b) XPS and (c) TEM analyses of the products collected from electrodes.

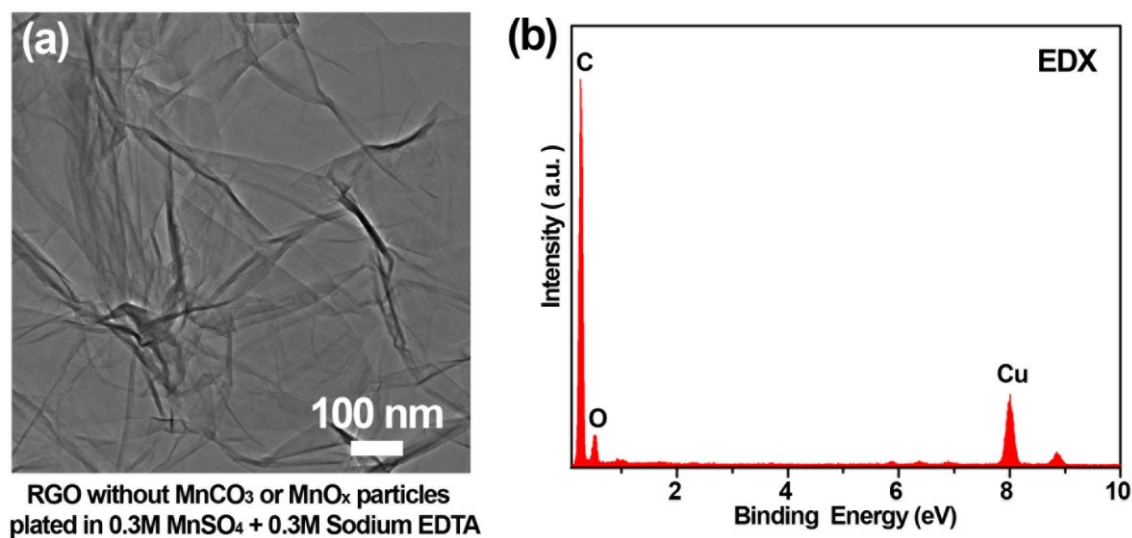


Figure 3-3. TEM and EDX analyses of the products collected from the plating solution of 0.3 M MnSO₄ and 0.3 M sodium EDTA. All other parameters were controlled exactly the same as those in DFE method in Figure 3-1(a).

Structural characterization of graphene-wrapped MnCO₃ MSCs

The morphology and microstructure of the composite materials electrodeposited from DFE method shown in Figure 3-4(a) have been carefully characterized. Low-magnification scanning electron microscopy (SEM) image (Figure 3-4(b), Figure 3-4(c)) shows that the deposited particles are composed of Mn, C and O (Figure 3-4(a)), and have an ellipsoid shape or rice-like shape with the length of ~700 nm and the width of ~250 nm. A thin layer of graphene was found to wrap around the particle (Figure 3-4(c)), forming a graphene-wrapped morphology. The structure and thickness of reduced graphene oxides were confirmed and tested by TEM and AFM results as shown in Figure 3-4. In addition, these graphene-wrapped particles are imbedded in the connected graphene matrix (Figure 3-1(b) and Figure 3-5), indicating

the formation of a 3D, conductive composite structure. In few uncovered areas on the surface of the particle, the high-magnification SEM image (Figure 3-7(d)) reveals a mesoporous structure for the particles, with the pore size being in the range of 5 to 10 nm. A cross-section view of the particles is also shown in Figure 3-6, in which a mesoporous structure is clearly observed in the inner part of the particles. This cross-section was formed natural but was selected carefully.

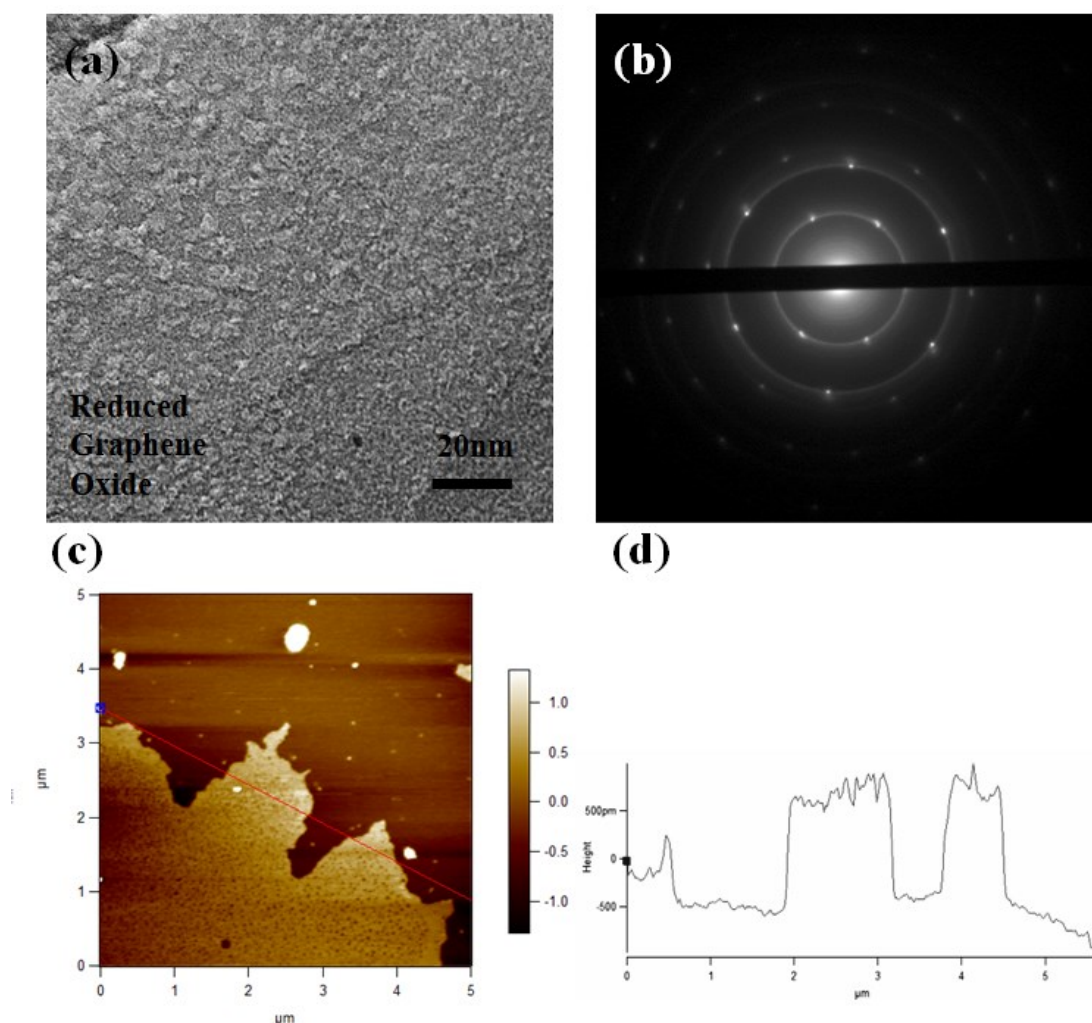


Figure 3-4. (a) TEM morphology of reduced graphene oxide. (b) The selected area electron diffraction pattern of reduced graphene oxides. (c) AFM results of reduced graphene oxides. (e) The profile of reduced graphene oxides which shows there is around 3 layers of reduced graphene oxides sheets.

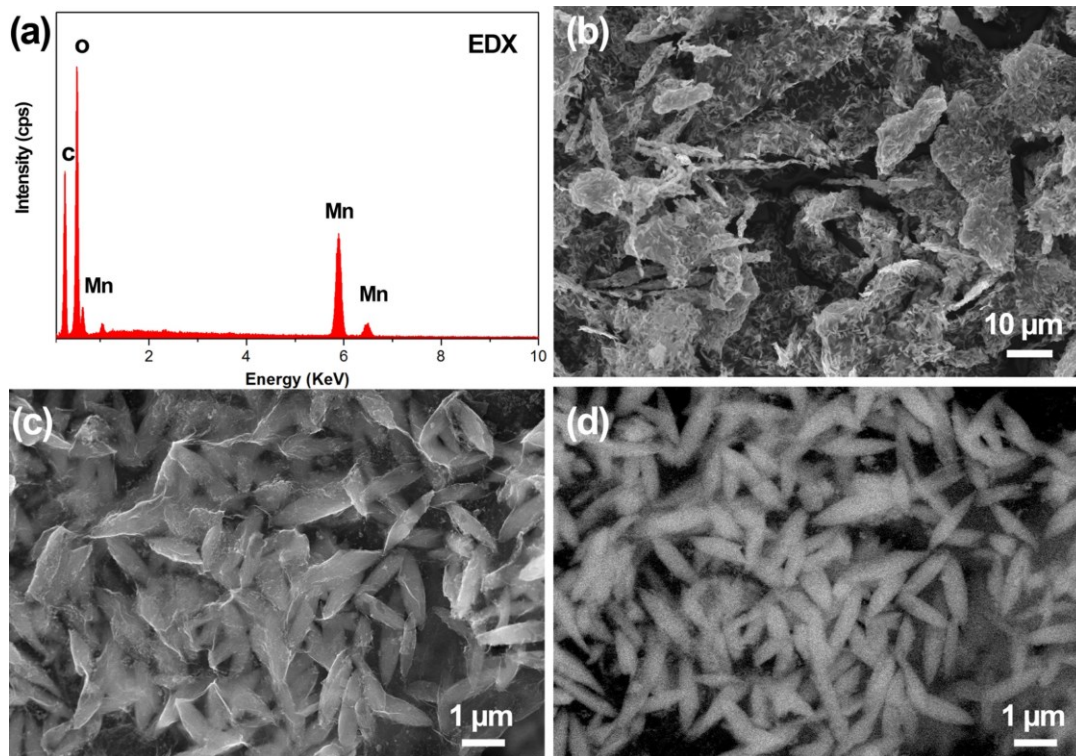


Figure 3-5. (a) EDX analysis and (b) SEM image of graphene-wrapped MnCO_3 MSCs. (c) Secondary and (d) back-scattered SEM images taken from the same location of the novel composite.

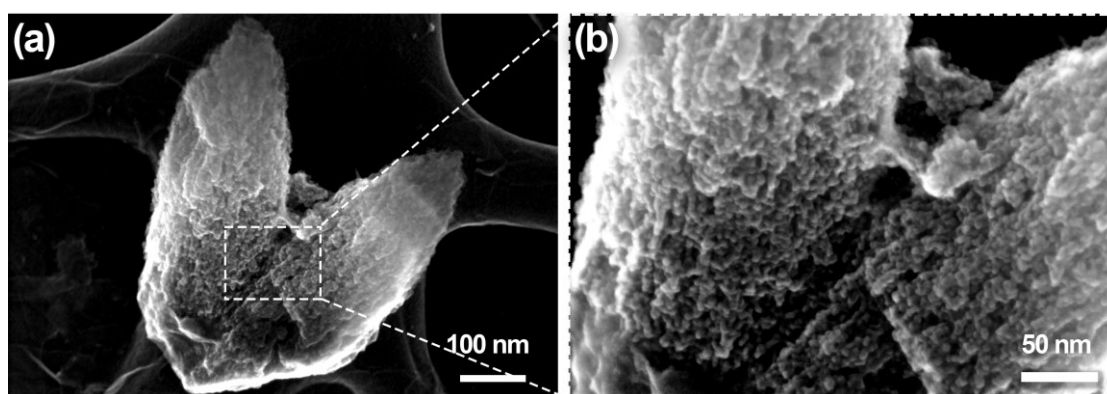


Figure 3-6. Cross-sectional SEM images of MnCO_3 MSCs.

The powder X-ray diffraction (XRD) pattern of the as-deposited composite materials

(black pattern in Figure 3-7(a)) shows that all the sharp peaks can be assigned to the rhombohedral phase of MnCO_3 (JCPDS No. 44-1472, the standard spectrum shown as red in Figure 3-7(a)) with the space group of $R\bar{3}c$. Although a small bump at small angles can be observed, the characteristic peak of graphene is not clearly identified in the XRD pattern, which may be due to the low concentration of graphene in the composite materials and will be discussed later. The peaks in the XRD pattern are so sharp that the peak widths are much narrower than those for nanocrystalline MnCO_3 synthesized before¹⁵, indicating the large-size and well-crystallized particles formed in this novel DFE method. Interestingly, electron diffraction (Figure 3-1(c)) taken from the complete particle in Figure 3-1(b) produces the Laue diffraction pattern that was indexed to [100] zone axis of Rhombohedral phase of MnCO_3 , suggesting that the resulted particles are mesoporous single crystals. High-resolution transmission electron microscopy (HRTEM) image in Figure 3-6 (d) further confirms that, although each rice-like MnCO_3 particle is mesoporous (indicated as white circles), its scaffold as a whole is a single crystal.

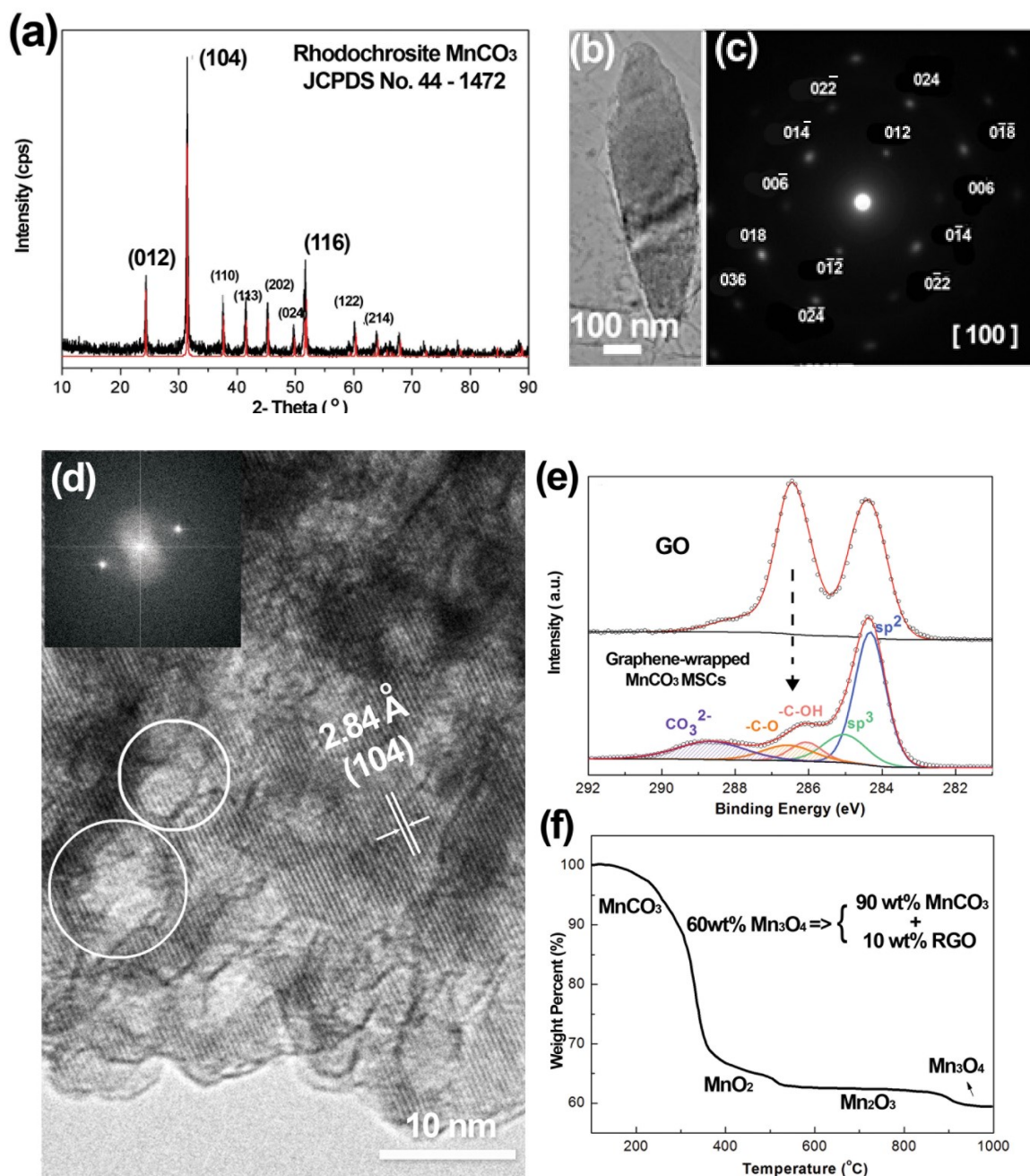


Figure 3-7. (a) XRD pattern of graphene-wrapped MnCO_3 MSCs, (b) TEM image of graphene-wrapped MnCO_3 MSCs. (c) Electron diffraction Laue pattern collected from a complete mesoporous crystal in (b) assigned to rhodochrosite MnCO_3 with [100] zone axis. (d) HRTEM image and the inserted fast Fourier transform (FFT). (e) XPS C 1s spectra of as-prepared GOs and graphene-wrapped MnCO_3 MSCs. (f) TGA of graphene-wrapped MnCO_3 MSCs used for electrochemical measurements.

XPS analyses in Figure 3-7(e) compare C1s spectra obtained from GOs (upper spectrum) and the as-deposited composite materials (lower spectrum). The significant decrease of the peaks for the oxygenated groups, as indicated by the dashed arrow in Figure 3-7 (e), suggests the successful reduction of GOs to RGOs during DFE process. Mn 3s spectrum in Figure 3-8(c) shows that Mn ions keep their valence at +2, while O1s spectrum in Figure 3-8(d) implies the presence of CO_{3-6} anions, both of which suggest the formation of MnCO_3 particles in the composite materials. These results agree well with those from SEM, TEM and XRD observations.

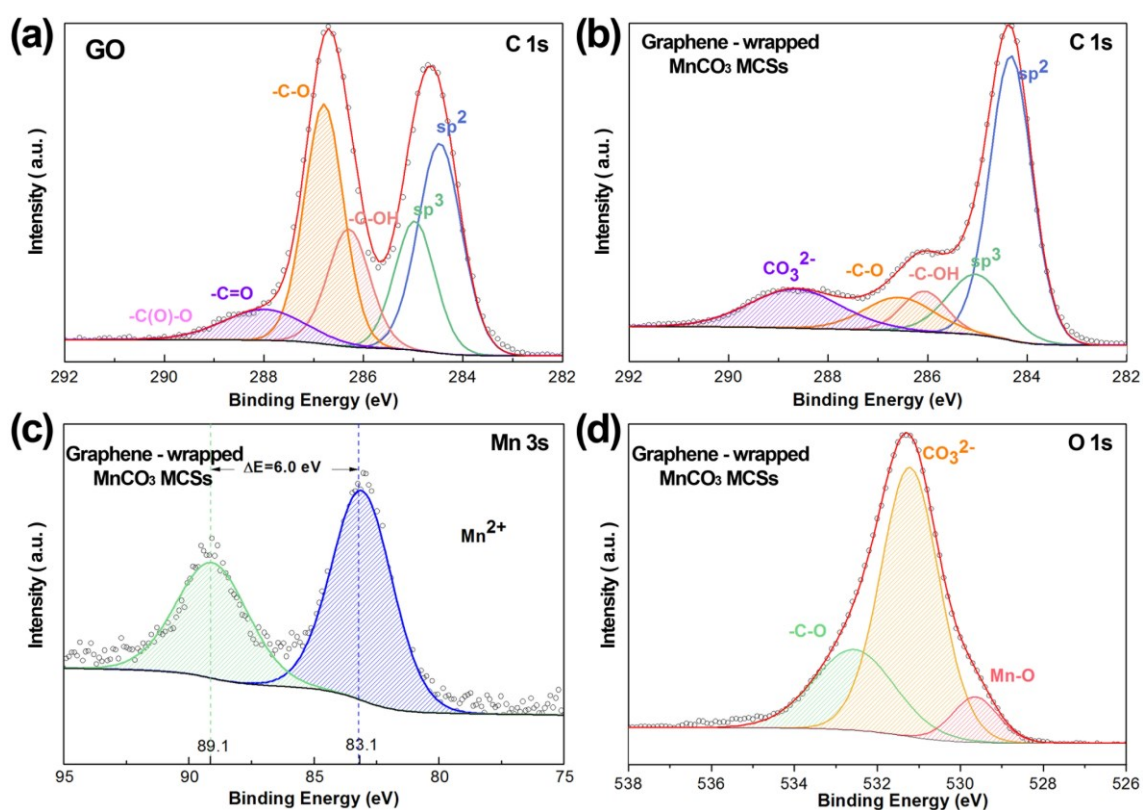


Figure 3-8. XPS analyses of GO (a) C1s and (b) C1s, (c) Mn 3s, and (d) O 1s of graphene-wrapped MnCO_3 MSCs.

Figure 3-7 and Figure 3-8 reveal that the obtained composite materials from DFE method are submicron, graphene-wrapped MnCO_3 MSCs. It is the first time that MSCs were electrodeposited from an aqueous bath in such a low temperature and template-free process. This method also provides a new strategy to synthesize graphene-wrapped composite materials.

3.3.2 Superior electrochemical performance of graphene-wrapped MnCO_3 MSCs

The resulting submicron, graphene-wrapped MnCO_3 MSCs were used directly as the electrochemically active materials in LIBs. Although nanometer-size active materials have demonstrated improved performance when normalized to the weight of active materials only, these nanomaterials require a high percentage of conductive and binding materials in the electrodes, normally over 20 wt% in total, sacrificing the final performance of the full cell³⁴. Their low tap density (The tapped density is obtained by mechanically tapping a graduated cylinder containing the sample until little further volume change is observed) also results in a low volumetric energy density³⁵. In this sense, the structure of submicron, graphene-wrapped MSCs is an ideal structure to be used as active materials in LIBs, since it adopts the advantages of high tap density from microparticles, large tolerance to volume expansion from mesoporosity, and high conductivity from graphene. In addition, high graphene loadings in the composite materials would also reduce their tap density; and hence, the graphene

loading in this work was controlled at a low level, 10 wt% of the total composite materials (Figure 3-7(f)). The weight percentage of graphene in graphene-wrapped MnCO_3 MSCs was also calculated to be 9.7 wt%, which was made based on the amount of Mn_2O_3 measured at 800°C as shown in Figure 3-7(f). The conductive additive, Super-C65 carbon black, and the binder material, polyvinylidene fluoride, used in this work were kept as low as 6wt% and 4wt%, respectively. Accordingly, all the performance data below are normalized against the total weight of graphene and MnCO_3 MSCs.

Figure 3-9 shows the electrochemical performance of graphene-wrapped MnCO_3 MSCs when used as the anode for LIBs. The electrochemical measurements were conducted within the potential range of 0.01~3.0 V and at different current densities ranging from 100 mA/g to 5,000 mA/g. As shown in Figure 3-9(a), there is a long flat potential plateau at ~0.3 V in the first discharging curve at a current density of 100 mA/g, which offers 1,279 mAh/g for the initial reduction process. The first charging capacity of 867 mAh/g was recorded, corresponding to the coulombic efficiency of 67.8%. The low coulombic efficiency in the first cycle was attributed to the formation of solid electrolyte interface (SEI) film on the surface of active particles¹⁵. In the second cycle, the discharging capacity keeps at a high value of 900 mAh/g and the coulombic efficiency increases up to 96.7%. During the following cycles, the discharging capacity slowly increases up to 954 mAh/g at the 10th cycle and up to 1,000 mAh/g at the 130th cycles.

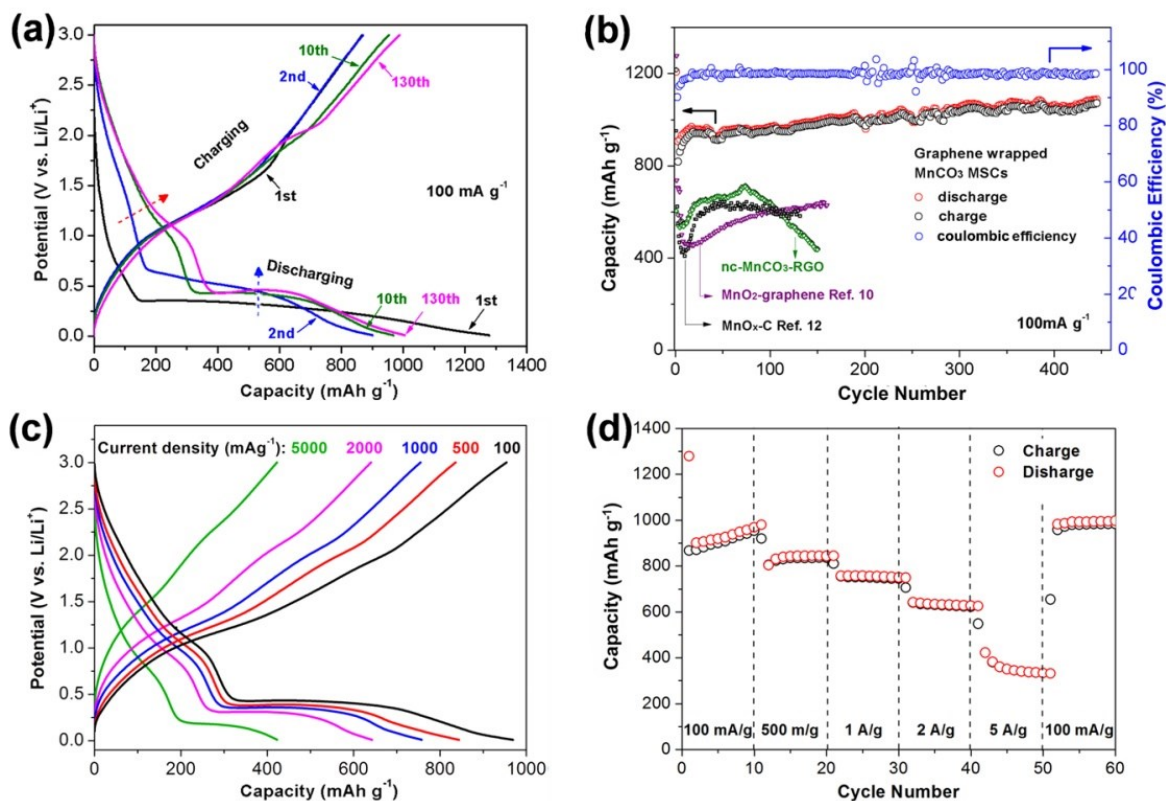


Figure 3-9. (a) Charging-discharging curves and (b) cyclability data of graphene-wrapped MnCO_3 MSCs within 0.01~3.0 V at 100 mA/g. (c) Charging-discharging curves and (d) cyclability data of graphene-wrapped MnCO_3 at different current densities, ranging from 100 mA/g to 5,000 mA/g.

Accordingly, the coulombic efficiency also increases to over 98% after 10 cycles. The reported discharging capacity in Figure 3-9(b) is much higher than the theoretical capacities of both MnCO_3 (466 mAh/g)¹⁵ and Graphene (744 mAh/g)¹¹, suggesting the high accessibility for lithium insertion and extraction on the graphene-wrapped MnCO_3 MSCs. Similar phenomenon has also been found for MnO ¹¹ and MnO_x ¹²

with the valence of Mn ions smaller than +4. The reason for this high capacity will be discussed later. More interestingly, the graphene-wrapped MnCO₃ MSCs deliver the reversible capacity higher than 1,000mAh/g for over 400 cycles at 100 mA/g (Figure 3-9(b)).

In addition, high rate capability has also been obtained for the anodes made from graphene-wrapped MnCO₃ MSCs. Figure 3-9(c) shows that a reversible capacity of 640 mAh/g has been reached at a high current density of 2,000 mA/g. At a current density of 5000 mA/g, a high capacity of 422 mAh/g can be delivered. Figure 3-9(d) further shows that the reversible capacity is stable at different current densities ranging from 100 mA/g to 5,000 mA/g. Therefore, graphene-wrapped MnCO₃ MSCs demonstrate high capacity, high rate capability and excellent cycling performance in Figure 3-8. To the best of our knowledge, this electrochemical performance are the best results that have been reported for MnCO₃ so far, and even better than most of the results reported for MnO_x^{8,9,10}. Although a relatively large potential range, 0.01~3.0 V, was still used in this paper, the shortcoming arising from this large potential range can be compensated by the significantly improved capacity and cycle life shown in Figure 3, demonstrating their practical potential to be used in LIBs. Considering its low cost^{13,15}, MnCO₃ has been proven to be a new promising candidate as the anode material for LIBs.

3.3.3 Structural advantages from graphene-wrapped MnCO₃ MSCs

In order to understand the superior electrochemical performance in Figure 3-9 and to elucidate the advantages of the graphene-wrapped MSCs structures, hydrothermal nanocrystalline MnCO₃-RGO (nc-MnCO₃-RGO) (Figure 3-10) and MnO₂ nanoflakes-RGO (nano-MnO₂-RGO)³⁶ (Figure 3-11) composites were synthesized and their electrochemical performance was evaluated. Figure 3-12(a) shows the cyclic voltammetry (CV) curves of graphene-wrapped MnCO₃ MSCs in the initial 10 scans within 0.01~3.0 V at a scan rate of 0.02 mV/s. In the first cycle, a broad reduction peak beginning from 0.44 V and centered at 0.22 V corresponds to the formation of a SEI layer and the complete reduction of Mn²⁺ to Mn⁰^{10,11,12}. The main oxidation peak at 1.22 V could be ascribed to the oxidation of Mn⁰ to Mn²⁺ in the cathodic process³⁷. During the second cycle, the intensity of the main reduction peak decreases and shifts significantly up to 0.43 V. In the reversed scan of the second cycle, a new oxidation peak at 1.85 V starts to appear and gets stronger and stronger in the following cycles. At the fifth cycle, another broad oxidation peak at a higher potential of 2.30 V appears. In accordance with two new oxidation peaks, a new reduction peak at 1.06 V becomes evident gradually after the second cycle. The new oxidation peaks at potentials higher than 1.22 V reveal that new oxidation reactions were occurring in the system. It is suggested that Mn²⁺ has been further oxidized to higher oxidation states^{11,12}. To clarify this point, charging discharging curves at the 10th cycle for the samples of nano-MnO₂-RGO (with Mn⁴⁺) were obtained, which were compared with those for graphene-wrapped MnCO₃ MSCs (with Mn²⁺) in Figure 3-12(b). It shows that both

samples demonstrate similar charge discharge curves at the 10th cycle, especially the appearance of the potential plateau at 1.0 V in the discharging curves.

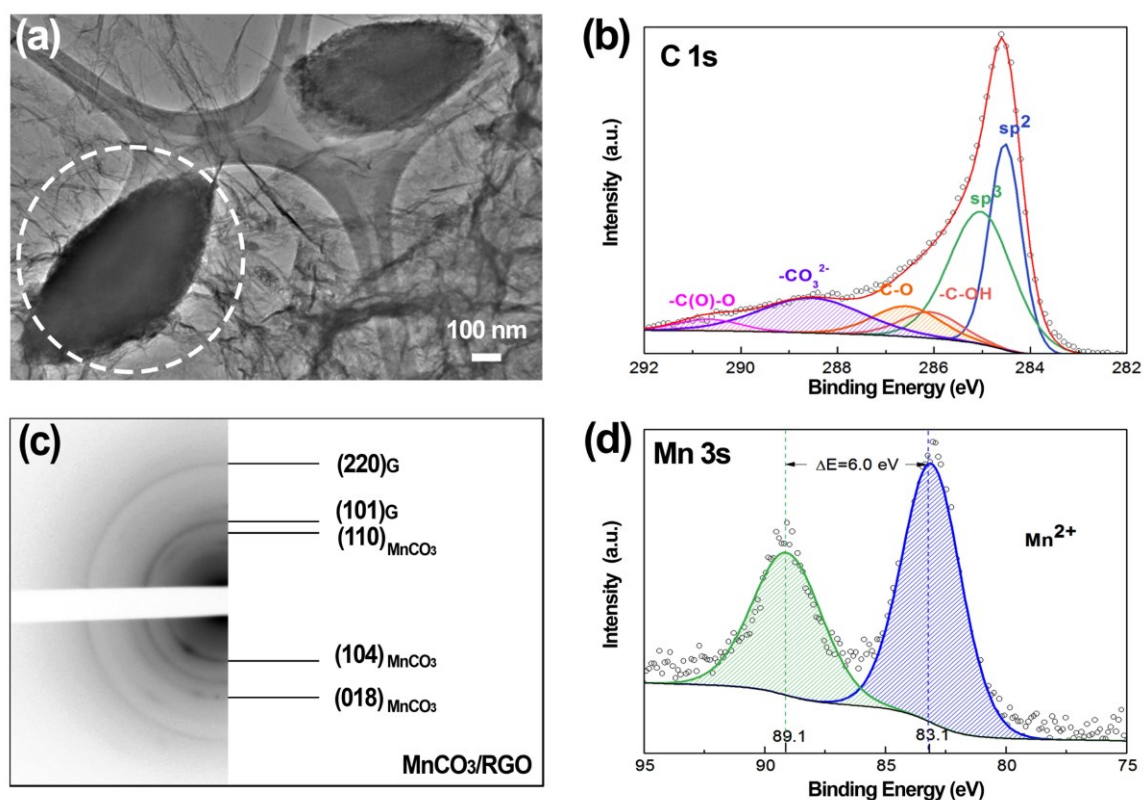


Figure 3-10. (a) TEM image, XPS spectra of (b) C 1s and (d) Mn 3s of nc-MnCO₃-RGO composite, these C1s is not come from the sample supporter because the carbon on the Cu grid is amorphous carbon. (c) electron diffraction from the selected area in the white circle in (a).

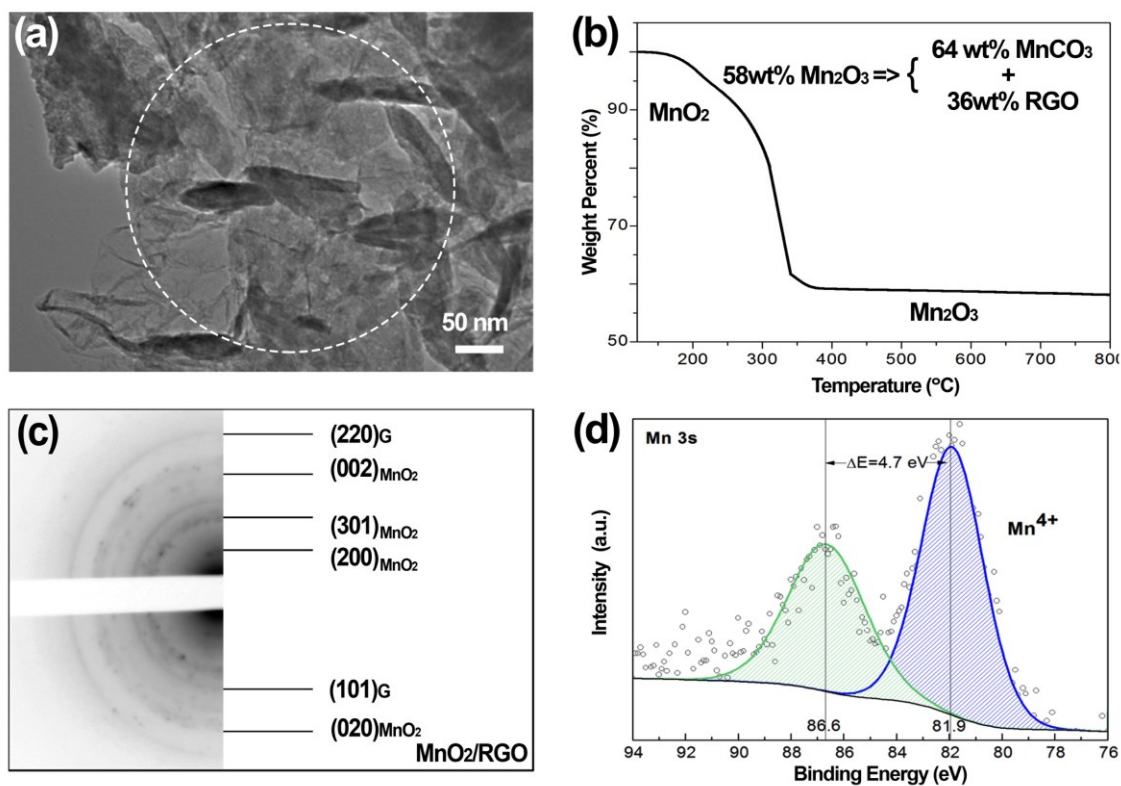


Figure 3-4. (a) TEM image, (b) TGA, (c) electron diffraction from the selected area in the white circle in (a). (d) XPS spectrum of Mn 3s of nano-MnO₂-RGO composite.

In addition, both samples demonstrate a potential plateau at around 1.85 V in the charging curves, which is consistent with the CV curves in Figure 3-12(a). Although this new potential plateau for graphene-wrapped MnCO₃ MSCs is not as obvious as that for nano-MnO₂-RGO in Figure 3-12(b), it gets stronger and stronger in the following cycles, which can be seen from the charging curve after 130 cycles in

Figure 3-9(a). It indicates that the redox reactions for graphene-wrapped MnCO_3 MSCs in the potential range higher than 1.0 V is the reversible reactions between Mn^{2+} and high oxidation state Mn associated with lithium-ion extraction and insertion. Similar phenomenon has also been found for MnO /graphene and MnO_x /carbon electrodes with the valence of Mn ions smaller than +4. It is noted that the reported discharging capacity higher than the theoretical capacity of MnCO_3 in Figure 3-9(b) can be attributed to the new oxidation reactions occurred in the system, which is suggested to be the further oxidation of Mn^{2+} to higher oxidation state.

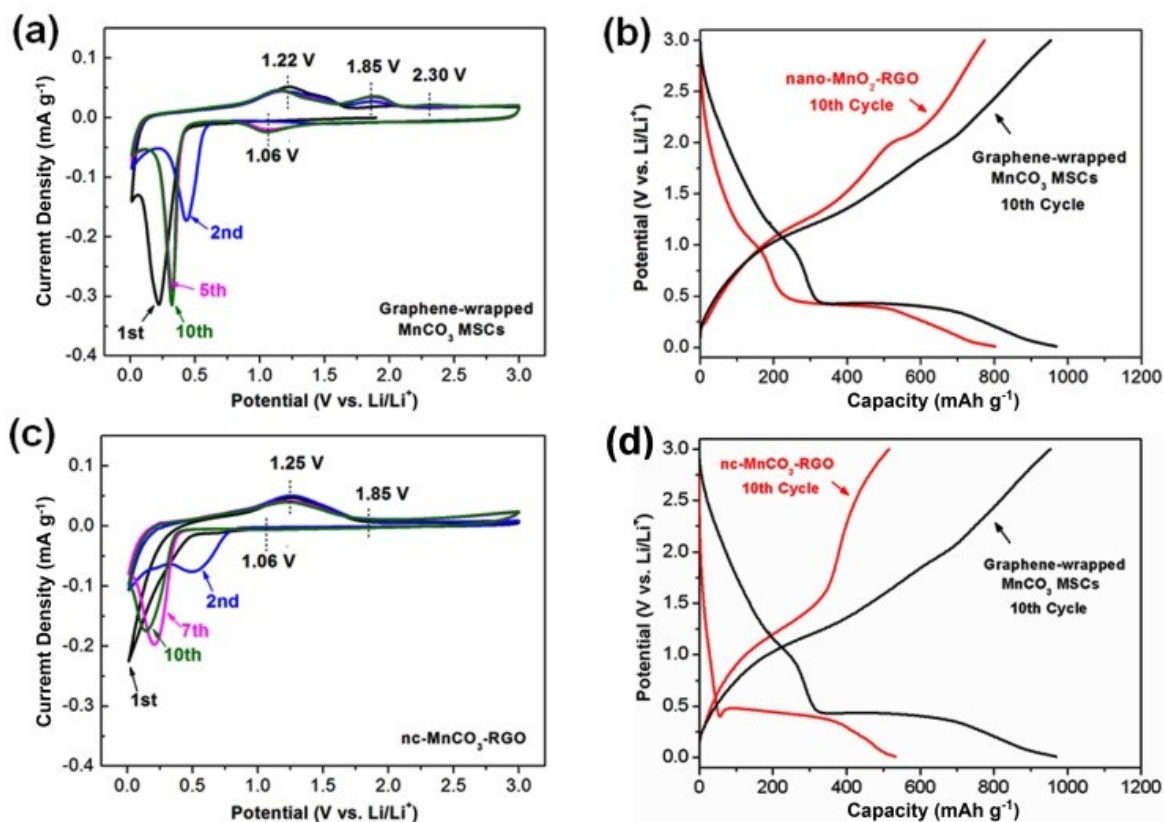


Figure 3-5. (a) Cyclic voltammety measurements of graphene-wrapped MnCO₃ MSCs. (b) Comparison of charging-discharging curves between graphene-wrapped MnCO₃ MSCs and nano-MnO₂-RGO at the 10th cycle.(c) Cyclic voltammety measurements of nc-MnCO₃-RGO. (d) Comparison of charging-discharging curves between graphene-wrapped MnCO₃ MSCs and nc-MnCO₃-RGO at the 10th cycle.

In contrast to the CV curves of graphene-wrapped MnCO₃ MSCs (Figure 3-12a), CV curves in Figure 3-12(c) shows that Mn²⁺ in nc-MnCO₃-RGO could not be re-oxidized to higher oxidation states in the initial 10 cycles. Accordingly, the discharging curve of nc-MnCO₃-RGO at the 10th cycle (Figure 3-12(d) and Figure

3-13(a)) did not demonstrate a clear potential plateau at 1.0 V, which is in agreement with the CV curves in Figure 3-12(c). Hence, nc-MnCO₃-RGO in Figure 3-12(d) demonstrates a low reversible capacity of 582 mAh/g within 0.01~3.0 V.

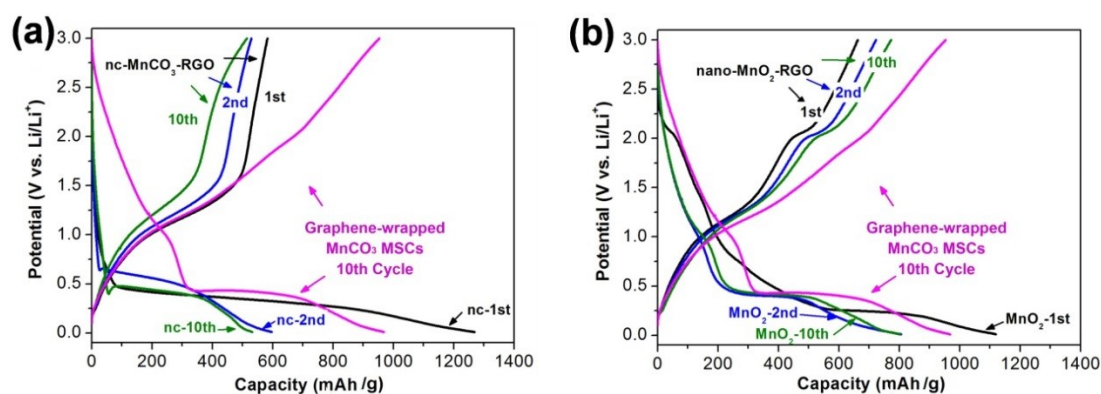


Figure 3-6. The 1st, 2nd and 10th activation charging-discharging curves of (a) nc-MnCO₃-RGO and (b) nano-MnO₂-RGO, compared with the 10th activation cycle of graphene-wrapped MnCO₃ MSCs.

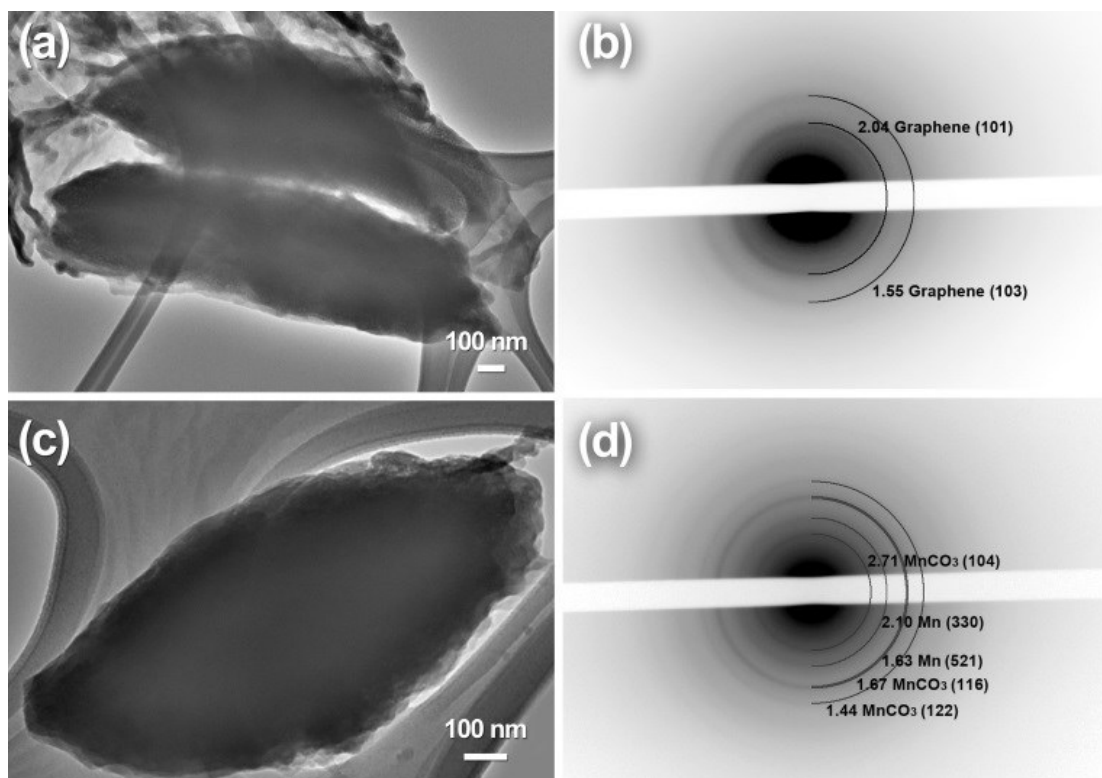


Figure 3-7. (a) TEM and (b) selected-area diffraction of graphene-wrapped MnCO_3 MSCs after 10 cycles. (c) TEM and (d) selected-area diffraction of nc- MnCO_3 -RGO after 10 cycles.

Comparing Figure 3-12(a) with Figure 3-12(c), it is interesting to see that the initial microstructure of the active particle (i.e., precursor particles) significantly affects their electrochemical performance. Poizot et al. also found that the morphology of the precursor particles, e.g., the particle size of metal oxides, affects the state of division of the conversion reaction products, and hence the electrochemical performance¹⁷. In order to further illustrate how the microstructure of the precursor particles affects their electrochemical performance, the cycled graphene-wrapped MnCO_3 MSCs and nc- MnCO_3 -RGO samples were investigated by TEM and selected-area diffraction.

Figure 3-14a and Figure 3-14b show that, after 10 cycles, the single crystal structure of MnCO_3 has been evolved to the amorphous structure. In Figure 3-9(a), it has been shown that the new potential plateau at 1.0 V in the discharging curves becomes more and more pronounced (dashed red arrow in Figure 3-9(a), and the over-potential decreases for the conversion reaction at potentials lower than 0.5 V (dashed blue arrow in Figure 3-9(a)), after cycling. It is, therefore, concluded that the evolution of microstructure from single crystals to the amorphous structures lowers the over-potential of the conversion reaction and creates the new reversible reactions at potentials higher than 1.0 V. Maier and coworkers reported that amorphization of crystalline RuO_2 could enhance the lithiation potential (i.e., lower the over-potential of lithiation) owing to the enhanced Gibbs free energy compared with the crystalline bulk RuO_2 ³⁸. It is also reported that amorphous structure of manganese oxide effectively lowers the resistance for the conversion reaction¹². These are consistent with the conclusion obtained in Figure 3-14(a) and Figure 3-14(b). On the contrary, MnCO_3 in nc- MnCO_3 -RGO keeps nanocrystalline structure after 10 cycles (Figure 3-14(c) and Figure 3-14(d)) and the new potential plateau at 1.0 V has not been activated after 10 cycles. It further proves that it is the evolution of microstructure from single crystals to the amorphous structures that creates the new reversible reactions. It also implies that nanocrystalline MnCO_3 is more difficult to be transformed to the amorphous structure after cycling; and hence, the discharging capacity is lower for nc- MnCO_3 -RGO than that for graphene-wrapped MnCO_3 MSCs. It is suggested that the lithiation of nanocrystalline MnCO_3 starts from their grain

boundaries. This first-step lithiation exposes fresh surfaces to the electrolyte and forms additional SEI films, which, in turn, retards further lithiation of inner part of MnCO_3 .

The ease of the transformation from single crystals to the amorphous structure lowers the over-potential of the conversion reaction and activates the new reversible reactions at potentials higher than 1.0 V, leading to the high capacities presented in Figure 3-8a. In addition, the phase transformation during cycling causes the loss of electrical contact for the active materials^{11,12,15}, which can be minimized by the graphene-wrapped morphology (Figure 3-9(b)). As shown in Figure 3-15, graphene-wrapped morphology has been retained after cycling. This phase transformation also induces large volume change, which can be accommodated by the mesoporous structure of the precursor particles. As a result, graphene-wrapped mesoporous structure demonstrates the cycling performance superior to nc- MnCO_3 -RGO (Figure 3-9(b)). Furthermore, the high conductivity shell provided by the graphene-wrapped morphology can be attributed to the high rate capability presented in Figure 3-9(c) and Figure 3-9(d). Therefore, it is the designed structure, graphene-wrapped MSCs, of MnCO_3 that is attributed to the superior electrochemical performance presented in Figure 3-9.

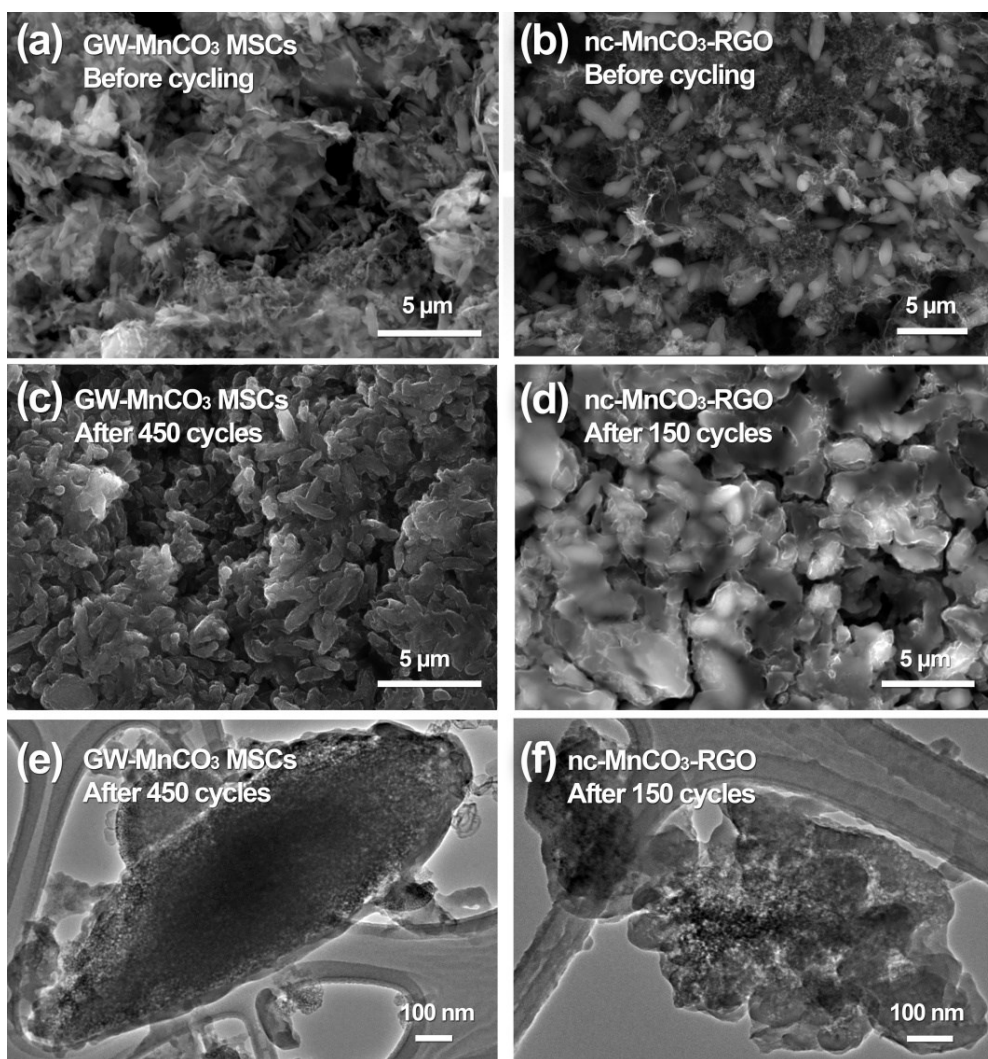


Figure 3-8. (a), (b), (c) and (d) SEM images of graphene-wrapped (GW) MnCO₃ MSCs and nc-MnCO₃-RGO before and after cycles. (e) and (f) TEM images of graphene-wrapped (GW) MnCO₃ MSCs and nc-MnCO₃-RGO before and after cycles.

3.4 Conclusions

In conclusions, a unique structure of graphene-wrapped mesoporous single crystals was designed and applied on low-cost MnCO₃ for lithium-ion storage. In order to synthesize this unique structure, we, for the first time, reported a low-temperature

(70°C) and template-free electrodeposition method, referred to as dynamic floating electrodeposition. During DFE process, graphene oxides were dynamically floating between two electrodes, which were first reduced at cathode, transported to anode for the deposition of MnCO₃ MSCs, and wrapped up in the subsequent floating. This DFE method is facile, cost effective and scalable, which is believed to establish a new platform to synthesize various graphene-wrapped composite materials for many applications. The resulting submicron, graphene-wrapped MnCO₃ MSCs reached a high reversible capacity of 900 mAh/g after the initial cycle and delivered over 1,000 mAh/g after 130 cycles. In addition, the reversible capacity kept at this high level for more than 400 cycles, and maintained 422 mAh/g at a high rate of 5,000 mA/g. It is also the first time that this high performance has been achieved on MnCO₃ for lithium-ion storage. Furthermore, the superior electrochemical performance was found to be highly related to the designed novel structure. The graphene-wrapped MnCO₃ MSCs are able to deliver high capacities because of the easy transformation from single crystal structure to the amorphous structure during cycling, and exhibit the high cyclability because of the graphene-wrapped morphology. The insightful gains from this work, such as the structural design of the active materials, the DFE synthesis method and the high performance for lithium-ion storage, provide new avenues to the future development of high performance energy storage systems.

3.5 References

- 1 Y. M. Lin, P. R. Abel, A. Heller, C. B. Mullins, *J. Phys. Chem. Lett.*, 2011, 2, 2885-2891.
- 2 X. Jia, Z. Chen, X. Cui, Y. Peng, X. Wang, G. Wang, F. Wei, Y. Lu, *ACS Nano*, 2012, 6, 9911-9919.
- 3 Z. S. Wu, W. Ren, L. Wen, L. Gao, J. Zhao, Z. Chen, G. Zhou, F. Li, H. M. Cheng, *ACS Nano*, 2010, 4, 3187-3194.
- 4 J. S. Chen, T. Zhu, Q. H. Hu, J. Gao, F. Su, S. J. Qiao, X. W. Lou, *ACS Appl. Mater. Interfaces*, 2010, 2, 3628-3635.
- 5 Y. S. Lin, J. G. Duh, M. H. Hung, *J. Phys. Chem. C*, 2010, 14, 13136-13141.
- 6 J. Lin, Z. Peng, X. Xiang, G. Ruan, Z. Yan, D. Natelson, J. M. Tour, *ACS Nano*, 2013, 7, 6001-6006.
- 7 X. Zhou, L. J. Wan, Y. G. Guo, *Adv. Mater.*, 2013, 25, 2152-2157.
- 8 H. Xia, M. Lai, L. Lu, *J. Mater. Chem.*, 2010, 20, 6896-6902.
- 9 A. L. M. Reddy, M. M. Shaijumon, S. R. Gowda, P. M. Ajayan, *Nano Lett.* 2009, 9, 1002-1006.
- 10 L. Li, A. R. O. Raji, J. M. Tour, *Adv. Mater.*, 2013, 25, 6298- 6302.
- 11 Y. Sun, X. Hu, W. Luo, F. Xia, Y. Huang, *Adv. Funct. Mater.*, 2013, 23, 2436-2444.
- 12 J. Guo, Q. Liu, C. Wang, M. R. Zachariah, *Adv. Funct. Mater.*, 2012, 22, 803-811.
- 13 S. Lei, Z. Liang, L. Zhou, K. Tang, *Materials Chemistry and Physics*, 2009, 113, 445-450.
- 14 M. Zheng, H. Zhang, X. Gong, R. Xu, Y. Xiao, H. Dong, X. Liu, Y. Liu, *Nanoscale Research Letters*, 2013, 8, 166.
- 15 Y. Yan, Y. Zhu, Y. Yu, J. Li, T. Mei, Z. Zhu, Y. Qian, *J. Nanosci. Nanotechnol.*, 2012, 12, 7334-7338.
- 16 S. Devaraj, H. Y. Liu, P. Balaya, *J. Mater. Chem. A.*, 2014, 2, 4276-4281.
- 17 P. Poizot, S. Laruelle, S. Grugeon, L. Dupont, J-M. Tarascon, *Nature.*, 2000, 407, 496-499.
- 18 E. J. W. Crossland, N. Noel, V. Sivaram, T. Leijtens, J. A. Alexander-Webber, Snaith, H. J. *Nature*, 2013, 495, 215-219.
- 19 D. Su, S. Dou, G. Wang, *Nano Res.*, 2014, 7, 794-803.
- 20 D. Su, M. Ford, G. Wang, *Sci Rep.*, 2012, 2, 924.
- 21 J. Weickert, R. B. Dunbar, H. C. Hesse, W. Wiedemann, L. Schmidt-Mende, *Adv. Mater.*, 2011, 23, 1810-1828.
- 22 C. Dickinson, W. Zhou, R. P. Hodgkins, Y. Shi, D. Zhao, H. He, *Chem. Mater.*, 2006, 18, 3088-3095.
- 23 P. Yang, D. Zhao, D. I. Margolese, B. F. Chmelka, G. D. Stucky, *Nature*, 1998, 396, 152-155.
- 24 K. Jiao, B. Zhang, B. Yue, Y. Ren, S. Liu, S. Yan, C. Dickinson, W. Zhou, H. He, *Chem. Commun.*, 2005, 45, 5618-5620.
- 25 H. Wang, Y. Yang, Y. Liang, J. T. Robinson, Y. Li, A. Jackson, Y. Cui, H. Dai,

-
- Nano Lett. 2011, 11, 2644-2647.
- 26 C. Y. Su, A. Y. Lu, Y. Xu, F. R. Chen, A. N. Khlobystov, L. J. Li, ACS Nano, 2011, 5, 2332-2339.
- 27 X. Xu, D. Huang, H. Cao, M. Wang, S. M. Zakeeruddin, M. Gratzel, Sci Rep., 2013, 3, 1489.
- 28 H. L. Guo, X. F. Wang, Q. Y. Qian, F. B. Wang, X. H. Xia, ACS Nano, 2009, 9, 2653-2659.
- 29 W. S. Hummers Jr, R. E. Offeman, J. Am. Chem. Soc., 1958, 80, 1339-1339.
- 30 T. Chen, B. Zeng, J. L. Liu, J. H. Dong, X. Q. Liu, Z. Wu, X. Z. Yang, Z. M. Li, J. Phys. Conf. Ser., 2009, 188, 012051.
- 31 W. Chen, L. Yan, and P. R. Bangal, Carbon, 2010, 48, 1146-1152.
- 32 O. Compton, D. A. Dikin, K. W. Putz, L. C. Brinson and S. T. Nguyen, Advanced Materials, 2010, 22, 892-896.
- 33 G. Trettenhahn, A. Koberl, Electrochimica Acta., 2007, 52, 2716-2722.
- 34 X. Cui, J. Chen, T. Wang, W. Chen, Sci Rep., 2014, 4, 5310.
- 35 Y. Deng, Y. Zhou, Z. Shi, X. Zhou, X. Quan, G. Chen, J. Mater. Chem. A, 2013, 1, 8170-8177.
- 36 J. Qu, L. Shi, C. He, F. Gao, B. Li, Q. Zhou, H. Hu, G. Shao, X. Wang, J. Qiu, Carbon, 2014, 66, 485-492.
- 37 H. Wang, L. Cui, Y. Yang, H. S. Casalongue, J. T. Robinson, Y. Liang, Y. Cui, H. Dai, J. Am. Chem. Soc., 2010, 132, 13978-13980.
- 38 O. Delmer, P. Balaya, L. Kienle, J. Maier, Adv. Mater., 2008, 20, 501-505.

Chapter 4 Electrochemical deposition of MnO_x on Reduced Graphene Oxides for Pseudo-capacitive Lithium-ion Storage

4.1 Introduction

In the past decades, extensive efforts have been devoted to develop energy storage technologies in order to meet growing requirements for portable electronic devices, industrial equipment and electric vehicles. Lithium ion battery (LIB) has been widely used due to its high energy density and acceptable cycle life. But its poor rate capability limits its development. Electrochemical double-layer supercapacitor (EDLC) also attracts much attention because of its high power density and excellent cyclability. But its low energy density constrains EDLC from being used in many industrial applications. Lithium-ion capacitor (LIC), considered as a new hybrid device, is expected to take advantage of both LIBs and EDLCs to achieve high energy density, high power density and acceptable cyclability in one cell, by coupling a lithium intercalation electrode with a capacitive charge storage electrode. However, the high working voltage of more than 4.0V causes electrolyte decomposition in LICs, especially at the negative electrode¹, which limits their cyclability and efficiency after long-time cycling. Recently, Augustyn et al. reported lithium-ion intercalation pseudo-capacitance on $\text{T-Nb}_2\text{O}_5$ ², where high capacitance and high-rate capability

were achieved. Although the cyclability of T-Nb₂O₅, when tested between 1.2 – 3.0 V vs Li/Li⁺ ², is still unknown, it raises the significance of using metal oxides with the optimized structure to increase the rate capability of lithium-ion storage towards EDLCs.

Among a wide range of metal oxides, such as MnO_x, Nb₂O₅, RuO₂, TiO₂, CoO_x, MnO_x has attracted more attention due to its excellent electrochemical performance and abundance in the earth. Over the past few years, MnO_x and its composites with different morphologies were synthesized such as nanowires/graphene ³, nanoflakes/carbon nanohorns⁴, nanoflowers/graphene^{5,6}, etc. However, when studied for lithium-ion storage, these manganese oxide-based composites were discharged to the potential below 0.5 V vs Li/Li⁺, where conversion reactions occur, leading to a high capacity but a sluggish reaction rate and a limited cycle life. To the best of our knowledge, the electrochemical performance of manganese oxide-based composites in the potential range of 0.7 – 2.8V vs Li/Li⁺ has not been investigated. This potential range is worth investigation, because the valence of manganese in this region was found to be varied without causing phase transformations, and as such, a much improved rate capability and a long cycle life are expected. It may also provide a novel approach to achieve a balanced performance among energy density, power density and cycle life.

Here, graphene-wrapped MnCO₃ mesoporous single crystals (MSCs) synthesized

from dynamic floating electrodeposition (DEF)⁷ were used as precursors for making graphene-wrapped amorphous (GWA) manganese oxides composite. Such GWA manganese oxide composites show distinct microstructural features and demonstrate excellent electrochemical performance between 0.7 – 2.8 V. The highest capacitance was measured to be 430 F/g at a sweeping rate of 0.2 mV/s and the capacitance of 200 F/g was also obtained under a high sweeping rate of 10 mV/s. After 400 cycles, the capacitance of GWA manganese oxide composites reaches 91% of the original value (305 F/g), and still maintains 86% even after 2,000 cycles. It was found, for the first time, that GWA manganese oxide composites showed high performance, pseudo-capacitive lithium-ion storage in the potential range of 0.7 – 2.8 V, making this study a new avenue for constructing lithium-ion based energy storage devices

4.2 Experimental Method

4.2.1 Material synthesis

GO preparation: The graphite oxide was synthesized from natural graphite powders according to modified Hummers method^{8,9}. After two hours sonication graphite oxide was exfoliated to graphene oxide. After filtration and rinse by deionized water, homogeneous GO (2.0 mg/mL) was obtained.

Synthesis of graphene-wrapped MnCO₃ MSCs by DFE method: The dynamic floating electrodeposition was carried out by Gamry PC4/750 potentiostat/galvanostat. Three

electrodes were used in this DFE system. Ag/AgCl was used as the reference electrode. The anodic electrode was a 52 mesh woven platinum sheet with dimensions of 20 mm × 10 mm. The cathodic electrode was ferritic stainless steel substrates with dimensions of 20 mm × 10 mm × 1 mm. Galvanostatic test was carried between anode and cathode by 30 mA/cm² current density. After mixing 0.3 M sodium citrate and 0.3 M MnSO₄ uniformly the pH value of solution was adjusted to 6.7~7.0. The ratio of GO solution and plating solution is 1:25. Here 40mL GO was introduced into 1L plating solution and agitated at a speed of 700 rpm. The temperature of plating solution was set to 70°C during 4 hours plating process. The final products were filtered and rinsed by deionized water before 10 hours freeze-dried (Savant supermodulyo freeze dryer, Thermo Electron Corporation).

Synthesis of nano-crystalline MnO₂-RGO (nano-MnO₂-RGO): For nano-MnO₂-RGO synthesis 0.23g KMnO₄ was slowly added to 10 mL of the homogeneous GO/MnSO₄ solution. After 2 hours refluxing at 80°C GO/MnO₂ composites were obtained. 0.8 g of glucose and 0.76 mL of ammonia solution (25 wt%) were added into solution to reduce GO to RGO. After one hour refluxing at 95°C nano-MnO₂-RGO was obtained.

4.2.2 Characterization

The morphology and structure of graphene-wrapped amorphous (GWA) manganese oxides composites, nano-MnO₂-RGO were analyzed by transmission electron microscopy (TEM, JEOL JEM-2100 with LaB₆ cathode, 200 kV and JEOL 2100 attached with 4pi EDXS system), and scanning electron microscopy (SEM, Hitachi S-5500, Hitachi S- 4800, and Zeiss EVO SEM equipped with a Bruker Silicon Drift Detector for Energy Dispersive X-Ray analysis). X-ray Diffraction (XRD) analyses were conducted on a Siemens D5000 X-ray diffractometer with Cu K α as the radiation source ($\lambda= 1.5418$ A). X-ray photoelectron spectroscopy (XPS) was carried out using a Kratos AXIS Ultra-x-ray photoelectron spectrometer. The standard X-ray source is supplied with aluminium and magnesium anodes. The XPS results were analyzed by CasaXPS software.

4.2.3 Electrochemical measurement

The electrochemical experiments were performance using 2032-type coin cells. The testing electrode was made of graphene-wrapped MnCO₃ MSCs, Super-C65 carbon black, and polyvinylidene fluoride with mass ratio 90:6:4. The same ratio was used for making nano-MnO₂- RGO electrodes. After uniformly mixing in N-methyl pyrrolidone (NMP) the obtained slurry was coated on Cu foils and dried at 120°C overnight. The total loading mass of the material on Cu foil was ~ 2 mg/cm², the thickness of active electrode is around 75 μ m. The electrodes were finally cut into

disk with 15mm diameter and then assembled in Argon-filled glove box. A lithium embedded active carbon was as a counter electrode. Celgard 2500 was used as separators. The electrolyte was 1M LiPF_6 in ethylene carbonate/diethyl carbonate/dimethyl carbonate (EC/DEC/DMC, vol 1:1:1) (MTI Corporation). The galvanostatic charge/discharge tests, cyclic voltammetry (CV) tests and cycle performance tests were carried out at $22 \pm 1^\circ\text{C}$ using a 1470E multi potentiostat/celltest system (Solartron).

4.3 Results and Discussion

4.3.1 Morphology and structure

The GWA MnO_x composites were obtained through dynamic floating electrodeposition (DEF) of graphene-wrapped mesoporous MnCO_3 single crystals (MnCO_3 MSCs) (Figure 4-1) and in-situ electrochemical activation. DFE method is a facile, cost effective and scalable method to synthesize graphene-wrapped composite materials for many applications. The electrodeposition system is composed of a Pt mesh anode, a stainless steel plate cathode and an aqueous electrolyte with metallic ions. During DEF, GOs were first reduced to RGOs on the cathode through cathodic reduction, which were then transported to the surface of the anode where pulse anodic deposition of mesoporous MnCO_3 single crystals on RGOs took place. Subsequently, mesoporous MnCO_3 single crystals were wrapped by RGOs when the composite floats away from Pt anode. This graphene-wrapped mesoporous MnCO_3 MSCs were

further activated by constant current charging-discharging (galvanostatic) process between 0.01 – 3.0 V vs Li/Li^+ . After 10 activation cycles, MnCO_3 MSCs were evolved into graphene-wrapped amorphous (GWA) MnO_x composites, as shown in Figure 4-2. The electrochemical characteristics of GWA MnO_x composites were further investigated between 0.7 – 2.8 V vs Li/Li^+ .

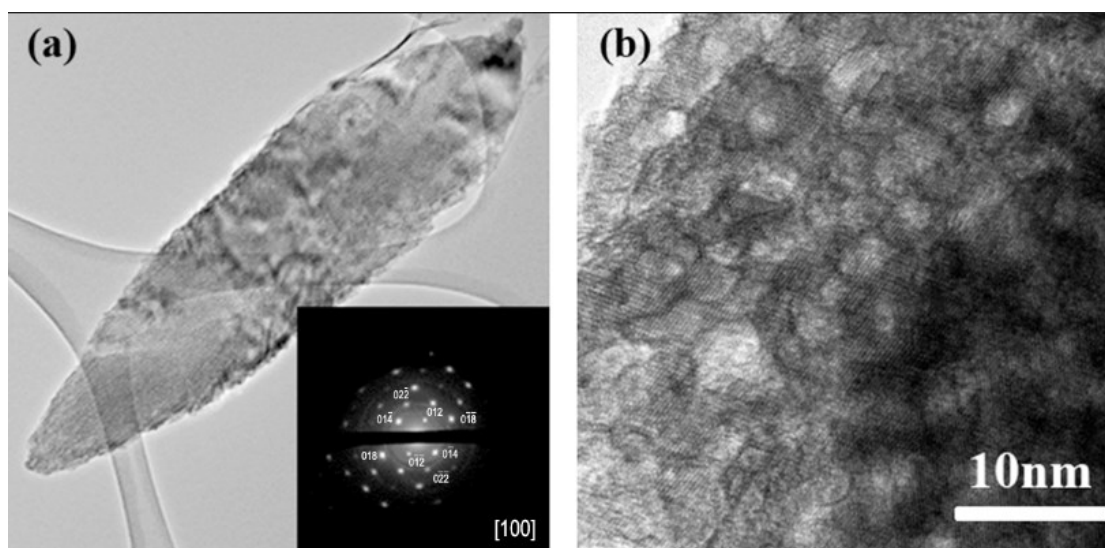


Figure 4-1. TEM morphology of precursor MnCO_3 MSCs. (a) TEM morphology of MnCO_3 MSCs and its electron diffraction pattern. (b) HTEM morphology of MnCO_3 MSCs from JEOL JEM-2100 with LaB6 cathode

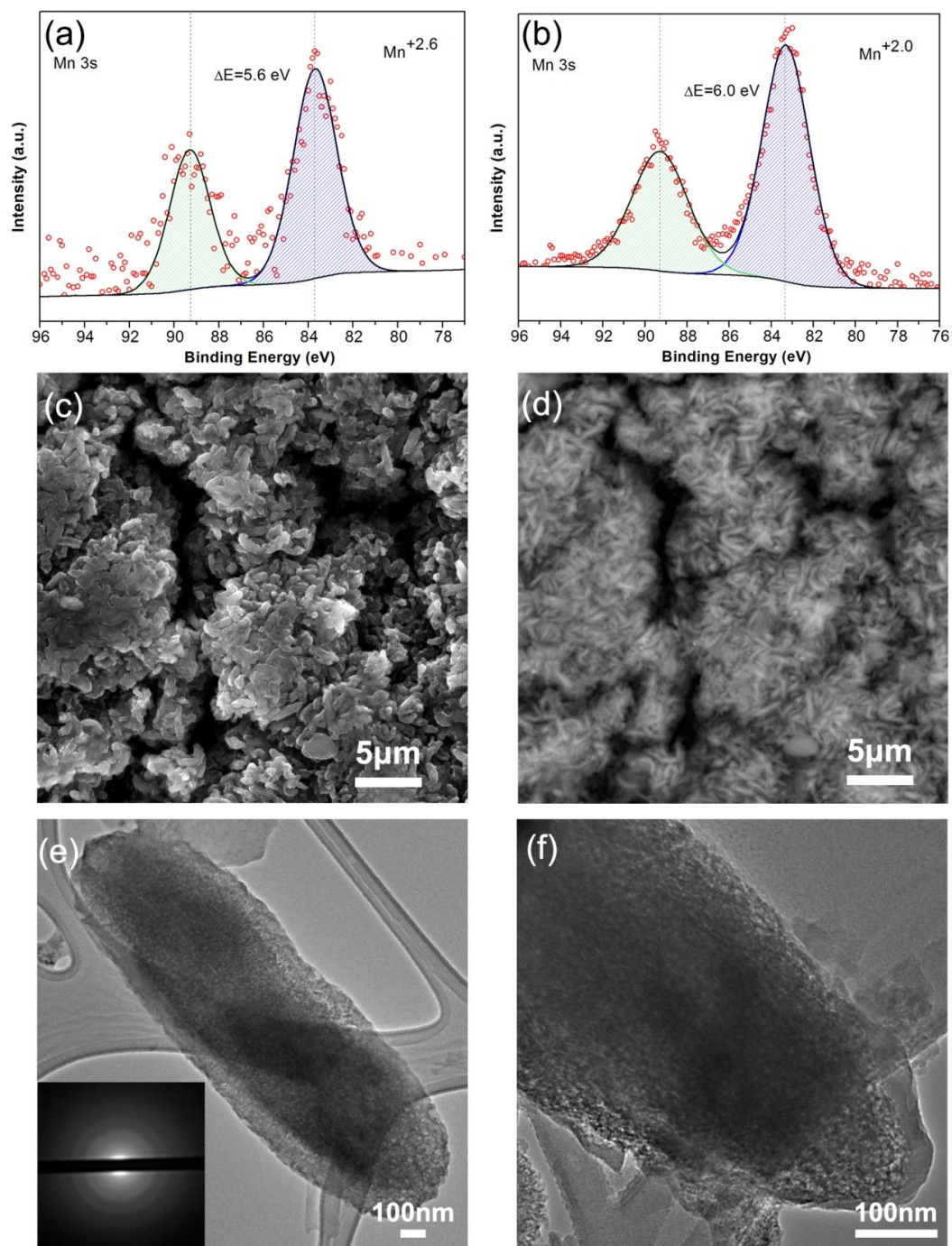


Figure 4-2. (a) Mn 3s high-resolution spectrum of GWA MnO_x composites at 2.8 V vs Li/Li⁺. (b) Mn 3s high-resolution spectrum of GWA MnO_x composites at 0.7 V vs Li/Li⁺. (c) Secondary SEM image of GWA MnO_x composites. (d) Backscattered SEM image of GWA MnO_x composites. (e, f) TEM images of GWA MnO_x composites and the electron diffraction pattern of GWA MnO_x composites is shown in (e).

The structure and chemical composition of GWA MnO_x composites were characterized by X-ray Photoelectron Spectroscopy (XPS), Scanning Electron Microscopy (SEM) and Transmission Electron Microscope (TEM). XPS was used to exam the valence of manganese ions when the composite was charged and discharged to 2.8 V and 0.7 V, respectively. Two characteristic peaks at 83.8eV and 89.4eV appear in Mn 3s high-resolution spectrum as shown in Figure 4-2a. The doublet Mn 3s peaks are the results of parallel spin coupling between electrons in the 3s and 3d orbitals. The oxidation states of Mn are highly related to Mn 3s peak splitting widths. When the valence of the Mn ions increases, the oxidized level is deeper and less electrons exist in the 3d orbitals; and correspondingly, the peak splitting width decreases^{10,11}. The width of the binding energy (ΔE) between these two characteristic peaks in GWA composites at 2.8 V is 5.6 eV, which correspond to an average oxidation valence of +2.6 based on linear interpolation between splitting width (ΔE) and the Mn oxidation state^{12,13}. This value is higher than the valence of manganese ions in GWA composites when discharged to 0.7 V (Figure 4-2(b)), whose width of binding energy between two characteristic peaks is 6.0 V corresponding to a +2.0 oxidation valence. It is also higher than the valence of the manganese ions in the precursor (Figure 4-3(a)). In addition, the carbonated group ($-\text{CO}_3$) located at 289.0 eV in C1s spectrum disappears after activation cycles, as shown in Figure 4-3(b). Therefore, the material is denoted as MnO_x composite.

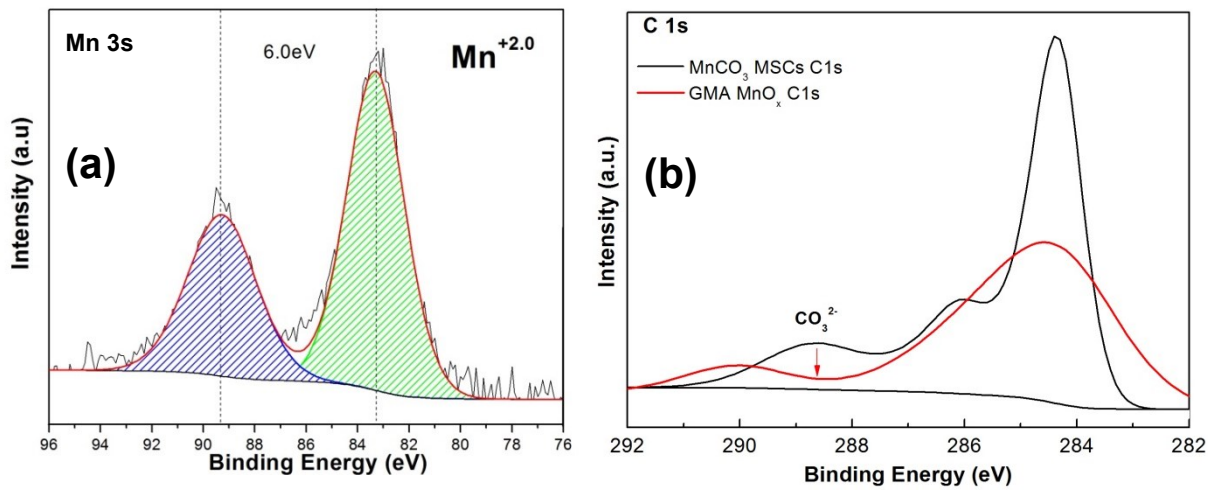


Figure 4-3. XPS results for the precursor of MnCO_3 MSCs (a), Mn 3s high-resolution spectrum of MnCO_3 MSCs composites. (b), Comparison of C1s high-resolution spectrum for GMA MnO_x and MnCO_3 MSCs indicating disappearance of carbonated group ($-\text{CO}_3$).

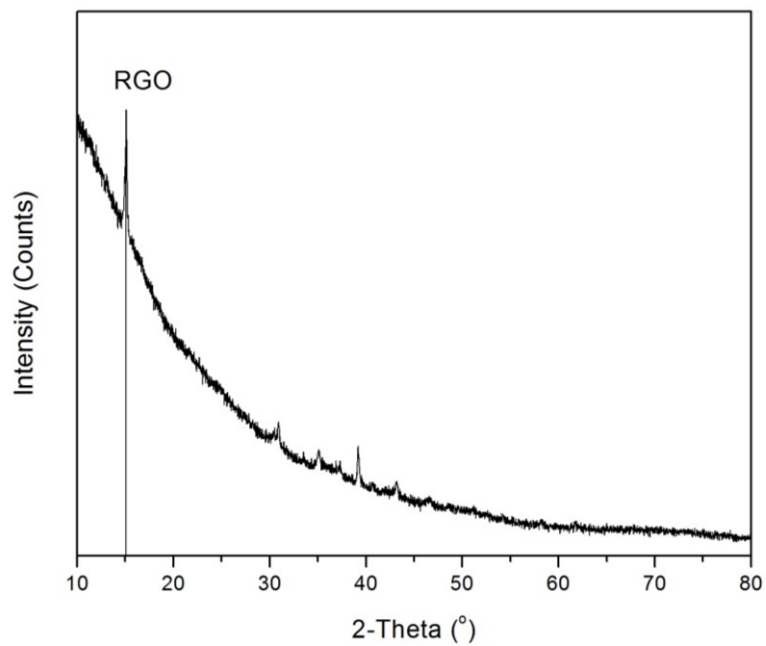


Figure 4-4. XRD pattern of GWA MnO_x composites.

The structure of GWA MnO_x composites was also confirmed by XRD pattern as shown in Figure 4-4. Comparing with its precursor MnCO₃ MSCs there is only one prominent peak located at 15° which is the peak of RGO. The reason wasn't observed in the XRD pattern of MnCO₃ MSCs is the intensity of RGO is too weak to be discerned comparing with other strong crystal plane peaks of MnCO₃ MSCs.

The structure of MnO_x composite was further studied by SEM and TEM. As shown in Figures 4-2(c) and 4-2(d), MnO_x particles show a rice-like shape, neither fragmented nor agglomerated together. The integrity of each of the rice shaped particles is well persevered from its precursor, MnCO₃ MSCs. Furthermore, the diffuse diffraction pattern (the inset image in Figure 4-2(e)) indicates the amorphous structure of the whole MnO_x particle. The amorphous MnO_x particle is also clearly displayed in TEM images shown in Figures 2(e) and 2(f), where the pores in particles interconnect with each other to form a porous sponge like structure. In addition, Figure 4-2(e) also shows two diffraction rings at 2.04 Å and 1.55 Å, representing the lattice d-spacing of RGOs and implying the presence of RGOs. The difference between Figure 4-2(c) and 1d also suggests that a large amount of MnO_x particles were wrapped by thin graphene layers. Figure 4-2 confirms that the obtained material is graphene-wrapped amorphous MnO_x composite.

4.3.2 Electrochemical performance

The electrochemical behavior of transition metal oxides, including MnO_x , were normally tested in the potential range of 0.01 – 3.0 V, because conversion reactions occur at the potential below 0.5 V leading to a high capacity. However, the conversion reaction also causes slow charge transfer response, hindering the rate of reactions, and deteriorates the structural integrity of crystal, and as such, shortens the cycle life. In addition, high potential hysteresis comes along with the conversion reaction at 0.01 – 3.0 V, resulting in a low energy efficiency. In order to avoid the occurrence of conversion reactions, transition metal oxides should be tested in the potential range higher than 0.5 V. However, to the best of our knowledge, their electrochemical behavior, including capacitance, rate capability, and cycle life, has not been reported in the potential range of 0.7 – 2.8 V. Here, GWA MnO_x composites were, for the first time, tested between 0.7 – 2.8 V in order to investigate their electrochemical characteristics and potential applications for lithium-ion storage.

Figure 4-5(a) and Figure 4-5(b) show the cyclic voltammetric curves at different sweeping rates from 0.2 – 20 mV/s. Accordingly, the specific capacitance of GWA MnO_x composites was calculated. As shown in Figure 4-5(c), the capacitance reaches 430 F/g at 0.2 mV/s and also achieves 200 F/g at a high sweep rate of 10 mV/s. The CV curves

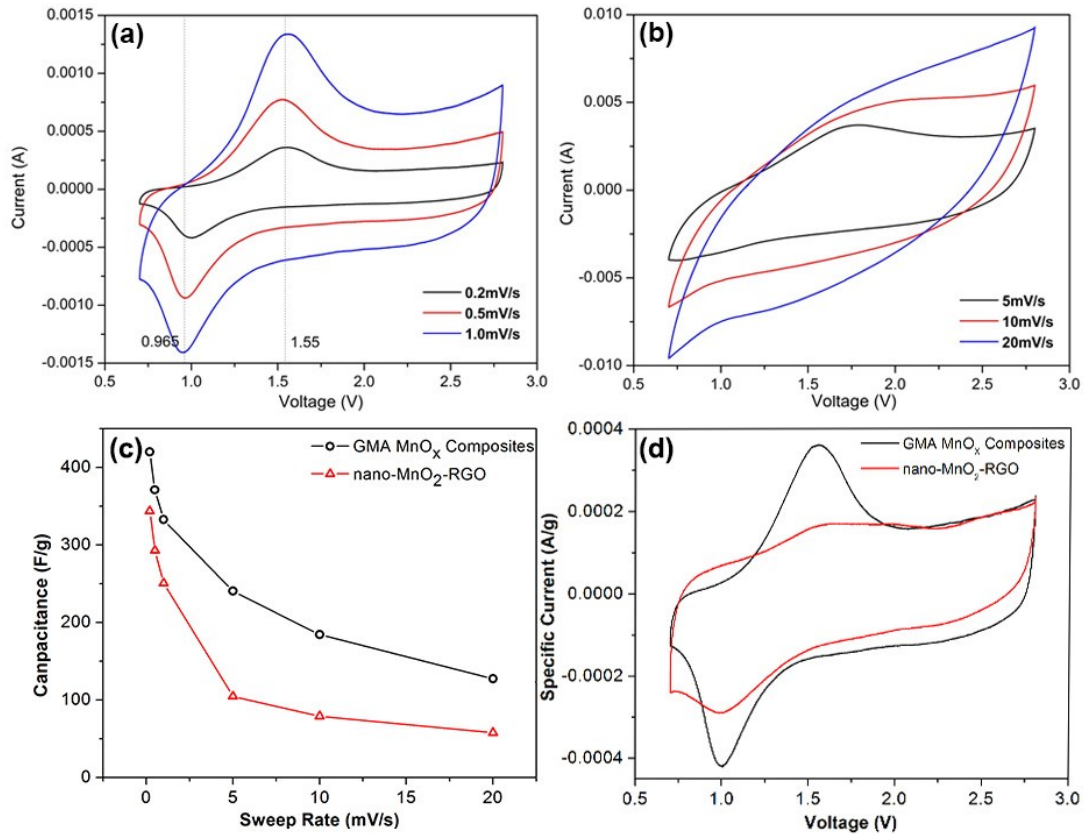


Figure 4-5. (a) Cyclic voltammetric curves at different sweeping rates from 0.2 mV/s – 1.0mV/s. (b) Cyclic voltammetric curves at different sweeping rates from 5mV/s – 20mV/s. (c) Capacitance of GMA MnO_x and nano-crystalline MnO₂-RGO at different sweeping rates . (d) CV curves of GMA MnO_x and nano-crystalline MnO₂-RGO at 0.2 mV/s sweeping rate and same voltage window.

of GWA MnO_x composites reveal a pair of redox peaks (cathodic peak at 1.0 V as well as anodic peak at 1.55V), which is also symmetric under different sweeping rates. A similar pair of redox peaks can also be observed for other manganese oxides when cycled between 0.01 – 3.0V^{6,14,15}, but their redox peaks are too weak to have practical significance. GWA MnO_x composites, however, exhibit a pair of strong and symmetric redox peaks at 1.0 V and 1.55 V in the potential range of 0.7 – 2.8 V,

leading to exceptional high capacitance in Figure 4-2c. In addition, no morphology or structure change has been found as shown in SEM and TEM results (Figures 4-2(c)-4-1(f)) when the valence of manganese ions in the composites is varying (XPS results in Figures 2(a) and 2(b)). It indicates that the strong redox reactions in GWA MnO_x composites are highly reversible during charging-discharging process between 0.7 – 2.8 V.

The strong redox peaks observed from GWA MnO_x composites can be attributed to their amorphous structure and graphene wrapped morphology. In order to illustrate the microstructural advantages of GWA MnO_x composites, graphene-wrapped nano-crystalline MnO_2 composites (nano- MnO_2 -RGO) were also synthesized and tested between 0.7 – 2.8 V, in comparison with GWA MnO_x composites. Nano-crystalline structure was selected in control experiment, due to its enhanced electrochemical reactivity resulting from its large active area and short ion-diffusion length¹⁶. However, when cycled between 0.7 – 2.8 V shown in Figure 4-5(d), the amorphous MnO_x (the black curve) obtained in this study present much more distinct and stronger redox peaks than those from nano-crystalline MnO_2 (the red curve), revealing a higher electrochemical reactivity for amorphous MnO_x than that for nano-crystalline MnO_2 . It is reported that the amorphization of crystals can increase the Gibbs free energy and reduce the energy barrier of electrochemical reactions¹⁷. It is also suggested that, comparing to nano-crystalline structure, amorphous structure has more ion-diffusion paths so that the kinetics of electrochemical reactions can be

enhanced. Hence, the electrochemical performance of GWA MnO_x composites is superior to graphene-wrapped nano-crystalline MnO₂ (Figure 4-5(d)). Furthermore, the superior electrical conductivity of RGO also facilitates the transport of electrons and enhances reaction rate in the composites. Therefore, the amorphous structure and the graphene wrapped morphology of GWA MnO_x composites are suggested to promote the strong and reversible reactions; and hence, the high capacitance between 0.7 – 2.8 V is obtained.

It is noted that the valence of Mn ions varies between +2.0 and +2.6 during the reversible reactions (Figures 2(a) and 2(b)). In addition, the potential range of 0.7 – 2.8 V was selected to avoid of occurrence of conversion reactions, and no phase transformation has been observed in SEM and TEM results in Figure 4-2. It is suggested that the strong reversible reactions between 0.7 – 2.8 V (Figure 4-5) are the reversible lithiation and delithiation process of GWA MnO_x composites.

4.3.3 Pseudo-capacitive lithium-ion storage

In order to further investigate rate capability of the GWA MnO_x composites, cyclic voltammetric data under different sweeping rates are carefully analysed. As shown in Figure 4-6(a), the relationship between peak currents of CV curves and the sweeping rates is portrayed by logarithmic form according to power law¹⁸, which is used to estimate the kinetics of electrochemical processes

$$i = av^b \quad (1)$$

Here i is current, v is sweeping rate, a and b are adjustable values. The b value is the slope of the fitted line in logarithmic diagram and is a critical factor to determine the type of electrochemical reactions.

Two different b values are well defined during cycling. When $b=1.0$, current is proportional to the sweeping rate which is representative of surface-controlled process and is indicative of non-faradaic reaction. Electric double layer capacitive effect (EDLC) is a typical surface-controlled process and almost occurs on all capacitive materials. When the b value is equal to 0.5, the current of reaction is controlled by semi-infinite linear diffusion. This process is often related to charge-transfer process which is a faradaic charge storage process usually coming with redox reactions.

For most electrochemical capacitors, b value is between 0.5 and 1.0 because EDLC's surface-controlled charge storage mechanism and faradaic charge storage mechanism co-exist in electrodes during charging-discharging process. When the value of b is close to 1, it presents fast reactions towards capacitor, implying a fast pseudo-capacitive effect. If the b value is close to 0.5, the rate of faradaic reaction is slow and induces to poor rate capability.

As shown in Figure 4-6(a), two regions can be defined for GWA MnO_x composites, Region 1 for the sweeping rate smaller than 10 mV/s and Region 2 for the sweeping rate larger than 10 mV/s. The slopes, indicative of b value, in Regions 1 and 2 are

0.75 and 0.7, respectively. These results demonstrate that the charge storage mechanism of GWA MnO_x composites is towards surface-controlled charge storage, indicating a fast pseudo-capacitive behavior. Compared to b values of other metal oxide materials also suggested to exhibit pseudo-capacitive behavior, 0.66 for Fe_3O_4 ¹⁹, 0.7 for TiO_2 ²⁰, 0.57 for NiMn_2O_4 ²¹ and 0.75 for V_2O_5 ²², the GWA MnO_x composites with $b=0.75$ obtained in this study presents higher kinetics than most other metal oxide materials. For the sweeping rate higher than 10 mV/s in Figure 4-6(a), b value decreases to 0.7 because of the ohmic contribution or diffusion constraints, as also suggested by Augustyn et al²³..

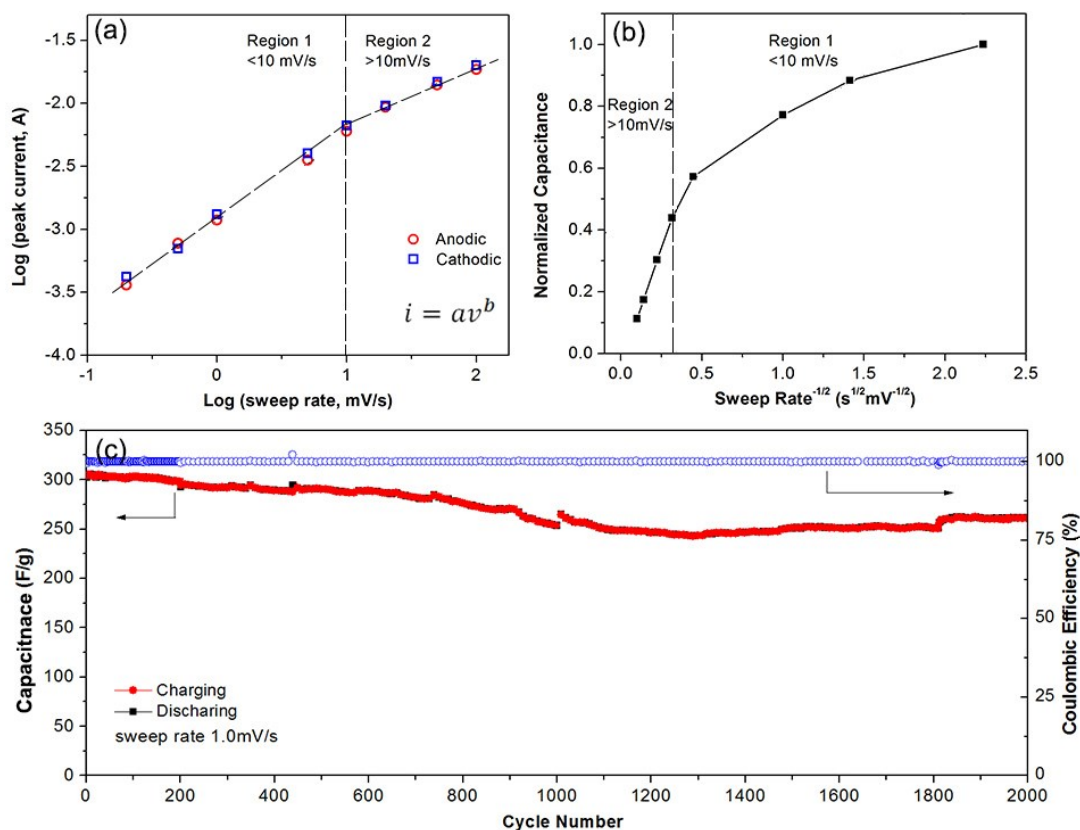


Figure 4-6. (a) b-value determination of the peak anodic and cathodic currents on different log(sweep rates). (b) Capacitance versus $v^{-1/2}$ for the separation of diffusion-controlled capacitance and capacitive-controlled capacitance. (c) Cycle performance and coulombic efficiency of GWA MnO_x composites for 2000 cycle under 1.0 mV/s sweeping rate.

The relationship between capacitance and sweeping rate is another evidence to evaluate the high rate capability of GWA MnO_x composite electrode. It can also be employed to reveal limiting steps at different sweep rates²⁴. A plot of capacitance Q versus sweeping rate $v^{-1/2}$ for GWA MnO_x composites is displayed in Figure 4-6(b). In Region 1, at sweep rate <math>< 10 \text{ mV/s}</math>, the capacitance is almost independent of $v^{-1/2}$. In this region, lithium ions diffuse into the bulk of amorphous MnO_x without obvious

solid-state, lithium-ion diffusion limitation; and therefore, the capacitance can be reached to 430 F/g. In Region 2, from 10 mV/s to 100 mV/s, the linear relationship between capacitance and $v^{-1/2}$ is evident. This linear relationship reveals that the capacitance is limited by semi-infinite linear diffusion and the diffusion control is the main rate-limiting step at high sweep rates²⁵. Figure 4-6(b) indicates that the sweeping rate of 10 mV/s is a critical point to assess the rate capability of GWA MnO_x composites. At this sweep rate, 10 mV/s, the charging process can be completed within 3.5 minutes between 0.7 – 2.8 V while the capacitance can be retained up to 200 F/g. The capacitance of 200 F/g is even higher than the specific capacitance of most transition metal oxides swept at much slower rates, < 1mV/s. These results are consistent with power law analysis in Figure 4-6(a). Figures 4-6(a) and 4-6(b) reveal that a high extent of lithiation can be achieved within GWA MnO_x composites at a high rate, indicating pseudo-capacitive lithium-ion storage for GWA MnO_x composites when cycled between 0.7 – 2.8 V.

As discussed in Figure 4-5(d), this noticeable rate capability of GWA MnO_x composites can also be ascribed to their unique graphene-wrapped, amorphous structure. Amorphous structure can provide numerous diffusion paths in the composite particles, and hence, enhance the Gibbs free energy and kinetics of the reactions. The superior electrical conductivity of RGO also facilitates the transport of electrons and enhances reaction rate in the composites, leading to lithium-ion pseudo-capacitive behavior of GWA MnO_x composites.

The practical significance of pseudo-capacitive lithium-ion storage also depends on its cyclability. As shown in Figure 4-6(c), GWA MnO_x composites demonstrate excellent cycling performance in the potential range of 0.7 – 2.8 V. After 400 cycles, the capacitance of GWA manganese oxide composites reaches 91% of the original value (306 F/g), and still maintains 86% even after 2,000 cycles. Comparing with the cyclability of other transition metal oxides, for example, 200 cycles for TiO₂²⁶, 300 cycles for Manganese oxide/multiwalled carbon nanotubes²⁷ and 500 cycles for Li₂Ti₃O₇²⁸, GWA MnO_x composites exhibit distinct cyclability in Figure 4-6(c). The reported excellent cycling performance may arise from the stable graphene-wrapped, amorphous structure as discussed on TEM and SEM characterizations shown in Figure 4-2. Furthermore, the porous structure in GWA MnO_x composites can also effectively buffer the volume change during cycling.

4.3.4 Lithium-ion pseudo-capacitors (LIPC)

As discussed above, GWA MnO_x composites were found to possess high performance, pseudo-capacitive lithium-ion storage between 0.7 – 2.8V vs Li/Li⁺, due to their unique graphene-wrapped, amorphous structure. It is, therefore, suggested that GWA MnO_x composite can be used as the positive electrode in lithium-ion capacitors (LICs). Since GWA MnO_x composites exhibit distinct lithium-ion pseudo-capacitive behavior resulting from the strong reversible redox reactions found in Figure 4-5, when

coupling with lithium-doped graphite anodes, such a hybrid device is referred to as a Lithium-ion Pseudo-capacitor (LIPC).

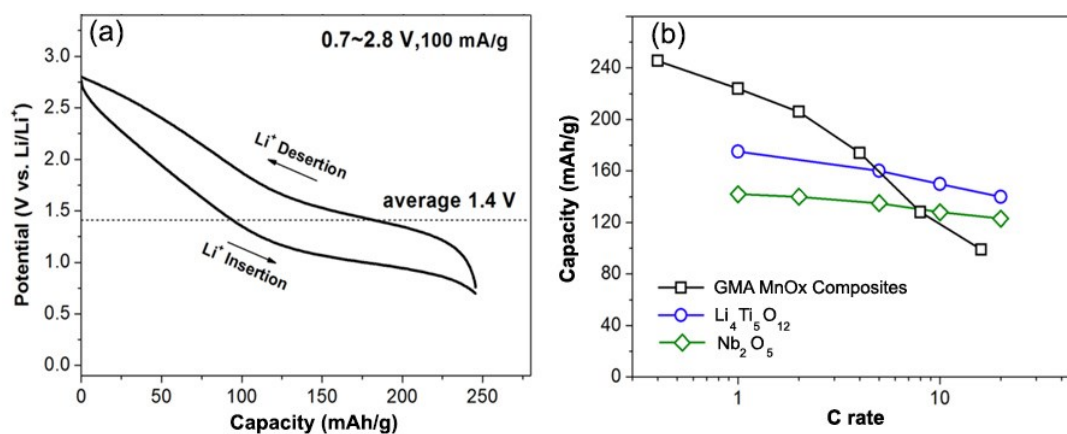


Figure 4-7. (a) Galvanostatic cycling of GWA MnO_x composite electrodes. (b) Comparison of the rate capability of GWA MnO_x composites with Li₄Ti₅O₁₂ and Nb₂O₅ at different C-rates.

The capacity and the rate capability of GWA-MnO_x composites can be shown in Figure 4-7, when used as the cathode in LIPCs. As shown in Figure 4-7(a), charging/discharging curves exhibit a high capacity of 245 mAh/g at a rate of 100 mA/g (0.4 C) between 0.7 – 2.8 V. In addition, the potential hysteresis in Figure 4-7(a) is much smaller than that cycled between 0.01 – 3.0 V (Figure 4-8), indicating the practical significance of this performance. The rate capability of GWA MnO_x composites were also tested and concluded in Figure 4-7(b). Since Li₄Ti₅O₁₂²⁹ (lithium-ion intercalation reactions) and T-Nb₂O₅³⁰ (lithium-ion intercalation pseudo-capacitance) are two promising cathodes for LIPCs, their performance was also used and compared with that of GWA MnO_x composites in Figure 4-7(b) at C

rates ranging from 0.1 C to 20 C. As shown in Figure 4-7(b), the capacity of GWA MnO_x composites is 225 mAh/g at 1 C, which is 28% higher than that of $\text{Li}_4\text{Ti}_5\text{O}_{12}$ and 58% higher than Nb_2O_5 at the same rate. Even when the charging rate is around 20 C, its capacity is still comparable to that of $\text{Li}_4\text{Ti}_5\text{O}_{12}$ and Nb_2O_5 , demonstrating superior pseudo-capacitive lithium-ion storage for GWA MnO_x composites to that of $\text{Li}_4\text{Ti}_5\text{O}_{12}$ and Nb_2O_5 .

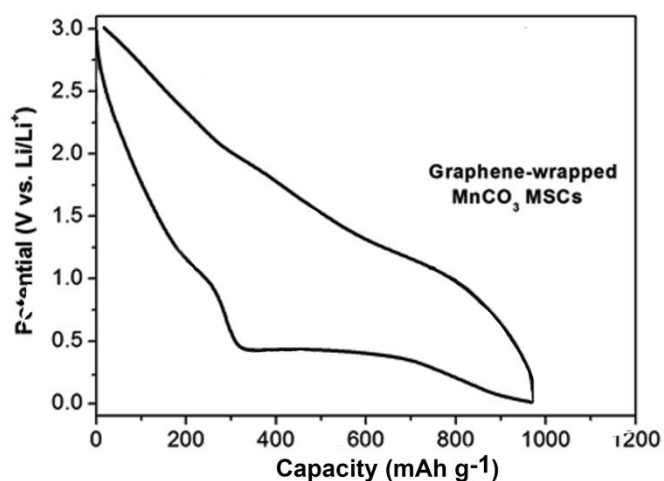


Figure 4-8. Galvanostatic cycling of MnCO_3 MSCs from 0.01V-3.0V demonstrating high potential hysteresis.

4.4 Conclusion

In conclusion, graphene-wrapped, amorphous MnO_x composites were in-situ formed from their precursor, graphene-wrapped MnCO_3 mesoporous single crystals. Such GWA MnO_x composites show distinct microstructural features and demonstrate excellent electrochemical performance when cycled in the potential range of 0.7 – 2.8 V vs Li/Li^+ . The highest capacitance was measured to be 430 F/g at 0.2 mV/s sweeping rate, and the capacitance of 200 F/g was also obtained under 10 mV/s high sweeping rate. After 400 cycles, the capacitance of GWA manganese oxide composites reaches 91% of the original value (306 F/g), and still maintains 86% even after 2,000 cycles. It was found, for the first time, that GWA MnO_x composites presented high performance, pseudo-capacitive lithium-ion storage between 0.7 – 2.8 V, due to their unique graphene-wrapped, amorphous structure. When coupled with lithium-doped graphite anodes, this composite material demonstrates superior pseudo-capacitive lithium-ion storage to that of $\text{Li}_4\text{Ti}_5\text{O}_{12}$ and Nb_2O_5 . The understanding of lithium-ion pseudo-capacitive behavior of GWA MnO_x composites and their possible application as the cathode in lithium-ion pseudo-capacitors may offer a novel approach to bridge the performance gap between supercapacitors and LIBs.

4.5 References

- 1 K. Naoi, Y. Nagano, W. Naoi, Tanso, 2013, 256, 22-32.
- 2 V. Augustyn, J. Come, M. A. Lowe, J. W. Kim, P. L. Taberna, S. H. Tolbert, H. D. Abruna, P. Simon, B. Dunn, Nature Materials, 2013, 12, 518–522.
- 3 Y. Xiong, Y. Xie, Z. Li, C. Wu, Chem-Eur J., 2003, 9, 1645–51.
- 4 H. Lai, J. Li, Z. Chen, Z. Huang, ACS Appl. Mater. Interfaces, 2012, 4, 2325–2328.
- 5 W. Li, K. Xu, B. Li, J. Sun, F. Jiang, Z. Yu, R. Zou, Z. Chen, J. Hu, ChemElectroChem, 2014, 1, 1003-1008.
- 6 Q. Chen, J. Tang, J. Ma, H. Zhang, N. Shinya, L. Qin, Carbon, 2011, 49, 2917 – 2925.
- 7 Gao, M. et al. J. Mater. Chem. A, 2015, 3, 14126-14133.
- 8 H. L. Guo, X. F. Wang, Q. Y. Qian, F. B. Wang, X. H. Xia, ACS Nano, 2009, 9, 2653-2659.
- 9 W. S. Hummers Jr, R. E. Offeman, J. Am. Chem. Soc., 1958, 80, 1339-1339.
- 10 J. C. Carver, G. K. Schweitzer, T. A. Carlson, J. Chem. Phys., 1972, 57, 973-982.
- 11 M. Chigane, M. J. Ishikawa, Electrochem. Soc., 2000, 147, 2246-2251.
- 12 B. Djurfors, J. N. Broughton, M. J. Brett, D.G. Ivey, Acta Mater., 2005, 53, 957–965.
- 13 M. Nakayama, A. Tanaka, Y. Sato, T. Tonosaki, K. Ogura, Langmuir, 2005, 21 5907-5913.
- 14 Z. Li, J. Wang, L. Sheng, X. Liu, S. Yang, Journal of Power Sources, 2011, 196, 8160 – 8165.
- 15 H. Jiang, Y. Hu, S. Guo, C. Yan, P. S. Lee, C. Li, ACS nano, 2014, 8, 6038–6046.
- 16 J. Qu, L. Shi, C. He, F. Gao, B. Li, Q. Zhou, H. Hu, Carbon, 2014, 66, 485-492.
- 17 O. Delmer, P. Blaya, L. Kienle, J. Maier, Adv. Mater., 2008, 20, 501-505.
- 18 H. Lindström, S. Sodergren, A. Solbrand, H. Rensmo, J. Hjelm, A. Hagfeldt, S. E. Lindquist, J. Phys. Chem. B, 1997, 101, 7717-7722.
- 19 R. Li, J. Liu, Electrochimica Acta, 2014, 120, 52–56.
- 20 K. Zhu, Q. Wang, J. H. Kim, A. A. Pesaran, A. J. Frank, J. Phys. Chem. C, 2012, 116, 11895–11899.
- 21 K. V. Sankar, S. Surendran. K. Pandi, A.M. Allin, V. D. Nithya, Y. S. Lee, R. K. Selvan, RSC Adv., 2015, 5, 27649–27656.
- 22 H. Yin, C. Song, Y. Wang, S. Li, M. Zeng, Z. Zhang, Z. Zhu, K. Yu, Electrochimica Acta, 2013, 111, 762– 770.
- 23 M. Park, M. Park, X. Zhang, M. Chung, G. B. Less, A. M. Sastry, J. Power Sources, 2010, 195, 7904-7929.
- 24 S. Ardizzone, G. Fregonara, S. Trasatti, Electrochim. Acta, 1990, 35, 263-267.
- 25 D. Baronetto, N. Krstajic, S. Trasatti, Electrochim. Acta, 1994, 39, 2359-2362.
- 26 Y. Cai, B. Zhao, J. Wang, Z. Shao, Journal of Power Sources, 2014, 253, 80-89.
- 27 G. Wang, B. Zhang, Z. Yu, M. Qu, Solid State Ionics, 2005, 176. 1169-1174.
- 28 F. Chen, R. Li, M. Hou, L. Liu, R. Wang, Z. Deng, Electrochimica Acta, 2005, 51, 61–65.

29 N. Zhang, Z. Liu, T. Yang, C. Liao, Z. Wang, K. Sun. *Electrochem. Commun.*, 2011, 13, 654-656.

30 K. Brezesinski, J. Wang, J. Haetge, C. Reitz, S. O. Steinmueller, S. H. Tolbert, B. M. Smarsly, B. Dunn, T. Brezensinski, *J. Am. Chem. Soc.*, 2010, 132, 6982–6990.

Chapter 5 Electrochemical Deposition of Co-MnCO₃ on Reduced Graphene Oxides as anode of LIBs

5.1 Introduction

Rechargeable lithium ion batteries (LIBs) are the prevalent energy storage devices for portable electronic equipment due to their large capacity and high cyclability.^{1,2,3,4,5} However, the challenges for LIBs always remain. The limitation of conventional LIB electrode materials such as graphite, lithium cobalt oxides, and transition metal oxides are an increasing concern because of the growing demands of the energy market. These demands include large capacity batteries for modern electronic devices and strict power requirements for electrical vehicles. It is necessary to develop electrode materials with excellent electrochemical performances including high capacitance, high power density and good rate ability.

One new method to improve the electrochemical performance of electrode materials^{6,7} has involved introducing substitutional metal ions into oxide or carbonate hosts. Cobalt-doped manganese oxides^{8,9,10} or carbonates^{11,12,13} have many properties superior to those of single metal oxides or carbonates like manganese oxides (MnO), cobalt oxides and manganese carbonates. First, the cobalt-doped structure can inherit

the high capacity performance of the host crystals, allowing cobalt-doped crystals to store lithium ions as much as its host structure.¹⁴ In addition, compared to manganese-based crystals, cobalt-doped manganese oxides or carbonates can improve mechanical stability.^{15,16,17,18} Furthermore, substitutional elements can influence the morphology of final products. Some morphology is beneficial to the electrochemical performance of electrode materials. By adjusting the fabrication method, the shape, morphology and phase of crystals can be carefully controlled, and desired electrochemical performance can be obtained.

The methods for synthesizing multi-transition metal oxides for the electrode of LIBs have been investigated for decades.^{19,20,21} MnCo_2O_4 spinel hollow spheres with porous surfaces have been synthesized recently. The LIB assembled with an anode fabricated from MnCo_2O_4 spinel hollow spheres can achieve a 610 mAh/g capacity with 100 cycles.^{22,23} The $\text{Mn}_{1.5}\text{Co}_{1.5}\text{O}_4$ core shell microsphere also delivered a good performance; it was able to be cycled 300 times and maintain a capacity above 600 mAh/g.²⁴ However, there is not much literature about transition metal-doped manganese carbonates and their use as electrodes for LIBs. Shadi et al. investigated the performance of cobalt-doped manganese carbonate when it was used as an anode material in LIBs.¹⁴ By adjusting the content of cobalt, the highest capacity of cobalt-doped manganese carbonate can reach 1300 mAh/g but drop to 550 mAh/g after 80 cycles.

The aim of this work is to fabricate cobalt-doped MnCO_3 (Co-MnCO_3) using the Dynamic Floating Electrodeposition (DFE) method, to study the performance of cobalt-doped MnCO_3 crystals (Co-MnCO_3) as an anode for LIBs, and at the same time to gain further knowledge on lithium storage mechanisms in Co-MnCO_3 electrodes. Based on the above considerations, several Co-MnCO_3 crystals with varied Co content were prepared for the first time by DFE. Controlling the composition of the electrodeposition solutions and the electrodeposition current density in DFE makes it possible to tailor the morphology and structure of the final products. The electrochemical performances of the LIBs made of Co-MnCO_3 electrodes are also discussed in detail in this chapter.

5.2 Experimental Procedure

5.2.1 Material synthesis

GO preparation: The graphite oxide was synthesized from natural graphite powders (MTI Corporation) based on a modified Hummers method. The exfoliation of graphite oxide to GO was achieved by sonication for two hours (Branson 2510, 1000 W, 20% amplitude), and then GOs were filtered and rinsed with deionized water. Finally, a homogeneous GO in deionized water solution (2.0 mg mL^{-1}) was obtained and used for electrodeposition.

Synthesis of graphene-wrapped cobalt-doped MnCO₃ crystals using the dynamic floating electrodeposition (DFE) method:²⁵ DFE was carried out by a Gamry PC4/750 potentiostat/galvanostat in a three-electrode cell configuration under the galvanostatic control of the current density at two different current densities, 10 mA/cm² and 50mA/cm², where Ag/AgCl was used as the reference electrode. The cathodic electrode was ferritic stainless steel substrates with dimensions of 20 mm× 10 mm × 1 mm, and the anodic electrode was a 52-mesh woven platinum sheet with dimensions of 20 mm× 10 mm. The cathodic and anodic electrodes were set in a vertical position opposite to each other with a distance of 10 cm. The electrodeposition solution used was 0.3M sodium citrate, 0.3M MnSO₄ and CoSO₄ mixed solution with three different atom ratios:Mn:Co which are 1:1, 4:1 and 8:1. Here the pH value was adjusted to be 7.0. A 20 mL GO (2.0 mg/mL) solution was dispersed into a 500 mL electrodeposition solution and agitated with a Teflon-coated stirring bar at 700 rpm. During the electrodeposition, the temperature of the electrodeposition solution was controlled to be 70°C. After electrodeposition for four hours, graphene-wrapped Co-MnCO₃ was filtered from the electrodeposition solution and rinsed with deionized water before being freeze-dried (Savant supermodulyo freeze dryer, Thermo Electron Corporation) for more than 10 hours.

5.2.2 Characterization

The morphology and structure of graphene-wrapped Co-MnCO₃ were analyzed by transmission electron microscopy (TEM, JEOL JEM-2100 with LaB₆ cathode, 200

kV and JEOL 2010 attached with 4pi EDS system) and scanning electron microscopy (SEM, Zeiss EVO SEM equipped with a Bruker Silicon Drift Detector for Energy Dispersive X-Ray analysis). EDS results of the final product were tested at several different locations and the atom ratio of elements was the average value of atom ratios at different locations. X-ray Diffraction (XRD) analyses were conducted on a Siemens D5000 X-ray diffractometer with Cu K α as the radiation source ($\lambda= 1.5418 \text{ \AA}$).

5.2.3 Electrochemical measurement

The electrochemical experiments were performed using 2032-type coin cells. To prepare the working electrodes, graphene-wrapped Co-MnCO₃ crystals, Super-C65 carbon black, and polyvinylidene fluoride with a mass ratio of 90:6:4 were mixed uniformly in N-methyl pyrrolidone (NMP). The obtained slurry was pasted onto Cu foils, vacuum dried at 120°C overnight. The total loading mass of the material on Cu foil was $\sim 4 \text{ mg/cm}^2$. The testing electrode was cut into a disk with 15mm diameter, the electrodes were assembled in an Argon-filled glove box, using a pure lithium metal foil (MTI Corporation) as a counter electrode, Celgard 2500 polymer film as separator, and the electrolyte of 1M LiPF₆ in ethylene carbonate/diethyl carbonate/dimethyl carbonate (EC/DEC/DMC, vol 1:1:1) (MTI Corporation). The galvanostatic charge/discharge tests, cyclic voltammetry (CV) tests, and cycle performance tests were carried out at $22 \pm 1^\circ\text{C}$ using a 1470E multi potentiostat/celltest system (Solartron).

5.3 Results

5.3.1 Synthesis and Morphology Analysis

As detailed in Chapter 3, the size of the MnCO_3 single crystals after electrodeposition was sensitive to electrodeposition current density. Based on the findings in Chapter 3, two different electrodeposition current densities (-50 mA/cm^2 and -10 mA/cm^2) were selected for Co and Mn co-electrodeposition. The concentration of MnSO_4 and CoSO_4 in the electrodeposition solution was adjusted to achieve different Mn:Co atom ratios, which were 1:1, 4:1 and 8:1. Solutions with different Mn:Co atom ratios were used to electrodeposit Co-doped MnCO_3 at different electrodeposition current densities.

Table 5-1 lists the Mn to Co ratios of the Co-doped MnCO_3 obtained from the deposition at two current densities in three electrolytes with different atom ratios of MnSO_4 and CoSO_4 in solution. The data in Table 5-1 have also been plotted in Figure 5-1 for the purpose of better comparison. At a lower electrodeposition current density, the amount of Co being doped into MnCO_3 decreased as the Co:Mn ratio increased in the electrodeposition solution, while an opposite trend was found when the electrodeposition current density was higher.

Table 5-1. Mn:Co atom ratio of Co-doped MnCO₃ obtained at different electrodeposition conditions as determined by EDX.

Atom ratio of Mn ²⁺ and Co ²⁺ in solution	10 mA/cm ²	50 mA/cm ²
1:1	Mn:Co = 67.3:1	Mn:Co = 12.7:1
4:1	Mn:Co = 44.4:1	Mn:Co = 23.1:1
8:1	Mn:Co = 21.4:1	Mn:Co = 48.2:1

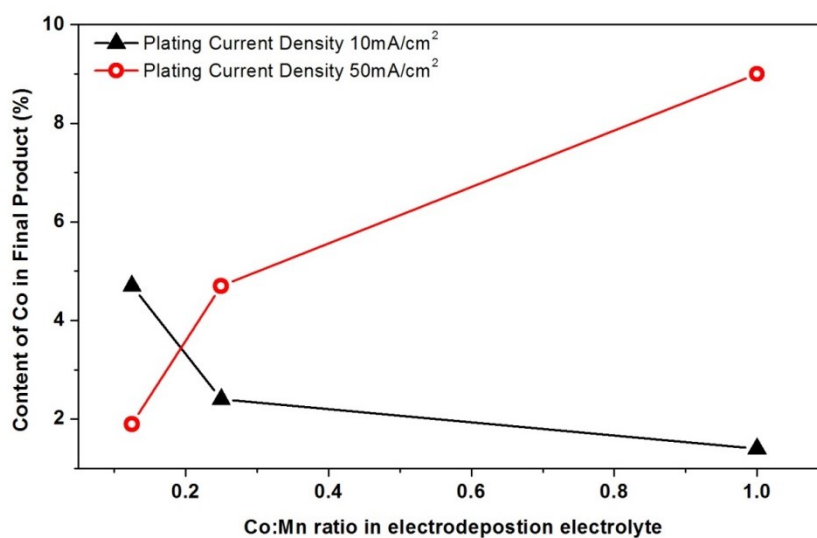


Figure 5-1. Effect of Co:Mn ratio in the electrodeposition electrolyte and electrodeposition current density on the Co content being incorporated into MnCO₃.

The morphologies of Co-doped MnCO₃ were characterized by SEM and TEM, as shown in Figure 5-2. The wrapping of electrodeposition products by reduced graphene oxide sheets is clearly seen from the SEM images at lower magnification and TEM images. This wrapping effect is quite similar to the RGO-wrapping of the MnCO₃ single crystal fabricated by the DFE method as detailed in Chapter 3.

The selected area electron diffraction (SAED) pattern confirms that the Co-doped MnCO_3 has a structure the same as MnCO_3 , according to PDF #860172 and the SAED pattern shown in Figure 5-2(d).

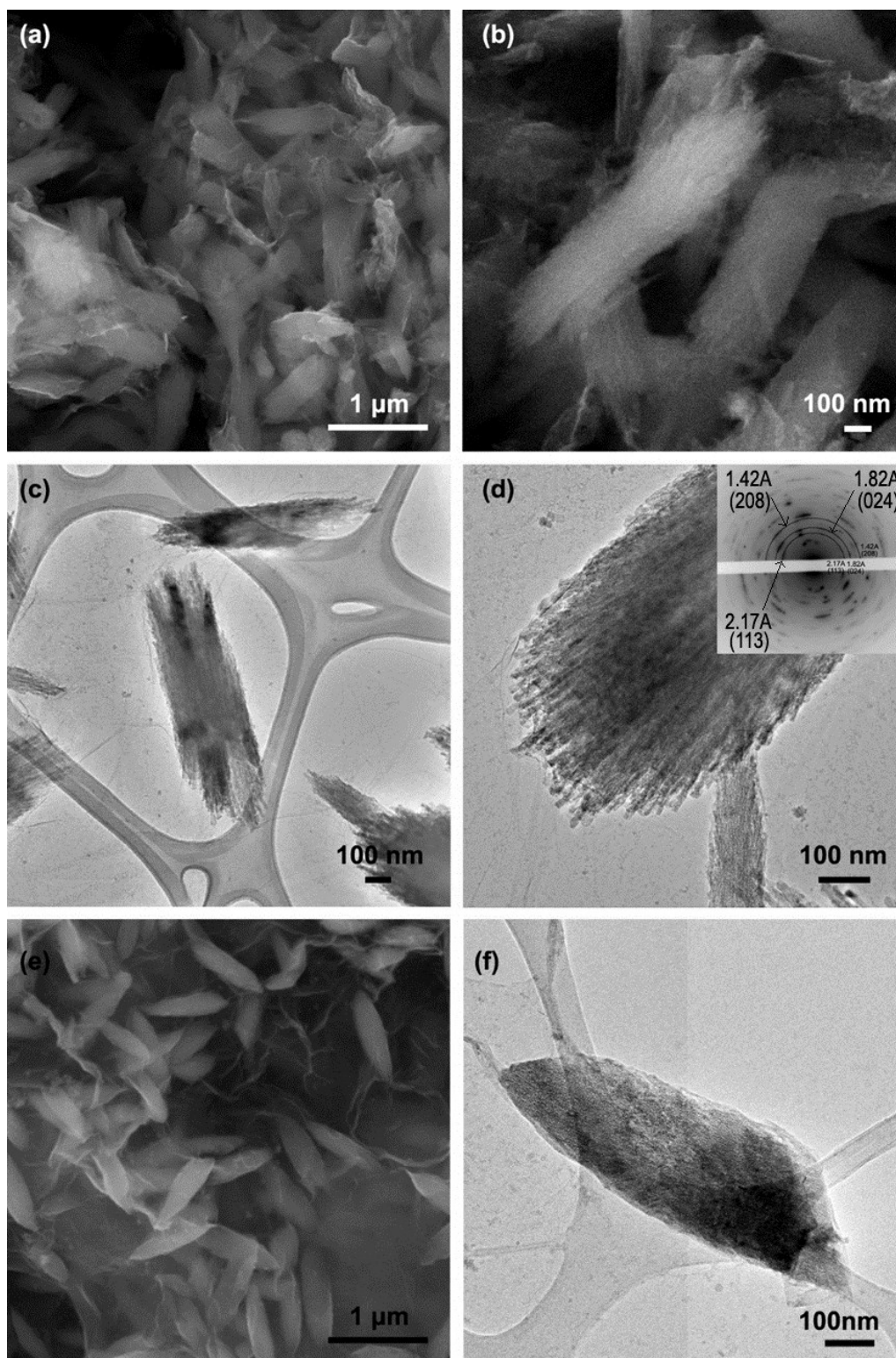


Figure 5-2. (a) SEM result of Co-MnCO₃ plated under -50mA/cm² electrodeposition current density with a 4:1 atom ratio of Mn:Co in the electrodeposition solution. (b) High magnification of Co-MnCO₃ plated under -50mA/cm² electrodeposition current density with a 4:1 atom ratio of Mn:Co in the electrodeposition solution. (c) TEM result of Co-MnCO₃ plated under -50mA/cm² electrodeposition current density with a 4:1 atom ratio of Mn :Co in the electrodeposition solution. (d) Details of the nano crystal tube of Co-MnCO₃ plated under -50mA/cm² electrodeposition current density with a 4:1 atom ratio of Mn :Co in the electrodeposition solution. (e) SEM morphology of the MnCO₃ single crystal synthesized by DFE under -50mA/cm². (f) TEM morphology of the MnCO₃ single crystal synthesized by DFE under -50mA/cm².

The doping of Co was found to have altered the morphology of MnCO₃. The latter has a rice-like shape with closing ends, as shown in Figures 5-2e and 5-2f. Although Co-doped MnCO₃ generally retains a rice-like shape similar to that of the un-doped MnCO₃, the Co-doped MnCO₃ rice has open ends, resembling a broom with bristles, as shown in Figure 5-a)-d). The “bristles” in Co-doped MnCO₃ appear to be made of an aligned nano-rod, as shown in Figure 5-2(d).

The morphology of Co-doped MnCO₃ has also been affected by electrodeposition current density and the concentration of CoSO₄ in the electrodeposition solutions. At lower electrodeposition current density, -10 mA/cm², more Co was doped into MnCO₃ when the Mn:Co ratio in the electrodeposition solution was lower (Figure 1). As shown in Figure 5-3, a electrodeposition solution with a higher Co content or with

a lower Mn:Co ratio has produced Co-doped MnCO_3 with smaller rice-shaped particles, and fewer and smaller bristle-like features. That is to say, MnCO_3 deposits with higher Co-doping are larger and are more open-ended.

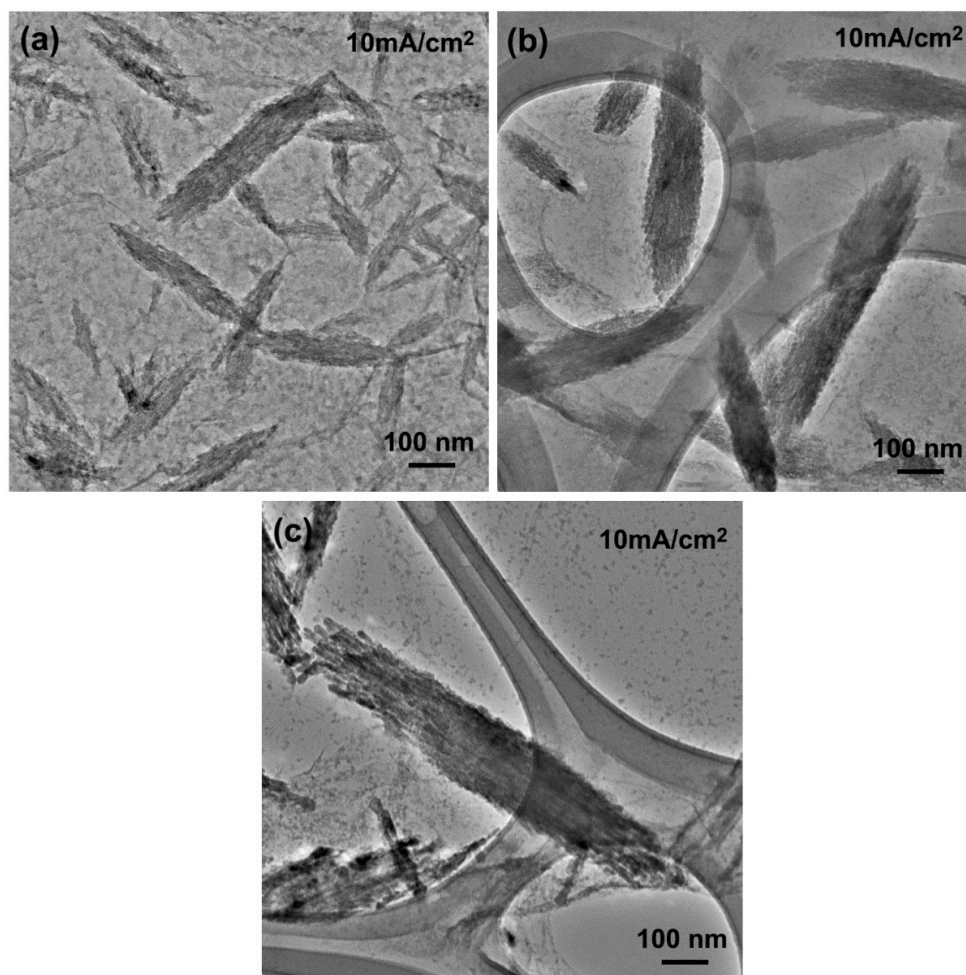


Figure 5-3. (a) TEM bright field result of Co-MnCO_3 plated with a 1:1 atom ratio of Mn:Co in an electrodeposition solution under $-10\text{mA}/\text{cm}^2$ electrodeposition current density. (b) TEM bright field result of Co-MnCO_3 plated with a 4:1 atom ratio of Mn:Co in an electrodeposition solution under $-10\text{mA}/\text{cm}^2$ electrodeposition current density. (c) TEM bright field result of Co-MnCO_3 plated with an 8:1 atom ratio of Mn:Co in an electrodeposition solution under $-10\text{mA}/\text{cm}^2$ electrodeposition current density.

The effect of electrodeposition conditions on the morphology of Co-doped MnCO_3 plated at a higher electrodeposition current density is different from those seen at lower electrodeposition current density. As shown in Figure 5-4, the sizes of Co- MnCO_3 deposits are much bigger and the shape of crystals varies dramatically with the concentration of Co in the electrodeposition solution. At a higher electrodeposition density, the amount of Co being incorporated into MnCO_3 increases as the Co content in the electrodeposition solution increases. A higher concentration of Co^{2+} in the electrodeposition solution, and therefore, higher Co-doping in MnCO_3 , results in larger deposits with more open ends. At a Mn:Co ratio of 1:1 in the electrodeposition solution, deposits with a dumbbell-like morphology were observed, as shown in Figure 5-4a. The reduction of Co content in the electrodeposition solution or the deposits makes the ends of deposits less open; it gives them a pointy shape.

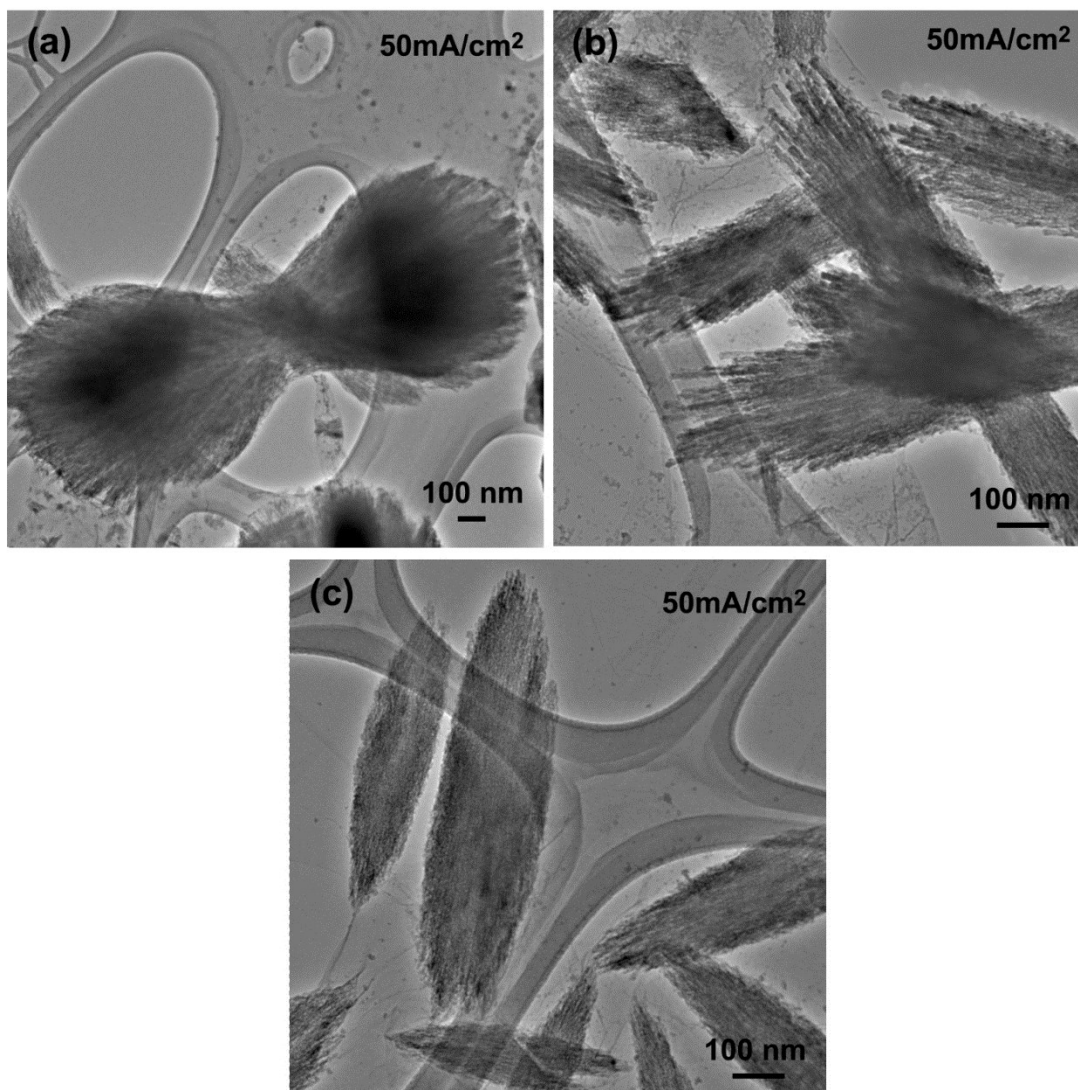


Figure 5-4. (a) TEM bright field result of Co-MnCO₃ plated with a 1:1 atom ratio of Mn:Co in an electrodeposition solution under -50mA/cm² electrodeposition current density. (b) TEM bright field result of Co-MnCO₃ plated with a 4:1 atom ratio of Mn:Co in an electrodeposition solution under -50mA/cm² electrodeposition current density. (c) TEM bright field result of Co-MnCO₃ plated with an 8:1 atom ratio of Mn:Co in an electrodeposition solution under -50mA/cm² electrodeposition current density.

5.3.2 Structural analysis

The phase and structure of the products synthesized under different electrodeposition conditions were characterized by XRD and selected area electron diffraction (SAED). Two samples were selected, which represent the Co-doped-MnCO₃ crystals with high (Mn:Co=12.7:1) and low cobalt (Mn:Co=44.4:1) content. As shown in Fig. 5-5a, the XRD diffraction patterns of the two samples are consistent with the calcite structure (rhombohedral lattice, $R\bar{3}c$ space group) and their diffraction patterns are identical except for a slight shift of peak positions from the standard peak positions. The shift of these peaks to a slightly higher diffraction angle appears when the cobalt content in the products is increased. According to the previous studies on cobalt-doped manganese carbonates,^{14,26} Mn²⁺ in the calcite structure can be substituted randomly by Co²⁺ because rhodochrosite MnCO₃ and spherocobaltite CoCO₃ have similar crystal structure, as shown in Figure 5-5(b), but are slightly different in their cell parameters, with the lattice parameters of CoCO₃ crystals (a=4.66, b=14.96) smaller than those of MnCO₃ crystals (a=4.79, b=15.69). This difference will lead to lattice parameters of Co-doped MnCO₃ that are slightly smaller than those of pure MnCO₃. It will also cause diffraction angles to shift to higher values according to Bragg's law.

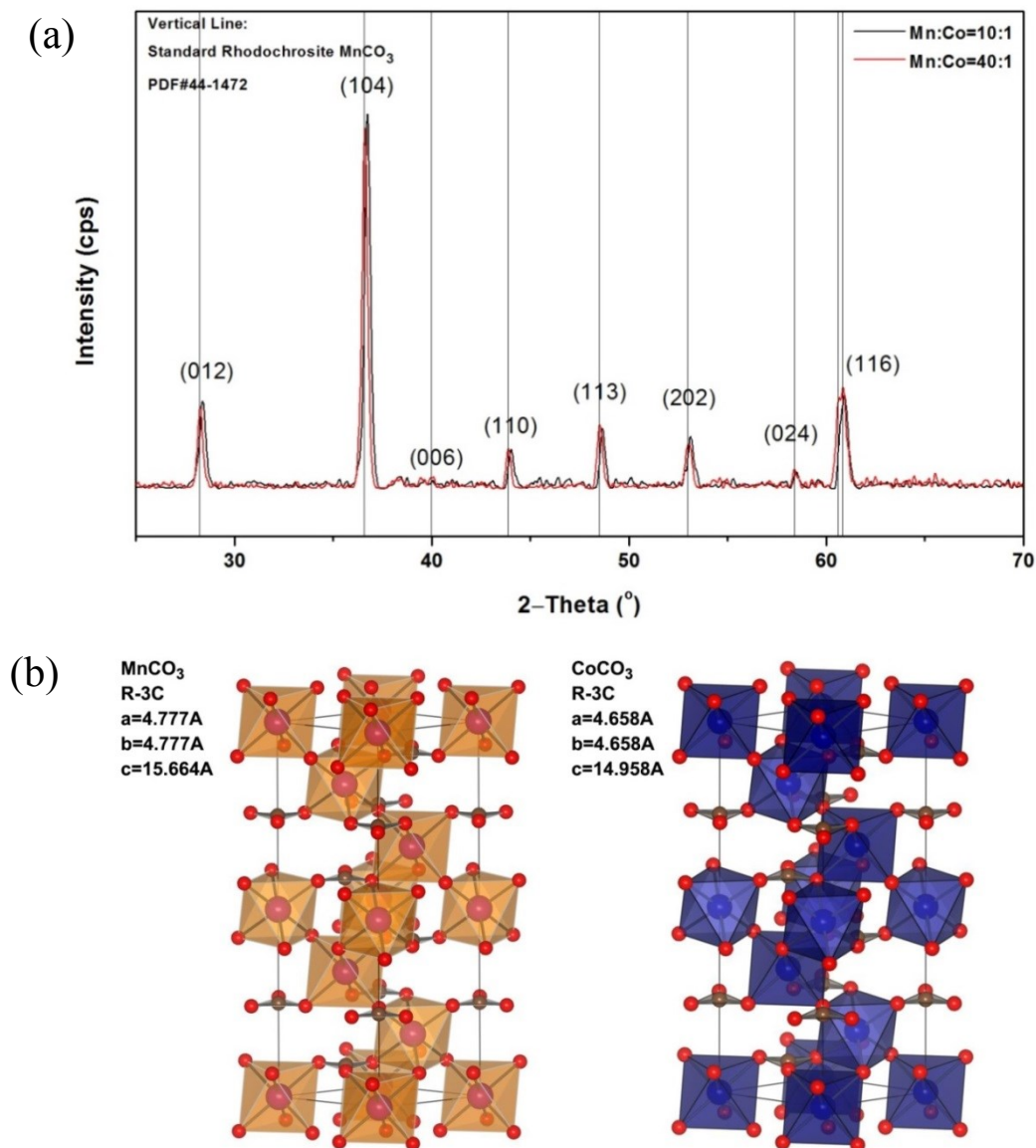


Figure 5-5. (a) The XRD results of Co- MnCO_3 crystals with different cobalt content whose Mn:Co atom ratios are 44:1 and 12:1. (b) The polyhedral crystal structure of MnCO_3 and CoCO_3 .

The differences in crystal structure between Co- MnCO_3 and MnCO_3 were further characterized by SAED. In addition to the two samples characterized by XRD, the Co- MnCO_3 crystal synthesized under low electrodeposition current density (-10

mA/cm^2) with the lowest cobalt doping content (Mn:Co=67.3:1) was also selected for SAED characterization. As shown in Fig. 5-6, the SAED patterns of the three samples were analyzed and confirmed to be rhombohedral ($R\bar{3}c$) MnCO_3 crystals, the differences in their micro- or nano-structures are prominent. The reciprocal lattice diffraction pattern shown in Figure 5-6(b) represents a typical single crystal structure of MnCO_3 , which was from the MnCO_3 with the lowest Co-doping. The rice-shaped MnCO_3 particles with the lowest Co-doping consist of nano-rods, far fewer than those with higher Co-doping. The fact that the lowest Co-doped MnCO_3 possesses the diffraction pattern of a single crystal suggests that the nano-rods are aligned into the same crystallographic orientation, forming a porous single crystal.

With increasing cobalt content, the porous crystals become polycrystalline, as evidenced with the observation of diffraction rings displayed in Figures 5-6(c) and (d). The ring pattern shown in Figure 5-6(d) for the MnCO_3 with mediate doping of Co (Mn:Co=44.4:1) is still discrete with discernable dots. This observation suggests that a limited number of nano-crystals in the area are being selected for diffraction. The rings of the diffracted pattern of the highest Co-doped MnCO_3 (Mn:Co=12.7:1) are much more continuous, as shown in Figures 5-6(e) and (f), indicating much more nano-entities of the same crystal structure in the same selected area.

The theory proposed at the beginning of this chapter is, therefore, proved by SAED results: there is no damage or significant modification on the original crystal frame for element doping during cobalt doping and the phase transformation process. Therefore, the ability of storing lithium ions of final products should be same with its host. In these samples, no other peaks appear — no MnO_x , cobalt oxides or cobalt carbonate in XRD results — which indicates a pure homogeneous formation of Co-doped manganese carbonates. This is very important because the presence of impurities will affect the electrochemical performance. Impurities are difficult to remove and purification is usually very expensive.

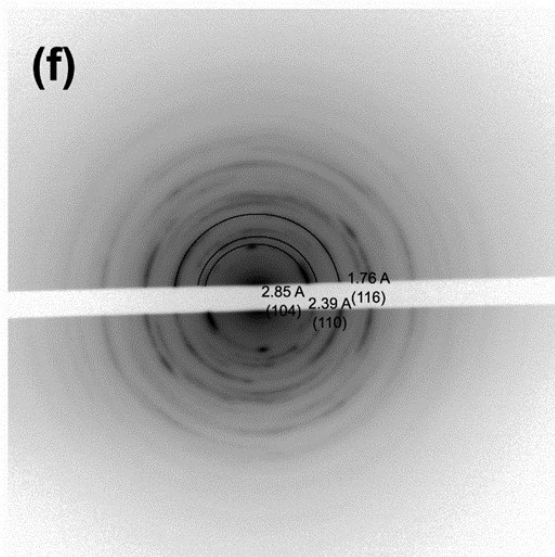
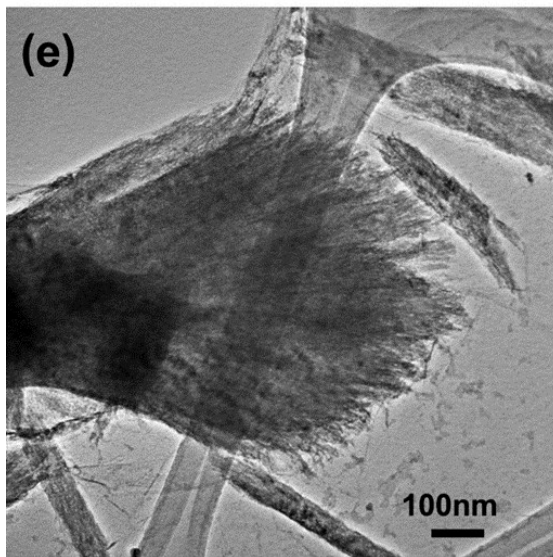
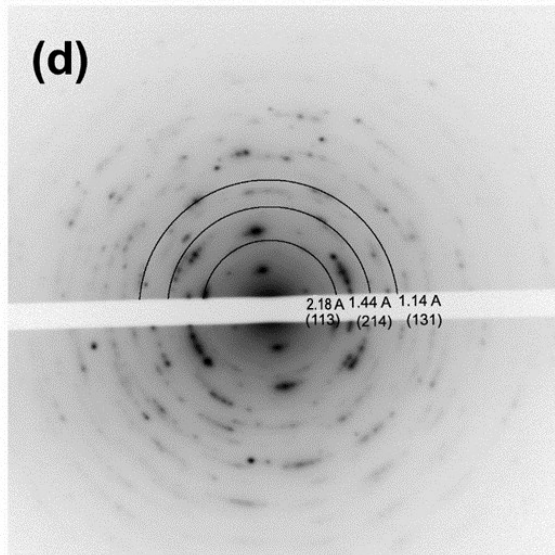
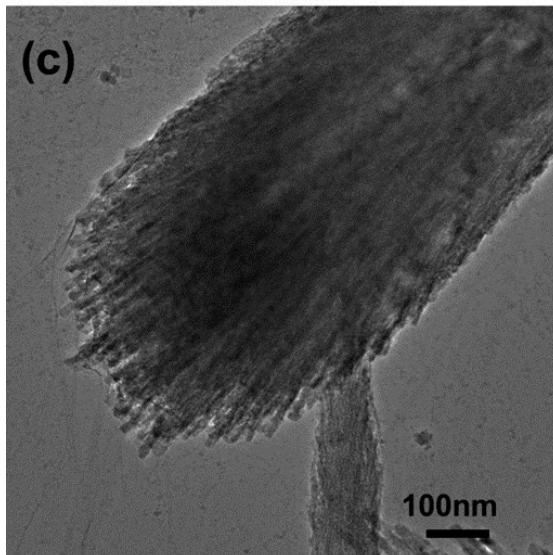
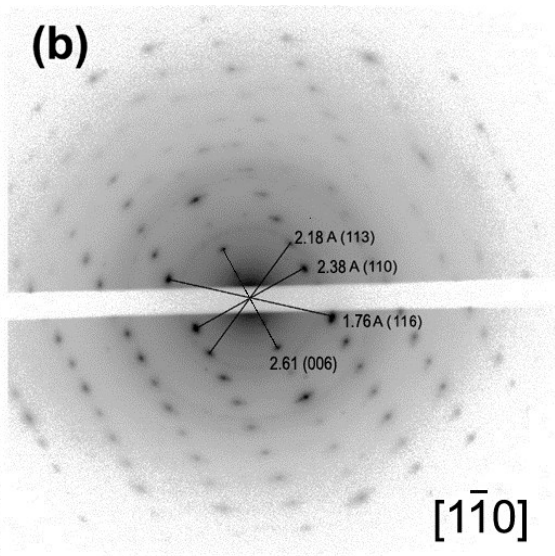
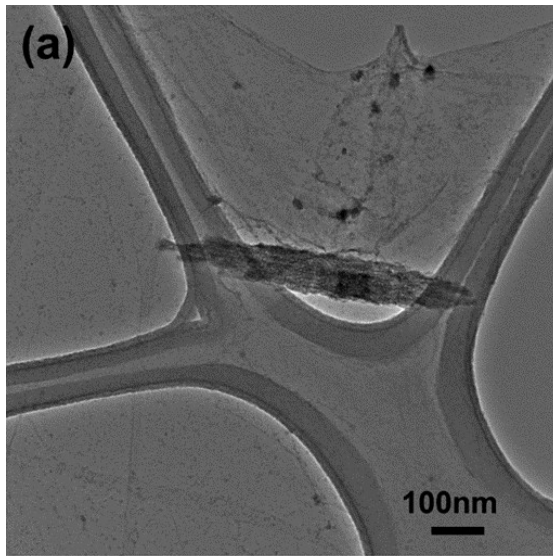


Figure 5-6. (a) TEM result of Co-MnCO₃ plated with a 1:1 atom ratio of Mn:Co in an electrodeposition solution under -10mA/cm² electrodeposition current density. (b) Selected area electron diffraction pattern of sample displayed in (a). (c) TEM result of Co-MnCO₃ plated with a 4:1 atom ratio of Mn:Co in an electrodeposition solution under -10mA/cm² electrodeposition current density. (d) Selected area electron diffraction pattern of sample displayed in (c). (e) TEM result of Co-MnCO₃ plated with a 1:1 atom ratio of Mn:Co in an electrodeposition solution under -50mA/cm² electrodeposition current density. (f) Selected area electron diffraction pattern of sample displayed in (e).

5.3.3 Electrochemical performance of Co-MnCO₃ as a anode in LIBs

The electrochemical performances of two selected materials with high (Mn:Co=12.7:1) and low (44.4:1) cobalt content were tested. The influences of the morphology of active materials on electrochemical properties were also investigated when they were used as anodes in LIBs.

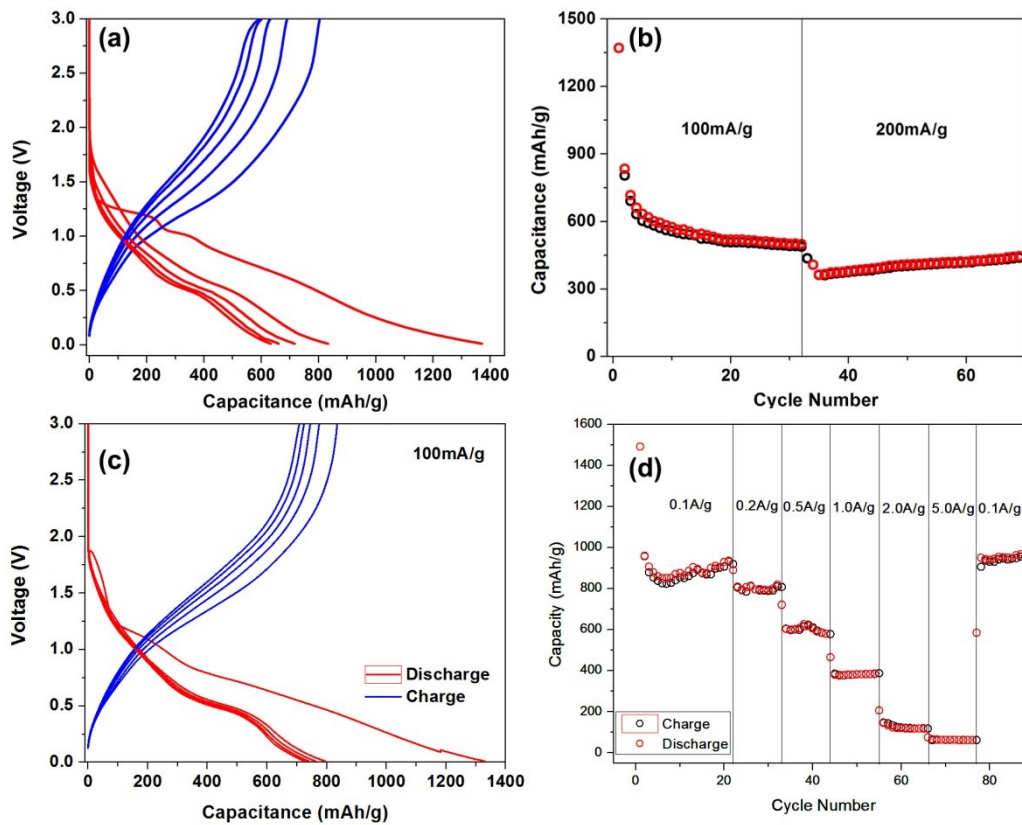


Figure 5-7. (a) Charging-discharging curves and (b) cyclability data of graphene-wrapped Co-MnCO₃ crystals within 0.01~3.0 V at 100mA/g. These crystals are plated in under 10mA/cm² electrodeposition current density. The Mn:Co ratio in these crystals is 40:1 (c) Charging-discharging curves and (d) cyclability data of graphene-wrapped Co- MnCO₃ at different current densities, ranging from 100 mA/g to 5,000 mA/g. These crystals are plated under 50mA/cm² electrodeposition current density. The Mn:Co ratio in these crystals is 10:1.

The sample being electrodeposited under high electrodeposition current density has a dumbbell shape and the highest Co content. In contrast, the size of crystals electrodeposited at a lower current density is smaller and the cobalt content in the final product is much lower than that of the dumbbell-like crystals. A galvanostatic charge-discharge was used to estimate Co- MnCO₃ crystals' capacity and discharging

voltage plateau with a 0.01-3.0V voltage window under 100 mA/g current density as shown in Figure 5-6 (a) and Figure 5-6(c). The discharging curves of both samples have a similar shape and trend. During the first discharging process, two distinct discharging plateaus occur at both samples. These discharging voltage plateaus are located at around 1.25V and 0.75V vs Li/Li⁺, which are different from the voltage plateaus of the MnCO₃ crystals found during the first discharging process but are similar to those being reported for Co-MnCO₃ crystals.¹⁴ This confirms indirectly that cobalt ions were successfully doped into the MnCO₃ host. Both samples exhibit high initial discharge and charge capacities, which are more than 1300 mAh/g and 800 mAh/g, respectively, and are much higher than the capacity of MnOs commonly reported. The increased discharge (Li⁺ insertion) capacity could be related to the initial formation of the solid–electrolyte interface (SEI) film which is generated from electrolyte degradation. It is also a common phenomenon of many transition metal-based anodes when the discharge voltage goes below 1.0V vs. Li/Li⁺. Such SEI films could be partly decomposed during the charge cycle, contributing to the charge capacity.^{27,28,29} Hence, the large irreversible capacity loss in the first cycle is mainly due to the incomplete decomposition of the SEI film. However, compared to the dumbbell-like crystals, MnCO₃ crystals with low-Co content experienced a rapid capacity loss after several charge-discharge cycles and dropped to 500mAh/g after slightly more than 30 cycles (Figure 5-7(b)). The rate capability of rice-shaped Co-MnCO₃ crystals is worse than that of dumbbell-shaped Co-MnCO₃ crystals. Under 200 mA/g current density the capacity of the rice-shaped Co-MnCO₃ crystals is only

400 mAh/g. In contrast, the dumbbell-shaped Co-MnCO₃ crystals exhibit excellent rate capability. At different charging/discharging current densities their capacity does not drop dramatically and still remains at a capacity of 400 mAh/g under 1000 mA/g current density and drops to 100 mAh/g under 2000 mA/g. Despite the large capacity loss in the second cycle, this material shows good capacity retention from the second cycle and delivers a reversible capacity of about 1000 mAh/g after 100 cycles, corresponding to 75.1% of the first discharge capacity. The excellent electrochemical performances of Co-MnCO₃ crystals with high cobalt content are related to their unique dumbbell-like shape, porous morphology and conductive network provided by RGOs. This dumbbell shaped crystal has open ends that are loosely packed, which guarantees fast Li⁺ ion diffusion across the interface. Reduced graphene oxide sheets ensure reliable mechanical adhesion and, more importantly, good electrical contact with the current collector in the electrode. These structures are favorable for efficient contact between the surface of active materials and the electrolyte at high charging rates. In addition, the open and porous morphology could better improve the electrode stability by releasing the internal mechanical stress during charging-discharging processes and preventing agglomeration of nano particles.

5.4 Discussion: Crystal Transformation Mechanism

A Pourbaix diagram of the Mn and Co system was constructed to analyze the formation mechanism of the Co-doped MnCO₃ crystals and their growth process

under different electrodeposition conditions. In this research, the Pourbaix diagram was constructed using free chemical equilibrium diagrams calculation software — Medusa 2.1 as shown in Figure 5-8.

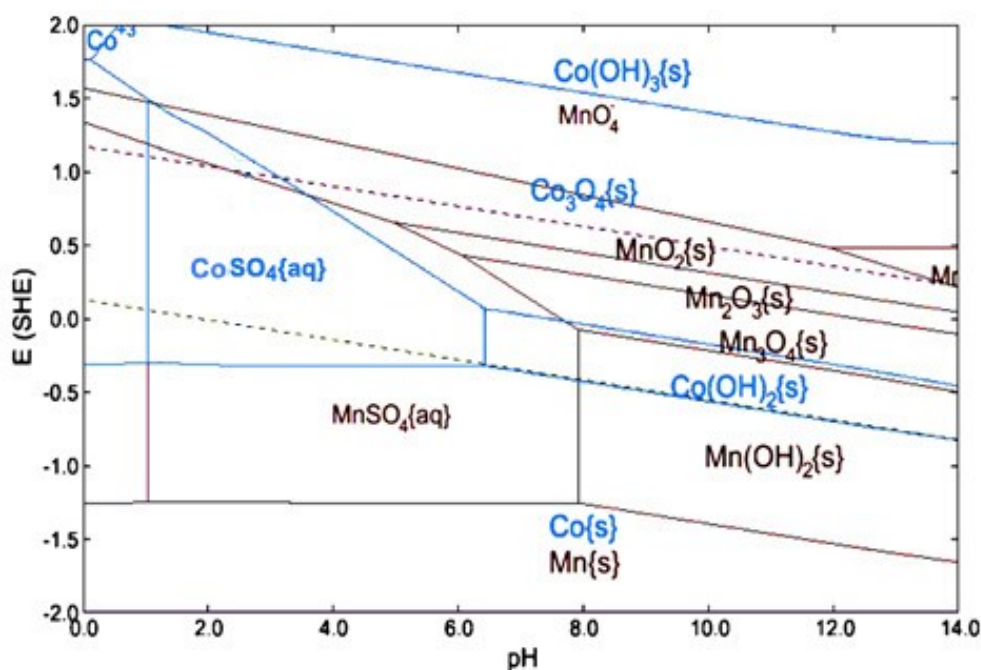
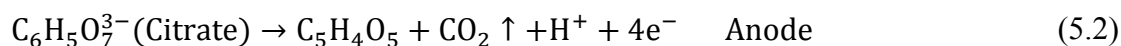


Figure 5-8. Calculated Pourbaix diagrams for 0.3M sodium citrate solutions with 0.3M $\text{CoSO}_4 \cdot 7\text{H}_2\text{O} + \text{MnSO}_4 \cdot 7\text{H}_2\text{O}$ at 70°C .

This diagram shows that Mn(OH)_2 can be formed in a rather large range of voltage from -125 mV to -6 mV vs. SHE when the experiment is carried at 70°C in solutions with a pH value above 8.0. However, for the Co^{2+} system, Co(OH)_2 can be formed only in a narrow voltage window, which is from -40 mV to -2 mV vs. SHE. According to available literature, the transition metal hydroxide is important to fabricate transition metal carbonate crystal.^{30,31,32,33} Reactions taking place on anode and cathode can be expressed by the following equations:



Metal hydroxides will be formed on the reduced graphene oxide sheets at appropriate voltage when RGOs touch the surface of the anode, because reduction reactions on a cathode will increase the pH of the solution closed to the cathode, either by the consumption of H^+ ions or the generation of OH^- ions. When these graphene oxide sheets are floated to the anode, the metal hydroxides on RGOs will react with CO_2 in a relatively acidic environment closed to the anode to form carbonate crystals. Such processes repeat as RGOs' hydroxides circulate, leading to the growth of carbonate crystals.

Compared to Mn^{2+} in the Pourbaix diagram, $\text{Co}(\text{OH})_2$ exists only within a narrow range of voltage when the pH is above 8.0. In this research, the voltage of the cathode electrodeposition electrode fluctuates at around -50 mV vs. SHE under the lower current density -10 mA/cm². It is outside of the voltage window of $\text{Co}(\text{OH})_2$ precipitation and, as a result, the crystal formed under -10 mA/cm² current density is mainly MnCO_3 . Additionally, the lower concentration of Mn^{2+} in the electrodeposition solution and the lower reaction current density can greatly reduce the speed of crystal growth. Consequently, these crystals, as shown in Figure 5-3 (a),

are small and lack the characteristics of crystal nano-rods. The cobalt content in the final product is low because there are not many Mn^{2+} sites in the host to be substituted.

When the Mn^{2+} concentration in the solution is increased, the crystal grows bigger and the crystal nano-rods become thicker. Therefore, it is difficult for Co^{2+} to substitute Mn^{2+} in the host structure when two parameters of electrodeposition (electrodeposition current density and MnSO_4 concentration) are both weak. In contrast, under higher electrodeposition current density, -50 mA/cm^2 , the voltage on cathode is more negative, and the growth rate of MnCO_3 crystals is accelerated. Even in the solution with a low Mn^{2+} concentration ($\text{Mn}:\text{Co}=1:1$), MnCO_3 still grows faster at -50 mA/cm^2 than at -10 mA/cm^2 . Either by increasing the electrodeposition current density or by increasing the MnSO_4 concentration in the electrolyte will enhance opportunities for Co^{2+} can to replace the Mn^{2+} in the host. However, this investigation showed that it is more effective to substitute Mn^{2+} in the host for Co^{2+} by altering the electrodeposition current density than by adjusting the MnSO_4 concentration in the electrodeposition solution. It is also proven that doping Co^{2+} ions is significant only when MnCO_3 crystals can grow at a relatively fast rate.

The evolution of the microstructure from the rice-like shape to the dumbbell-like shape is associated with an improvement of the active material's electrochemical performance. The nano-rods of Co-MnCO_3 crystals with a dumbbell-like shape are loosely packed, probably resulting from a high rate of cobalt substitution. Such a

structure must have a larger surface area and would facilitate the diffusion of lithium ions, therefore improving the rate capability of whole electrode. Besides, such a structure can better accommodate the expansion and contraction of the electrode material during lithation/delithation, yielding better cyclability. Furthermore, wrapping the active materials by graphene provides excellent electrical conductivity.

5.5 Conclusions

A facile method have been developed to synthesize Co-doped MnCO_3 crystals wrapped in reduced graphene oxide sheets through electrodeposition. The structure and morphology of the Co-doped MnCO_3 crystals can be easily controlled by adjusting ionic ratios of Co and Mn in the electrolyte and/or by altering electrodeposition current density. The Co- MnCO_3 crystals with a dumbbell-like shape exhibit outstanding electrochemical performance as integrated electrodes for lithium-ion batteries. The specific capacities can reach 400 mAh/g at the high current density of 1000 mA/g and a capacity as high as 1000 mAh/g can be maintained when charged at 100 mA/g current density for more than 100 cycles. This investigation provides a new strategy/method for synthesizing advanced electrode materials for LIBs.

5.6 References

- 1 J. B. Goodenough and Y. Kim, *Chem. Mater.*, 2010, 22, 587.
- 2 V. Etacheri, R. Marom, R. Elazari, G. Salitra and D. Aurbach, *Energy Environ. Sci.*, 2011, 4, 3243.
- 3 H. Q. Li and H. S. Zhou, *Chem. Commun.*, 2012, 48, 1201.
- 4 Z. Y. Wang, L. Zhou and X. W. Lou, *Adv. Mater.*, 2012, 24, 1903.
- 5 P. G. Bruce, B. Scrosati and J. M. Tarascon, *Angew. Chem., Int. Ed.*, 2008, 47, 2930.
- 6 R. Alcántara, P. Lavela, J. L. Tirado, R. Stoyanova, and E. Zhecheva, *J. Electrochem. Soc.* 1998, 145, 730.
- 7 R. Alcántara, M. Jaraba, P. Lavela, J. L. Tirado, Ph. Biensan, A. de Guibert, C. Jordy, and J. P. Peres, *Chem. Mater.* 2003, 15, 2376.
- 8 R. Alcántara, M. Jaraba, P. Lavela, and J. L. Tirado, *J. Solid State Chem.* 2002, 166, 330.
- 9 A. V. Chadwick, S. L. Savin, S. Fiddy, R. Alcantara, D. F. Lisbona, P. Lavela, G. Ortiz, and J. L. Tirado, *J. Phys. Chem. C* 2007, 111, 4636.
- 10 C. Vidal-Abarca, P. Lavela, and J. L. Tirado, *J. Phys. Chem. C*, 2010, 114, 12828.
- 11 M. J. Aragón, C. P. Vicente, and J. L. Tirado, *Electrochem. Commun.* 2007, 9, 1744.
- 12 M. J. Aragón, B. León, C. P. Vicente, J. L. Tirado, A. V. Chadwick, A. Berko, and S. Y. Beh, *Chem. Mater.* 2009, 21, 1834.
- 13 K. Saravanan, M. Nagarathinam, P. Balaya, and J. J. Vittal, *J. Mater. Chem.* 2010, 20, 8329.
- 14 S. Mirhashemihaghighi, B. León, and J. R. de Paz, *Inorg. Chem.* 2012, 51, 5554–5560
- 15 L. J. Wang, B. Liu, S. H. Ran, L. M. Wang, L. N. Gao, F. Y. Qu, D. Chen and G. Z. Shen, *J. Mater. Chem. A*, 2013, 1, 2139.
- 16 L. F. Hu, L. M. Wu, M. Y. Liao, X. H. Hu and X. S. Fang, *Adv. Funct. Mater.*, 2012, 22, 998.
- 17 B. Liu, J. Zhang, X. F. Wang, G. Chen, D. Chen, C. W. Zhou and G. Z. Shen, *Nano Lett.*, 2012, 12, 3005.
- 18 Z. Y. Wang, Z. C. Wang, W. T. Liu, W. Xiao and X. W. Lou, *Energy Environ. Sci.*, 2013, 6, 87.
- 19 S. H. Shen, P. H. Guo, D. A. Wheeler, J. G. Jiang, S. A. Lindley, C. X. Kronawitter, J. Z. Zhang, L. J. Guo and S. S. Mao, *Nanoscale*, 2013, 5, 9867–9874.
- 20 P. Sun, L. You, Y. F. Sun, N. K. Chen, X. B. Li, H. B. Sun, J. Ma and G. Y. Lu, *CrystEngComm*, 2012, 14, 1701–1708.
- 21 Q. Li, L. W. Yin, Z. Q. Li, X. K. Wang, Y. X. Qi and J. Y. Ma, *ACS Appl. Mater. Interfaces*, 2013, 5, 10975–10984.
- 22 J. F. Li, S. L. Xiong, X. W. Li and Y. T. Qian, *Nanoscale*, 2013, 5, 2045.
- 23 L. J. Wang, B. Liu, S. H. Ran, L. M. Wang, L. N. Gao, F. Y. Qu, D. Chen and G. Z. Shen, *J. Mater. Chem. A*, 2013, 1, 2139.
- 24 J. F. Li, S. L. Xiong, X. W. Li and Y. T. Qian, *J. Mater. Chem.*, 2012, 22, 23254.
- 25 M. Gao, X. Cui, R. Wang, T. Wang, and W. Chen. *J. Mater. Chem. A*, 2015, 3, 14126–14133.
- 26 X. Niu, H. Wei, W. Liu, S. Wang, J. Zhang and Y. Yang. *RSC Adv.*, 2015, 5, 33615–33622.

-
- 27 K. Xu, Chem. Rev., 2004, 104, 4303.
 - 28 E. Peled, J. Electrochem. Soc., 1979, 126, 2047.
 - 29 D. Aurbach, J. Power Sources, 2000, 89, 206.
 - 30 R. S. Jayashree, and P. V. J.Kamath, Appl. Electrochem. 1999, 29, 449-454.
 - 31 M. Dixit, P. V. Kamath, V. G.Kumar, N. Munichandraiah, and A. K. J. Shukla, Power Sources 1996, 63, 167-171.
 - 32 W. Salant and L.E. Wise. J. Biol. Chem. 1916, 28, 27-58.
 - 33 O. Berkh, L. Burstein, Y. Shacham-Diamand, and E. Giladi. Journal of The Electrochemical Society, 2011, 158, 85-91.

Chapter 6 Electrochemical deposition of LiMn_2O_4 on Reduced Graphene Oxides for LIBs

6.1 Introduction

The development of lithium ion batteries (LIBs) is revolutionary and has flourished in the past two decades because of the increasing demands of electrical devices and the booming growth of nano technology.^{1,2,3} Because they are safe, have a long cycle life, high energy and high power density, lithium ion batteries have been attracting significant interest from academics and industrial professionals. Many efforts have been made to improve LIBs' electrochemical performance in areas including cyclability, capacity, energy, and power density.^{4,5,6} Research has shown that conventional LIBs were mainly limited by their cathode electrode material, LiCoO_2 .^{7,8,9} As a result, Li–Mn–O compounds such as LiMn_2O_4 ^{10,11} and LiMnO_2 ^{12,13} were proposed to replace LiCoO_2 . In particular, spinel LiMn_2O_4 is one of the most promising cathode candidates due to its intrinsic high theoretical capacity, high voltage vs Li/Li^+ , abundant availability, and safety. But there are still a lot of challenges to be resolved before LiMn_2O_4 can be used as a cathode of LIBs.

Nano technology is widely adopted to improve the performance of LiMn_2O_4 because the nano structure of LiMn_2O_4 has large surface areas, which can reduce the lithium ion migration path, which is critical to a good rate performance. Lee et al. successfully synthesized ultrathin nanowires with a 5-10 nm diameter, which can deliver 100 and 78 mAh/g at 60C and 150C, respectively.¹⁴ Nano rods of LiMn_2O_4 were fabricated by Ahn et al.¹⁵ These hollow nano rods exhibit a higher capacity (110 mAh/g) and less capacity retention (81%) after 100 cycles. Porous morphology is also beneficial to the performance of electrode materials because it can achieve the nano-sized effect without other shortcomings, such as high strain/stress during lithiation/delithiation and aggregation of nano particles. The porous LiMn_2O_4 nano-rods had a longer cycle life and maintained 86% capacity after 500 cycles.¹⁶ Mesoporous LiMn_2O_4 crystals inherited the mesoporous structure of their precursor—mesoporous MnCO_3 and were able to deliver 192 mAh/g and maintained more than 90 mAh/g capacity after 100 cycles.¹⁷

Although researchers have synthesized LiMn_2O_4 crystals that perform exceptionally well, the complicated and expensive synthesis routes hinder the path of commercial and industrial applications. Usually, a two-step synthesis process is necessary: precursors such as MnCO_3 , MnO_2 or Mn_2O_3 are fabricated using a hydrothermal process and then LiOH powders are mixed with precursors and calcined under a high temperature (>700 °C). It is very important to cultivate a simple and economic way to fabricate LiMn_2O_4 that delivers the desired performance. The dynamic floating

electrodeposition (DFE) method is a feasible one-step method to prepare electrode materials. The DFE method was successfully applied to fabricate MnCO_3 single crystals and Co-MnCO_3 crystals as discussed in previous chapters. The easy set-up and adjustable parameters make this method highly promising for commercialization. However, lithium salts usually have high melting points and strong covalent bonds which cannot be easily broken up in an aqueous solution. It seems that DFE cannot be used to synthesize the cathode material of LIBs.

Recently Deng et al. developed a eutectic molten-salt method to reduce the melting point of mixed lithium salts to 200°C .¹⁸ This method could be integrated with the DFE method developed from this thesis investigation to fabricate lithium manganese oxides (MnOs). The eutectic molten-salt method can improve the rate of reaction because of the enhanced diffusion and reaction kinetics at high temperatures.¹⁹ In this research, the Li-containing molten-salt bath developed by Deng et al. is used for DFE to synthesize lithium manganese oxides. The whole synthesis process was carried out at 210°C in a relatively short processing time (five hours). The structural design and the DFE in eutectic molten lithium salts system in this work will provide new ideas for developing advanced materials for energy storage systems.

6.2 Experimental

6.2.1 Material synthesis

GO preparation: The graphite oxide was synthesized from natural graphite powders according to a modified Hummers method.^{20,21} The exfoliation of graphite oxide to GO was achieved after two hours of sonication (Branson 2510, 1000 W, 20% amplitude). After that, GOs were filtered and rinsed with deionized water. Finally, a homogeneous GO in a deionized water solution (2.0 mg/mL) was obtained and used for electrodeposition.

Synthesis of graphene-wrapped MnCO₃ MSCs by DFE method: The DFE was carried out by a Gamry PC4/750 potentiostat/galvanostat. Three electrode were used in DFE system. Ag/AgCl was used as the reference electrode. Platinum sheet with dimensions of 20 mm × 10 mm was used as anode. Ferritic stainless steel plate with dimensions of 20 mm × 10 mm × 1 mm was used as cathode. The plating current density was set to 30mA/cm². Plating solution used was 0.3 M sodium citrated and 0.3 M MnSO₄. The pH value of solution was adjusted to 7.0. After introducing 40 mL GO solution into a 1L plating solution, Teflon-coated stirring bar was used to agitate solution at 700 rpm 70°C. After four hours electrodeposition, deionized water filtration and 10 hours freeze-dried graphene-wrapped MnCO₃ MSCs were obtained

Synthesis of Porous LiMn₂O₄ polycrystalline: Porous LiMn₂O₄ crystals were synthesized by a eutectic molten salt electrodeposition method. For 10 minutes, 1.0g MnCO₃ MSCs, 8.0g LiOH and 38.0g LiNO₃ were mixed in a grinder. The mixed chemicals were transferred into a 400-ml beaker which was immersed into an oil bath. The mixed chemicals were stirred and heated to 210 °C for one hour. Three electrodeposition current densities, 50mA/cm², 70mA/cm², and 100mA/cm², were applied between two electrodes which are stainless steel cathode and platinum mesh (anode). The length of plating time was controlled to four hours. After plating, the chemicals were poured into distilled water, which was cooled to room temperature and filtrated to obtain the as-synthesized LiMn₂O₄ crystals.

6.2.2 Characterization

The morphology and structure of graphene-wrapped porous LiMn₂O₄ crystals were analyzed using scanning electron microscopy (SEM) (Zeiss EVO SEM equipped with a Bruker Silicon Drift Detector for Energy Dispersive X-Ray analysis) and transmission electron microscopy (TEM) (JEOL 2010 attached with a 4pi EDXS system). X-ray Diffraction (XRD) analyses were conducted on a Siemens D5000 X-ray diffractometer with Cu K α as the radiation source ($\lambda= 1.5418 \text{ \AA}$).

6.2.3 Electrochemical measurement

The electrochemical experiments were performed using 2032-type coin cells. To prepare the working electrodes, graphene-wrapped porous LiMn_2O_4 polycrystalline, Super-C65 carbon black, and polyvinylidene fluoride with a mass ratio of 90:6:4 were mixed homogeneously in N-methyl pyrrolidone (NMP). The obtained slurry was pasted onto Al foils, vacuum dried at 120°C overnight, and pressed. The total loading mass of the material on Al foil was then determined to be $\sim 15 \text{ mg/cm}^2$. After the foil was cut into a disk with 15 mm diameter, the electrodes were assembled in an Argon-filled glove box. Lithium metal foil was used as counter electrode, Celgard 2500 was used as separator and 1M LiPF₆ in ethylene carbonate/diethyl carbonate/dimethyl carbonate (EC/DEC/DMC, vol 1:1:1) (MTI Corporation) was used as electrolyte. cyclic voltammetry (CV) tests and cycle performance tests were carried out at $22 \pm 1^\circ\text{C}$ using a 1470E multi potentiostat/celltest system (Solartron).

6.3 Results and Discussion

6.3.1 Synthesis and structural analysis

Figure 6-1 illustrates the steps involved in synthesizing LiMn_2O_4 polycrystallines. First, the rice-shaped MnCO_3 mesoporous single crystals (MSCs) prepared using the method described in Chapter 3 were mixed with the lithium salts (LiNO_3 and LiOH) in a beaker. The mixture was then heated to 210°C and stirred at that temperature for

one hour to allow the dispersion of MnCO₃ MSCs in the eutectic molten lithium salts solution and the diffusion of lithium salts into the porous MnCO₃ MSCs. After stirring for one hour, electroplating was performed to electrodeposit LiMn₂O₄ polycrystalline at different current densities (50 mA/cm², 70 mA/cm² and 100mA/cm²). The deposition was achieved through the following chemical reactions according to the experience of synthesizing Mn₂O₃ and LiMn₂O₄.²²

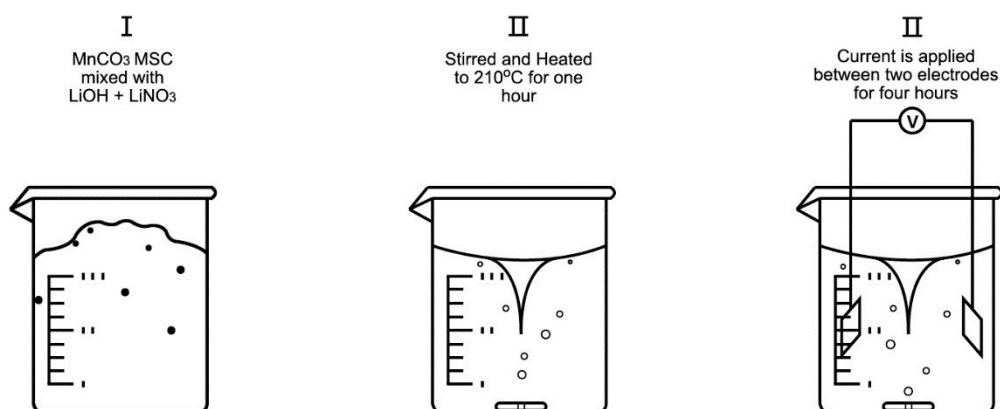
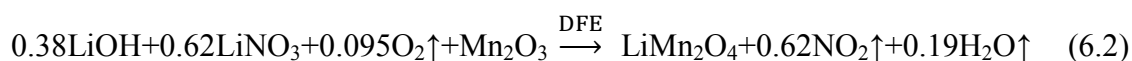


Figure 6-1. The schematic diagram of DFE in a eutectic molten salt solution.

The structure of the as-synthesized products from molten salt electrodeposition was analyzed first by X-ray diffraction (XRD). For comparison, Figure 6-2 displays the diffraction patterns of the precursor, MnCO₃ mesoporous single crystals (MSCs). The diffraction peaks of the original precursor are sharp, but the peaks of the final products fabricated under different electrodeposition current densities are wider than MnCO₃ precursor which suggests that the original single crystal structure was

destructured or transformed to new polycrystalline particles. The XRD results of the products obtained under low current densities ($50\text{mA}/\text{cm}^2$ and $70\text{mA}/\text{cm}^2$) are same and are identified as Mn_2O_3 crystal according to PDF#01-071-0636. However, all the diffraction peaks of the product obtained from electrodeposition at high current density correspond to LiMn_2O_4 crystals (PDF#01-53-1236); no other peaks, such as Mn_2O_3 diffraction peaks, appear. This means that 1.0 g MnCO_3 single crystals can be fully oxidized to LiMn_2O_4 crystals within four hours of electrodeposition. The cell parameter is 8.24 \AA (calculated by the Jade software), which is close to the standard value of 8.20 \AA . This demonstrates that LiMn_2O_4 with good crystallinity can be obtained from this low temperature molten salt electrodeposition.

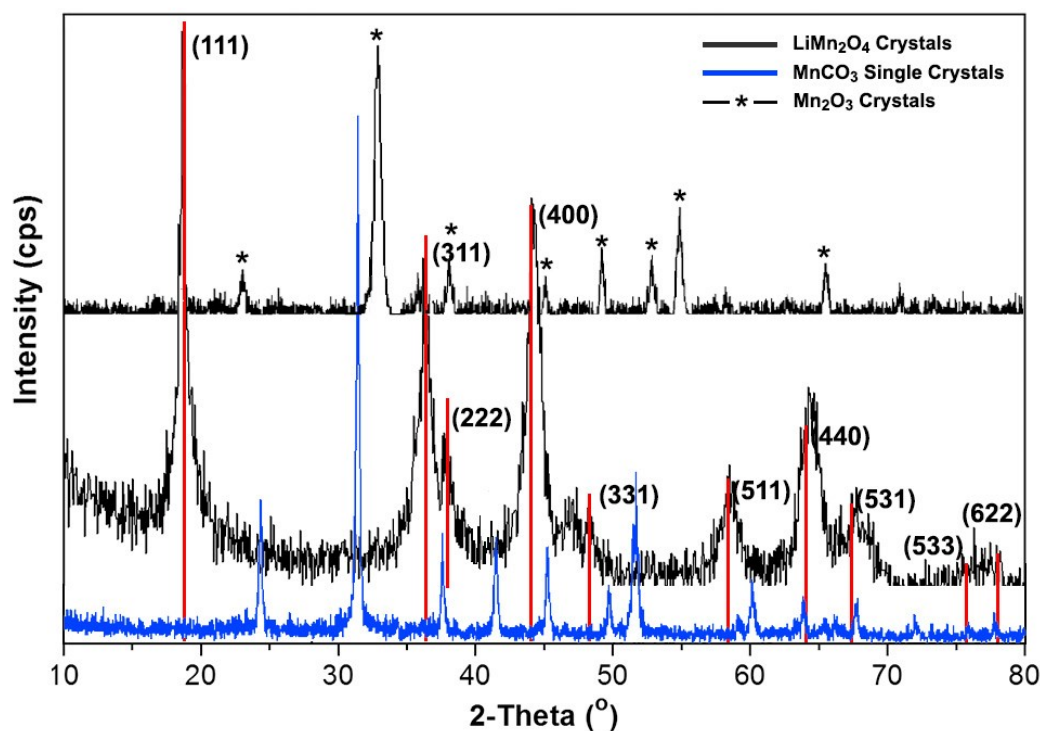


Figure 6-2. XRD results of final products of eutectic electrodeposition under 50, 70 and 100mA/cm² electrodeposition current densities. The precursor MnCO₃ MSCs are shown in blue. XRD patterns of products from 50 and 70 mA/cm² electrodeposition current densities are the same, they are Mn₂O₃ crystals. The XRD peaks of the product from 100mA/cm² are shown in red denoted peaks.

6.3.2 Morphology

Figure 6-3 displays the SEM images of as-synthesized spinel LiMn₂O₄ crystals from the DFE method at 210°C. As shown in Figure 6-3, the LiMn₂O₄ particles have an irregular shape which is not like the rice-like shape of their precursor MnCO₃ MSCs. These crystals are aggregated together but the average sizes are around 100 nm, which is much smaller than the MnCO₃ MSCs. The surface morphology of these particles

cannot be resolved clearly by SEM because of SEM's resolution limit and because most of particles are wrapped tightly by reduced graphene oxide sheets. The small size of the LiMn_2O_4 crystals could be a result of the internal straining and gas evolution induced by thermal decomposition and electrochemical reactions during electrodeposition. The internal straining and gas emission can destroy the original porous single crystal structure and make the precursor grains disintegrate into nano-sized particles.

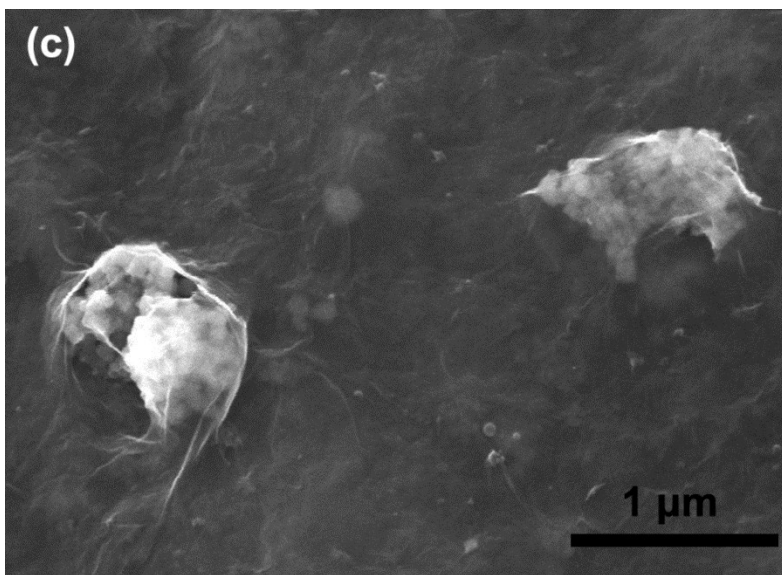
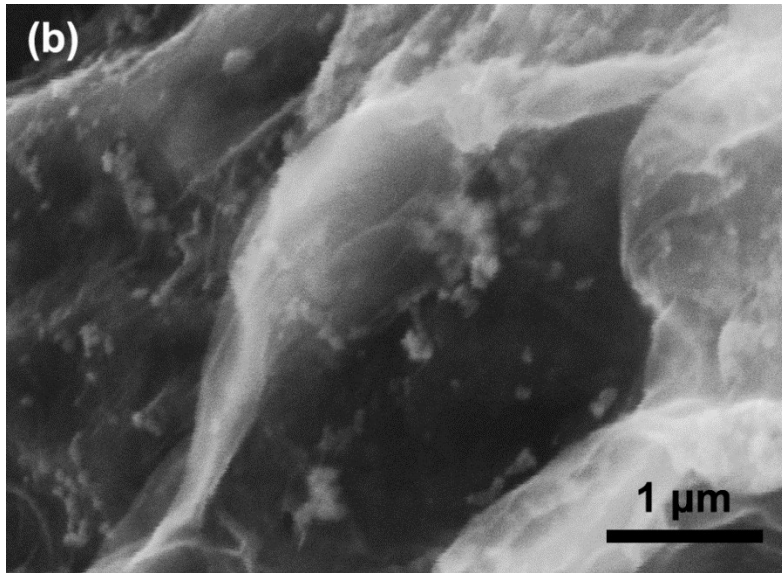
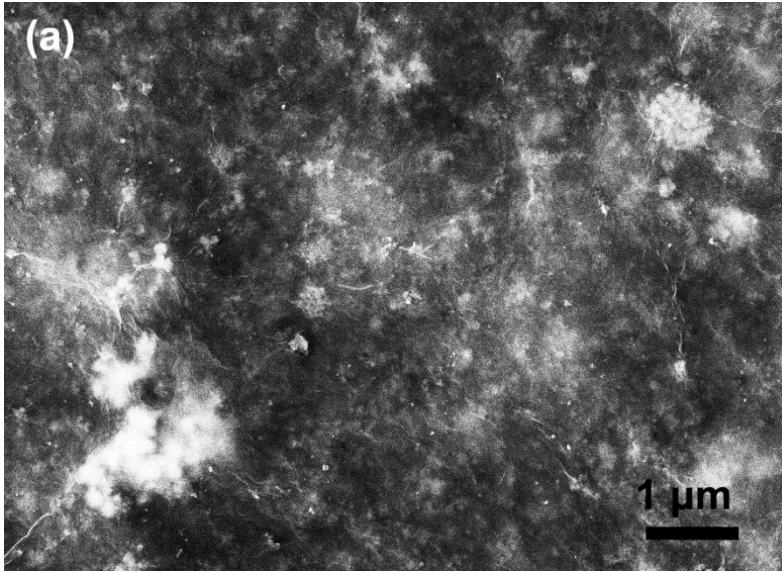


Figure 6-3. SEM image of as-synthesized graphene-wrapped LiMn_2O_4 crystals by different magnifications. These products are fabricated under $100\text{mA}/\text{cm}^2$ electrodeposition current density at 210°C .

TEM and selected area electron diffraction (SAED) were used to investigate the morphology and structure of LiMn_2O_4 crystals. As shown in Figure 6-4 (a), Figure 6-4(c) and Figure 6-4(e), morphologies of these crystals are porous, which inherited from their precursor and/or was formed from LiMn_2O_4 crystals fracture because of NO_2 gas emissions during electrodeposition. The LiMn_2O_4 particles are around 100 nm which is consistent with SEM observations. The SAED pattern demonstrates that this polycrystalline structure of the final product is different from its precursor MnCO_3 as displayed in Figure 6-4 (b), Figure 6-4(d), and Figure 6-4(e). The measured diffraction rings from different areas are the same, and one set of rings has been used to determine the structure of the as-synthesized products. According to electron diffraction PDF card #881087, the d-spacings of the four main rings are (111), (311), (400), and (511) crystal planes, which is consistent with the XRD results. This further confirms the spinel LiMn_2O_4 crystal structure. LiMn_2O_4 crystals obtained from electrodeposition in molten salts consist of small nano-sized clusters. This structure is similar to their precursor, which is composed of loosely packed nanorods. Such a structure possesses large surface areas and can reduce the path of diffusion for lithium ions during the charging/discharging process.

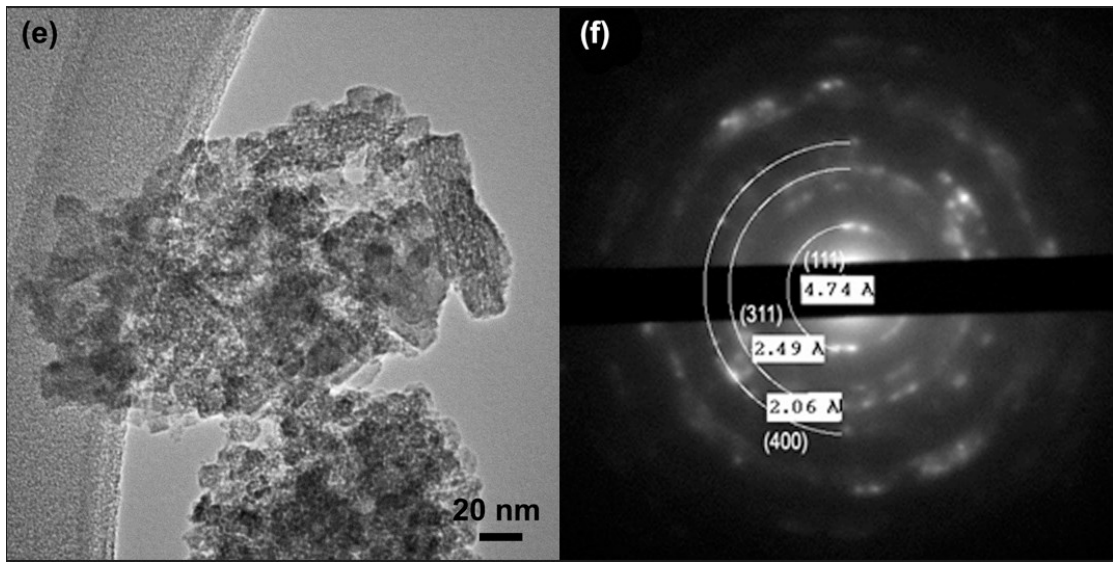
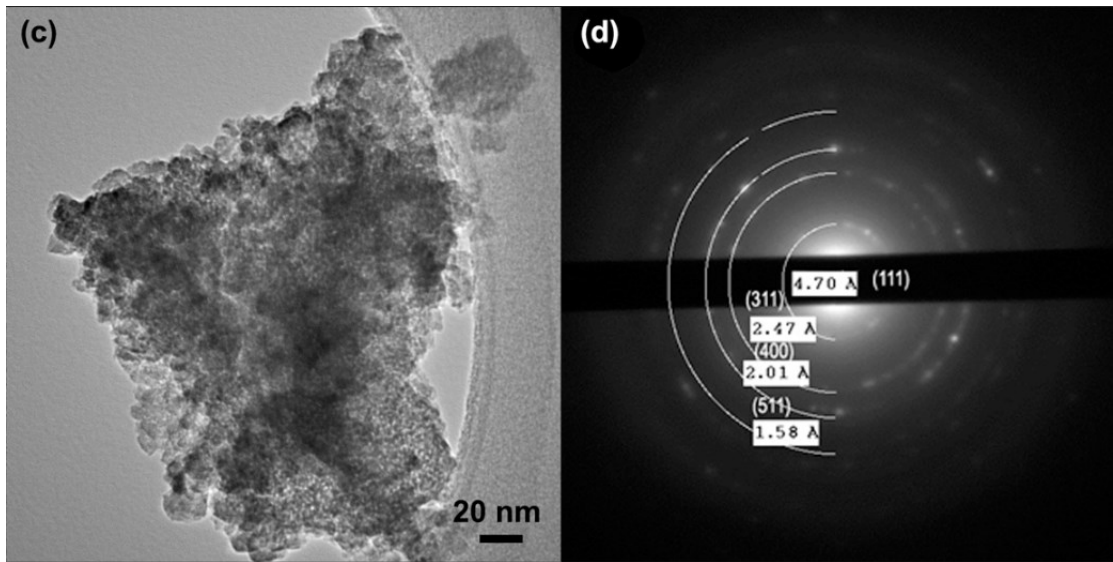
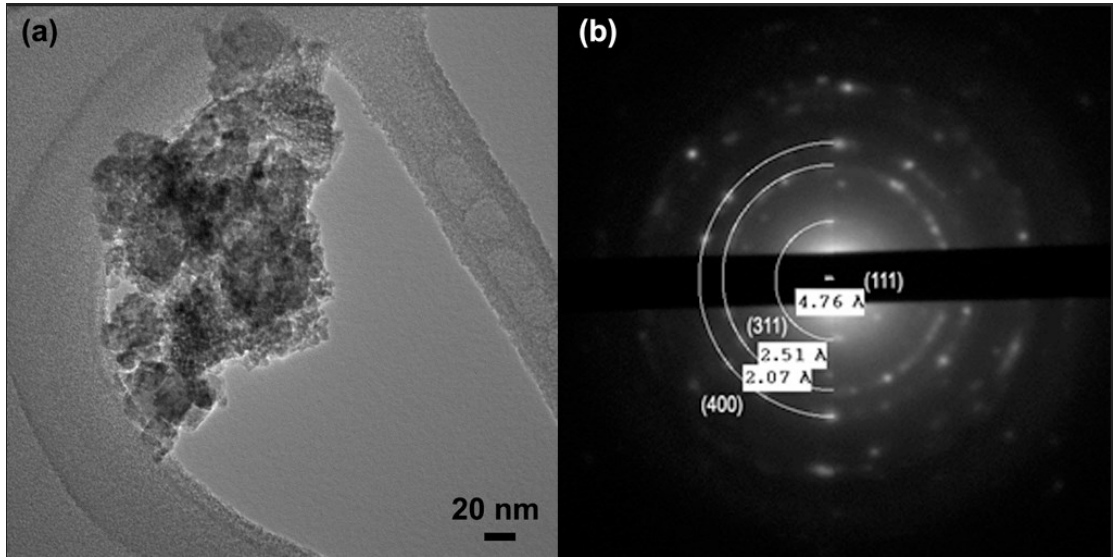


Figure 6-4. TEM images of LiMn_2O_4 polycrystalline and LiMn_2O_4 polycrystalline selected area electron diffraction patterns. (a), (c), and (e) are morphology images of products from 100 mA/cm^2 electrodeposition current density at 210°C . (b), (d), and (f) are SAED results of samples in the (a), (c), and (e) areas respectively.

6.3.3 Electrochemical performance of LiMn_2O_4 Crystals

The electrochemical lithiation/delithiation behavior of porous spinel LiMn_2O_4 was examined by cyclic voltammetry (CV) tests and galvanostatic charge–discharge cycling using coin cells. As shown in Figure 6-5(a), two pairs of separated redox peaks are clearly observed from the thick industrial grade electrode ($100 \mu\text{m}$), suggesting that lithium ions were extracted from and inserted into the spinel phase in a two-step process. The extraction/insertion of Li^+ ions from/into the 8a sites of the tetrahedral which is displayed in Figure 1-5 of Chapter 1.2.2 (Spinel-type LiMn_2O_4) with Li-Li interaction at $4.09/3.94 \text{ V}$ (vs. Li/Li^+) and that from/into the other 8a sites of the tetrahedral without Li-Li interaction at $4.21/4.07 \text{ V}$ (vs. Li/Li^+)²³. From the CV curves, porous spinel LiMn_2O_4 exhibits high symmetrical redox peaks, revealing a high crystallinity of the spinel LiMn_2O_4 and superior reversibility of Li^+ ions being transported through interface of spinel LiMn_2O_4 in bulk material. This is also consistent with the two charge/discharge plateaus in the first charge/discharge curves plotted in Figure 6-5(b). These two plateaus are ascribed to a two-phase transition of $\text{Li}_{0.5}\text{Mn}_2\text{O}_4/\text{LiMn}_2\text{O}_4$ at about 3.94 V vs. Li/Li^+ and $\lambda\text{-MnO}_2/\text{Li}_{0.5}\text{Mn}_2\text{O}_4$ at about

4.07 V vs. Li/Li⁺ respectively.²⁴ The first total discharge capacity of porous spinel LiMn₂O₄ is about 130 mAh/g, but the second discharge capacity drops to 117 mAh/g with 90% coulombic efficiency. This low coulombic efficiency of the first discharge capacity is caused by the solid electrolyte interphase (SEI) formation during the first charge/discharge cycling.^{25,26} However, the following coulombic efficiency can reach to almost 100% which proves the good reversibility of electrode materials as shown in Figures 6-5(b) and (d).

To evaluate their power capability, the porous LiMn₂O₄ crystals from the molten salt electrodeposition were cycled at different charge–discharge current densities (1 to 4C). Figure 6-5(c) shows the rate performance of the porous LiMn₂O₄ crystal in a thick industrial-grade electrode. Under a rate of 2C, capacity of LiMn₂O₄ is 63 mAh/g, which is almost half of the capacity under the 1C discharging rate (117 mAh/g). Even under a rate of 4C, a discharge capacity of 45 mAh/g can still be obtained. When the discharging rate is decreased from 4C to 1C, the discharge capacity can go back up to 114 mAh/g. Compared with other commercial electrodes, the rate capability of porous LiMn₂O₄ crystal is prominent, indicating its superior reversibility. This superior reversibility also manifests that the porous structure of electrode materials has an excellent ability to accommodate large volume changes of active materials during charging/discharging as provided by the wrapping of crystals by RGOs. The trend of cycle performance of porous LiMn₂O₄ crystal is similar to that of other electrode materials synthesized by the DFE method as shown in Figure 6-5(d). The capacity

drops quickly at the first several cycles but can go back to a higher value during subsequent cycling. After 50 cycles at 1C this electrode still maintain a specific capacity of 118 mAh/g, which proves a good cyclability of the porous LiMn_2O_4 crystal electrode.

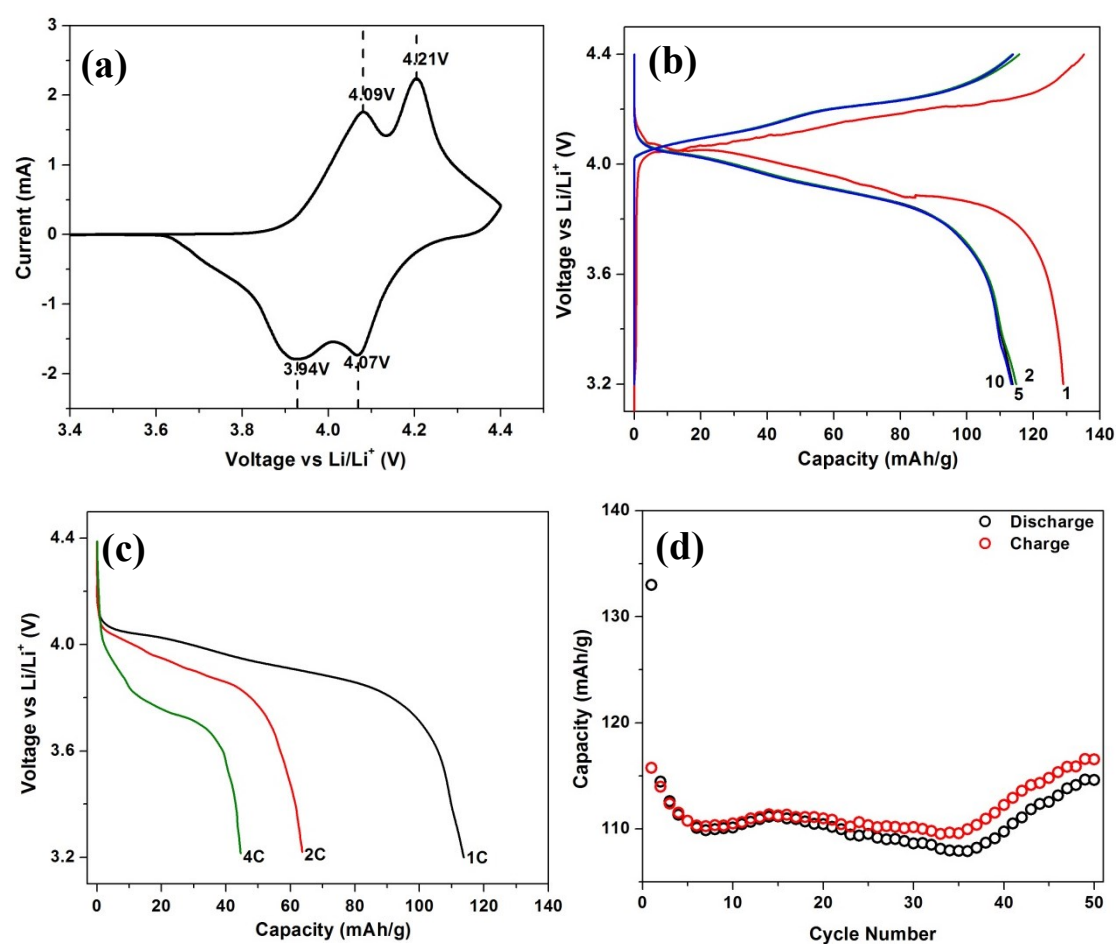


Figure 6-5. (a) CV results of a porous spinel LiMn_2O_4 electrode at a scan rate of 0.50 mV/s. (b) Galvanostatic charge/discharge curves of the porous spinel LiMn_2O_4 crystals from the first to 10th cycles. (c) Galvanostatic discharge curves of the porous spinel LiMn_2O_4 crystals at different discharging rates. (d) Cycle performance of porous spinel LiMn_2O_4 crystals under 1C rate.

This superior reversibility also manifests that the porous structure of electrode materials has an excellent ability to accommodate large volume changes of active materials during charging/discharging as provided by the wrapping of crystals by RGOs. The trend of cycle performance of porous LiMn_2O_4 crystal is similar to that of other electrode materials synthesized by the DFE method as shown in Figure 6-5(d). The capacity drops quickly at the first several cycles but can go back to a higher value during subsequent cycling. After 50 cycles at 1C this electrode still maintain a specific capacity of 118 mAh/g, which proves a good cyclability of the porous LiMn_2O_4 crystal electrode.

6.3.3 Discussion of Morphology Mechanism

The transformation mechanism by eutectic molten salt electrodeposition has also been investigated. Samples obtained from different reaction times were selected for analysis. Figure 6-6 (a) and Figure 6-6 (b) are TEM images and SAED patterns of the product obtained after electrodeposition for an hour. It is evident that the MnCO_3 precursor still keeps its original rice-like shape and is wrapped by reduced graphene oxide sheets. However, the pores on the surface of MnCO_3 crystals under high magnification show the disintegration of the porous crystal. Consequently, the electron diffraction pattern is featured with diffraction dots and weak rings, instead of one set of a dot pattern of a single crystal (reciprocal lattice).

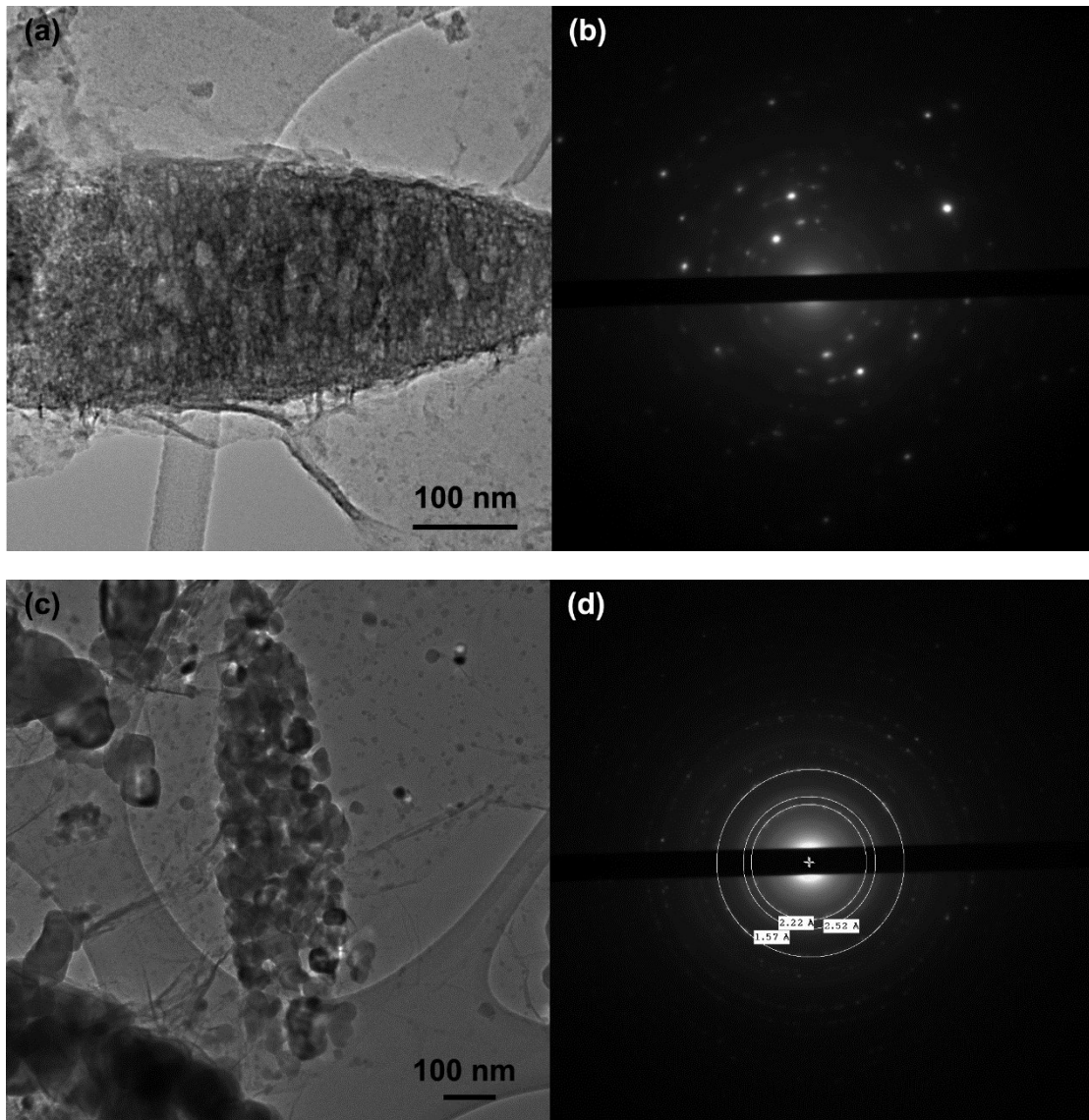


Figure 6-6. (a) TEM image of samples from the eutectic molten salt electrodeposition process after an hour reaction under $100\text{mA}/\text{cm}^2$ electrodeposition current density at 210°C . (b) SAED result of samples from the area as shown in (a). (c) TEM image of samples from eutectic molten salt electrodeposition process after a two-hour reaction under $100\text{mA}/\text{cm}^2$ electrodeposition current density at 210°C . (d) SAED result of samples from the area as shown in (c).

After electrodeposition for two hours, samples from molten salt were washed and filtered for characterization. As shown in Figure 6-6 (c) and Figure 6-6 (d), the whole MnCO_3 crystal grain disintegrated into many smaller particles with irregular shapes, although these small particles are still held together in a rice-like shape. The porous network of the original rice-shaped particle disappeared. No pores were observed on the surface of individual nano particles after disintegration. The SAED pattern corresponding to the disintegrated nano-particles features a typical ring structure, indicating the nano polycrystalline nature of the particles after disintegration. The d-spacing of these rings was determined to be consistent with that of cubic Mn_2O_3 crystals (PDF#01-071-0636).

Figure 6-7 shows the process of the formation and disintegration of the electrochemical products obtained during electrodeposition in the eutectic molten salt bath. The information in the figure is based on the characterizations described in the preceding paragraphs. The MnCO_3 mesoporous single crystals are mixed up with LiOH and LiNO_3 salts and are heated to 210°C for an hour to achieve a homogenous salt solution. The initial two-hour electrodeposition leads to the decomposition and disintegration of single crystal MnCO_3 MSCs into nano Mn_2O_3 crystals. The subsequent two-hour electrodeposition allows the electrochemical reaction of Mn_2O_3 with LiOH and LiNO_3 to form spinel porous LiMn_2O_4 polycrystalline. It seems that the porous structure found on the individual LiMn_2O_4 crystal is not inherited from the precursor, but results from the reaction between Mn_2O_3 and the LiOH - LiNO_3 salts.

This is because the surface of the Mn_2O_3 crystals obtained from the decomposition and disintegration of MnCO_3 MSCs is non-porous before the LiMn_2O_4 -formation. It is believed that the generation of NO_2 gas when the Mn_2O_3 crystals react with the LiOH - LiNO_3 salts at the anode might be responsible for the porous formation. The complete conversion of the individual Mn_2O_3 particle to LiMn_2O_4 may require multiple impingements of the Mn_2O_3 particle onto the anode because of the particle's short anode contact time, which creates dense pores on the surface of the crystals. A similar situation has been found during the synthesis of MnCO_3 MSCs as described in Chapter 3.

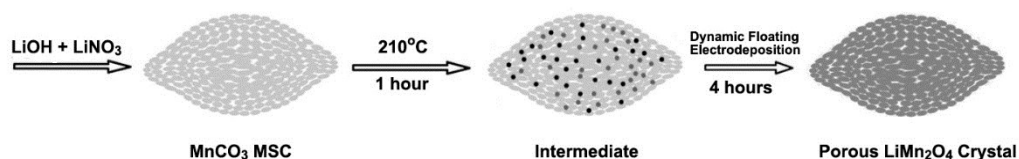


Figure 6-7. The schematic diagram of the porous LiMn_2O_4 polycrystalline formation process.

6.4 Conclusions

A facile and economic method has been developed to fabricate porous LiMn_2O_4 polycrystalline. It is a two-step electrodeposition process consisting of the DFE electrodeposition to form MnCO_3 MSCs, as described in Chapter 2, and the formation of LiMn_2O_4 polycrystalline in a Li-containing eutectic molten salt bath. The synthesized product, spinel porous LiMn_2O_4 polycrystalline, exhibited the desired rate

capability and cyclability. The specific discharge capacity reached 117, 63, and 45 mAh/g at 1, 2 and 4C, respectively. The good rate performance and cyclability are believed to be rooted to the porous and nano nature of LiMn₂O₄ polycrystalline that favors to a fast Li intercalation/deintercalation, and the graphene wrapping of the LiMn₂O₄ polycrystalline particles that provides a good electric conductivity of the active materials. Furthermore, the good performance of porous LiMn₂O₄ polycrystalline makes it promising as a better cathode material for LIBs. This work also provides new ideas for developing high performance energy storage systems.

6.5 References

-
- 1 G. J. Jeong, Y. U. Kim, Y. J. Kim and H. J. Sohn, *Energy Environ. Sci.*, 2011, 4, 1986-2002.
 - 2 M. Winter and R. J. Brodd, *Chem. Rev.*, 2004, 104, 4245–4270.
 - 3 J. Chen and F. Cheng, *Acc. Chem. Res.*, 2009, 42, 713–723.
 - 4 F. Cheng and J. Chen, *Chem. Soc. Rev.*, 2012, 41, 2172–2192.
 - 5 F. Cheng, J. Liang, Z. Tao and J. Chen, *Adv. Mater.*, 2011, 23, 1695–1715.
 - 6 M. S. Islam and C. A. J. Fisher, *Chem. Soc. Rev.*, 2014, 43, 185–204.
 - 7 W.A. Van Schalkwijk, B. Scrosati (Eds.), *Advances in Lithium-Ion Batteries*, Kluwer Acad./Plenum Publ, New York, USA, 2002.
 - 8 J. Fua, Y. Baia,b, C. Liua, H. Yua, Y. Mo. *Materials Chemistry and Physics*, 2009, 115, 105 – 109.
 - 9 Z. Chen, and J.R. Dahn, *Electrochim. Acta*, 2004, 49, 1079-1090.
 - 10 Y. Yang, C. Xie, R. Ruffo, H. Peng, D. K. Kim, Y. Cui, *Nano Lett.* 2009, 9, 4109–4114.
 - 11 C. M. Lieber, *Solid State Commun.* 1998, 107, 607–616.
 - 12 P. He, H. Yu, D. Li and H. Zhou, *J. Mater. Chem.*, 2012, 22, 3680–3695.
 - 13 T. J. Kim, D. Son, J. Cho and B. Park, *J. Power Sources*, 2006, 154, 268–272.
 - 14 H.W. Lee, P. Muralidharan, R. Ruffo, C. M. Mari, Y. Cui, and D. K. Kim, *Nano Lett.* 2010, 10, 3852—3856.
 - 15 D. Ahna, J. Gimc, N. Shina, Y. M. Koo, J. Kimc, and T. J. Shina, *Electrochimica Acta.* 2010, 55, 8888 – 8893.
 - 16 D. K. Kim , P. Muralidharan , H. W. Lee , R. Ruffo , and Y. Yang , C. K. Chan ,

-
- H. Peng , R. A. Huggins , Y. Cui , *Nano Lett.* 2008 , 8 , 3948-3952 .
- 17 F. Jiao , J. Bao , A. H. Hill , P. G. Bruce , *Angew. Chem. Int. Ed.* 2008 , 47 , 9711-9716.
- 18 Y. Deng, Y. Zhou, Z. Shi, X. Zhou, X. Quanc and G. Chen. *J. Mater. Chem. A*, 2013, 1, 8170–8177
- 19 Z. R. Chang, Z. J. Chen, F. Wu, X. Z. Yuan and H. J. Wang, *Electrochim. Acta*, 2009, 54, 6529-6535.
- 20 W. S. Hummers Jr, R. E. Offeman, *J. Am. Chem. Soc.*, 1958, 80, 1339-1339.
- 21 T. Chen, B. Zeng, J. L. Liu, J. H. Dong, X. Q. Liu, Z. Wu, X. Z. Yang, Z. M. Li, *J. Phys. Conf. Ser.*, 2009, 188, 012051.
- 22 L. Zhou, D. Y. Zhao and X. W. Lou, *Angew. Chem., Int. Ed.*, 2012, 51, 239-241.
- 23 M. M. Thackeray , W. I. F. David , P. G. Bruce , and J. B. Goodenough , *Mater. Res. Bull.* 1983 , 18 , 461-472 .
- 24 Y. Y. Xia and M. Yoshio, *J. Electrochem. Soc.*, 1996, 143, 825-833.
- 25 K. Xu, *Chem. Rev.*, 2004, 104, 4303-4418.
- 26 E. Peled, *J. Electrochem. Soc.*, 1979, 126, 2047-2051.

Chapter 7 General conclusions and recommendations

A summary of main conclusions obtained from this thesis investigation is given below.

The summary includes both the synthesis of manganese-based electrode materials using the Dynamic Floating Electrodeposition (DFE) method and the electrochemical evaluation and structural characterization of the electrode materials obtained.

7.1 Dynamic Floating Electrodeposition (DFE) for the synthesis of manganese-based electrode materials

1. Electrodeposition is an effective way to synthesize MnO_2 -CNTs composites under atmospheric pressure and at low temperatures, which can reduce the fabrication cost of electrode materials and at the same time improve the performance of lithium ion batteries (LIBs). The amount of manganese oxides (MnOs) decorated on carbon nanotubes (CNTs) per unit weight can be controlled by plating time and current density. TEM analyses revealed that the deposited MnO on the wall of CNTs was MnO_2 .
2. For the first time, Dynamic Floating Electrodeposition (DFE) was used to synthesize manganese carbonates/graphene composites. The reduction of GOs to RGOs, the deposition of MnCO_3 mesoporous single crystals (MSCs) on graphene,

and graphene-wrapped morphology, all three goals in one electrochemical process were achieved by DFE. This method makes it possible for a large amount of MSCs to be effectively wrapped by reduced graphene oxides consisting of a few graphene sheets as clearly shown in SEM images. TEM results revealed the mesoporous morphology and rhombohedral single crystals of the as-synthesized deposits.

3. DFE can be utilized to synthesize Co-doped MnCO_3 crystals wrapped by reduced graphene oxide sheets. The structure and the morphology of the Co-doped MnCO_3 crystals can be easily controlled by adjusting ionic ratios of Co over Mn in the electrolyte and/or by altering electrodeposition current density. The shape of as-synthesized products can be controlled from a rice-like shape to a dumbbell-like shape. A higher cobalt concentration in a plating solution can facilitate the substitution of manganese ions in host crystals.
4. Porous LiMn_2O_4 crystals can also be fabricated by DFE methods in a molten lithium salt bath at 210°C . This involves a two-step electrodeposition process consisting of the DFE electrodeposition to form the MnCO_3 MSCs precursor, and the formation of LiMn_2O_4 crystals in a Li-containing eutectic molten salt bath. The success of the electrodeposition of LiMn_2O_4 has extended the use of the DFE method for fabricating new electrode materials.

7.2 Electrochemical evaluations of electrode materials synthesized by Dynamic Floating Electrodeposition.

1. By adjusting electrodeposition current density, a different weight ratio of MnO₂-functionalized CNTs composites was obtained. The weight percentage of MnO₂ in the MnO₂-CNTs composite was 63% when electrodeposition current density was at 30 mA/cm². This weight percentage was the lowest compared to other conditions (70 mA/cm²: 77%; 90 mA/cm²: 91%). The MnO₂-CNTs composite prepared by electrodeposition at 70 mA/cm² has a relatively higher discharging voltage plateau, around 0.5V. In addition, the capacity of MnO₂-CNTs composite was as high as 1003 mAh/g. Although this value of capacity was not the highest compared to other samples obtained in different conditions (30mA/cm²: 1445 mAh/g; 90mA/cm²: 585 mAh/g), it exhibited the best cyclability, which was determined to be more than 100 cycles.
2. The resulting submicron, graphene-wrapped MnCO₃ MSCs from the DFE method reached a high reversible capacity of 900 mAh/g after the initial cycle and delivered over 1,000 mAh/g after 130 cycles. In addition, the reversible capacity was maintained at this high level for more than 400 cycles, and maintained 422 mAh/g at a high rate of 5,000 mA/g. This was also the first time that this level of performance was achieved on MnCO₃ for lithium-ion storage. The superior electrochemical performance was found to be highly related to the novel structure obtained. The graphene-wrapped MnCO₃ MSCs are able to

deliver high capacities because of the easy transformation of the single crystal structure to the amorphous structure during cycling. The high cyclability was achieved because of the effects of graphene-wrapping of the active materials.

3. GWA MnO_x composites showed distinct microstructural features and demonstrated excellent electrochemical performance when they were used in pseudocapacitors and cycled in the potential range of 0.7 – 2.8 V vs Li/Li^+ . The highest capacitance was measured to be 430 F/g at a sweeping rate of 0.2 mV/s. A capacitance of 200 F/g was also obtained under a high sweeping rate of 10 mV/s. After 400 cycles, the capacitance of GWA manganese oxide composites reached 91% of the original value (306 F/g), and was maintained at a level of 86% even after 2,000 cycles. It was found, for the first time, that GWA MnO_x composites presented high performance, pseudo-capacitive lithium-ion storage between 0.7 – 2.8 V, due to their unique graphene-wrapped amorphous structure. When coupled with lithium-doped graphite anodes, this composite material demonstrated pseudo-capacitive lithium-ion storage superior to that of $\text{Li}_4\text{Ti}_5\text{O}_{12}$ and Nb_2O_5 .
4. The Co-MnCO_3 crystals with a dumbbell-like shape exhibited outstanding electrochemical performance as integrated electrodes for lithium-ion batteries. The specific capacities can reach to 400 mAh/g at the high current density of 1000mA/g. And a capacity as high as 1000 mAh/g can be maintained when charged at 100 mA/g current density for more than 100 cycles. This investigation

provides a new strategy/method for synthesizing advanced electrode materials for LIBs.

5. The spinel porous LiMn_2O_4 polycrystalline synthesized by DFE exhibited a much improved rate capability and cyclability. The specific discharge capacity reached 117.0, 63.0 and 45.0 mAh/g at 1, 2 and 4C, respectively. The good rate performance and cyclability are believed to be rooted to the porous and nano nature of LiMn_2O_4 polycrystalline that is favorable to a fast Li intercalation/deintercalation, and the graphene wrapping of the LiMn_2O_4 polycrystalline particles that provides good electric conductivity of the active materials.

7.3 Recommendations

1. For the electrodeposition of MnO_x on the wall of CNTs, additional work is needed to explore how CNTs with different functional groups can affect the shape, structure, and amount of deposited MnO_x crystals and the performances of the composites obtained.
2. It is recommended to fabricate other types of metal carbonates or metal oxides, such as MnO_x , CoO_x , NiO_x , by using the DFE methods being developed in current investigations.
3. The electrochemical performance of cobalt-doped MnCO_3 crystals could be

further optimized. A broader range of plating conditions including the amount of ions in the plating solution and electrodeposition current densities could be investigated. Also, Co-MnCO_3 crystals can be used as electrodes for pseudocapacitors because of their unique morphologies, which are capable of rapid ion diffusion.

4. The mechanisms of electrodeposition in molten salts need to be further explored. A broader ratio of a precursor over the remaining electrolytes should be investigated to explore new products with better electrochemical performances. Finally, Co-MnCO_3 crystal can also be used as precursor in molten salts electrodeposition to synthesize $\text{Co-LiMn}_2\text{O}_4$ crystals. These morphologies and electrochemical performances also need to be investigated.

References

- 1 International Energy Agency, Coal statistics, <http://www.iea.org/statistics/topics/coal/>.
- 2 Enerdata, Global Energy Statistical Yearbook 2016, <https://yearbook.enerdata.net/>
- 3 EIA report, Analysis of the Impacts of the Clean Power Plan, <http://www.eia.gov/analysis/requests/powerplants/cleanplan/>.
- 4 International Energy Agency, Energy Balances of OECD Countries (2013) and Energy Balances of Non-OECD Countries (2013), <http://www.iea.org/statistics/online-dataservice>.
- 5 M. Sughantha, P. A. Ramakrishnan, A. M. Hermann, C. P. Warmsingh and D. S. Ginley, *Int. J. Hydrogen Energy*, 2003, 28, 597–600.
- 6 N. Kijima, Y. Takahashi, J. Akimoto and J. Awaka, *J. Solid State Chem.*, 2005, 178, 2741–2750.
- 7 F. Jiao and P. G. Bruce, *Adv. Mater.*, 2007, 19, 657–660.
- 8 Q. Liu, S. Wang and H. Cheng, *Int. J. Electrochem. Sci.*, 2013, 8, 10540–10548.
- 9 S. Wang, Q. Liu, J. Yu and J. Zeng, *Int. J. Electrochem. Sci.*, 2012, 7, 1242–1250.
- 10 F. Cheng, J. Zhao, W. Song, C. Li, H. Ma, J. Chen and P. Shen, *Inorg. Chem.*, 2006, 45, 2038–2044
- 11 S. Jouanneau, S. Sarciaux, A. Le Gal La Salle and D. Guyomard, *Solid State Ionics*, 2001, 140, 223–232.
- 12 W. M. Dose and S. W. Donne, *J. Power Sources*, 2014, 247, 852–857.
- 13 J. Chen and F. Cheng, *Acc. Chem. Res.*, 2009, 42, 713–723.
- 14 C. Li, F. Cheng, W. Ji, Z. Tao and J. Chen, *Nano Res.*, 2009, 2, 713 – 721.
- 15 F. Cheng, J. Chen, X. Gou and P. Shen, *Adv. Mater.*, 2005, 17, 2753–2756.
- 16 S. Chou, F. Cheng and J. Chen, *J. Power Sources*, 2006, 162, 727–734.
- 17 Z. Yang, J. Liang, F. Cheng, Z. Tao and J. Chen, *Microporous Mesoporous Mater.*, 2012, 161, 40–47.
- 18 M. R. Palacin, *Chem. Soc. Rev.*, 2009, 38, 2565–2575.
- 19 J. Maier, *Nat. Mater.*, 2005, 4, 805–815.
- 20 J. Liu, F. Liu, K. Gao, J. S. Wu and D. F. Xue, *J. Mater. Chem.*, 2009, 19, 6073-6084.
- 21 F. Chen, Z. Tao, J. Liang and J. Chen, *Chem. Mater.*, 2008, 20, 667-681.
- 22 Y. Wang and J. Y. Lee, *Angew. Chem., Int. Ed.*, 2006, 45, 7039-7042.
- 23 W. van Schalkwijk, and B. Scrosati (Eds.), *Advances in Lithium-ion Batteries*, Kluwer Academic/Plenum, Boston, 2004.
- 24 M. Yoshio, R. J. Brodd, and A. Kozawa, *Lithium batteries, science and technologies*. Springer, New York, 2009.
- 25 U. Sacken, E. Nodwell, A. Sundher, J.R. Dahn, *Power Sources*, 1995, 54, 240-245.
- 26 H. Ota, Y. Sakata, X. Wang, J. Sasahara, and Eiki Yasukawa, *J. Electrochem. Soc.* 2004, 151, 437-446.
- 27 Y. Sun, X. Hu, W. Luo, F. Xia and Y. Huang, *Adv. Funct.Mater.*, 2013, 23, 2436–

- 2444.
- 28 X. Zhang, F. Cheng, J. Yang and J. Chen, *Nano Lett.*, 2013, 13, 2822–2825.
- 29 N. Yabuuchi, K. Yoshii, S. T. Myung, I. Nakai and S. Komaba, *J. Am. Chem. Soc.*, 2011, 133, 4404–4419.
- 30 D. Zeng, J. Cabana, W. S. Yoon and C. P. Grey, *Chem. Mater.*, 2010, 22, 1209–1219.
- 31 F. Jiao and P. G. Bruce, *Adv. Mater.*, 2007, 19, 657–660.
- 32 J. Zhao, Z. Tao, J. Liang and J. Chen, *Cryst. Growth Des.*, 2008, 8, 2799–2805.
- 33 H. Wang, L. Cui, Y. Yang, H. Sanchez Casalongue, J. T. Robinson, Y. Liang, Y. Cui and H. Dai, *J. Am. Chem. Soc.*, 2010, 132, 13978–13980.
- 34 H. Jiang, Y. Hu, S. Guo, C. Yan, P. S. Lee and C. Li, *ACS Nano*, 2014, 8, 6038–6046.
- 35 T. J. Kim, D. Son, J. Cho and B. Park, *J. Power Sources*, 2006, 154, 268–272.
- 36 S. B. Schougaard, J. Breger, M. Jiang, C. P. Grey and J. B. Goodenough, *Adv. Mater.*, 2006, 18, 905–909.
- 37 F. Cheng, H. Wang, Z. Zhu, Y. Wang, T. Zhang, Z. Tao and J. Chen, *Energy Environ. Sci.*, 2011, 4, 3668–3675.
- 38 D. Choi, D. Wang, I. T. Bae, J. Xiao, Z. Nie, W. Wang, V. V. Viswanathan, Y. J. Lee, J. G. Zhang, G. L. Graff, Z. Yang and J. Liu, *Nano Lett.*, 2010, 10, 2799–2805.
- 39 P. Poizot, S. Laruelle, S. Grugeon, L. Dupont, and J. M. Tarascon, *Nature.*, 2000, 407, 496–499.
- 40 X. Yu, Y. He, J. Sun, K. Tang, H. Li, L. Chen and X. Huang, *Electrochem. Commun.*, 2009, 11, 791–794.
- 41 K. Zhong, B. Zhang, S. Luo, W. Wen, H. Li, X. Huang and L. Chen, *J. Power Sources*, 2011, 196, 6802–6808.
- 42 X. Li, D. Li, L. Qiao, X. Wang, X. Sun, P. Wang and D. He, *J. Mater. Chem.*, 2012, 22, 9189–9194.
- 43 M. M. Thackeray, W. I. F. David, P. G. Bruce and J. B. Goodenough, *Mater. Res. Bull.*, 1983, 18, 461–472.
- 44 M. M. Thackeray, P. J. Johnson, L. A. de Picciotto, P. G. Bruce and J. B. Goodenough, *Mater. Res. Bull.*, 1984, 19, 179–187.
- 45 J. M. Tarascon and D. Guyomard, *J. Electrochem. Soc.*, 1991, 138, 2864–2868.
- 46 J. M. Tarascon, E. Wang, F. K. Shokoohi, W. R. McKinnon and S. Colson, *J. Electrochem. Soc.*, 1991, 138, 2859–2864.
- 47 F. Jiao, J. Bao, A. H. Hill and P. G. Bruce, *Angew. Chem., Int. Ed.*, 2008, 47, 9711–9716.
- 48 D. K. Kim, P. Muralidharan, H.-W. Lee, R. Ruffo, Y. Yang, C. K. Chan, H. Peng, R. A. Huggins and Y. Cui, *Nano Lett.*, 2008, 8, 3948–3952.
- 49 S. M. Bak, K. W. Nam, C. W. Lee, K. H. Kim, H. C. Jung, X. Q. Yang and K. B. Kim, *J. Mater. Chem.*, 2011, 21, 17309–17315.
- 50 D. Linden and T. B. Reddy, *Handbook of Batteries*, McGraw-Hill, New York, 2002.
- 51 R. M. Dell and D. A. J. Rand, *Understanding Batteries*, Royal Society of Chemistry, Cambridge, 2001.

- 52 R. Kotz, S. Muller, M. Bartschi, B. Schnyder, P. Dietrich, F. N. Buchi, A. Tsukada, G. G. Scherer, P. Rodatz, O. Garcia, P. Barrade, V. Hermann and R. Gally, *Electrochemical Society Proceedings*, 2001, 21, 564-575.
- 53 X. Dong, W. Shen, J. Gu, L. Xiong, Y. Zhu, H. Li and J. Shi, *J. Phys. Chem. B*, 2006, 110, 6015-6019.
- 54 W. Sugimoto, H. Iwata, Y. Murakami and Y. Takasu, *J. Electrochem. Soc.*, 2004, 151, 1181-1187.
- 55 M. S. Wu and P. C. Chiang, *Electrochem. Solid-State Lett.*, 2004, 7, 123-126.
- 56 B. E. Conway, *Electrochemical Supercapacitors*, Kluwer Academic/Plenum Press, New York, 1999
- 57 G. Wang, L. Zhang and J. Zhang, *Chem. Soc. Rev.*, 2012, 41, 797–828
- 58 Y. Zhang, H. Feng, X. Wu, L. Wang, A. Zhang, T. Xia, H. Dong, X. Li and L. Zhang, *Int. J. Hydrogen Energy*, 2009, 34, 4889-4899.
- 59 B. E. Conway, V. Birss and J. Wojtowicz, *J. Power Sources*, 1997, 66, 1-14
- 60 C. Ming Chuang, C. W. Huang, H. Teng and J. M. Ting, *Energy Fuels*, 2010, 24, 6476-6482.
- 61 A. Burke, *J. Power Sources*, 2000, 91, 37-50.
- 62 M. Kisacikoglu, M. Uzunoglu and M. Alam, *Int. J. Hydrogen Energy*, 2009, 34, 1497-1507.
- 63 S. Ma, K. Nam, W. Yoon, X. Yang, K. Ahn, K. Oh and K. Kim, *Electrochem. Commun.*, 2007, 9, 2807-2811.
- 64 G. Wang, L. Zhang and J. Zhang, *Chem. Soc. Rev.*, 2012, 41, 797–828.
- 65 V. Subramanian, H. Zhu and B. Wei, *J. Power Sources*, 2006, 159, 361–364.
- 66 C. C. Hu and T. W. Tsou, *Electrochem. Commun.*, 2002, 4, 105–109.
- 67 E. Macheaux, T. Brousse, D. Be´langer and D. Guyomard, *J. Power Sources*, 2007, 165, 651–655.
- 68 S. W. Donne, A. F. Hollenkamp and B. C. Jones, *J. Power Sources*, 2010, 195, 367–373.
- 69 H. Xia, J. Feng, H. Wang, M. O. Lai and L. Lu, *J. Power Sources*, 2010, 195, 4410–4413.
- 70 E. Beaudrouet, A. Le Gal La Salle and D. Guyomard, *Electrochim. Acta*, 2009, 54, 1240–1248.
- 71 H. K. Lee, D. Sakemi, R. Selyanchyn, C. G. Lee and S. W. Lee, *ACS Appl. Mater. Interfaces*, 2014, 6, 57–64.
- 72 S. Devaraj, H. Y. Liu and P. Balaya, *J. Mater. Chem. A*, 2014, 2, 4276–4281.
- 73 Q. Li, L. W. Yin, Z. Q. Li, X. K. Wang, Y. X. Qi and J. Y. Ma, *ACS Appl. Mater. Interfaces*, 2013, 5, 10975–10984.
- 74 G. N. Zhang, L. Zheng, M. Zhang, S. H. Guo, Z. H. Liu, Z. P. Yang and Z. L. Wang, *Energy Fuels*, 2012, 26, 618–623.
- 75 T. Kokubu, Y. Oaki, H. Uchiyama, E. Hosono, H. Zhou and H. Imai, *Chem.–Asian J.*, 2010, 5, 792-798.
- 76 M. M. Thackeray, H. K. Sun, S. J. Christopher, J. T. Vaughey, R. Benedek and S. A. Hackney, *J. Mater. Chem.*, 2007, 17, 3112-3125.
- 77 M. M. Thackeray, W. I. F. David, P. G. Bruce and J. B. Goodenough, *Mater. Res.*

- Bull., 1983, 18, 461-472.
- 78 H. Uchiyama, E. Hosono, H. Zhou and H. Imai, *J. Mater. Chem.*, 2009, 19, 4012-4016.
- 79 F. Dang, T. Hoshino, Y. Oaki, E. Hosono, H. Zhou and H. Imai, *Nanoscale*, 2013, 5, 2352-2357.
- 80 X. Niu, H. Wei, W. Liu, S. Wang, J. Zhang and Y. Yang, *RSC Adv.*, 2015, 5, 33615–33622.
- 81 L. Yu, L. Zhang, H. Wu, G. Zhang and X. Lou, *Energy Environ. Sci.*, 2013, 6, 2664–2671.
- 82 M. J. Aragón, B. León, C. Pérez Vicente and J. L. Tirado, *J. Power Sources*, 2011, 196, 2863–2866.
- 83 S. Lei, Z. Liang, L. Zhou and K. Tang, *Materials Chemistry and Physics* 2009, 113, 445–450.
- 84 H. Li, X. Zhang, R. Ding, L. Qi and H. Wang, *Electrochim. Acta*, 2013, 108, 497–505.
- 85 X. F. Chen, L. Qie, L. L. Zhang, W. X. Zhang and Y. H. Huang, *J. Alloys Compd.*, 2013, 559, 5–10
- 86 W. Kang, D. Y. W. Yu, W. Li, Z. Zhang, X. Yang, T. Ng, R. Zou, Y. Tang, W. Zhang and C. Lee, *Nanoscale*, 2015, 7, 10146
- 87 S. Devaraj, H. Y. Liuc and P. Balaya, *J. Mater. Chem. A*, 2014, 2, 4276–4281
- 88 A. L. M. Reddy, M. M. Shaijumon, S. R. Gowda and P. M. Ajayan, *Nano Lett.*, 2009, 9, 1002-1006.
- 89 H. Xia, M. Lai and L. Lu, *J. Mater. Chem.*, 2010, 20, 6896–6902.
- 90 H. Wang, L. Cui , Y. Yang, H. S.Casalongue, J. T. Robinson, Y. Liang, Y. Cui, and H. Dai, *J. Am. Chem. Soc.* 2010, 132, 13978–13980
- 91 A. Yu, H. W. Park, A. Davies, D. C. Higgins, Z. Chen, and X. Xiao, *J. Phys. Chem. Lett.* 2011, 2, 1855–1860.
- 92 C.S. Wang, G.T. Wu, W.Z. Li, *Journal of Power Sources* , 1998,76, 1–10.
- 93 C. Casas, W. Li, *Journal of Power Sources*,2012, 208, 74 - 85.
- 94 B. Peng, M. Locascio, P. Zapol, S. Li, S. L. Mielke, G. C. Schatz, H. D. Espinosa, *Nature Nanotechnology*, 2008, 3, 626–631.
- 95 S. Bellucci, *Physica Status Solidi C*, 2005, 2, 34-37.
- 96 L. Zhang and X. S. Zhao, *Chem. Soc. Rev.*, 2009, 38, 2520-2531.
- 97 S. Yang, J. Huo, H. Song, X. Chen, *Electrochimica Acta*, 2008, 53, 2238–2244.
- 98 K. Nishidate, M.Hasegawa, *Physical Review B*, 2005, 71, 1-6.
- 99 C. H. Mi, G. S. Cao, X. B. Zhao. *Journal of Electroanalytical Chemistry*. 2004, 562, 217-221.
- 100 H. Shimoda, B. Gao, X. P. Tang, A. Kleinhammes, L. Fleming, Y. Wu, O. Zhou, *Physical Review Letters*, 2002, 88, 015502,1-4.
- 101 L. Cui, Y. Yang, C. Hsu, Y. Cui, *Nano Letters*. 2009, 9, 3370-3374.
- 102 S. Liu, J. Zhang, K. Huang, J. Yu. *Journal of the Brazilian Chemical Society*. 2008, 19, 1078-1083.
- 103 X. Zhao, C. M. Hayner, H. H. Kung. *Journal of Materials Chemistry*. 2011, 21, 17297-17303.

- 104 W. Tang, X.J. Wang, Y.Y. Hou, L.L. Li, H. Sun, Y.S. Zhu, Y. Bai, Y.P. Wu, K. Zhu, T. van Ree, *Journal of Power Sources*. 2012, 198, 308-311.
- 105 C. Niu, E. K. Sichel, R. Hoch, D. Moy and H. Tennent, *Appl. Phys. Lett.*, 1997, 70, 1480-1482.
- 106 X. Cui, J. Chen, T. Wang and W. Chen, *Scientific Reports*, 2014, 4, 5310.
- 107 A. G. Pandolfo and A. F. Hollenkamp, *J. Power Sources*, 2006, 157, 11-27.
- 108 Y. B. Zhang, Y. W. Tan, H. L. Stormer, P. Kim, *Nature*, 2005, 438, 201–204.
- 109 V. I. Fal'ko, A. K. Geim, *The European Physical Journal—Special Topics*, 2007, 148, 1-3.
- 110 Y. Kopelevich, P. Esquinazi, *Advanced Materials*, 2007, 19, 4559–4563.
- 111 M. Pumera, *The Chemical Record*, 2009, 9, 211–223.
- 112 E. Yoo, J. Kim, E. Hosono, H. Zhou, T. Kudo, I. Honma, *Nano Letters*, 2008, 2277–2282.
- 113 P. Guo, H. H. Song, X. H. Chen, *Electrochemistry Communications*, 2009, 11, 1320–1324.
- 114 G. X. Wang, X. P. Shen, J. Yao, J. Park, *Carbon*, 2009, 47, 2049–2053.
- 115 S. R. C. Vivekchand, C. S. Rout, K. S. Subrahmanyam, A. Govindaraj, and C. N. R. Rao, *Journal of Chemical Sciences*, 2008, 120, 9–13.
- 116 Y. Wang, Z. Q. Shi, Y. Huang, Y. F. Ma, C. Y. Wang, M. M. Chen, and Y. S. Chen, *The Journal of Physical Chemistry C*, 2009, 113, 13103–13107.
- 117 Z. Wua, G. Zhou, L. Yin, W. Ren, F. Li, and H. Cheng, *Nano Energy*, 2012, 1, 107–131.
- 118 Z. Guo, K. Konstantinov, G. Wang, H. Liu, and S. Dou. *Journal of Power Sources*, 2003, 119, 221-225
- 119 Z. Fan, J. Chen, M. Wang, K. Cui, H. Zhou, and W. Kuang. *Diamond and Related Materials*, 2006, 9, 1478-1483.
- 120 W. Wei, W. Chen, and D. G. Ivey, *Journal of Power Sources*, 2009, 186, 428 - 434.
- 121 A. Anders, *Journal of Physics D-Applied Physics*, 2007,40.
- 122 G. Hodes, *Electrochemistry of Nanomaterials*; Wiley-VCH: Weinheim, Germany, 2001.
- 123 G. H. A. Therese, and P. V. Kamath, *Chem. Mater.* 2000, 12, 1195-1204.
- 124 M. Dixit, P. V. Kamath, V. G. Kumar, N. Munichandraiah, and A. K. J. Shukla, *Power Sources* 1996, 63, 167-171.
- 125 R. S. Jayashree, and P. V. J. Kamath, *Appl. Electrochem.* 1999, 29, 449-454.
- 126 K. R. J. Bullock, *Electroanal. Chem.* 1987, 222, 347-366.
- 127 E. J. Preisler, *Appl. Electrochem.* 1989, 19, 559-565.
- 128 A. Wold, and D. Bellavance, In *Preparative Methods in Solid State Chemistry*; Hagenmuller, P., Ed.; Academic Press: New York, 1972.
- 129 J. Tellefson, *Nature*, 2008, 456, 436-440.
- 130 W. Schalkwijk, B. Scrosati, *Advances in Lithium-ion Batteries*, Kluwer Academic/Plenum, Boston, 2004.
- 131 B. Scrosati, J. Garche, *Journal of Power Sources*, 2010, 195, 2419–2430.
- 132 G. Pistoia, *Lithium batteries : new materials, developments and perspectives*.

- Amsterdam ; London: Elsevier; 1994.
- 133 B. Gao, A. Kleinhammes, X. Tang, C. Bower, L. Fleming, Y. Wu, O. Zhou, *Chemical Physics Letters*, 1999, 307, 153-157.
- 134 F. Leroux, K. Metenier, S. Gautier, E. Frackowiak, S. Bonnamy, F. Beguin , *Journal of Power Sources*. 1999, 81, 317-322.
- 135 A. Claye, J. Fischer, C. Huffman, A. Rinzler, R. Smalley, *Journal of the Electrochemical Society*. 2000, 147, 2845-2852.
- 136 S. Yang, J. Huo, H. Song, X. Chen. *Electrochimica Acta*. 2008, 53, 2238-2244.
- 137 C. Mi, G. Cao, X. Zhao. *Journal of Electroanalytical Chemistry*. 2004, 562, 217-221.
- 138 K. Nishidate, M. Hasegawa, *Physical Review B*. 2005, 71, 245418.
- 139 V. Meunier, J. Kephart, C. Roland, J. Bernholc. *Physical Review Letters*, 2002, 88, 075506.
- 140 T. Kumar, R. Ramesh, Y. Lin, G. Fey. *Electrochemistry Communications*, 2004, 6, 520-525.
- 141 B. Gao, C. Bower, J. D. Lorentzen, L. Fleming, A. Kleinhammes, X. P. Tang, L. E. MnNeil, Y. Wu, O. Zhou, *Chemical Physics Letters*. 2000, 327, 69-75.
- 142 H. Shimoda, B. Gao, X. P. Tang, A. Kleinhammes, L. Fleming, Y. Wu, O. Zhou, *Physical Review Letters*, 2002, 88, 015502.
- 143 Z. Yang, H. Wu, *Materials Letters*, 2001, 50, 108-114.
- 144 G. Maurin, Ch. Bousquet, F. Henn , P. Bernier, R. Almairac, B. Simon, *Solid State Ionics*, 2000, 136, 1295-1299.
- 145 L. Cui, Y. Yang, C. Hsu, Y. Cui, *Nano Letters*, 2009, 9, 3370-3374.
- 146 X. Cui, W. Wei, W. Chen, *MRS Online Proceeding Library*, 2011, 1204.
- 147 J. H. Kim, K. H. Lee, L. J. Overzet, G. S. Lee. *Nano Letters*, 2011, 11, 2611-2617.
- 148 A. L. M. Reddy, M. M. Shaijumon, S. R. Gowda, P. M. Ajayan. *Nano Letters*, 2009, 9, 1002-1006.
- 149 H. Zhang, G. Cao, Z. Wang, Y. Yang, Z. Shi, Z. Gu. *Nano Letters*, 2008, 8, 2664-2668.
- 150 Y. M. Lin, P. R. Abel, A. Heller, C. B. Mullins, *J. Phys. Chem. Lett.*, 2011, 2, 2885-2891.
- 151 X. Jia, Z. Chen, X. Cui, Y. Peng, X. Wang, G. Wang, F. Wei, Y. Lu, *ACS Nano*, 2012, 6, 9911-9919.
- 152 Z. S. Wu, W. Ren, L. Wen, L. Gao, J. Zhao, Z. Chen, G. Zhou, F. Li, H. M. Cheng, *ACS Nano*, 2010, 4, 3187-3194.
- 153 J. S. Chen, T. Zhu, Q. H. Hu, J. Gao, F. Su, S. J. Qiao, X. W. Lou, *ACS Appl. Mater. Interfaces*, 2010, 2, 3628-3635.
- 154 Y. S. Lin, J. G. Duh, M. H. Hung, *J. Phys. Chem. C*, 2010, 14, 13136-13141.
- 155 J. Lin, Z. Peng, X. Xiang, G. Ruan, Z. Yan, D. Natelson, J. M. Tour, *ACS Nano*, 2013, 7, 6001-6006.
- 156 X. Zhou, L. J. Wan, Y. G. Guo, *Adv. Mater.*, 2013, 25, 2152-2157.
- 157 H. Xia, M. Lai, L. Lu, *J. Mater. Chem.*, 2010, 20, 6896-6902.
- 158 A. L. M. Reddy, M. M. Shaijumon, S. R. Gowda, P. M. Ajayan, *Nano Lett.* 2009,

- 9, 1002-1006.
- 159 L. Li, A. R. O. Raji, J. M. Tour, *Adv. Mater.*, 2013, 25, 6298- 6302.
- 160 Y. Sun, X. Hu, W. Luo, F. Xia, Y. Huang, *Adv. Funct. Mater.*, 2013, 23, 2436-2444.
- 161 J. Guo, Q. Liu, C. Wang, M. R. Zachariah, *Adv. Funct. Mater.*, 2012, 22, 803-811.
- 162 S. Lei, Z. Liang, L. Zhou, K. Tang, *Materials Chemistry and Physics*, 2009, 113, 445-450.
- 163 M. Zheng, H. Zhang, X. Gong, R. Xu, Y. Xiao, H. Dong, X. Liu, Y. Liu, *Nanoscale Research Letters*, 2013, 8, 166.
- 164 Y. Yan, Y. Zhu, Y. Yu, J. Li, T. Mei, Z. Zhu, Y. Qian, *J. Nanosci. Nanotechnol.*, 2012, 12, 7334-7338.
- 165 S. Devaraj, H. Y. Liu, P. Balaya, *J. Mater. Chem. A.*, 2014, 2, 4276-4281.
- 166 P. Poizot, S. Laruelle, S. Grugeon, L. Dupont, J-M. Tarascon, *Nature.*, 2000, 407, 496-499.
- 167 E. J. W. Crossland, N. Noel, V. Sivaram, T. Leijtens, J. A. Alexander-Webber, Snaith, H. J. *Nature*, 2013, 495, 215-219.
- 168 D. Su, S. Dou, G. Wang, *Nano Res.*, 2014, 7, 794-803.
- 169 D. Su, M. Ford, G. Wang, *Sci Rep.*, 2012, 2, 924.
- 170 J. Weickert, R. B. Dunbar, H. C. Hesse, W. Wiedemann, L. Schmidt-Mende, *Adv. Mater.*, 2011, 23, 1810-1828.
- 171 C. Dickinson, W. Zhou, R. P. Hodgkins, Y. Shi, D. Zhao, H. He, *Chem. Mater.*, 2006, 18, 3088-3095.
- 172 P. Yang, D. Zhao, D. I. Margolese, B. F. Chmelka, G. D. Stucky, *Nature*, 1998, 396, 152-155.
- 173 K. Jiao, B. Zhang, B. Yue, Y. Ren, S. Liu, S. Yan, C. Dickinson, W. Zhou, H. He, *Chem. Commun.*, 2005, 45, 5618-5620.
- 174 H. Wang, Y. Yang, Y. Liang, J. T. Robinson, Y. Li, A. Jackson, Y. Cui, H. Dai, *Nano Lett.* 2011, 11, 2644-2647.
- 175 C. Y. Su, A. Y. Lu, Y. Xu, F. R. Chen, A. N. Khlobystov, L. J. Li, *ACS Nano*, 2011, 5, 2332-2339.
- 176 X. Xu, D. Huang, H. Cao, M. Wang, S. M. Zakeeruddin, M. Gratzel, *Sci Rep.*, 2013, 3, 1489.
- 177 H. L. Guo, X. F. Wang, Q. Y. Qian, F. B. Wang, X. H. Xia, *ACS Nano*, 2009, 9, 2653-2659.
- 178 W. S. Hummers Jr, R. E. Offeman, *J. Am. Chem. Soc.*, 1958, 80, 1339-1339.
- 179 T. Chen, B. Zeng, J. L. Liu, J. H. Dong, X. Q. Liu, Z. Wu, X. Z. Yang, Z. M. Li, *J. Phys. Conf. Ser.*, 2009, 188, 012051.
- 180 W. Chen, L. Yan, and P. R. Bangal, *Carbon*, 2010, 48, 1146-1152.
- 181 O. Compton, D. A. Dikin, K. W. Putz, L. C. Brinson and S. T. Nguyen, *Advanced Materials*, 2010, 22, 892-896.
- 182 G. Trettenhahn, A. Koberl, *Electrochimica Acta.*, 2007, 52, 2716-2722.
- 183 X. Cui, J. Chen, T. Wang, W. Chen, *Sci Rep.*, 2014, 4, 5310.
- 184 Y. Deng, Y. Zhou, Z. Shi, X. Zhou, X. Quan, G. Chen, *J. Mater. Chem. A*, 2013, 1, 8170-8177.

- 185 J. Qu, L. Shi, C. He, F. Gao, B. Li, Q. Zhou, H. Hu, G. Shao, X. Wang, J. Qiu, *Carbon*, 2014, 66, 485-492.
- 186 H. Wang, L. Cui, Y. Yang, H. S. Casalongue, J. T. Robinson, Y. Liang, Y. Cui, H. Dai, *J. Am. Chem. Soc.*, 2010, 132, 13978-13980.
- 187 O. Delmer, P. Balaya, L. Kienle, J. Maier, *Adv. Mater.*, 2008, 20, 501-505.
- 188 K. Naoi, Y. Nagano, W. Naoi, *Tanso*, 2013, 256, 22-32.
- 189 V. Augustyn, J. Come, M. A. Lowe, J. W. Kim, P. L. Taberna, S. H. Tolbert, H. D. Abruna, P. Simon, B. Dunn, *Nature Materials*, 2013, 12, 518-522.
- 190 Y. Xiong, Y. Xie, Z. Li, C. Wu, *Chem-Eur J.*, 2003, 9, 1645-51.
- 191 H. Lai, J. Li, Z. Chen, Z. Huang, *ACS Appl. Mater. Interfaces*, 2012, 4, 2325-2328.
- 192 W. Li, K. Xu, B. Li, J. Sun, F. Jiang, Z. Yu, R. Zou, Z. Chen, J. Hu, *ChemElectroChem*, 2014, 1, 1003-1008.
- 193 Q. Chen, J. Tang, J. Ma, H. Zhang, N. Shinya, L. Qin, *Carbon*, 2011, 49, 2917 - 2925.
- 194 Gao, M. et al. *J. Mater. Chem. A*, 2015, 3, 14126-14133.
- 195 H. L. Guo, X. F. Wang, Q. Y. Qian, F. B. Wang, X. H. Xia, *ACS Nano*, 2009, 9, 2653-2659.
- 196 W. S. Hummers Jr, R. E. Offeman, *J. Am. Chem. Soc.*, 1958, 80, 1339-1339.
- 197 J. C. Carver, G. K. Schweitzer, T. A. Carlson, *J. Chem. Phys.*, 1972, 57, 973-982.
- 198 M. Chigane, M. J. Ishikawa, *Electrochem. Soc.*, 2000, 147, 2246-2251.
- 199 B. Djurfors, J. N. Broughton, M. J. Brett, D.G. Ivey, *Acta Mater.*, 2005, 53, 957-965.
- 200 M. Nakayama, A. Tanaka, Y. Sato, T. Tonosaki, K. Ogura, *Langmuir*, 2005, 21, 5907-5913.
- 201 Z. Li, J. Wang, L. Sheng, X. Liu, S. Yang, *Journal of Power Sources*, 2011, 196, 8160 - 8165.
- 202 H. Jiang, Y. Hu, S. Guo, C. Yan, P. S. Lee, C. Li, *ACS nano*, 2014, 8, 6038-6046.
- 203 J. Qu, L. Shi, C. He, F. Gao, B. Li, Q. Zhou, H. Hu, *Carbon*, 2014, 66, 485-492.
- 204 O. Delmer, P. Balaya, L. Kienle, J. Maier, *Adv. Mater.*, 2008, 20, 501-505.
- 205 H. Lindström, S. Sodergren, A. Solbrand, H. Rensmo, J. Hjelm, A. Hagfeldt, S. E. Lindquist, *J. Phys. Chem. B*, 1997, 101, 7717-7722.
- 206 R. Li, J. Liu, *Electrochimica Acta*, 2014, 120, 52-56.
- 207 K. Zhu, Q. Wang, J. H. Kim, A. A. Pesaran, A. J. Frank, *J. Phys. Chem. C*, 2012, 116, 11895-11899.
- 208 K. V. Sankar, S. Surendran. K. Pandi, A.M. Allin, V. D. Nithya, Y. S. Lee, R. K. Selvan, *RSC Adv.*, 2015, 5, 27649-27656.
- 209 H. Yin, C. Song, Y. Wang, S. Li, M. Zeng, Z. Zhang, Z. Zhu, K. Yu, *Electrochimica Acta*, 2013, 111, 762-770.
- 210 M. Park, M. Park, X. Zhang, M. Chung, G. B. Less, A. M. Sastry, *J. Power Sources*, 2010, 195, 7904-7929.
- 211 S. Ardizzone, G. Fregonara, S. Trasatti, *Electrochim. Acta*, 1990, 35, 263-267.
- 212 D. Baronetto, N. Krstajic, S. Trasatti, *Electrochim. Acta*, 1994, 39, 2359-2362.
- 213 Y. Cai, B. Zhao, J. Wang, Z. Shao, *Journal of Power Sources*, 2014, 253, 80-89.

- 214 G. Wang, B. Zhang, Z. Yu, M. Qu, *Solid State Ionics*, 2005, 176, 1169-1174.
- 215 F. Chen, R. Li, M. Hou, L. Liu, R. Wang, Z. Deng, *Electrochimica Acta*, 2005, 51, 61–65.
- 216 N. Zhang, Z. Liu, T. Yang, C. Liao, Z. Wang, K. Sun. *Electrochem. Commun.*, 2011, 13, 654-656.
- 217 K. Brezesinski, J. Wang, J. Haetge, C. Reitz, S. O. Steinmueller, S. H. Tolbert, B. M. Smarsly, B. Dunn, T. Brezensinski, *J. Am. Chem. Soc.*, 2010, 132, 6982–6990.
- 218 J. B. Goodenough and Y. Kim, *Chem. Mater.*, 2010, 22, 587.
- 219 V. Etacheri, R. Marom, R. Elazari, G. Salitra and D. Aurbach, *Energy Environ. Sci.*, 2011, 4, 3243.
- 220 H. Q. Li and H. S. Zhou, *Chem. Commun.*, 2012, 48, 1201.
- 221 Z. Y. Wang, L. Zhou and X. W. Lou, *Adv. Mater.*, 2012, 24, 1903.
- 222 P. G. Bruce, B. Scrosati and J. M. Tarascon, *Angew. Chem., Int. Ed.*, 2008, 47, 2930.
- 223 R. Alcántara, P. Lavela, J. L. Tirado, R. Stoyanova, and E. Zhecheva, *J. Electrochem. Soc.* 1998, 145, 730.
- 224 R. Alcántara, M. Jaraba, P. Lavela, J. L. Tirado, Ph. Biensan, A. de Guibert, C. Jordy, and J. P. Peres, *Chem. Mater.* 2003, 15, 2376.
- 225 R. Alcántara, M. Jaraba, P. Lavela, and J. L. Tirado, *J. Solid State Chem.* 2002, 166, 330.
- 226 A. V. Chadwick, S. L. Savin, S. Fiddy, R. Alcantara, D. F. Lisbona, P. Lavela, G. Ortiz, and J. L. Tirado, *J. Phys. Chem. C* 2007, 111, 4636.
- 227 C. Vidal-Abarca, P. Lavela, and J. L. Tirado, *J. Phys. Chem. C*, 2010, 114, 12828.
- 228 M. J. Aragón, C. P. Vicente, and J. L. Tirado, *Electrochem. Commun.* 2007, 9, 1744.
- 229 M. J. Aragón, B. León, C. P. Vicente, J. L. Tirado, A. V. Chadwick, A. Berko, and S. Y. Beh, *Chem. Mater.* 2009, 21, 1834.
- 230 K. Saravanan, M. Nagarathinam, P. Balaya, and J. J. Vittal, *J. Mater. Chem.* 2010, 20, 8329.
- 231 S. Mirhashemihaghighi, B. León, and J. R. de Paz. *Inorg. Chem.* 2012, 51, 5554–5560
- 232 L. J. Wang, B. Liu, S. H. Ran, L. M. Wang, L. N. Gao, F. Y. Qu, D. Chen and G. Z. Shen, *J. Mater. Chem. A*, 2013, 1, 2139.
- 233 L. F. Hu, L. M. Wu, M. Y. Liao, X. H. Hu and X. S. Fang, *Adv. Funct. Mater.*, 2012, 22, 998.
- 234 B. Liu, J. Zhang, X. F. Wang, G. Chen, D. Chen, C. W. Zhou and G. Z. Shen, *Nano Lett.*, 2012, 12, 3005.
- 1 Z. Y. Wang, Z. C. Wang, W. T. Liu, W. Xiao and X. W. Lou, *Energy Environ. Sci.*, 2013, 6, 87.
- 235 S. H. Shen, P. H. Guo, D. A. Wheeler, J. G. Jiang, S. A. Lindley, C. X. Kronawitter, J. Z. Zhang, L. J. Guo and S. S. Mao, *Nanoscale*, 2013, 5, 9867–9874.
- 236 P. Sun, L. You, Y. F. Sun, N. K. Chen, X. B. Li, H. B. Sun, J. Ma and G. Y. Lu, *CrystEngComm*, 2012, 14, 1701–1708.
- 237 Q. Li, L. W. Yin, Z. Q. Li, X. K. Wang, Y. X. Qi and J. Y. Ma, *ACS Appl. Mater. Interfaces*, 2013, 5, 10975–10984.
- 238 J. F. Li, S. L. Xiong, X. W. Li and Y. T. Qian, *Nanoscale*, 2013, 5, 2045.
- 239 L. J. Wang, B. Liu, S. H. Ran, L. M. Wang, L. N. Gao, F. Y. Qu, D. Chen and G. Z. Shen, *J. Mater. Chem. A*, 2013, 1, 2139.

- 240 J. F. Li, S. L. Xiong, X. W. Li and Y. T. Qian, *J. Mater. Chem.*, 2012, 22, 23254.
- 241 M. Gao, X. Cui, R. Wang, T. Wang, and W. Chen. *J. Mater. Chem. A*, 2015,3, 14126-14133.
- 242 X. Niu, H. Wei, W. Liu, S. Wang, J. Zhang and Y. Yang. *RSC Adv.*, 2015, 5, 33615–33622.
- 243 K. Xu, *Chem. Rev.*, 2004, 104, 4303.
- 244 E. Peled, *J. Electrochem. Soc.*, 1979, 126, 2047.
- 245 D. Aurbach, *J. Power Sources*, 2000, 89, 206.
- 246 R. S. Jayashree, and P. V. J.Kamath, *Appl. Electrochem.* 1999, 29, 449-454.
- 247 M. Dixit, P. V. Kamath, V. G.Kumar, N. Munichandraiah, and A. K. J. Shukla, *Power Sources* 1996, 63, 167-171.
- 248 W. Salant and L.E. Wise. *J. Biol. Chem.* 1916, 28, 27-58.
- 249 O. Berkh, L. Burstein, Y. Shacham-Diamand, and E. Gileadi. *Journal of The Electrochemical Society*,2011, 158, 85-91.
- 250 G. J. Jeong, Y. U. Kim, Y. J. Kim and H. J. Sohn, *Energy Environ. Sci.*, 2011, 4, 1986-2002.
- 251 M. Winter and R. J. Brodd, *Chem. Rev.*, 2004, 104, 4245–4270.
- 252 J. Chen and F. Cheng, *Acc. Chem. Res.*, 2009, 42, 713–723.
- 253 F. Cheng and J. Chen, *Chem. Soc. Rev.*, 2012, 41, 2172–2192.
- 254 F. Cheng, J. Liang, Z. Tao and J. Chen, *Adv. Mater.*, 2011, 23, 1695–1715.
- 255 M. S. Islam and C. A. J. Fisher, *Chem. Soc. Rev.*, 2014, 43, 185–204.
- 256 W.A. Van Schalkwijk, B. Scrosati (Eds.), *Advances in Lithium-Ion Batteries*, Kluwar Acad./Plenum Publ, New York, USA, 2002.
- 257 J. Fua, Y. Baia,b, C. Liua, H. Yua, Y. Mo. *Materials Chemistry and Physics*, 2009, 115, 105 – 109.
- 258 Z. Chen, and J.R. Dahn, *Electrochim. Acta*, 2004, 49, 1079-1090.
- 259 Y. Yang, C. Xie, R. Ruffo, H. Peng, D. K. Kim, Y. Cui, *Nano Lett.* 2009, 9, 4109–4114.
- 260 C. M. Lieber, *Solid State Commun.* 1998, 107, 607–616.
- 261 P. He, H. Yu, D. Li and H. Zhou, *J. Mater. Chem.*, 2012, 22, 3680–3695.
- 262 T. J. Kim, D. Son, J. Cho and B. Park, *J. Power Sources*, 2006, 154, 268–272.
- 263 H.W. Lee, P. Muralidharan, R. Ruffo, C. M. Mari, Y. Cui, and D. K. Kim, *Nano Lett.* 2010, 10, 3852—3856.
- 264 D. Ahna, J. Gimc, N. Shina, Y. M. Koo, J. Kimc, and T. J. Shina, *Electrochimica Acta.* 2010, 55, 8888 – 8893.
- 265 D. K. Kim , P. Muralidharan , H. W. Lee , R. Ruffo , and Y. Yang , C. K. Chan ,